MICROMECHANICS MODELING OF THE MULTIFUNCTIONAL NATURE OF CARBON NANOTUBE-POLYMER NANOCOMPOSITES

A Dissertation

by

GARY DON SEIDEL

Submitted to the Office of Graduate Studies of
Texas A&M University
in partial fulfillment of the requirements for the degree of

DOCTOR OF PHILOSOPHY

August 2007

Major Subject: Aerospace Engineering

MICROMECHANICS MODELING OF THE MULTIFUNCTIONAL NATURE OF CARBON NANOTUBE-POLYMER NANOCOMPOSITES

A Dissertation

by

GARY DON SEIDEL

Submitted to the Office of Graduate Studies of
Texas A&M University
in partial fulfillment of the requirements for the degree of

DOCTOR OF PHILOSOPHY

Approved by:

Chair of Committee,	Dimitris C. Lagoudas
Committee members,	James G. Boyd
	John C. Slattery
	Junuthula N. Reddy
Head of Department,	Helen L. Reed

August 2007

Major Subject: Aerospace Engineering

ABSTRACT

Micromechanics Modeling of the Multifunctional Nature of Carbon
Nanotube-Polymer Nanocomposites. (August 2007)
Gary Don Seidel, B.S., Texas A&M University;
M.S., Texas A&M University
Chair of Advisory Committee: Dr. Dimitris Lagoudas

The present work provides a micromechanics approach based on the generalized self-consistent composite cylinders method as a non-Eshelby approach towards for assessing the impact of carbon nanotubes on the multi-functional nature of nanocomposites in which they are a constituent. Emphasis is placed on the effective elastic properties as well as electrical and thermal conductivities of nanocomposites consisting of randomly oriented single walled carbon nanotubes in epoxy. The effective elastic properties of aligned, as well as clustered and well-dispersed nanotubes in epoxy are discussed in the context of nanotube bundles using both the generalized self-consistent composite cylinders method as well as using computational micromechanics techniques. In addition, interphase regions are introduced into the composite cylinders assemblages to account for the varying degrees of load transfer between nanotubes and the epoxy as a result of functionalization or lack thereof. Model predictions for randomly oriented nanotubes both with and without interphase regions are compared to measured data from the literature with emphasis placed on assessing the bounds of the effective nanocomposite properties based on the uncertainty in the model input parameters.

The generalized self-consistent composite cylinders model is also applied to model

the electrical and thermal conductivity of carbon nanotube-epoxy nanocomposites. Recent experimental observations of the electrical conductivity of carbon nanotube polymer composites have identified extremely low percolation limits as well as a perceived double percolation behavior. Explanations for the extremely low percolation limit for the electrical conductivity of these nanocomposites have included both the creation of conductive networks of nanotubes within the matrix and quantum effects such as electron hopping or tunneling. Measurements of the thermal conductivity have also shown a strong dependence on nanoscale effects. However, in contrast, these nanoscale effects strongly limit the ability of the nanotubes to increase the thermal conductivity of the nanocomposite due to the formation of an interfacial thermal resistance layer between the nanotubes and the surrounding polymer. As such, emphasis is placed here on the incorporation of nanoscale effects, such as electron hopping and interfacial thermal resistance, into the generalized self-consistent composite cylinder micromechanics model.

To my wife, whose love and support I cherish greatly.

ACKNOWLEDGMENTS

I would first and foremost like to express my sincerest gratitude to Dr. Dimitris Lagoudas, my advisor and chair of my Ph.D. advisory committee, for his guidance and support, and for providing me with numerous opportunities for professional growth and development. In particular, I am most appreciative for the opportunities to work closely with him in the preparation of course materials and research proposals as well as the opportunities to present our research at technical conferences and to directly interact with our collaborators in government laboratories. These experiences will undoubtedly be immensely beneficial in my future professional endeavors. But most of all, I would like to thank Dr. Lagoudas for being a mentor both academically and professionally. From his intense desire to see students succeed comes many challenges, and from his dedication to education comes much learning. I have learned a great deal from him, and am truly grateful.

I would also like to express my sincerest thanks to my graduate advisory committee: Dr. John Slattery, Dr. J.N. Reddy and Dr. James Boyd for their service in my educational process and for their assistance in critiquing this work. Their constructive criticism has served to improve the quality of the final form of this dissertation. In addition, I would like to thank Dr. Zoubeida Ounaies for also reviewing this work and providing additional constructive criticism which has had a beneficial impact on this dissertation. It has truly been a pleasure to learn from and interact with these faculty members, and to have them as role models both as teachers and researchers.

I am also grateful for the support provided by Sandia National Laboratories and Texas A&M University through the Sandia National Laboratories/Texas A&M University Doctoral Fellowship in Engineering. Here I would also like to express my

gratitude to Jay Foulk and Daniel Hammerand at Sandia National Laboratories for serving as my Sandia liaisons, and to Joe Tillerson, also at Sandia National Laboratories, for his enthusiastic support and encouragement throughout all of my interactions with Sandia.

I have been privileged throughout my Ph.D. studies to interact and collaborate with several researchers at government laboratories. Specifically I would like to acknowledge Daniel Hammerand at Sandia National Laboratories and Sarah Frankland at the National Institute of Aerospace. The collaborative efforts in which we have been engaged have both directly and indirectly influenced the material presented in this dissertation. In this regard I would also like to acknowledge my colleagues, Ricardo Perez-Suarez and Yordanos Bisrat, for the many fruitful technical conversations and for the sessions of bouncing ideas off of one another. I am especially indebted to Ricardo for his time and effort in contributing to the final form of this document through his thorough proof reading. I would also like to acknowledge my colleauge, Piyush Thakre, for providing the high quality TEM images used in Figure 23 with material produced in the laboratory of Dr. Rick Barrera at Rice University.

I am personally indebted to Dr. David Allen and his former Ph.D. student, Dr. Kayleen Helms, for plucking me from their undergraduate continuum mechanics class and exposing me to the possibilities of pursuing graduate degrees and a career in academics.

Also on a personal level, I would like to acknowledge the special friendship which has formed between myself and my colleagues Bjoern Kiefer and Olivier Godard. They have been a constant source of intellectual and personal growth and encouragement for me throughout my graduate studies, and have taught me the value of kindred spirits. I would similarly like to thank Chad Searcy and Luciano Machado. They are the very definition of peer mentors. It is also incumbent upon me to acknowledge my former

officemate, Khairul Chowdhury, for the many spirited debates, technical, political, and otherwise, in which we learned a lot from each other, and became good friends. Special thanks are due to a number of other colleagues and co-workers with whom I have had the great pleasure to interact with both on a technical and professional level, and on a personal level: Piyush Thakre, Amnaya Awasthi, Matthew Wilkins, Andrew Sinclair, Lesley Weitz, D. Todd Griffith, Pam McConal, Samantha Vaitkunas, and Eun-Souk Oh.

Last in this list but first in my heart, I would like to acknowledge the love, support, patience and understanding of my lovely wife, Bridgette. With her grace and courage she has made the good times even better, and the difficult times a lot easier.

TABLE OF CONTENTS

CHAPTER Page

CHAPTER Page

CHAPTER Page

CHAPTER Page

LIST OF TABLES

TABLE Page

LIST OF FIGURES

FIGURE Page

FIGURE Page

FIGURE Page

FIGURE Page

FIGURE Page

FIGURE Page

FIGURE Page

CHAPTER I

INTRODUCTION AND LITERATURE REVIEW

Nanocomposites are composites which contain one or more phases having a length scale on the order of nanometers (e.g., nanotubes, nanofibers, nanoclays, etc.). The interest in nanocomposites comes from the unique properties inherent to the nanoinclusions employed, which allows for dramatic changes in composite properties with the addition of just a small amount of nanoinclusions. One such nanoinclusion receiving much attention are carbon nanotubes.

A. Carbon Nanotube-Polymer Nanocomposites

Since the discovery of carbon nanotubes (CNTs) by Iijima [1], CNTs have become a subject of much research across a multitude of disciplines. A single-wall carbon nanotube (SWCNT) can be viewed as a single sheet of graphite (i.e. graphene), which has been rolled into the shape of a tube [2]. In addition to SWCNTs, there are also multi-wall carbon nanotubes (MWCNTs) which can similarly be viewed as multiple graphene sheets stacked and rolled into the shape of tube (see Figure 1). CNTs have radii on the order of nanometers and lengths on the order of micrometers resulting in large aspect ratios beneficial to their use in composites [2, 6], especially given the exceptional properties CNTs are believed to posses. For example, carbon nanotubes (CNTs) are reported to have a Young's modulus along the tube axis in the range of 300-1000 GPa, up to five times the stiffness of SiC fibers and with half the density (see Table I which provides a comparison of CNTs with other common fiber reinforcement materials), in addition to having a theoretically predicted elongation to break of 30-

---

The journal model is International Journal of Engineering Science.

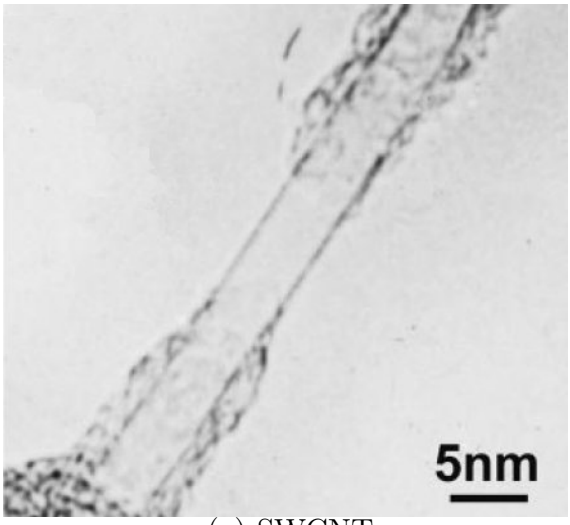

(a) SWCNT

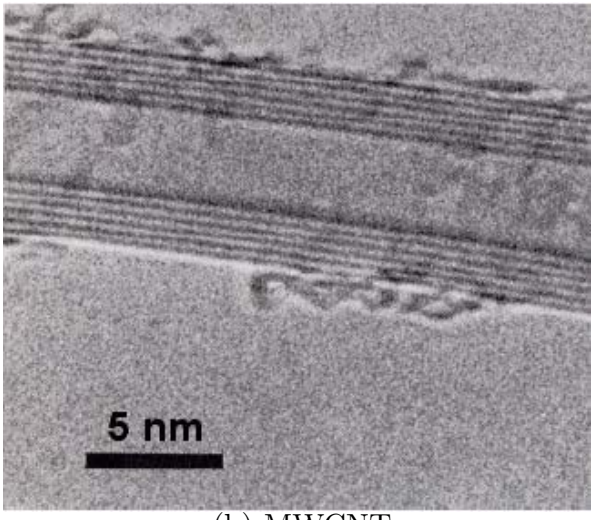

(b) MWCNT

Fig. 1. High resolution TEM images of single- and multi-walled carbon nanotubes. 1(a) A single wall carbon nanotube[3, 4]. 1(b) A multi-walled carbon nanotube [5].

40% [7–13]. In addition, CNTs can be either metallic or semi-conducting depending on the tubes chiral, or roll-up angle, which indicates the orientation of the hexagonal carbon rings relative to the tube axis [2, 4, 6][1]. Metallic CNTs have been observed to conduct electrons ballistically, (with no scattering) having coherence lengths of several microns [14] and with a current density measured [15] as high as 109 A/cm^2 (the highest of any known material). Similarly, CNT bundles have been observed to have a measured resistivity of $1E-3$ ohm-cm at 300 K [16], resulting in a conductivity higher than any other known fiber. Finally, looking at thermal properties, CNTs have now been shown to have a thermal conductivity at least twice that of diamond [17][2].

[1]Zigzag CNTs (n,0) have a chiral angle of 0° and are typically semi-conducting, armchair CNTs (n,n) have a chiral angle of 30° and are always metallic, chiral CNTs (m,n) with angles between 0° and 30° provide a spectrum between semi-conducting and conducting behavior.[4]

[2]For a summary of some of the reported values of carbon nanotube properties, see Section A1 of Appendix A

Table I. Properties of carbon nanotubes in comparison with other common fiber reinforcement materials.[12]

Fiber	**Diameter** (μm)	**Density** (g/cm^3)	**Tensile Strength** (GPa)	**Modulus** (GPa)
Carbon	7	1.66	2.4-3.1	120-170
S-glass	7	2.5	3.4-4.6	90
Aramid	12	1.44	2.8	70-170
Boron	100-140	2.5	3.5	400
Quartz	9	2.2	3.4	70
SiC fibers	10-20	2.3	2.8	190
SiC whiskers	0.002	2.3	6.9	-
CNTs	0.001-0.1	~ 1.33	Up to ~ 50	Up to ~ 1000

Given their unique properties, carbon nanotubes have been proposed as nanoscale inclusions capable of imparting multifunctionality to composites in which they are a constituent. For example, one proposed implementation of CNTs is as structural enhancement of traditional carbon fiber/epoxy composite laminates, where it is believed that the selective use of CNTs as surface treatments can improve interface strength between the carbon fibers and epoxy, and thereby improve the fracture toughness of the composite [18] and indicating a need for multiscale analysis [19, 20]. Another example of particular interest, nanotubes have been introduced into non-conducting polymers in attempts to make light-weight[3] conducting polymer composites which can serve in structural applications while performing additional functions such as improving electromagnetic interference shielding efficiency and assisting in meeting electro-static discharge and grounding requirements for aircraft and spacecraft[22, 23].

Applications for CNTs in engineering systems are likely to focus in the near term on the enhancement of the mechanical, thermal and electrical properties of materials currently in use. As such, a wide variety of composites containing CNTs have been manufactured to take advantage of the reported high stiffness ($\sim$ 1 TPa [24]), high strength ($\sim$ 150 GPa [25]), as well as high thermal and electrical conductivities ($\sim 2000\ W/mK$ [26] and $1000 - 200,000\ S/cm$ [27], respectively) of CNTs. Peigney et al. [28] have fabricated composites specimens of CNTs embedded in ceramic powders while Milo et al. [29] have embedded CNTs in poly(vinyl alcohol). Meltmixing has been used by Potschke et al. [30] to introduce CNTs into a polyethylene matrix. Such efforts have identified several key challenges in the fabrication of CNT composites. Adequate dispersion of CNTs within the matrix has been a key issue given the tendency of CNTs to form bundles due to interatomic forces (van der Waals

[3]The reported densities of carbon nanotubes are comparable to epoxies[12, 21], making the increase in weight with the addition of CNTs into epoxies negligible

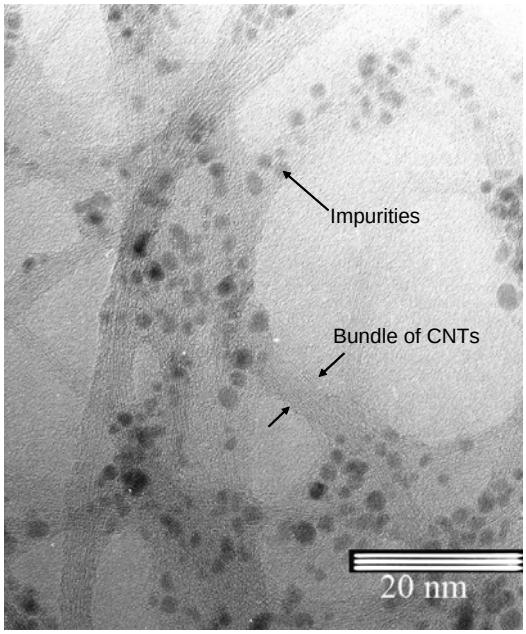

Fig. 2. TEM image of CNTs forming bundles. Image was taken using a JEOL 1200 EX TEM operating at an accelerating voltage of 100kV at Texas A&M University (by P. Thakre).

forces)[12, 31–33] (see Figure 2). Adhesion of the CNTs to the surrounding matrix has been another key issue [34] as has manipulating the orientation of CNTs and bundles of CNTs within the matrix [35] to form aligned CNT composites.[32, 36, 37].

Efforts to address the adhesion and dispersion issues in particular from a processing point of view have identified chemical functionalization of carbon nanotubes as one solution, leading to an increased importance of the interphase region between carbon nanotubes and the surrounding matrix[33, 34, 38–41]. Differing forms of carbon nanotube functionalization affect both interphase thickness and how the material properties within the interphase vary through the thickness. The interphase region in these composites can therefore be modeled as a functionally graded material. An example of both clustering and interphase regions as observed in TEM imaging is

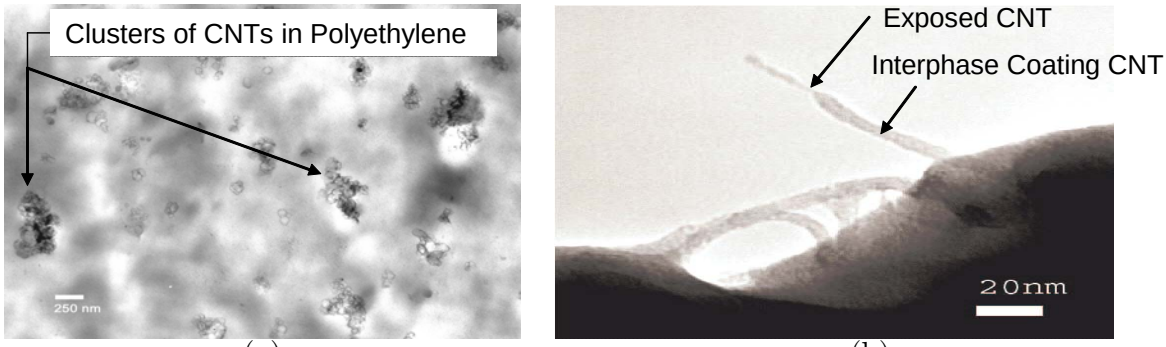

(a) (b)

Fig. 3. TEM images depicting the presence of clustering and interphase regions CNT-polymer composites. 3(a) demonstrates regions of clustered bundles of CNTs. 3(b) demonstrates the presence of an interphase region coating a CNT which has been exposed on a fracture surface. Both images are for CNTs in polypropylene and were taken using a JEOL 1200 EX TEM operating at an accelerating voltage of 100kV at Texas A&M University (by P. Thakre).

provided in Figure 3.

Many efforts have sought to measure the multifunctional properties of nanotube composites, looking at mechanical (modulus, yield strength, viscosity) plus electrical or thermal properties[30, 42–47]. For example, enhancements in elastic Young's modulus of unfunctionalized CNTs in CNT-epoxy composites of up 20% in tension and 75% in compression have been observed for CNT weight percents of just 5% [36], with similar increases in the effective modulus of CNT reinforced polystyrene observed to be on the order of 40% for just 1% weight CNTs[48]. For functionalized CNTs, that is CNTs which have been chemically altered to better interact with a given matrix, increases in Young's modulus of 30% and 60% have been observed at weight percents of 1 and 4%, respectively [33, 49]. A brief review of the mechanical, electrical and thermal properties of carbon nanotube composites is provided in [50] including the interfacial bonding properties, mechanical performance, electrical percolation of

nanotube/polymer and nanotube/ceramic composites are also reviewed.[4]

Experimental measurements of the electrical conductivity of polymer nanocomposites have shown substantial increase (seven or more orders of magnitude at 1% wt.) in conductivity at very low volume fractions of carbon nanotubes [30, 44, 45, 51–53]. A variety of carbon nanotube-polymer nanocomposites have been produced and their electrical conductivity measured. Some efforts have focused on adding nanotubes to epoxies [21, 51, 53–55]. Other efforts have looked at carbon nanotubes in PMMA [22, 42, 56], polycarbonate [30, 57, 58], polystyrene [59, 60], PmPV [61, 62], as well as a wide variety of other polymer matrices [43–45, 52, 63–66].[5]

A common theme amongst much of the observed electrical conductivity data for these nanocomposites is what a appears to be a double percolation phenomena [21, 22, 30, 44, 45, 51, 54, 55, 59, 61, 62, 64, 66], often at values below the expected geometric percolation limit [30, 44, 45, 51–53], with a range of typically measured values for percolation between 0.5 and 1.5% wt. While it is difficult to identify a unique percolation threshold (see pg. 232 of [67]), many have used models based on networks of connected fibers or the volume exclusion method in attempts to analytically identify a contact percolation threshold [21, 55, 64]. Such estimates have placed the percolation limit between 0.12 and 2.7% wt. Computational estimates for the percolation limit have focused on random volume filling of sticks and Monte Carlo random walk modeling [64, 68–70], and have identified a range between 0.74 and 3% volume.

Some explanations for why percolation is achieved prior to what might be the

[4]For a summary of some of the reported values of CNT-polymer composite Young's moduli, see Section A2 of Appendix A

[5]For a summary of some of the reported values of CNT-polymer composite electrical conductivities, see Section A3 of Appendix A

geometric limit have centered on electron hopping or quantum tunneling [42, 59, 71], with [71] indicating that, "variations in the thickness of the polymer coatings, as well as nanotube-nanotube separation, varies the tunnel barrier and this fluctuation induced tunneling determines the intertube transport." [59] suggest two charge transport mechanisms, "charge hopping in low MWCNT loadings (0.02-0.6 wt%) and ballistic quantum conduction in high loadings (0.6-0.9 wt%)." Others have cited molecular influences on conducting network formation [53]. [6]

In contrast to electrical conductivity measurements, efforts to measure the impact of carbon nanotubes on the thermal conductivity of polymer nanocomposites[7] have not found as significant of an increase in the nanocomposite conductivity (a factor of three or less at 1% wt.) relative to the neat polymer [72–76].[8] Some have proposed that despite the high thermal conductivity of nanotubes, it is a nanoscale effect at the interface between the nanotube and the polymer which governs the composite thermal conductivity [77, 78] due to the presence of an interface thermal resistance often referred to as the Kapitza resistance. As it is difficult to directly probe the interface between carbon nanotubes and the polymers in which they are embedded in the lab, some[78–80] have used molecular dynamics simulations to estimate the interfacial thermal resistance. However, many [73, 79, 81–84] have used the *effective medium approach* [85] to estimate the thermal resistance by comparison with nanocomposite measurements. Such efforts have confirmed that the interfacial thermal resistance

[6] Du et al.[42] have indicated a tube-tube distance of less than 5 nm results in nanocomposites becoming electrically conductive based on the electron hopping mechanism.

[7] For a summary of some of the reported values of CNT-polymer composite thermal conductivities, see Section A4 of Appendix A

[8] This is of interest because, from a continuum point of view, the equations for thermal and electrical conductivity are mathematically analogous. Thus this differences points to the difference in nanoscale mechanisms between the conductivities.

can have a significant impact on the effective thermal conductivity of CNT-polymer nanocomposites.

B. Nanocomposite Modeling

Modeling of composites containing CNTs has also received attention in recent years. One clear challenge to the modeling of nanocomposites is that the nanocomposite is a macro, continuum scale composite, but the individual phases can range from the continuum scale down to the nanometer scale, and therefore are approaching discrete limits. Presently, there are models which address material behavior at the various length scales.

For example, quantum mechanics (*ab initio*) modeling is applied on the sub nanometer scale to obtain electronic structure information of a CNT using the Schrödinger equation (see for example Yakobson et al. [86]). Such simulations are in practice computationally limited to a few hundred atoms, but can be representative of larger structures using periodic boundary conditions. At the tens to hundreds of nanometers scale, molecular statics (MS) or molecular dynamics (MD) simulations, which consist of a statistical energy minimization of atomic conformations using Newtons Second Law, can be used to model both individual CNTs (see for example Yakobson et al. [87]) and the interactions between CNTs and the polymer matrix (see for example references [78, 88]). MS/MD simulations are in practice computationally limited to tens of thousands of atoms, but can also be representative of larger structures using periodic boundary conditions. At submicron scales or larger, *micromechanics modeling*, which consists of traditional continuum mechanics approaches for passing information about the influence of smaller scale inhomogeneities up to larger scales where engineering loads are applied, are used to homogenize nanocomposites con-

taining large numbers of CNTs distributed in the polymer matrix (see for example [37, 89–91]). Finally, macroscale continuum modeling (e.g., finite element analysis) is applied on millimeter and larger scales to reflect useful composite shapes and loads for desired applications.

Much research in *ab initio* and MD modeling of carbon nanotubes has been explored in terms of understanding both mechanical and electrical properties of carbon nanotubes [10, 92–96]. Some [88, 97] have used MD to obtain the stress-strain behavior of CNTs embedded in a polymer matrix. Other researchers have used atomistic simulations of epoxy/nanotube composites in order to address nanotube pull-out from the epoxy [98]. Recently, molecular dynamics simulations have revealed the presence of a functionally graded interphase even in non-functionalized carbon nanotube reinforced polymer matrix composites [99–101]. A more recent MD study has addressed the impact of functionalization on the elastic properties of nanotubes chemically bonded to an epoxy matrix with various grafting densities [102]. However, such modeling efforts are computationally limited to modeling either relatively short nanotubes or to infinitely long nanotubes (through the use of periodic boundary conditions), and typically to time scales on the order of picoseconds for individual carbon nanotubes [92, 93]. As such, carbon nanotubes, and indeed any composites in which they are a constituent, seem natural candidates for the development of multiscale modeling techniques (see for example [103–105]). Computational limitations make it difficult for quantum mechanics and molecular dynamics simulations to capture interactions through the polymer matrix between multiple CNTs. However, when used in combination with micromechanics approaches, the resulting multiscale model can become a powerful modeling tool.

Multiscale models have been applied using both atomistic simulations and micromechanics to assess the constitutive properties of various functionalized nanotube

materials [106–111]. Liu and Chen [112] studied the mechanical response in tension of a single CNT embedded in polymer via finite element analysis. In a series of papers, Odegard and Gates [89] and Odegard et al. [113–116] have modeled CNT composites using the equivalent continuum method in conjunction with the Mori-Tanaka micromechanics method to obtain the effective elastic constants for both aligned and misaligned CNTs and found effective elastic moduli to be several times that of the matrix for aligned CNTs and almost one and a half times the matrix value for misaligned CNTs at a volume fraction of 1% CNTs with a matrix consisting of a thermoplastic polyimide LaRC-SI.

Experimentally obtained values for effective Young's modulus being substantially lower, other research efforts have sought to include additional aspects of CNT composites in the calculation of effective properties. For example, the effects of nanotube waviness on the effective composite properties have been studied of polystyrene reinforced with carbon nanotubes by Fisher [12] and Fisher et al. [37, 117] using finite element analysis in conjunction with the Mori-Tanaka method and found to lower the effective modulus. Buckling of CNTs within an epoxy matrix has been considered by Hadjiev et al. [118]. Other efforts have focused on the inclusion of less than ideal CNT adhesion to the matrix in CNT composite modeling [100, 119–121].

Modeling of the thermal and electrical conductivity of nanocomposites has focused primarily on nanoscale effects such as thermal interface resistance and low volume fraction percolation. Gang and Li [122] have studied the dependence of thermal conductivity of single walled nanotubes on chirality and isotope impurity by nonequilibrium molecular dynamics and found that, contrary to electronic conductivity, the thermal conductivity is insensitive to the chirality. As it is difficult to directly probe the interface between carbon nanotubes and the polymers in which they are embedded in the lab, some[78, 79] have used molecular dynamics simulations to esti-

mate the interfacial thermal resistance. However, many [73, 77, 79, 81–84, 123] have used the *effective medium approach* [85] or derivatives thereof [124] to estimate the thermal resistance by comparison with nanocomposite measurements. Others [53, 90] have employed a Mori-Tanaka approach proposed by Hatta and Taya to model the effective thermal conductivities of nanotubes nanocomposites both with and without interfacial thermal resistance. Still others [74] have used the Nielsen model in comparing with experimental observations of nanocomposite conductivity. A control volume finite element method was employed by Song and Youn [72] to obtain the effective thermal conductivity of nanocomposites.

However, as the electrical conductivity results for nanocomposites are dominated by a percolation behavior, the majority of the nanocomposite modeling efforts have focused on traditional percolation theory. The post-percolation increase in conductivity is often modeled by the relationship described by the equation $\sigma = A(c_f - c_f^p)^t$ where σ is the conductivity of the composite, c_f is the volume fraction of the inclusion in the composite, c_f^p is the critical volume fraction (volume fraction at percolation), and A and t are fitted constants [64, 125], assuming the source of the percolation is a conducting network. Others [126] have attempted simple models of sticks in series to describe the conductive network conductivity. However, there is a shortage of models to describe the pre-percolation behavior of nanocomposites.

C. Micromechanics Models for Elastic, Electrical and Thermal Properties of Composites

1. Micromechanics Techniques for Elastic Properties

As will be discussed in greater detail in Chapter II, many micromechanics approaches center on volume averaging to determine the effective properties of composites through

the use concentration tensors. There are a variety of approaches for determining the stress or strain concentration tensors for use in determining the effective properties of composite materials. One of the most widely used approaches is the Mori-Tanaka method (see Section C Part 2 of Chapter II) [127–129], followed by the self-consistent method [129, 130]. These approaches take advantage of the Eshelby solution [131] in individually determining the stress and strain concentration tensor for each ellipsoidal homogeneous inclusion in the composite, with the key difference being between the two approaches being the selection of the embedding material in the application of the Eshelby solution. The Mori-Tanaka method takes as the embedding material the matrix material of the composite perturbed by an additional amount of stress/strain to account for inclusion interactions in determining the dilute concentration tensors from which the total concentration tensor is defined. In contrast, the self-consistent method (see Section C Part 1 of Chapter II) [130] accounts for inclusion interactions by taking as the embedding material the unknown effective in determining total concentration factors and therefore makes the solutions for the effective properties a set of nonlinear equations.

The success of the Mori-Tanaka and self-consistent methods have lead to efforts to extend them to include non-ellipsoidal and non-homogeneous inclusions. For example, Benveniste et al. [132] applied the composite cylinders method in a two-step process in the determination of dilute stress concentration tensors for use in a Mori-Tanaka method for determining the effective thermoelastic properties of coated fiber composites. Dasgupta and Bhandarkar [133] followed a similar approach as Benveniste et al. in the determination of dilute stress concentration tensors, but instead made use of the generalized self-consistent composite method. Finite element calculations were employed by Fisher et al. [117] to calculate the Young's modulus of wavy fibers which was then used to determine strain concentration tensors via the

Mori-Tanaka method. Other efforts have focused on what could be referred to as non-Eshelby approaches towards determining stress and strain concentration tensors. For example, Bradshaw et al. [134] have used the finite element method in a Mori-Tanaka approach where the dilute strain concentration factor is determined directly from finite element results as opposed to through the use of the Eshelby solution.

The effects of interphase regions on the effective properties of composites have been approached using a variety of techniques, mostly in the context of coated fiber inclusions[91, 132, 133, 135–140]. Others have identified methods which have been applied in determining the effective properties of composites containing fibers coated with graded interphase regions. Achenbach and Zhu [141] applied the boundary element method for obtaining marcomechanical behavior for transverse loading of hexagonal array of fibers with an interphase region represented by a spring layer. Sancaktar and Zhang [142] made use of a differential scheme for determining stresses and strains in a single fiber composite with nonlinear viscoelastic interphase. The method of cells was used by Gardner et al. [143] and by Low et al. [144] to determine the effective elastic properties of coated fiber composites. A good summary of the analytical interphase modeling approaches prior to 1993 was provided by Jayaraman et al. [145]. More recent efforts have relied on finite element modeling [91, 146] and even on a Cosserat shell model [147] to determine effective properties of graded interphase fiber composites.

A number of research efforts have sought to ascertain the effects of clustering on the effective elastic properties of composites. Many research efforts have used tessellation techniques to identify what constitutes a clustered arrangement as well as to delineate different amounts of clustering [148–153]. Ghosh and Moorthy [154] and Ghosh et al. [150] used the Voronoi cell finite element method to obtain the stress-strain response for clustered fiber reinforced composites and observed increases

in the transverse stress as a result of clustering. Tszeng [155] studied the elastoplastic response of clusters of spherical particles in metal matrix composites using and equivalent inclusion approach and found no significant effect of clustering on the effective modulus. Boyd and Lloyd [156] used FEA analysis to study the effects of particle clustering on the fracture toughness in metal matrix composites. Bhattacharryya and Lagoudas [153] derived a form of the self-consistent model for the effective properties of clustered fiber reinforced composites based on local volume fraction distributions and applied it to bimodal distributions where increases in transverse elastic properties for clustered distributions were found. For aligned short fiber composites, Kataoko and Taya [157] obtained the effect of clustering on the local stress-strain response, but surprisingly found a decrease in the effective axial stiffness[9]. It should be noted that these previous efforts were more focused on the stress-strain response as opposed to the effective properties, and generally observed the effects of clustering at a single global volume fraction for more traditional composite systems such as carbon fiber reinforced and metal matrix composites.

a. The Composite Cylinder Method

Many micromechanics efforts focused on the estimation of the effective properties of aligned fiber composites have made use of what came to be known as the Composite Cylinders Model, or Method. The Composite Cylinders Model was originally proposed by Hashin and Rosen [158] in an effort to determine bounds on and expressions for the effective elastic properties of aligned, circular fiber reinforced materials. The model made use of the direct strain energy equivalency between the effective material response and the response of a *composite cylinder assemblage* consisting of concentric

[9]This is a surprising result as it is generally expected and observed that the axial stiffness tends to follow the rule of mixtures and therefore is unaffected by clustering

circular cylinders of fiber and matrix which was taken as representative of aligned fibers randomly dispersed in the matrix. Five sets of both traction and displacement boundary conditions were applied to the composite cylinder assemblage in order to determine a set of five independent elastic constants for the effective material: the longitudinal Young's modulus, the longitudinal stiffness, the plane strain bulk modulus, the longitudinal shear and the transverse shear. In all but one case, the transverse shear, the application of the boundary conditions resulted in coincident bounds and as such, an expression for the effective property.

In an effort to determine coincident bounds, and therefore, an expression for the shear modulus of spherical particles in a matrix, Christensen and Lo [159] proposed a generalized self-consistent approach. In this approach, a composite sphere assemblage consisting of the spherical inclusion and the matrix was embedded in a third phase, the material properties of which were taken to be those of the effective material, and which could be taken to extend to infinity. The Eshelby strain energy equivalency between the assemblage and effective material is then invoked which, as a result of the third phase being the effective material, leads to an expression in which the interaction energy for the assemblage must be zero. The bounds determined for the shear modulus of the generalized self-consistent composite sphere were observed to be coincident, and, given the relative similarity between the solutions of the two problems, Christensen and Lo were able to use the same approach to develop an expression for the transverse shear modulus of a generalized self-consistent composite cylinder assemblage. In a much later work, Christensen [160] compares the results of this generalized self-consistent composite cylinder approach to obtaining the effective transverse modulus with other micromechanics approaches and notes good agreement with the Mori-Tanaka method [127, 128] which the present authors also observed in addition to good agreement with finite element simulations [161, 162]. While Chris-

tensen and Lo acknowledge the differences between the generalized self-consistent composite cylinders approach and Hashin and Rosen's original composite cylinders approach, others, including Hashin, sought to use both approaches in a unified effort towards determining a set of five independent elastic constants for the effective properties of aligned fiber composites [163–165]. This resulted in a multi-layer composite cylinders method where four of the five elastic constants are determined from the Hashin and Rose method and the fifth from Christensen and Lo's approach.

In an effort to determine the effective thermoelastic properties of graphitic carbon fibers, Hashin [163] employed the composite cylinders method [158] to determine the axisymmetric elastic properties, the axial shear modulus, the coefficient of thermal expansion, and the thermal conductivity, while using a generalized self-consistent composite cylinder approach [160] to determine the transverse shear modulus, transverse Young's modulus, and transverse Poisson's ratio. In a later work, Hervé and Zaoui [165] proposed to use the generalized self-consistent composite cylinders approach in determining all of the effective elastic constants of composite cylinder assemblages consisting of N- concentric phases, thereby making the effective material the $(N+1)^{\text{th}}$ phase. For two phase composite cylinder assemblages (i.e., $N = 2$), they were able to argue that an approach like the one taken by Hashin for graphitic carbon fibers was consistent in that the generalized self-consistent composite cylinder method would yield identical elastic constants as the original composite cylinders method for those properties identified to have coincident bounds.

The replacement of interphase by an interface in determining the effective thermoelastic properties of coated carbon fiber composites was investigated by Hashin [140, 166] through the incorporation of jump discontinuities in traction and displacement across the fiber-matrix interface in the composite cylinder assemblage.

Additional efforts have focused on the development of composite cylinders mod-

els to capture the effects of graded interphase regions. Jayaraman and Reifsnider [167] developed a solution for a graded interphase region having a radial power variation in Young's modulus (constant Poisson's ratio) in determining the thermoelastic radial and hoop stresses of coated carbon fibers composites. Jasiuk and Kouider [168] investigated the use of infinite series solutions in composite cylinders models for determining the effective elastic properties of coated fibers having graded interphase regions with radial linear variation in both Young's modulus and Poisson's ratio. Lutz and Ferrari [169] also developed an infinite series solution for a graded interphase region where the variation in both Lamé constants is a truncated power function plus a constant. In an alternative approach, the composite cylinders method has been used by Huang and Rokhlin [170] as part of an iterative process towards modeling a graded interphase region which they term the transfer matrix method (see also [132, 133]).

Several efforts have used the composite cylinders approach in determining the thermo-elastic stress distributions in fiber reinforced composites. In [136, 138, 167, 171], composite cylinders approaches are applied to obtain the thermal stresses (axial and hoop) in a fiber and matrix with and without an interphase region. Other efforts [169, 170, 172] have focused on modeling functionally graded interphase regions in fiber reinforced composites. Recently [161], multi-layer composite cylinders models have been applied to CNT reinforced epoxies wherein CNTs have been treated as continuum sheets of rolled graphene surrounded by interphase layers to simulate differing amounts of load transfer as a result of functionalization, but have lacked direct MD coupling.

Applications of the composite cylinder method have centered around the determination of the effective thermoelastic properties of aligned coated fiber composites. Nairn [171] employed a composite cylinders approach to determine axial and hoop stresses in response to thermal loads for carbon fiber composites with and without an

interphase region; work which Wagner [136, 138] later followed to estimate fiber break lengths due to residual stresses. Pagano and Tandon [173] made use of the composite cylinders method in a parametric study on the effects of an interphase region and of orientation on the thermoelastic properties of coated fiber composites. Carman et al. [164] used the composite cylinders method as part of an approach towards designing optimal interphase thermoelastic properties. Recently [161], multi-layer composite cylinders models have been applied to carbon nanotube reinforced epoxies wherein carbon nanotubes have been treated as continuum sheets of rolled graphene surrounded by interphase layers to simulate differing amounts of load transfer as a result of functionalization.

2. Micromechanics Techniques for Thermal and Electrical Properties

Continuum micromechanics models have long been used to determine the effective electrical conductivities of composites with well dispersed inhomogeneities. Beginning with single particle [174, 175] and arrays of particles [176] embedded in a matrix material, continuum mechanics descriptions for the effective conductivity of composites were developed, generally with the assumption that the inhomogeneity is fully enveloped by the matrix or an effective material. Based on the assumption that each crystal acts as if surrounded by a homogeneous medium whose properties are those of the mixture, Landauer [174] proposed a theory for predicting the electrical conductivity of a binary random mixture of metals having spherical grains. Kerner [175] extended this result for coated spheres. Later work was aimed at using variational principles to establish bounds on the effective composite properties [177–180], generally by mathematical analogy with other properties like magnetic permeability, effective dielectric constants, or elastic properties.

Subsequent micromechanics models were driven by effective medium approaches

[181–184] and the development of the differential scheme, the self-consistent method, and the Mori-Tanaka method for effective conductivity (noting again that many of these developments were for mathematically analogous properties) [183, 185–188] whose mechanical analogs form the backbone of micromechanics approaches for effective elastic properties. Some of these methods relied on Eshelby-like approaches, leading to equivalent inclusion methods[10] for incorporating coatings or interphase layers [53, 182, 183, 185, 187, 189–192]. Other methods have relied on computational micromechanics in the form of finite element [193] or finite difference [194] methods in addition to other theories (Halpin-Tsia, polarization) [72, 123] to determine the effective conductivity. Still other methods relied on the development of composite sphere or cylinder solutions to determine the effective conductivities coated spheres and fibers [163, 185, 186, 195, 196], at times to model functionally graded material regions. It is the latter which will be the focus of the modeling efforts in the present study using the multi-layer composite cylinder method to determine the concentration tensors.

D. Objectives and Outline of the Present Research

The present work seeks *to investigate the development and application of micromechanics techniques for use in multiscale models for CNT-polymer composites.* As a result of the hollow nature of CNTs and the presence of interphase regions, micromechanics methods which make use of the Eshelby solution, like the Mori-Tanaka and self-consistent methods, can not be used. As such, *emphasis is placed on the com-*

[10]The term equivalent inclusion method is traditionally used in describing the equivalency between a homogeneous inhomogeneity and an inclusion with an unknown eigenstrain. However, here it is meant that the inhomogeneous inhomogeneity (inhomogeneity plus the interphase) is replaced by and effective inhomogeneity prior to the application of the traditional equivalent inclusion method.

posite cylinders model as a non-Eshelby approach in the determination of effective CNT-polymer properties. Specifically, we seek to establish connections between general micromechanics averaging philosophy with generalized self-consistent composite cylinder modeling of hollow fibers coated with graded interphase regions as an approach to continuum level modeling of carbon nanotube enriched polymer composites, and to validate these models by comparison with equivalent inclusion Mori-Tanaka and self-consistent approaches as well as with computational micromechanics finite element simulations. Efforts are also made to use the composite cylinders model and computational micromechanics approaches to assess the impact of clustering, both with and without interphase regions, on the effective nanocomposite properties. In addition, the multifunctional nature of CNT-polymer composites are investigated using the multi-layer composite cylinders model to introduce nanoscale effects. Finally, as part of the multiscale model, connections to lower length scale modeling efforts, such as MD simulations, are made in the validation of CNT representations and in the determination of interphase geometry and properties which are then used to calculate effective nanocomposite properties for use in higher length scale models.

The multi-layer composite cylinders method is used to directly calculate the total stress concentration tensors at finite volume fractions. This approach is provided as a means to determining the effective elastic properties of composites containing multiple types of coated fibers and of composites with partially aligned or randomly oriented coated fibers through the use of general averaging methods. For CNTs and for CNTs with interphase regions the composite cylinders solutions can be used to obtain the components of the concentration tensors through volume averages of the stress and strain in the composite cylinder layers. Concentration tensors for CNTs with different functionalizations can then be obtained and averaged together to get the effective properties for epoxies containing a mixture of CNT types. Similarly, the

concentration tensors can then be used to introduce the effects of random orientation by considering each orientation of CNTs as a separate phase. The effective properties are then obtained by averaging over all possible orientations. However, with the concentration tenors determined directly from the composite cylinders approach, the random orientation averaging can take place without using the Mori-Tanaka method, and thereby allows for a more direct accounting for the presence of interphase regions.

The effects of interphase regions due to functionalization and polymer entanglement on the effective elastic properties are also investigated using a multi-layer composite cylinders approach. Herein the effects of interphase regions are modeled by taking advantage of the generalize self-consistent composite cylinder method. In the present work, the multi-layered, generalized self-consistent composite cylinders model is used to model a functionally graded interphase region with an increasing number of piecewise continuous subregions. The objective is to obtain the effective elastic constants of carbon nanotube reinforced composites from the micromechanical model, but to refine the number and properties of the subregions to approximate the density variations observed in the molecular structure. The generalized self-consistent composite cylinders technique is also used to model the graded interphase regions as continuous functions which will be compared to piecewise continuous solutions. For complicated variations in material properties, multiple layer sequences of continuous varying regions are explored.

Efforts are also made in the present work to elucidate the effects of clustering of carbon nanotubes within a polymer matrix on the effective elastic properties of such composites. TEM images have shown that within a given cluster, bundles of CNTs are often observed to have a high degree of alignment. As such, clustering of CNTs in a polymer matrix is modeled herein in the context of aligned CNT bundles. Both the independent and combined effects of interphase regions and clustering of high-

stiffness hollow fiber composites representing CNTs are studied using *computational* micromechanics techniques in the form of continuum finite element analysis (FEA). Finite element results are then compared to the corresponding results obtained by analytic micromechanics methods. In the analytic approach, a tessellation procedure to quantify clustering and the effects of clustering on the effective properties of CNT composites are modeled using a multi-layered composite cylinder method which is coupled to a multi-phase Mori-Tanaka approach to obtain the effective properties of aligned clustered fiber reinforced composites for a wide range of global volume fractions.

In assessing the multifunctionality of CNT-polymer nanocomposites, continuum micromechanics models are used to predict the pre-contact percolation behavior of carbon nanotube reinforced composites, with the nanoscale effects such as electron hopping modeled through the use of interphase zones. In the present work, a continuum micromechanics method in the form of a composite cylinders model is used to obtain the effective electrical conductivity of carbon nanotube-polymer composites, incorporating the nanoscale effects observed in the macroscale measurements of the effective electrical conductivity, namely premature percolation and a double percolation limit, through the incorporation of multiple interphase layers. [11] The composite cylinders method is used in determining non-dilute electric flux concentration tensors for use in micromechanics orientation averaging in modeling the carbon nanotube-polymer composites as a well-dispersed system of randomly oriented nanotubes.

In addition to assessing the multifunctionality of CNT-polymer composites in terms of electrical conductivity, a micromechanics approach based on the composite

[11] Using different interphase layers to represent various mesoscale electrical phenomena has also been applied by [197] for concentric spheres in what was termed a multi-core model.

cylinders model is applied as an alternate approach for assessing the impact of an interfacial thermal resistance on the effective thermal conductivity of nanocomposites. The composite cylinders assemblage is used to introduce the Kapitza layer and additional interphase layers in a manner which enforces concentric heat flux through each layer and accounts for the hollow interior of the nanotube. The lateral effects of the interfacial thermal resistance are readily introduced using interphase layers. In addition, we seek to introduce anisotropy into the carbon nanotubes by reducing the axial conductivity of the carbon nanotube in order to account for end effects. The degree of anisotropy is introduced in our model as an effect of the Kapitza layer by constructing a composite bar in series solution for the effective axial conductivity of the nanotube. In addition, the composite cylinders assemblage is used to directly determine concentration tensors for use in incorporating the effects of random orientation.

As part of the multiscale modeling effort, we seek to address phenomena occurring in the bulk polymer and attributed to the presence of nanotubes and their surrounding interphases. Evidence from MD simulations has indicated a region of perturbed polymer extending radially outward from the CNT surface, the thickness of which can be on the order of the CNT radius even for unfunctionalized CNTs. This thickness can be larger than the van der Waals cut-off radius used in MD simulations, and therefore is considered a long range interaction. It is postulated that this long range interaction can be best represented in the composite cylinders models as a separate phase between the CNT and undisturbed matrix defined as the interphase. At present MD simulations can identify the presence of the interphase in the form of disturbances in the density distribution in the surrounding polymer, but cannot identify the elastic properties of this region. Molecular dynamics (MD) simulations of unfunctionalized and functionalized CNTs embedded in a polymer ma-

trix will be used to calibrate micromechanics modeling efforts in the determination of appropriate interphase thicknesses and properties. Initial coupling between MD and composite cylinders solutions has relied on a postulated correspondence between density and stiffness [99]. Unfortunately, current MD simulations cannot directly probe the interphase region. As such, a more direct coupling between MD and the composite cylinders method is obtained here which uses the composite cylinders method in conjunction with MD simulations to ascertain appropriate elastic constants for the interphase region. MD simulations provide the interphase thickness based on density variations observed in the polymer. In addition, MD simulations will provide the effective properties for the CNT-polymer system from which the interphase properties in the composite cylinders solution are solved using the volume averaged strain energy equivalency. These interphase properties can then be used in the subsequent composite cylinders solutions to predict the local effective properties at volume fractions which would result in atomistic simulation boxes currently too large for MD simulations.

The remainder of this work is presented as follows. Chapter II provides a review of the general micromechanics averaging approaches based on energy equivalency and averaging methods. Focused is placed on the self-consistent and Mori-Tanaka methods in order to place the generalized self-consistent composite cylinders method employed herein into context. In addition, the general approach towards orientational averaging is presented. Chapter III provides a detailed description of the generalized self-consistent composite cylinders method. Chapter IV provides results for the effective elastic properties of nanocomposites as well as a description of the methods used and results obtained from interphase and cluster modeling using both analytic and computational micromechanics approaches. In addition, comparisons of the effective properties obtained with these micromechanics approaches with measured ex-

perimental data are provided. Chapter V provides results for the effective electrical conductivities of nanocomposites and provides a discussion on possible mechanisms leading to the observed early percolation behavior in the process of comparing predicted conductivities below the contact percolation limit with measured experimental data. Chapter VI provides results for the effective thermal conductivities of nanocomposites. A description of the methods for including both the lateral and end effects of the interfacial thermal resistance is provided and discussed in the context of comparisons with measured experimental data for nanocomposite thermal conductivity. Finally, Chapter VII summarizes the conclusions and discusses some future challenges for modeling of CNT-polymer nanocomposites.

CHAPTER II

REVIEW OF CLASSICAL MICROMECHANICS METHODS

This chapter provides a review of classical micromechanics, beginning with the identification of the relationship between the macroscale boundary value problem and the microscale representative volume element (RVE) in terms of the governing differential equations for elasticity and electrical and thermal conductivity and a discussion on volume averages in determining effective properties of composites. This is followed by descriptions of the self-consistent and Mori-Tanaka methods for elastic properties and thermal conductivities, and a discussion on orientational averaging. The chapter concludes with a discussion on the use energy of equivalencies as a preface to the discussion of the generalized self-consistent composite cylinder method of the following chapter. Throughout this and the remaining chapters of this work, the following notation conventions will be adopted: Extensive use of the summation convention for indicial notation will be used to clarify tensor products and order. In addition, fourth order tensor will be denoted by capital Latin letters. Second order tensor will be denoted with lower case Greek letters unless indicated otherwise, and vectors will be denoted by lower case Latin letters unless indicated otherwise. For clarity, definitions and derivations involving derivatives with respect to space expressed using the summation convention will be presented assuming a Cartesian coordinate system.

A. Identification of RVE and Governing Equations

1. RVE and Governing Differential Equations for Linear Elasticity

Much of the philosophy in micromechanics approaches[1] is centered around determining effective properties for composites containing microstructure for use in macroscale simulations of composite response to engineering loads. Effective properties are typically obtained by establishing an equivalency between the microscale RVE of the composite and a representation of that RVE as an effective homogeneous medium as shown schematically in Figure 4. For composites consisting of linear elastic materials, the governing differential equations for the macroscale and for the microscale RVE consist of the linearized elasticity equations[2]. It can be shown through the theory of multiple scale expansion (see for example the work of Jansson [202]) that, for linear materials and an asymptotic expansion of the displacement of order δ^2, where $\delta \ll 1$ is the scaling factor between the macro and microscales such that $x_i = X_i/\delta$, that the macroscale and microscale can be related to one another through the definition of the effective stiffness tensor[3], L^{eff}_{ijkl}. As such, the static equilibrium equations at the macroscale can be expressed as

$$\bar{\sigma}_{ji,\,j} + f_i = 0 \tag{2.1}$$

[1]Many texts on micromechanics provide the following equations. In particular, *Mechanics of Composite Materials* by Richard M. Christensen [198] and *Fundamentals of Micromechanics of Solids* by Qu and Cherkaoui [199] are provided as a references.

[2]Many texts on continuum mechanics and elasticity provide the following equations. In particular, *The Linearized Theory of Elasticity* by William S. Slaughter [200] and *Introduction to Continuum Mechanics* by Lai, Rubin and Krempl [201] are provided as references.

[3]In micromechanics literature, it is common to use L_{ijkl} for stiffness instead of C_{ijkl} which is commonly used in many texts on elasticity. As this chapter will be referencing the classical micromechanics literature, we will use the so-called Hill notation [203] and use L_{ijkl} for stiffness.

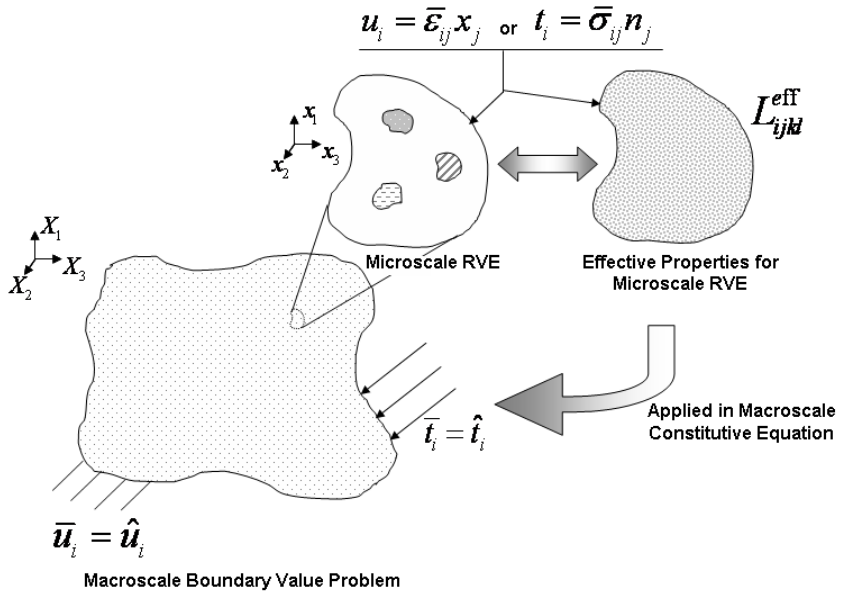

Fig. 4. General schematic representing the relationship between the macroscale boundary value problem and its corresponding microscale RVE from which effective elastic properties are determined. The microscale RVE is noted to be subjected to homogeneous displacements or tractions in terms of the macroscale average strain or stress which is depicted for a general composite microstructure having an assortment of irregularly shaped inhomogeneities.

where $\bar{\sigma}_{ij}$ is the macroscale Cauchy stress, f_i is the body force, and $\bar{\sigma}_{ij,\,j}$ denotes the divergence of the stress tensor in terms of the X_i coordinate system. The boundary conditions at the macroscale can be either specified tractions, $\bar{t}_i = \bar{\sigma}_{ji} n_j = \hat{t}_i$ (where n_i is the unit outward normal of the macroscale boundary), or specified displacements, $\bar{u}_i = \hat{u}_i$, or a nonintersecting combination of the two. The macroscale kinematic relations are expressed in terms of the linearized strain-displacement equations given by

$$\bar{\varepsilon}_{ij} = \frac{1}{2}\left(\bar{u}_{i,\,j} + \bar{u}_{j,\,i}\right) \tag{2.2}$$

where $\bar{\varepsilon}_{ij}$ is the infinitesimal strain tensor on the macroscale, $\bar{u}_i$ is the displacement vector of a macroscale material point, and $\bar{u}_{i,\,j}$ denotes the gradient of the displacement vector in terms of the macroscale X_i coordinate system. The macroscale constitutive relation can be identified as

$$\bar{\sigma}_{ij} = L^{\text{eff}}_{ijkl} \bar{\varepsilon}_{kl} \tag{2.3}$$

where the effective stiffness is obtained from the microscale RVE and is therefore a function of the microscale x_i coordinate system. It can further be shown that Eqn. 2.3 can alternatively be expressed as

$$\langle \sigma_{ij} \rangle = L^{\text{eff}}_{ijkl} \langle \varepsilon_{kl} \rangle \tag{2.4}$$

where $\langle \sigma_{ij} \rangle$ and $\langle \varepsilon_{ij} \rangle$ denote the volume averages of the stress and strain, respectively, over the microscale RVE, i.e.

$$\langle \bullet \rangle = \frac{1}{V} \int_V \bullet \, dV \tag{2.5}$$

where V is the volume of the RVE in the x_i coordinate system.

For the microscale RVE, the static equilibrium equations are expressed as

$$\sigma_{ij,\,j} = 0 \tag{2.6}$$

where σ_{ij} is the microscale Cauchy stress and $\sigma_{ij,\,j}$ denotes the divergence of the stress tensor in terms of the x_i coordinate system.[4] It is noted that the body force is not included in Eqn. 2.6 as it can be observed from the theory of multiple scale expansion that the body force need not be considered in the microscale equilibrium equations. The microscale kinematic relations are expressed in terms of the linearized strain-displacement equations given by

$$\varepsilon_{ij} = \frac{1}{2}\left(u_{i,\,j} + u_{j,\,i}\right) \tag{2.7}$$

where ε_{ij} is the infinitesimal strain tensor on the microscale, u_i is the displacement vector of a material point, and $u_{i,\,j}$ denotes the gradient of the displacement vector in terms of the microscale x_i coordinate system.

Assuming that all of the materials in the composite are linear elastic, the Cauchy stress is related to the infinitesimal strain tensor on the microscale through the constitutive relations given by

$$\sigma_{ij} = L_{ijkl}\varepsilon_{kl} \tag{2.8}$$

where L_{ijkl} is the fourth order stiffness tensor which varies in x_i depending on the microstructure of the composite. The inverse of the stiffness tensor is defined to be the compliance tensor, M_{ijkl}, so that Eqn. 2.8 can alternatively be expressed as

$$\varepsilon_{ij} = M_{ijkl}\sigma_{kl} \tag{2.9}$$

[4]It is noted that in the absence of body moments, the conservation of angular momentum indicates that the Cauchy stress is symmetric, i.e. $\sigma_{ij} = \sigma_{ji}$.

It is well known that, in general, a fourth order tensor has 81 independent components. However, since the infinitesimal strain tensor is symmetric, the number of independent components of the stiffness tensor is reduced to 54. Further, if the stress tensor is also symmetric, the number of independent components is reduced to 36. Finally, for linear elastic materials[5], the number of independent components of the stiffness tensor is reduced to 21. Additional assumptions regarding material symmetry can further reduce the number of independent components of the stiffness tensor. Of particular interest to the present work are orthotropic (9 independent components), transversely isotropic (5 independent components), and isotropic (2 independent components) material symmetries[6]. For example, the stiffness tensor for an orthotropic material can be expressed in engineering notation as

$$\begin{Bmatrix} \sigma_{11} \\ \sigma_{22} \\ \sigma_{33} \\ \sigma_{23} \\ \sigma_{13} \\ \sigma_{12} \end{Bmatrix} = \begin{bmatrix} L_{1111} & L_{1122} & L_{1133} & 0 & 0 & 0 \\ L_{1122} & L_{2222} & L_{2233} & 0 & 0 & 0 \\ L_{1133} & L_{2233} & L_{3333} & 0 & 0 & 0 \\ 0 & 0 & 0 & L_{2323} & 0 & 0 \\ 0 & 0 & 0 & 0 & L_{1313} & 0 \\ 0 & 0 & 0 & 0 & 0 & L_{1212} \end{bmatrix} \begin{Bmatrix} \varepsilon_{11} \\ \varepsilon_{22} \\ \varepsilon_{33} \\ 2\varepsilon_{23} \\ 2\varepsilon_{13} \\ 2\varepsilon_{12} \end{Bmatrix} \tag{2.10}$$

[5]The more general requirement is that the material be hyperelastic, i.e. that the strain energy density, $w(\varepsilon_{ij})$, which is given by $w(\varepsilon_{ij}) \equiv \int_0^{\varepsilon_{ij}} \sigma_{ij}\ d\varepsilon_{ij}$, is path independent in strain space.

[6]Orthotropic materials have three orthogonal planes of material symmetry, transversely isotropic material are symmetric with respect to an arbitrary rotation about the axis of material symmetry, and isotropic materials are symmetric with respect to *all* orthogonal transformations

or inverted and expressed in terms of the components of the compliance tensor as

$$\begin{Bmatrix} \varepsilon_{11} \\ \varepsilon_{22} \\ \varepsilon_{33} \\ 2\varepsilon_{23} \\ 2\varepsilon_{13} \\ 2\varepsilon_{12} \end{Bmatrix} = \begin{bmatrix} \frac{1}{E_{11}} & -\frac{\nu_{21}}{E_{22}} & -\frac{\nu_{31}}{E_{33}} & 0 & 0 & 0 \\ -\frac{\nu_{12}}{E_{11}} & \frac{1}{E_{22}} & -\frac{\nu_{32}}{E_{33}} & 0 & 0 & 0 \\ -\frac{\nu_{13}}{E_{11}} & -\frac{\nu_{23}}{E_{22}} & \frac{1}{E_{33}} & 0 & 0 & 0 \\ 0 & 0 & 0 & \frac{1}{\mu_{23}} & 0 & 0 \\ 0 & 0 & 0 & 0 & \frac{1}{\mu_{13}} & 0 \\ 0 & 0 & 0 & 0 & 0 & \frac{1}{\mu_{12}} \end{bmatrix} \begin{Bmatrix} \sigma_{11} \\ \sigma_{22} \\ \sigma_{33} \\ \sigma_{23} \\ \sigma_{13} \\ \sigma_{12} \end{Bmatrix} \tag{2.11}$$

where the E's, ν's, and μ's denote the Young's moduli, Poisson's ratios, and shear moduli, respectively, and where material symmetries indicate that $\frac{\nu_{21}}{E_{22}} = \frac{\nu_{12}}{E_{11}}$, $\frac{\nu_{31}}{E_{33}} = \frac{\nu_{13}}{E_{11}}$, and $\frac{\nu_{32}}{E_{33}} = \frac{\nu_{23}}{E_{22}}$.

In light of the constitutive equations, the equilibrium equations for the microscale RVE can be expressed as

$$(L_{ijkl}\varepsilon_{kl})_{,\,j} = L_{ijkl,\,j}\,\varepsilon_{kl} + L_{ijkl}\,\varepsilon_{kl,\,j} = 0 \tag{2.12}$$

where for homogeneous materials, $L_{ijkl,\,j}$ is identically zero[7] so that through the strain-displacement relations, the equilibrium equations become

$$\frac{1}{2}[L_{ijkl}\,u_{k,\,lj} + L_{ijkl}\,u_{l,\,kj}] = 0 \tag{2.13}$$

which for isotropic materials reduces to the familiar Lamé-Navier equations (for no inertial and no body forces), i.e.

$$(\lambda + \mu)u_{k,\,ki} + \mu u_{i,\,jj} = 0 \tag{2.14}$$

[7]In Chapters III and IV applications involving functionally graded materials, i.e. materials where $L_{ijkl,\,j} \neq 0$, will be discussed. For these functionally graded materials, solutions of the equilibrium equations will be dependent on the functional form of the material property gradation.

where μ and λ are the Lamé constants.

On the boundary of the microscale RVE, it can be shown from the theory of multiple scale expansion that the traction or displacement conditions[8] are homogeneous and consistent with the stress or strain at the macroscale, i.e.

$$t_i = \sigma_{ji} n_j = \bar{\sigma}_{ji} n_j \tag{2.15a}$$

$$u_i = \bar{\varepsilon}_{ij} x_j \tag{2.15b}$$

where n_i is the unit outward normal on the RVE surface. It can further be shown that, for linear materials and expansion of order δ^2, the multiple scale expansion is synonymous with equating the strain energy of the RVE with that of the homogeneous effective material.

For example, the strain energy density of the RVE is given by

$$w = \frac{1}{2}\sigma_{ij}\varepsilon_{ij} \tag{2.16}$$

so that the volume averaged strain energy in the RVE is defined as

$$W^{\mathrm{RVE}} = \frac{1}{2}\langle \sigma_{ij}\varepsilon_{ij} \rangle \tag{2.17}$$

which by the Hill-Mandel theorem (see for example [199]) can be expressed as

$$W^{\mathrm{RVE}} = \frac{1}{2}\langle \sigma_{ij} \rangle \langle \varepsilon_{ij} \rangle \tag{2.18}$$

Assuming the RVE is subject to the applied homogeneous displacement of Egn. 2.15b,

[8]The theory of multiple scale expansion as presented by Jansson [202] discusses the boundary conditions on the microscale RVE in terms of periodic boundary conditions.

it can be shown by use of the divergence theorem[9] that

$$W^{\text{RVE}} = \frac{1}{2}\langle\sigma_{ij}\rangle\bar{\varepsilon}_{ij} \tag{2.19}$$

Similarly, the volume averaged strain energy of the effective homogeneous material is defined as

$$W^{\text{eff}} = \frac{1}{2}\langle\sigma_{ij}^{\text{eff}}\varepsilon_{ij}^{\text{eff}}\rangle = \frac{1}{2}\langle\sigma_{ij}^{\text{eff}}\rangle\langle\varepsilon_{ij}^{\text{eff}}\rangle \tag{2.20}$$

where σ_{ij}^{eff} and $\varepsilon_{ij}^{\text{eff}}$ are the stress and strain in the effective homogeneous material having stiffness L_{ijkl}^{eff} and assumed applied displacements also given by Eqn. 2.15b, so that

$$W^{\text{eff}} = \frac{1}{2}L_{ijkl}^{\text{eff}}\bar{\varepsilon}_{kl}\bar{\varepsilon}_{ij} \tag{2.21}$$

Equating the volume averaged strain energy of the RVE with that of its effective homogeneous material[10], i.e.,

$$W^{\text{RVE}} = W^{\text{eff}} \tag{2.22}$$

it is noted that

$$\langle\sigma_{ij}\rangle = L_{ijkl}^{\text{eff}}\bar{\varepsilon}_{kl} = L_{ijkl}^{\text{eff}}\langle\varepsilon_{kl}\rangle \tag{2.23}$$

which is equivalent to Eqn. 2.4.

Finally, it is noted that, while the constituents of the microscale RVE may have a variety of material symmetries, the resulting effective properties of the composite will depend both on the material symmetries of the constituents and on the their arrangement in the microscale RVE. For example, a composite with aligned fibers which have either isotropic or transversely isotropic material symmetry will have effective properties which are transversely isotropic. In contrast, if those same fibers

[9]The divergence theorem is also known as the Gauss theorem.

[10]The equivalency of strain energy is rooted in minimum energy principles and is related to the equivalency of internal energy. See for example [198].

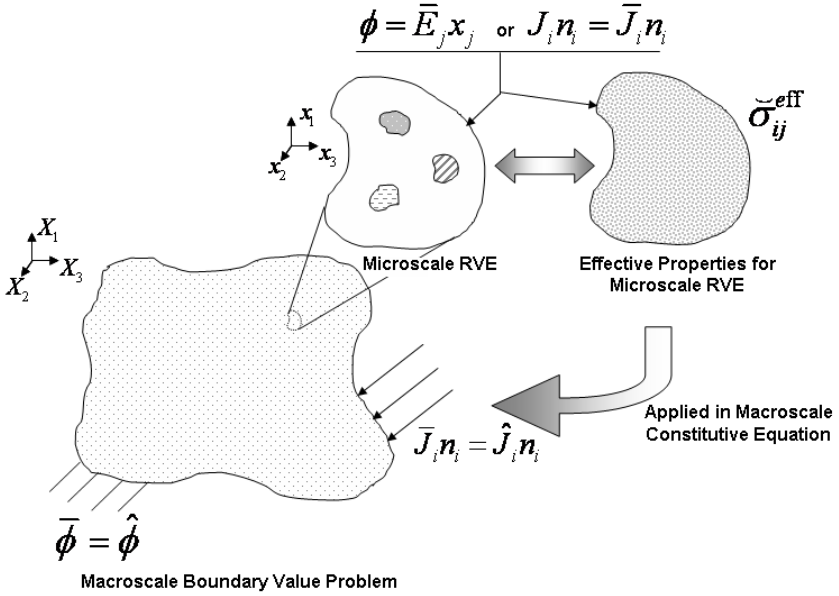

Fig. 5. General schematic representing the relationship between the macroscale boundary value problem and its corresponding microscale RVE from which effective electrical conductivity is determined. The microscale RVE is noted to be subjected to homogeneous potentials or electric flux in terms of the macroscale average electric field or electric flux which is depicted for a general composite microstructure having an assortment of irregularly shaped inhomogeneities.

are randomly oriented, the effective properties will be isotropic. These two cases are noted as they are relevant to CNT-polymer nanocomposites and as such, will be discussed in greater detail in the subsequent chapters.

2. RVE and Governing Differential Equations for Electrical Conductivity

As was the case with the effective elastic properties, the effective electrical conductivity is typically obtained by establishing an equivalency between the microscale RVE of the composite and a representation of that RVE as an effective homogeneous medium as shown schematically in Figure 5. The governing differential equations for

the macroscale and for the microscale RVE are obtained from the theory of electromagnetism of continuous media[11]. It can analogously be shown through the theory of multiple scale expansion that, for linear materials and an asymptotic expansion of the potential of order δ^2, that the macroscale and microscale can be related to one another through the definition of the effective electrical conductivity tensor, $\breve{\sigma}_{ij}^{\text{eff}}$, where the inverted chevron is used to distinguish the electrical conductivity tensor from the Cauchy stress. As such, the steady state conservation of charge equation at the macroscale can be expressed as

$$\bar{J}_{i,\,i} = 0 \tag{2.24}$$

where $\bar{J}_i$ is the macroscale electric flux vector[12] and $\bar{J}_{i,\,i}$ denotes the divergence of the electric flux vector in terms of the X_i coordinate system[13]. The boundary conditions at the macroscale can be either specified electric flux, $\bar{J}_i n_i = \hat{J}_i n_i$ where n_i is the unit outward normal of the boundary, or specified potential, $\bar{\phi} = \hat{\phi}$, or a nonintersecting combination of the two. The macroscale electric field vector, $\bar{E}_i$, is taken as irrotational[14], i.e.

$$\bar{E}_{j,\,i} e_{ijk} = 0 \tag{2.25}$$

where e_{ijk} is the permutation symbol with the left hand side of Eqn. 2.25 denoting the curl of the electric field in terms of the macroscale X_i coordinate system. As

[11]Many texts on electromagnetism of continuous media provide the following equations. In particular, *Electromagnetism of Continuous Media* by Fabrizio and Morro [204] is provided as a reference. (see also [205])

[12]J_i is also referred to as the current density vector where the current, i, is the charge per unit area per unit time and is related to the current density vector by $i_{\hat{n_j}} = J_j \hat{n_j}$ where $\hat{n_j}$ is the unit outward normal of the surface through which the current is flowing.

[13]It is noted that the forced current density J_i^f is assumed to be zero.

[14]This corresponds to the local form of Faraday's law in steady state.

such, it is implied that the macroscale electric field can be described in terms of the gradient (with respect to the macroscale coordinate system) of a scalar potential, $\bar{\phi}$, by

$$\bar{E}_i = -\bar{\phi}_{,\,i} \tag{2.26}$$

The macroscale constitutive relation describing the electric flux in terms of the electric field is identified by Ohm's law as

$$\bar{J}_i = \check{\sigma}_{ij}^{\text{eff}} \bar{E}_j \tag{2.27}$$

where the effective electrical conductivity is obtained from the microscale RVE and is therefore a function of the x_i coordinate system. It can further be shown that Eqn. 2.27 can alternatively be expressed as

$$\langle J_i \rangle = \check{\sigma}_{ij}^{\text{eff}} \langle E_j \rangle \tag{2.28}$$

where $\langle J_i \rangle$ and $\langle E_i \rangle$ denote the volume averages of the electric flux and field, respectively, over the microscale RVE.

For the microscale RVE, the steady state conservation of charge for a continuum is expressed as

$$J_{i,\,i} = 0 \tag{2.29}$$

where J_i is the microscale electric flux vector and $J_{i,\,i}$ denotes the divergence of electric flux in terms of the x_i coordinate system. The microscale electric field vector, E_i, is also taken as irrotational, i.e.

$$E_{j,\,i} e_{ijk} = 0 \tag{2.30}$$

with the left hand side of Eqn. 2.30 denoting the curl of the electric field with respect to the microscale x_i coordinate system, with the electric field described in terms of

the gradient of a scalar potential, ϕ by

$$E_i = -\phi_{,\,i} \tag{2.31}$$

Assuming that all of the materials in the composite are governed by Ohm's law, the microscale constitutive relation is expressed as

$$J_i = \check{\sigma}_{ij} E_j \tag{2.32}$$

where $\check{\sigma}_{ij}$ is the second order electrical conductivity tensor which varies in x_i depending on the microstructure of the composite. The inverse of electrical conductivity is defined to be the electrical resistivity tensor, $\check{\rho}_{ij}$, so that Eqn. 2.32 can alternatively be expressed as

$$E_i = \check{\rho}_{ij} J_j \tag{2.33}$$

As the electrical conductivity and resistivity are second order tensors, there are at most 9 independent tensor components. The number of independent components can be reduced by considering material symmetries. Again, of particular interest to the present work are orthotropic (3 independent components), transversely isotropic (2 independent components), and isotropic (1 independent component) material symmetries. For example, the electrical conductivity tensor for an orthotropic material can be expressed in engineering notation as

$$\left\{ \begin{array}{c} J_1 \\ J_2 \\ J_3 \end{array} \right\} = \left[\begin{array}{ccc} \check{\sigma}_{11} & 0 & 0 \\ 0 & \check{\sigma}_{22} & 0 \\ 0 & 0 & \check{\sigma}_{33} \end{array} \right] \left\{ \begin{array}{c} E_1 \\ E_2 \\ E_3 \end{array} \right\} \tag{2.34}$$

Thus, substituting the constitutive relation (Eqn. 2.32) and definition of the electric field (Eqn. 2.31) into Eqn. 2.29, the conservation of charge equation for the

microscale RVE can be written as

$$(\check{\sigma}_{ij}E_j)_{,\,i} = \check{\sigma}_{ij}\phi_{,\,ij} + \phi_{,\,i}\,\check{\sigma}_{ji,\,j} = 0 \tag{2.35}$$

which for homogeneous materials reduces to

$$\check{\sigma}_{ij}\,\phi_{,\,ij} = 0 \tag{2.36}$$

so that for isotropic materials the potential is obtained from the solution of Laplace's equation. On the boundary of the microscale RVE, it can be shown from the theory of multiple scale expansion that the electric flux or electric potential conditions are homogeneous and consistent with the electric flux or electric field at the macroscale, i.e.

$$J_i n_i = \bar{J}_i n_i \tag{2.37a}$$

$$\phi = \bar{\phi} x_j \tag{2.37b}$$

where n_i is the unit outward normal to the microscale RVE boundary. It can further be shown that, for linear materials and expansion of order δ^2, the multiple scale expansion is synonymous with equating a scalar function, analogous to the strain energy in elasticity, of the RVE to that of the homogeneous effective material, i.e.

$$W^{\mathrm{RVE}} = W^{\mathrm{eff}} \tag{2.38}$$

where

$$W^{\mathrm{RVE}} = \langle w \rangle = \frac{1}{2}\langle J_i E_i \rangle = \frac{1}{2}\langle J_i \rangle \langle E_i \rangle \tag{2.39a}$$

$$W^{\mathrm{eff}} = \langle w^{\mathrm{eff}} \rangle = \frac{1}{2}\langle J_i^{\mathrm{eff}} E_i^{\mathrm{eff}} \rangle = \frac{1}{2}\langle J_i^{\mathrm{eff}} \rangle \langle E_i^{\mathrm{eff}} \rangle \tag{2.39b}$$

where J_i^{eff} and E_i^{eff} are the electric flux and field, respectively, in the effective homogeneous material subject to boundary conditions as in Eqn. 2.37. For example,

assuming the RVE and effective homogeneous material are subject to the homogeneous potential in Eqn. 2.37b, then Eqn. 2.38 reduces to

$$\langle J_i \rangle = \breve{\sigma}_{ij}^{\text{eff}} \bar{E}_j = \breve{\sigma}_{ij}^{\text{eff}} \langle E_j \rangle \tag{2.40}$$

which is equivalent to Eqn. 2.28.

3. RVE and Governing Differential Equations for Thermal Conductivity

As was the case with the effective elastic properties and electrical conductivity, the effective thermal conductivity is typically obtained by establishing an equivalency between the microscale RVE of the composite and a representation of that RVE as an effective homogeneous medium as shown schematically in Figure 6. The governing differential equations for the macroscale and for the microscale RVE are obtained from general continuum theory for heat transfer in solids [15] in the form of the steady state heat conduction equation[16]. It can analogously be shown through the theory of multiple scale expansion that, for linear materials and an asymptotic of order δ^2, that the macroscale and microscale can be related to one another through the definition of the effective thermal conductivity tensor, k_{ij}^{eff}. As such, the steady state heat conduction equation at the macroscale can be expressed as

$$\bar{q}_{i,\,i} = 0 \tag{2.41}$$

---

[15] Many texts on continuum theory and heat transfer in solids provide the following equations. In particular, *Mechanics of Composite Materials* by Richard M. Christensen [198] and the work by Hashin [178] are provided as references.

[16] The local form of the conservation of energy (i.e., the first law of thermodynamics) can be written as $\rho \frac{dU}{dt} = \sigma_{ij} d_{ij} + \rho\, r - q_{i,\,i}$, where ρ is the density, U is the internal energy per unit mass, or the specific internal energy, σ_{ij} is the stress tensor, d_{ij} is the rate of deformation tensor, r is the heat source/sink per unit mass, and q_i is the heat flux vector. Under the assumptions of steady state conditions, no thermo-mechanical coupling, and no heat sources/sinks, the conservation of energy reduces to $q_{i,\,i} = 0$

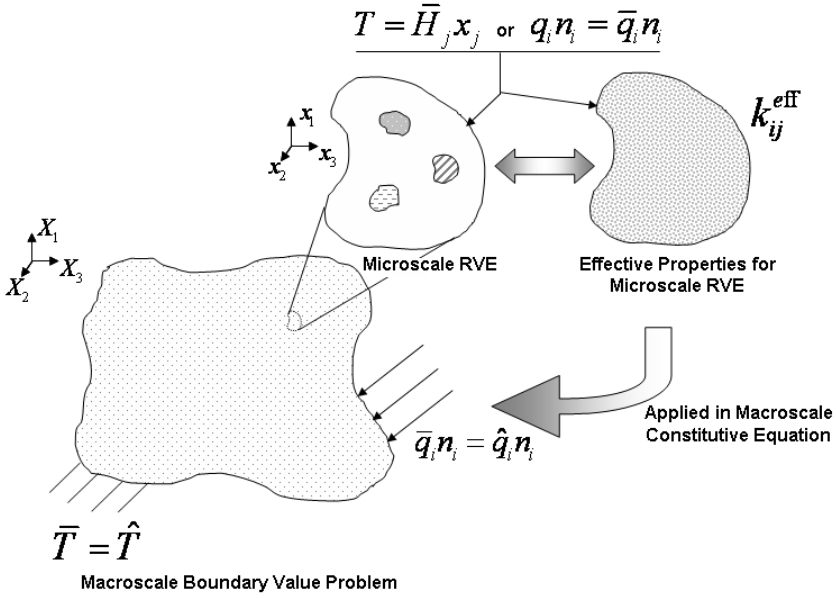

Fig. 6. General schematic representing the relationship between the macroscale boundary value problem and its corresponding microscale RVE from which effective thermal conductivity is determined. The microscale RVE is noted to be subjected to homogeneous temperature or heat flux in terms of the macroscale average heat intensity or heat flux which is depicted for a general composite microstructure having an assortment of irregularly shaped inhomogeneities.

where $\bar{q}_i$ is the macroscale flux vector and $\bar{q}_{i,\,i}$ denotes the divergence of the heat flux vector in terms of the X_i coordinate system. The boundary conditions at the macroscale can be either specified heat flux, $\bar{q}_i n_i = \hat{q}_i n_i$ where n_i is the unit outward normal of the boundary, or specified temperature, $\bar{T} = \hat{T}$, or a nonintersecting combination of the two. The macroscale heat intensity vector, $\bar{H}_i$, is defined in terms of the gradient (with respect to the macroscale coordinate system) of the temperature, $\bar{T}$, by

$$\bar{H}_i = -\bar{T}_{,\,i} \tag{2.42}$$

so that the heat intensity is also irrotational. The macroscale constitutive relation describing the heat flux in terms of the heat intensity is identified by Fourier's law as

$$\bar{q}_i = k_{ij}^{\text{eff}} \bar{H}_j \tag{2.43}$$

where the effective thermal conductivity is obtained from the microscale RVE and is therefore a function of the x_i coordinate system. It can further be shown that Eqn. 2.43 can alternatively be expressed as

$$\langle q_i \rangle = k_{ij}^{\text{eff}} \langle H_j \rangle \tag{2.44}$$

where $\langle q_i \rangle$ and $\langle H_i \rangle$ denote the volume averages of the heat flux and heat intensity, respectively, over the microscale RVE.

For the microscale RVE, the steady state heat conduction equation is expressed as

$$q_{i,\,i} = 0 \tag{2.45}$$

where q_i is the microscale heat flux vector and $q_{i,\,i}$ denotes the divergence of the heat flux in terms of the x_i coordinate system. The microscale heat intensity vector, H_i, is defined in terms of the gradient (with respect to the microscale x_i coordinate system)

of the temperature, T, by

$$H_i = -T_{,\,i} \tag{2.46}$$

Assuming that all of the materials in the composite are governed by Fourier's law, the microscale constitutive relation is expressed as

$$q_i = k_{ij} H_j \tag{2.47}$$

where k_{ij} is the second order thermal conductivity tensor which varies in x_i depending on the microstructure of the composite. The inverse of the thermal conductivity is defined to be the thermal resistivity tensor, ξ_{ij}, so that Eqn. 2.47 can alternatively be expressed as

$$H_i = \xi_{ij} q_j \tag{2.48}$$

As with the electrical conductivity and resistivity tensors, the thermal conductivity and resistivity are second order tensors, which can have orthotropic, transversely isotropic, and isotropic material symmetries which are of interest to the present study. Thus, similar to Eqn. 2.34, the thermal conductivity tensor for an orthotropic material can be expressed in engineering notation as

$$\left\{ \begin{array}{c} q_1 \\ q_2 \\ q_3 \end{array} \right\} = \left[\begin{array}{ccc} k_{11} & 0 & 0 \\ 0 & k_{22} & 0 \\ 0 & 0 & k_{33} \end{array} \right] \left\{ \begin{array}{c} H_1 \\ H_2 \\ H_3 \end{array} \right\} \tag{2.49}$$

Thus, substituting the Fourier's law (Eqn. 2.47) and the definition of the heat intensity (Eqn. 2.46) into Eqn. 2.45, the steady state heat conduction can be written as

$$(k_{ij} H_j)_{,\,i} = k_{ij} T_{,\,ij} + T_{,\,i}\, k_{ji,\,j} = 0 \tag{2.50}$$

which for homogeneous materials reduces to

$$k_{ij}T_{,\,ij} = 0 \tag{2.51}$$

so that for isotropic material the temperature is obtained from the solution of Laplace's equation. On the boundary of the microscale RVE, it can be shown from the theory of multiple scale expansion that the heat flux or heat intensity conditions are homogeneous and consistent with the heat flux or thermal intensity at the macroscale, i.e.

$$q_i n_i = \bar{q}_i n_i \tag{2.52a}$$

$$T = \bar{T} x_j \tag{2.52b}$$

where n_i is the unit outward normal to the microscale RVE boundary. It can further be shown that, for linear materials and expansion of order δ^2, the multiple scale expansion is synonymous with equating a scalar function, analogous to the strain energy in elasticity, of the RVE to that of the homogeneous effective material, i.e.

$$W^{\mathrm{RVE}} = W^{\mathrm{eff}} \tag{2.53}$$

where

$$W^{\mathrm{RVE}} = \langle w \rangle = \frac{1}{2}\langle q_i H_i \rangle = \frac{1}{2}\langle q_i \rangle \langle H_i \rangle \tag{2.54a}$$

$$W^{\mathrm{eff}} = \langle w^{\mathrm{eff}} \rangle = \frac{1}{2}\langle q_i^{\mathrm{eff}} H_i^{\mathrm{eff}} \rangle = \frac{1}{2}\langle q_i^{\mathrm{eff}} \rangle \langle H_i^{\mathrm{eff}} \rangle \tag{2.54b}$$

where q_i^{eff} and H_i^{eff} are the heat flux and heat intensity, respectively, in the effective homogeneous material subject to boundary conditions as in Eqn. 2.52. For example, assuming the RVE and effective homogeneous material are subject to the homogeneous potential in Eqn. 2.52b, then Eqn. 2.53 reduces to

$$\langle q_i \rangle = k_{ij}^{\mathrm{eff}} \bar{H}_j = k_{ij}^{\mathrm{eff}} \langle H_j \rangle \tag{2.55}$$

which is equivalent to Eqn. 2.44.

Finally, from Eqns. 2.29, 2.31, 2.32, 2.36, 2.37, and 2.38 describing the microscale electrical conductivity and from Eqns. 2.45, 2.46, 2.47, 2.51, 2.52, and 2.53 describing the microscale thermal conductivity, it is noted that the sets of equations are mathematically analogous. Hence, in some of the derivations which follow, only the thermal conductivity equations will be derived with the understanding that the subsequent derivations will be analogously applicable to the electrical conductivity. However, it is noted that the physical mechanisms of thermal and electrical conduction are observably different at the nanoscale[17], and thus may have, in addition to different conductivities, important nanoscale effects which become significant for nanoscale inhomogeneities.

B. General Averaging Methods for Effective Properties

It has been noted in Section A of this chapter that the effective properties of the composite can be expressed in terms of volume averages over the microscale RVE, i.e. for elastic stiffness and compliance

$$\langle \sigma_{ij} \rangle = L^{\text{eff}}_{ijkl} \langle \varepsilon_{kl} \rangle \tag{2.56a}$$

$$\langle \varepsilon_{ij} \rangle = M^{\text{eff}}_{ijkl} \langle \sigma_{kl} \rangle \tag{2.56b}$$

and for thermal conductivity and resistivity

$$\langle q_i \rangle = k^{\text{eff}}_{ij} \langle H_j \rangle \tag{2.57a}$$

$$\langle H_i \rangle = \xi^{\text{eff}}_{ij} \langle q_j \rangle \tag{2.57b}$$

[17]For example the scattering behaviors of phonons and electrons can be different.

It is further noted that, for composites containing materials with linear constitutive response[18], the effective properties are independent of the macroscale boundary conditions and geometry, i.e. the effective properties are not dependent on the variation of the macroscale stresses or displacements. As such, the focus in determining effective properties can be placed solely on the microscale RVE.

Within the microscale RVE, subsets of volume, V_J of the total RVE volume, V, corresponding to the separate phases identified in the RVE are used to define a volume fraction for that phase as

$$c_J \equiv \frac{V_J}{V} \tag{2.58}$$

such that for N phases

$$1 = \sum_{J=1}^{N} c_J \tag{2.59}$$

An explicit definition for what constitutes a phase within the RVE will be provided shortly. For the present discussion, the simplest assumption is made wherein each inhomogeneity in the RVE and the matrix in which the inhomogeneities are embedded are all considered to be separate phases. Thus, the volume averages of the stress and strain and the heat flux and heat intensity in the RVE can be expressed in terms of the volume averages of these quantities in each phase by

$$\langle \sigma_{ij} \rangle = \frac{1}{V} \left[\sum_{J=1}^{N} \frac{V_J}{V_J} \int_{V_J} \sigma_{ij}^J \, dV \right] \tag{2.60a}$$

$$\langle \varepsilon_{ij} \rangle = \frac{1}{V} \left[\sum_{J=1}^{N} \frac{V_J}{V_J} \int_{V_J} \varepsilon_{ij}^J \, dV \right] \tag{2.60b}$$

$$\langle q_i \rangle = \frac{1}{V} \left[\sum_{J=1}^{N} \frac{V_J}{V_J} \int_{V_J} q_i^J \, dV \right] \tag{2.60c}$$

[18]It is also noted that it is assumed that there is no damage evolution at the microscale.

$$\langle H_i \rangle = \frac{1}{V}\left[\sum_{J=1}^{N} \frac{V_J}{V_J} \int_{V_J} H_i^J \, dV\right] \tag{2.60d}$$

which can be written as

$$\langle \sigma_{ij} \rangle = \sum_{J=1}^{N} c_J \langle \sigma_{ij}^J \rangle \tag{2.61a}$$

$$\langle \varepsilon_{ij} \rangle = \sum_{J=1}^{N} c_J \langle \varepsilon_{ij}^J \rangle \tag{2.61b}$$

$$\langle q_i \rangle = \sum_{J=1}^{N} c_J \langle q_i^J \rangle \tag{2.61c}$$

$$\langle H_i \rangle = \sum_{J=1}^{N} c_J \langle H_i^J \rangle \tag{2.61d}$$

where the superscript J denotes value of the quantity within the J^{th} phase. Applying the constitutive relations in Eqns. 2.8 and 2.9 and in 2.47 and 2.48, the volume averages of these quantities in the RVE given in Eqn. 2.61 can be written as

$$\langle \sigma_{ij} \rangle = \sum_{J=1}^{N} c_J \langle L_{ijkl}^J \varepsilon_{kl}^J \rangle \tag{2.62a}$$

$$\langle \varepsilon_{ij} \rangle = \sum_{J=1}^{N} c_J \langle M_{ijkl}^J \sigma_{kl}^J \rangle \tag{2.62b}$$

$$\langle q_{ij} \rangle = \sum_{J=1}^{N} c_J \langle k_{ij}^J H_j^J \rangle \tag{2.62c}$$

$$\langle H_i \rangle = \sum_{J=1}^{N} c_J \langle \xi_{ij}^J q_j^J \rangle \tag{2.62d}$$

Assuming each phase is homogeneous, these volume averaged can further be written as

$$\langle \sigma_{ij} \rangle = \sum_{J=1}^{N} c_J L_{ijkl}^J \langle \varepsilon_{kl}^J \rangle \tag{2.63a}$$

$$\langle \varepsilon_{ij} \rangle = \sum_{J=1}^{N} c_J M_{ijkl}^J \langle \sigma_{ij}^J \rangle \tag{2.63b}$$

$$\langle q_i \rangle = \sum_{J=1}^{N} c_J k_{ij}^J \langle H_j^J \rangle \tag{2.63c}$$

$$\langle H_i \rangle = \sum_{J=1}^{N} c_J \xi_{ij}^J \langle q_j^J \rangle \tag{2.63d}$$

The concentration tensor is now defined as the tensor that transforms the average quantity (stress, strain, heat flux, and heat intensity) into a phase averaged quantity, i.e.

$$\langle \sigma_{ij}^J \rangle = B_{ijkl}^J \langle \sigma_{kl} \rangle \tag{2.64a}$$

$$\langle \varepsilon_{ij}^J \rangle = A_{ijkl}^J \langle \varepsilon_{ij} \rangle \tag{2.64b}$$

$$\langle q_i^J \rangle = B_{ij}^J \langle q_j \rangle \tag{2.64c}$$

$$\langle H_i \rangle = A_{ij}^J \langle H_j \rangle \tag{2.64d}$$

where in indicial notation it is clear that the concentration tensors in the context of elasticity are fourth order tensors where as in the context of heat conduction, they are second order tensors. It is also of interest to note that from Eqn. 2.64 and the definition of the volume average quantities in Eqn. 2.61 one can, for example, write

$$\langle \varepsilon_{ij} \rangle = \sum_{J=1}^{N} c_J A_{ijkl}^J \langle \varepsilon_{kl} \rangle \tag{2.65}$$

so that the following useful identities, known as the consistency conditions, are obtained as

$$I_{ijkl} = \sum_{J=1}^{N} c_J A_{ijkl}^J \tag{2.66a}$$

$$I_{ijkl} = \sum_{J=1}^{N} c_J B_{ijkl}^J \tag{2.66b}$$

$$I_{ij} = \sum_{J=1}^{N} c_J A_{ij}^J \tag{2.66c}$$

$$I_{ij} = \sum_{J=1}^{N} c_J B_{ij}^J \tag{2.66d}$$

where I_{ijkl} and I_{ij} are the fourth and second order identity tensors, respectively.

Substituting the definitions of the concentration tensors in Eqns. 2.64 into Eqns. 2.63, one can obtain

$$\langle \sigma_{ij} \rangle = \sum_{J=1}^{N} c_J L_{ijkl}^J A_{klmn}^J \langle \varepsilon_{mn} \rangle \tag{2.67a}$$

$$\langle \varepsilon_{ij} \rangle = \sum_{J=1}^{N} c_J M_{ijkl}^J B_{klmn}^J \langle \sigma_{mn} \rangle \tag{2.67b}$$

$$\langle q_i \rangle = \sum_{J=1}^{N} c_J k_{ij}^J A_{jm}^J \langle H_m \rangle \tag{2.67c}$$

$$\langle H_i \rangle = \sum_{J=1}^{N} c_J \xi_{ij}^J B_{jm}^J \langle q_m \rangle \tag{2.67d}$$

Therefore, from the definitions of the effective properties in Eqns. 2.56 and 2.57, it is observed from Eqn. 2.67 that the effective properties can be obtained as

$$L_{ijmn}^{\text{eff}} = \sum_{J=1}^{N} c_J L_{ijkl}^J A_{klmn}^J \tag{2.68a}$$

$$M_{ijmn}^{\text{eff}} = \sum_{J=1}^{N} c_J M_{ijkl}^J B_{klmn}^J \tag{2.68b}$$

$$k_{im}^{\text{eff}} = \sum_{J=1}^{N} c_J k_{ij}^J A_{jm}^J \tag{2.68c}$$

$$\xi_{im}^{\text{eff}} = \sum_{J=1}^{N} c_J \xi_{ij}^J B_{jm}^J \tag{2.68d}$$

In light of the consistency conditions in Eqn. 2.66, one can choose to rewrite Eqns. 2.68 without using one of the concentration tensors. Assuming one wants to discriminate against the matrix phase (phase N), one can rewrite the consistency

conditions as

$$c_N A^N_{ijkl} = I_{ijkl} - \sum_{J=1}^{N-1} c_J A^J_{ijkl} \tag{2.69a}$$

$$c_N B^N_{ijkl} = I_{ijkl} - \sum_{J=1}^{N-1} c_J B^J_{ijkl} \tag{2.69b}$$

$$c_N A^N_{ij} = I_{ij} - \sum_{J=1}^{N-1} c_J A^J_{ij} \tag{2.69c}$$

$$c_N B^N_{ij} = I_{ij} - \sum_{J=1}^{N-1} c_J B^J_{ij} \tag{2.69d}$$

Substituting Eqns. 2.69 into Eqns. 2.68, e.g.

$$L^{\text{eff}}_{ijmn} = \frac{c_N}{c_N} L^N_{ijkl} \left(I_{klmn} - \sum_{J=1}^{N-1} c_J A^J_{klmn} \right) + \sum_{J=1}^{N-1} c_J L^J_{ijkl} A^J_{klmn} \tag{2.70}$$

the effective properties can be written as

$$L^{\text{eff}}_{ijmn} = L^N_{ijmn} + \sum_{J=1}^{N-1} c_J (L^J_{ijkl} - L^N_{ijkl}) A^J_{klmn} \tag{2.71a}$$

$$M^{\text{eff}}_{ijmn} = M^N_{ijmn} + \sum_{J=1}^{N-1} c_J (M^J_{ijkl} - M^N_{ijkl}) B^J_{klmn} \tag{2.71b}$$

$$k^{\text{eff}}_{im} = k^N_{im} + \sum_{J=1}^{N-1} c_J (k^J_{ij} - k^N_{ij}) A^J_{jm} \tag{2.71c}$$

$$\xi^{\text{eff}}_{im} = \xi^N_{im} + \sum_{J=1}^{N-1} c_J (\xi^J_{ij} - \xi^N_{ij}) B^J_{jm} \tag{2.71d}$$

From the effective properties as expressed in Eqns. 2.71 one can see that, for a given RVE, inhomogeneities having the same material properties and concentration tensors can be considered a single phase, so that their individual volumes combine in determining the volume fraction of that phase. Whether or not a set of inhomogeneities in the RVE constitutes a single phase is therefore influenced by factors such as the shapes of the inhomogeneities, relative geometric orientation of the in-

homogeneities within the RVE, and orientation of the material symmetry within the inhomogeneities, among others. For example, for an RVE consisting of well-dispersed spheres with the same isotropic material properties (though perhaps of differing radii), the spheres would constitute a single phase. If however, these spheres had the same non-isotropic material property, then each distinct orientation of the material symmetry relative to the RVE coordinate system would constitute a separate phase. As another example, for an RVE consisting of well-dispersed self-similar ellipsoids with isotropic material properties, the ellipsoids can be considered a single phase if the ellipsoids are all aligned, or a separate phase for each orientation if the ellipsoids have different orientations relative to the RVE coordinate system. In the first example, both the material properties and concentration tensors are noted to differ between the two cases. In the second example, only the concentration tensor differs between the two cases. As the material properties for all of the phases are given, the emphasis is then on the determination of the concentration tensor for each phase.

In order to sufficiently represent all of the salient features of the microstructure, an RVE may contain a large number inhomogeneities. In some cases, a solution to the microscale RVE boundary value problem may be obtainable using periodic boundary conditions. In such cases, the effective properties are able to be determined through direct implementation of the multiple scale expansion theory, typically in a finite element model, and there is no need to determine concentration tensors. In other cases, for example when an RVE becomes too computationally intensive, it is common practice to take advantage of the grouping of inhomogeneities into phases and use either closed form solutions or approximate solutions (some of which may also involve finite element modeling) to approximate the concentration tensors for each phase for use in Eqn. 2.71. These approximations consider individual inhomogeneities (or even in small collections of inhomogeneities as in bundles or clusters) in determining the

concentration tensor(s) for a given phase, where the focus of the approximation is on how to account for the interactions of the individual inhomogeneities with all other inhomogeneities within the RVE. Three such approximations are the self-consistent method, the Mori-Tanaka method, an the generalized self-consistent method shown schematically in Figure 7 as applied towards determining the effective elastic properties.

In the self-consistent method [130, 206], the J^{th} inhomogeneity is embedded in an infinite medium[19] having the same material properties as the effective properties that are sought for the microscale RVE, e.g. L^{eff}_{ijkl}, and subject to far field homogeneous displacements or tractions equivalent to those identified for the microscale RVE. As the concentration tensor used to calculate the effective properties will therefore be a function of those same effective properties, Eqns. 2.71 becomes nonlinear in the self-consistent approximation. Interactions are therefore taken into account in the self-consistent method in the solution of the nonlinear equations as a result of the consistency conditions (Eqn. 2.66). In the Mori-Tanaka approximation [127, 128, 207], the J^{th} inhomogeneity is embedded in an infinite medium having the same material properties as the matrix, e.g. L^{N}_{ijkl}. In this case, the far field homogeneous displacements or tractions are taken as equivalent to those identified for the microscale RVE plus a perturbation (denoted by the tilde in Fig. 7(b)) which accounts for interactions in the application of the consistency conditions. In the generalized self-consistent [159, 178, 186], the J^{th} inhomogeneity is embedded in a small amount of matrix material[20], and this ensemble is then embedded in the effective medium.

[19] Approaches using closed form solutions often consider the inhomogeneity as embedded in an infinite medium. Computational approaches use finite sized computational domains with various criteria to identify how large is large enough to be effectively infinite.

[20] The question naturally arises as to how much matrix is needed in constructing

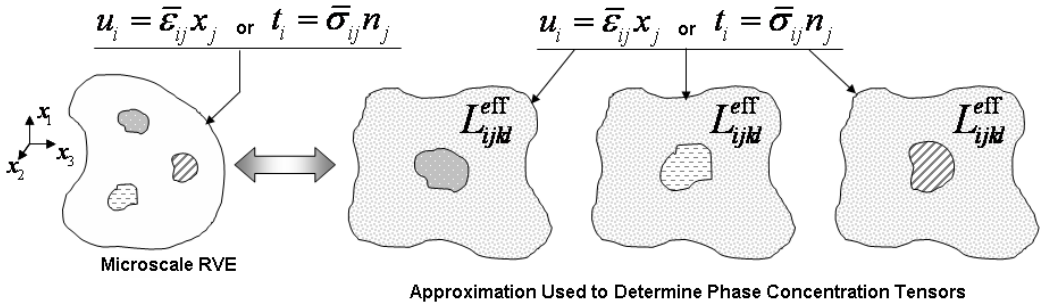

(a) Self-Consistent Approximation

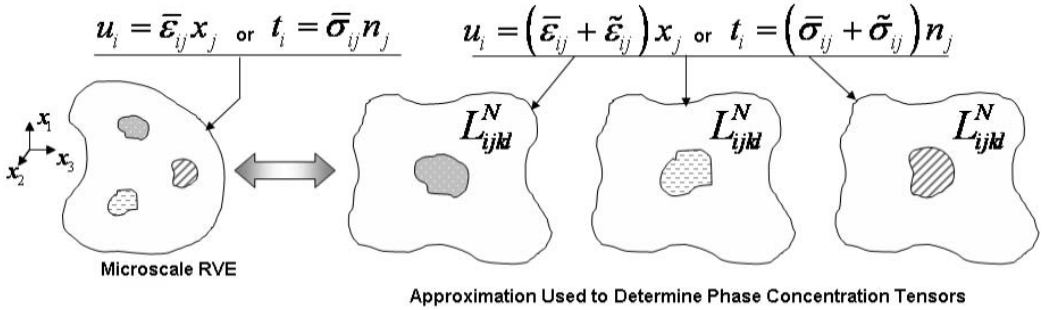

(b) Mori-Tanaka Approximation

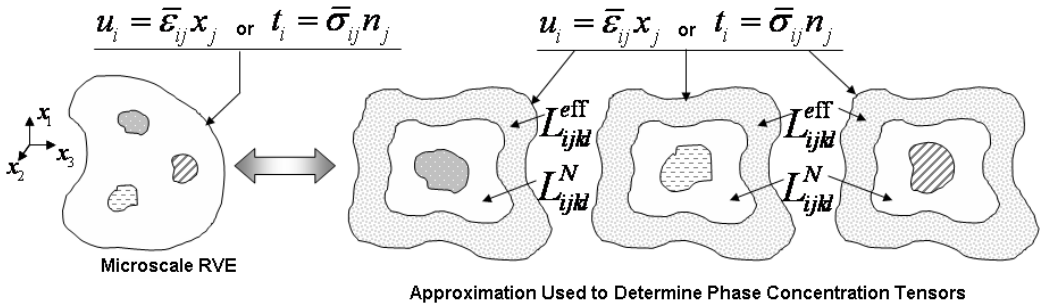

(c) Generalized Self-Consistent Approximation

Fig. 7. Approximations applied in determining phase concentration tensors by considering inhomogeneities individually in an infinite medium.

Thus, the far field displacements or tractions applied are equivalent to those applied in the self-consistent approximation.

Each of these three approximations can be carried out using closed form or approximate computational techniques. For complicated irregular shapes or distributions of inhomogeneities where detailed interactions are important such as in clusters or bundles, computational approaches may be preferable.[21] However, some shapes have convenient closed form solutions (e.g. homogeneous ellipsoidal shapes or heterogeneous shapes of special geometries like spheres and circular cylinders in regards to coated inhomogeneities) which can be taken advantage of in determining concentration tensors. For ellipsoidal inhomogeneities, the self-consistent and Mori-Tanaka approaches are readily applied through the use of Eshelby's equivalence principle[22] [131] making use of the Eshelby solution [131] for an ellipsoidal inclusion in an infinite matrix.

C. Closed Form Methods for Concentration Tensor Approximation

1. The Self-Consistent Method

The following equations provide a summary of the closed form approach to approximating the concentration tensors using the self-consistent method for determining both the effective elastic properties and effective conductivities. The summary follows the original derivation provided by Hill [130].

---

the generalized self-consistent model. This will be discussed in greater detail in the subsequent sections.

[21]It is noted that from a computational stand point, the Mori-Tanaka provides a more convenient implementation as compared to the self-consistent and generalized self-consistent approaches which are inherently nonlinear.

[22]This is sometimes referred to as the Eshelby equivalent inclusion method.

a. The Self-Consistent Method for Elastic Properties

To calculate the strain concentration tensor (or the stress concentration tensor) for homogeneous ellipsoidal inhomogeneities in a linear elastic matrix, one can take advantage of Eshelby's equivalence principle and the Eshelby solution by individually embedding each inhomogeneity into the effective medium subject to far field displacements or tractions consistent with those applied to the boundary of the microscale RVE, which are reflective of the average macroscale strain/strain (see Fig. 8).

Consider the J^{th} inhomogeneity embedded in an infinite body whose material properties are those of the unknown effective material (as shown in Figure 8), where the applied homogeneous displacement at infinity is reflective of the homogeneous displacement field applied to the boundary of the microscale RVE, i.e. the uniform strain in the applied displacement is $\varepsilon^A_{ij} = \bar{\varepsilon}_{ij}$ where it is recalled that $\bar{\varepsilon}_{ij} = \langle \varepsilon_{ij} \rangle$.

From the equivalence principle, the stress in the J^{th} inhomogeneity is related to the stress in an inclusion within the embedding material which is subject to an unknown eigenstrain, and is therefore given as

$$\sigma^J_{ij} = L^J_{ijkl}(\varepsilon^C_{kl} + \varepsilon^A_{kl}) = L^{\text{eff}}_{ijkl}(\varepsilon^C_{kl} + \varepsilon^A_{kl} - \varepsilon^T_{kl}) \tag{2.72}$$

where the strain in the inhomogeneity is $\varepsilon^J_{kl} = \varepsilon^C_{kl} + \varepsilon^A_{kl}$. Solving Eqn. 2.72 for the unknown eigenstrain for the J^{th} inhomogeneity, ε^T_{kl}, one obtains

$$L^J_{ijkl}\varepsilon^J_{kl} = L^{\text{eff}}_{ijkl}\varepsilon^J_{kl} - L^{\text{eff}}_{ijkl}\varepsilon^T_{kl} \tag{2.73}$$

so that

$$L^{\text{eff}}_{ijkl}\varepsilon^T_{kl} = (L^{\text{eff}}_{ijkl} - L^J_{ijkl})\varepsilon^J_{kl} \tag{2.74}$$

and thus one obtains the eigenstrain as

$$\varepsilon^T_{ij} = M^{\text{eff}}_{ijkl}(L^{\text{eff}}_{klmn} - L^J_{klmn})\varepsilon^J_{mn} \tag{2.75}$$

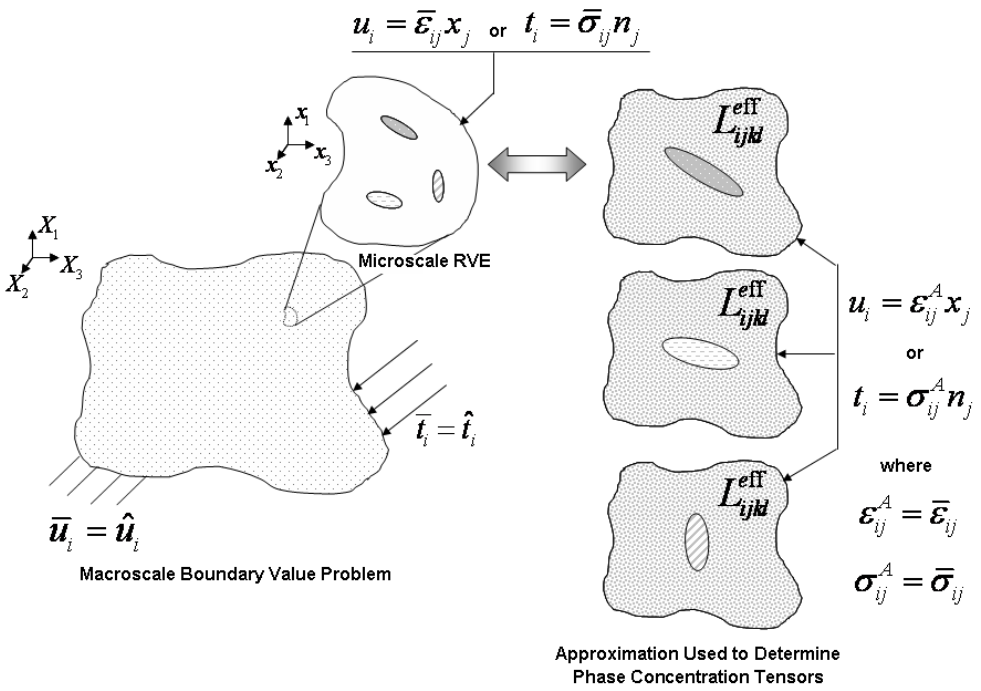

Fig. 8. Self-Consistent Approximation for Elastic Properties: the inhomogeneity is embedded in an infinite body whose material properties are those of the unknown effective material with far field homogeneous displacement applied consistent with the average strain in the RVE.

Since the strain in the inhomogeneity can be expressed as

$$\varepsilon_{kl}^{J} = \varepsilon_{kl}^{C} + \bar{\varepsilon}_{kl} \tag{2.76}$$

and using the Eshelby solution for homogeneous ellipsoids[23], i.e. $\varepsilon_{ij}^{C} = S_{ijkl}\varepsilon_{kl}^{T}$, the strain in the inhomogeneity becomes

$$\varepsilon_{ij}^{J} = S_{ijkl}\varepsilon_{kl}^{T} + \bar{\varepsilon}_{ij} \tag{2.77}$$

so that upon substitution of Eqn. 2.75 into Eqn. 2.77 one obtains

$$\varepsilon_{ij}^{J} = S_{ijkl}M_{klmn}^{\text{eff}}(L_{mnpq}^{\text{eff}} - L_{mnpq}^{J})\varepsilon_{pq}^{J} + \bar{\varepsilon}_{ij} \tag{2.78}$$

which leads to

$$[I_{ijpq} + S_{ijkl}M_{klmn}^{\text{eff}}(L_{mnpq}^{J} - L_{mnpq}^{\text{eff}})]\varepsilon_{pq}^{J} = \bar{\varepsilon}_{ij} \tag{2.79}$$

Thus one may write the strain in the inhomogeneity in terms of the average strain in the RVE as

$$\varepsilon_{pq}^{J} = [I_{ijpq} + S_{ijkl}M_{klmn}^{\text{eff}}(L_{mnpq}^{J} - L_{mnpq}^{\text{eff}})]^{-1}\bar{\varepsilon}_{ij} \tag{2.80}$$

One can define a tensor ${}^{SC}T_{ijkl}^{J}$ relating the strain in the J^{th} inhomogeneity to the uniform strain in the far field applied displacement, i.e. ε_{ij}^{A} which in this case is the average strain in the RVE, such that

$$\varepsilon_{pq}^{J} = {}^{SC}T_{pqij}^{J}\bar{\varepsilon}_{ij} \tag{2.81}$$

Therefore, from Eqn. 2.80, one can identify the tensor ${}^{SC}T_{pqij}^{J}$ as being given by

$${}^{SC}T_{pqij}^{J} = [I_{ijpq} + S_{ijkl}M_{klmn}^{\text{eff}}(L_{mnpq}^{J} - L_{mnpq}^{\text{eff}})]^{-1} \tag{2.82}$$

[23]Now the strain in the inhomogeneity becomes uniform. Also it is noted that the Eshelby tensor, S_{ijkl}, depends on the shape of the inclusion and the material properties of the material in which the inclusion is embedded, here the effective material.

Recalling the definition of the strain concentration tensor from Eqn. 2.64b, and noting that the strain in the ellipsoidal inhomogeneity is uniform, the concentration tensor is therefore identified in the self-consistent method from Eqn. 2.81 as

$$ {}^{SC}A^{J}_{pqij} = {}^{SC}T^{J}_{pqij} \tag{2.83} $$

The stress concentration tensor for the self-consistent method is obtained by the application of constitutive relations to Eqn. 2.81 so that the stress in the J^{th} inhomogeneity is given by

$$ \sigma^{J}_{ij} = L^{J}_{ijkl}\varepsilon^{J}_{kl} = L^{J}_{ijkl}\,{}^{SC}T^{J}_{klmn}\bar{\varepsilon}_{mn} \tag{2.84} $$

However, from the definition of the effective compliance in Eqn. 2.56b, one can write

$$ \bar{\varepsilon}_{mn} = M^{\text{eff}}_{mnpq}\bar{\sigma}_{pq} \tag{2.85} $$

so that the stress in the J^{th} inhomogeneity becomes

$$ \sigma^{J}_{ij} = L^{J}_{ijkl}\,{}^{SC}T^{J}_{klmn}M^{\text{eff}}_{mnpq}\bar{\sigma}_{pq} \tag{2.86} $$

One can define a tensor ${}^{SC}P^{J}_{ijkl}$ relating the stress in the J^{th} inhomogeneity to the uniform stress in the far field applied traction, i.e. σ^{A}_{ij} which in this case is the average stress in the RVE, such that

$$ \sigma^{J}_{ij} = {}^{SC}P^{J}_{ijpq}\bar{\sigma}_{pq} \tag{2.87} $$

so therefore from Eqn. 2.86 one obtains

$$ {}^{SC}P^{J}_{ijpq} = L^{J}_{ijkl}\,{}^{SC}T^{J}_{klmn}M^{\text{eff}}_{mnpq} \tag{2.88} $$

Recalling the definition of the stress concentration tensor from Eqn. 2.64b, and noting that the stress in the ellipsoidal inhomogeneity is uniform, the concentration tensor

is therefore identified in the self-consistent method from Eqn. 2.87 as

$$ {}^{SC}B^{J}_{ijpq} = {}^{SC}P^{J}_{ijpq} \tag{2.89} $$

It is noted that self-similar ellipsoidal inhomogeneities, i.e. ellipsoidal inhomogeneities with the same material properties, with proportional geometry, and with the same geometrical and material symmetry axes, will have the same concentration tensor.

b. The Self-Consistent Method for Thermal Conductivities

To calculate the heat intensity concentration tensor (or the heat flux concentration tensor) for homogeneous ellipsoidal inhomogeneities in a matrix material with linear constitutive behavior, one can apply the thermal equivalent to Eshelby's equivalence principle by individually embedding each inhomogeneity into the effective medium subject to far field temperature or heat flux consistent with those applied to the boundary of the microscale RVE, which are reflective of the average macroscale heat flux/intensity (see Fig. 9).

Consider the J^{th} inhomogeneity embedded in an infinite body whose material properties are those of the unknown effective material (as shown in Figure 9), where the applied homogeneous temperature at infinity is reflective of the homogeneous temperature applied to the boundary of the microscale RVE boundary, i.e. the uniform intensity in the applied temperature is $H^A_i = \bar{H}_i$ where it is recalled that $\bar{H}_i = \langle H_i \rangle$. Further, it is noted that, in an analogy with the total and elastic strains, the total intensity is decomposed into two parts, the intensity from the thermal gradient governed by Fourier's law and the intensity which results from an "eigen thermal gradient"[178], i.e. $H^{\text{Total}}_i = H^{\text{Fourier}}_i + H^T_i$ where H^T_i is the "eigen thermal gradient".

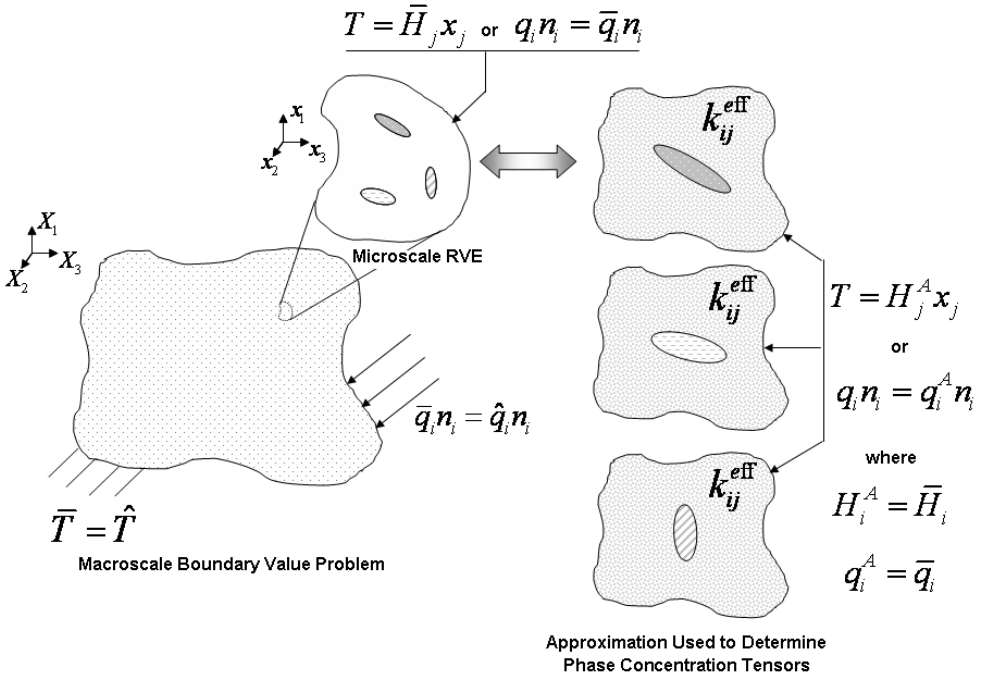

Fig. 9. Self-Consistent Approximation for Thermal Properties: the inhomogeneity is embedded in an infinite body whose material properties are those of the unknown effective material with far field homogeneous temperature applied consistent with the average heat intensity in the RVE.

From the equivalence principle, the heat flux in the J^{th} inhomogeneity is related to the heat flux in an inclusion within the embedding material which is subject to an unknown eigen thermal gradient, and is therefore given as

$$q_i^J = k_{ij}^J(H_j^C + H_j^A) = k_{ij}^{\text{eff}}(H_j^C + H_j^A - H_j^T) \tag{2.90}$$

where the thermal gradient in the inhomogeneity is $H_j^J = H_j^C + H_j^A$. Solving Eqn. 2.90 for the unknown eigen thermal gradient for the J^{th} inhomogeneity, H_j^T, one obtains

$$k_{ij}^J H_j^J = k_{ij}^{\text{eff}} H_j^J - k_{ij}^{\text{eff}} H_j^T \tag{2.91}$$

so that

$$k_{ij}^{\text{eff}} H_j^T = (k_{ij}^{\text{eff}} - k_{ij}^J) H_j^J \tag{2.92}$$

and thus one obtains the eigen thermal gradient as

$$H_i^T = \xi_{ij}^{\text{eff}}(k_{jk}^{\text{eff}} - k_{jk}^J) H_k^J \tag{2.93}$$

Since the thermal gradient in the inhomogeneity can be written as

$$H_k^J = H_k^C + \bar{H}_k \tag{2.94}$$

and using the thermal equivalent to the Eshelby solution[24], i.e. $H_i^C = S_{ij} H_j^T$, the thermal gradient in the inhomogeneity becomes

$$H_i^J = S_{ij} H_j^T + \bar{H}_i \tag{2.95}$$

so that upon substitution of the eigen thermal gradient from Eqn. 2.93 into Eqn. 2.95

[24]From the Eshelby solution it is observed that the thermal gradient in the ellipsoidal inhomogeneity is uniform. It is also noted that the Eshelby tensor, S_{ij}, depends on the shape of the inclusion and the material properties of the material in which the inclusion is embedded, here the effective material.

one obtains

$$H_i^J = S_{ij}\xi_{jk}^{\text{eff}}(k_{kl}^{\text{eff}} - k_{kl}^J)H_l^J + \bar{H}_i \tag{2.96}$$

which leads to

$$[I_{il} + S_{ij}\xi_{jk}^{\text{eff}}(k_{kl}^J - k_{kl}^{\text{eff}})]H_l^J = \bar{H}_i \tag{2.97}$$

Thus, one may write the thermal gradient in the inhomogeneity in terms of the average thermal gradient in the RVE as

$$H_l^J = [I_{il} + S_{ij}\xi_{jk}^{\text{eff}}(k_{kl}^J - k_{kl}^{\text{eff}})]^{-1}\bar{H}_i \tag{2.98}$$

One can define a tensor ${}^{SC}T_{ij}^J$ relating the intensity in the J^{th} inhomogeneity to the uniform intensity in the far field applied temperature, i.e. H_i^A which in this case is the average intensity of the composite, such that

$$H_l^J = {}^{SC}T_{li}^J\bar{H}_i \tag{2.99}$$

Therefore from Eqn. 2.98, one can identify the tensor ${}^{SC}T_{li}^J$ as being given by

$${}^{SC}T_{li}^J = [I_{il} + S_{ij}\xi_{jk}^{\text{eff}}(k_{kl}^J - k_{kl}^{\text{eff}})]^{-1} \tag{2.100}$$

Recalling the definition of the intensity concentration tensor in Eqn. 2.64d, and noting that the heat intensity in the ellipsoidal inhomogeneity is uniform, the concentration tensor is therefore identified in the self-consistent method from Eqn. 2.99 as

$${}^{SC}A_{li}^J = {}^{SC}T_{li}^J \tag{2.101}$$

The flux concentration tensor for the self-consistent method is obtained by the application of the constitutive relations to Eqn. 2.99 so that the heat flux in the J^{th} inhomogeneity is given by

$$q_i^J = k_{ij}^J H_j^J = k_{ij}^J\,{}^{SC}T_{jk}^J\bar{H}_k \tag{2.102}$$

However, from the definition of the effective resistivity in Eqn. 2.57b, one can write

$$\bar{H}_k = \xi^{\text{eff}}_{kl}\bar{q}_l \tag{2.103}$$

so that substituting Eqn. 2.103 into Eqn. 2.102 the heat flux in the J^{th} inhomogeneity becomes

$$q^J_i = k^J_{ij}\ {}^{SC}T^J_{jk}\xi^{\text{eff}}_{kl}\bar{q}_l \tag{2.104}$$

One can define a tensor ${}^{SC}P^J_{ij}$ relating the heat flux in the J^{th} inhomogeneity to the uniform heat flux in the far field applied heat flux, i.e. q^A_i which in this case is the average heat flux in the RVE, such that

$$q^J_i = {}^{SC}P^J_{ij}\bar{q}_j \tag{2.105}$$

so therefore from Eqn. 2.104 one obtains

$${}^{SC}P^J_{il} = k^J_{ij}\ {}^{SC}T^J_{jk}\xi^{\text{eff}}_{kl} \tag{2.106}$$

Recalling the definition of the flux concentration tensor from Eqn. 2.64c, and noting that the heat flux in the ellipsoidal inhomogeneity is uniform, the concentration tensor is therefore identified in the self-consistent method from Eqn. 2.105 as

$${}^{SC}B^J_{il} = {}^{SC}P^J_{il} \tag{2.107}$$

2. The Mori-Tanaka Method

The following equations provide a summary of the analytic approach to approximating the concentration tensors using the Mori-Tanaka method for determining both the effective elastic properties and effective conductivities. The summary follows the original derivation provided by Mori and Tanaka[127] and the subsequent derivation by Benveniste[128].

a. The Mori-Tanaka Method for Mechanical Properties

To calculate the strain concentration tensor (or the stress concentration tensor) for homogeneous ellipsoidal inhomogeneities in a linear elastic matrix, one can take advantage of Eshelby's equivalence principle and the Eshelby solution by individually embedding each inhomogeneity into the matrix material subject to far field displacements or tractions consistent with those applied to the boundary of the microscale RVE, which are reflective of the average macroscale stress/strain, plus some perturbation which accounts for interactions (see Fig. 10).

Consider the J^{th} inhomogeneity embedded in an infinite body whose material properties are those of the matrix material (as shown in Figure 10), where the applied homogeneous displacement at infinity is reflective of the homogeneous displacement field applied to the boundary of the microscale RVE plus an unknown perturbation which accounts for interactions amongst the inhomogeneities, i.e. the uniform strain in the applied displacement is $\varepsilon_{ij}^{A} = \bar{\varepsilon}_{ij} + \tilde{\varepsilon}_{ij}$ where it is recalled that $\bar{\varepsilon}_{ij} = \langle \varepsilon_{ij} \rangle$ and noted that the perturbation strain is defined as $\tilde{\varepsilon}_{ij} \equiv \frac{1}{V_N} \int_{V_N} \varepsilon_{ij}^{\text{Total}} - \bar{\varepsilon}_{ij} \, dV$.

From the equivalence principle, the stress in the J^{th} inhomogeneity is related to the stress in an inclusion within the embedding material which is subject to an unknown eigenstrain, and is therefore given as

$$\sigma_{ij}^{J} = L_{ijkl}^{J}(\varepsilon_{kl}^{C} + \varepsilon_{kl}^{A}) = L_{ijkl}^{N}(\varepsilon_{kl}^{C} + \varepsilon_{kl}^{A} - \varepsilon_{kl}^{T}) \tag{2.108}$$

where the strain in the inhomogeneity is $\varepsilon_{kl}^{J} = \varepsilon_{kl}^{C} + \varepsilon_{kl}^{A}$. Solving Eqn. 2.108 for the unknown eigenstrain for the J^{th} inhomogeneity, ε_{kl}^{T}, one obtains

$$L_{ijkl}^{J}\varepsilon_{kl}^{J} = L_{ijkl}^{N}\varepsilon_{kl}^{J} - L_{ijkl}^{N}\varepsilon_{kl}^{T} \tag{2.109}$$

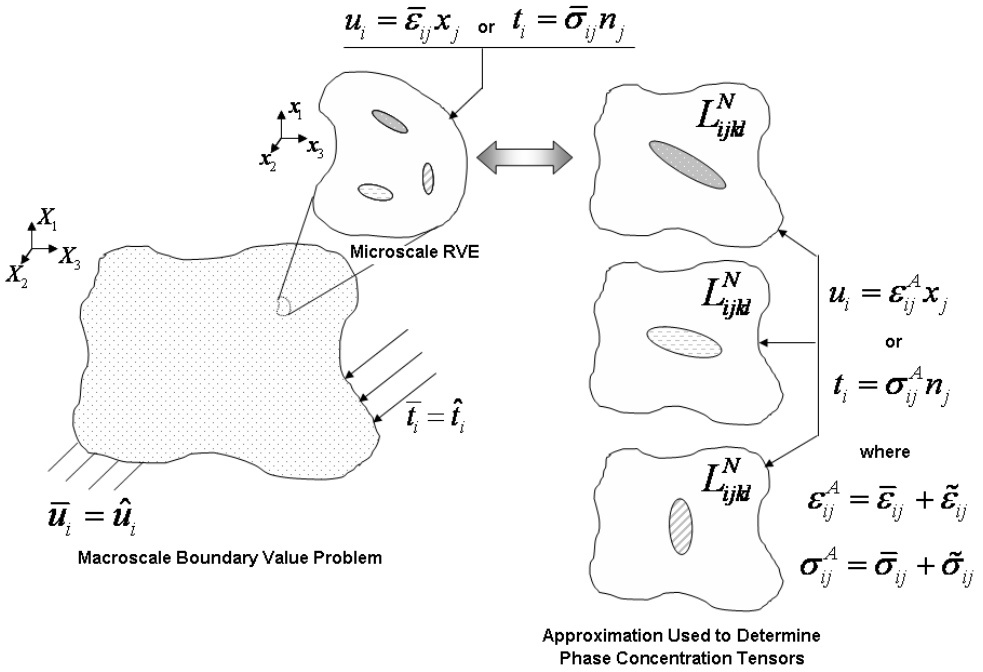

Fig. 10. Mori-Tanaka Approximation for Elastic Properties: the inhomogeneity is embedded in an infinite body whose material properties are those of the matrix material with far field homogeneous displacement applied which is consistent with the average strain in the RVE plus a perturbation.

so that

$$L^N_{ijkl}\varepsilon^T_{kl} = (L^N_{ijkl} - L^J_{ijkl})\varepsilon^J_{kl} \tag{2.110}$$

thus one obtains the eigenstrain as

$$\varepsilon^T_{ij} = M^N_{ijkl}(L^N_{klmn} - L^J_{klmn})\varepsilon^J_{mn} \tag{2.111}$$

Since the strain in the inhomogeneity can be expressed as

$$\varepsilon^J_{kl} = \varepsilon^C_{kl} + \bar{\varepsilon}_{kl} + \tilde{\varepsilon}_{kl} \tag{2.112}$$

and using the Eshelby solution for homogeneous ellipsoids[25], i.e. $\varepsilon^C_{ij} = S_{ijkl}\varepsilon^T_{kl}$, the strain in the inhomogeneity becomes

$$\varepsilon^J_{ij} = S_{ijkl}\varepsilon^T_{kl} + \bar{\varepsilon}_{ij} + \tilde{\varepsilon}_{ij} \tag{2.113}$$

so that upon substitution of Eqn. 2.111 into Eqn. 2.113 one obtains

$$\varepsilon^J_{ij} = S_{ijkl}M^N_{klmn}(L^N_{mnpq} - L^J_{mnpq})\varepsilon^J_{pq} + \bar{\varepsilon}_{ij} + \tilde{\varepsilon}_{ij} \tag{2.114}$$

which leads to

$$[I_{ijpq} + S_{ijkl}M^N_{klmn}(L^J_{mnpq} - L^N_{mnpq})]\varepsilon^J_{pq} = (\bar{\varepsilon}_{ij} + \tilde{\varepsilon}_{ij}) \tag{2.115}$$

Thus one may write the strain in the inhomogeneity in terms of the of the uniform strain in the applied far field displacement as

$$\varepsilon^J_{pq} = [I_{ijpq} + S_{ijkl}M^N_{klmn}(L^J_{mnpq} - L^N_{mnpq})]^{-1}(\bar{\varepsilon}_{ij} + \tilde{\varepsilon}_{ij}) \tag{2.116}$$

One can define a tensor, ${}^{MT}T^J_{ijkl}$, relating the strain in the J^{th} inhomogeneity

[25]Now the strain in the inhomogeneity becomes uniform. Also it is noted that the Eshelby tensor, S_{ijkl}, depends on the shape of the inclusion and the material properties of the material in which the inclusion is embedded, here the matrix material.

to the uniform strain in the far field applied displacement, i.e. ε_{ij}^{A} which in this case is the average strain in the RVE plus a perturbation, such that

$$\varepsilon_{pq}^{J} = {}^{MT}T_{pqij}^{J}\varepsilon_{ij}^{A} = {}^{MT}T_{pqij}^{J}(\bar{\varepsilon}_{ij} + \tilde{\varepsilon}_{ij}) \tag{2.117}$$

Therefore, from Eqn. 2.116, one can identify the tensor ${}^{MT}T_{pqij}^{J}$ as being given by[26]

$${}^{MT}T_{pqij}^{J} = [I_{ijpq} + S_{ijkl}M_{klmn}^{N}(L_{mnpq}^{J} - L_{mnpq}^{N})]^{-1} \tag{2.118}$$

Though the strain in the ellipsoidal inhomogeneity in the Mori-Tanaka method is again noted to be uniform, in comparing Eqn. 2.117 with the definition of the strain concentration tensor in Eqn. 2.64b it is observed that, unlike the self-consistent method, ${}^{MT}T_{pqij}^{J}$ is not equivalent to the strain concentration tensor, i.e. ${}^{MT}T_{pqij}^{J} \neq {}^{MT}A_{pqij}^{J}$.

In order to identify the relationship between ${}^{MT}T_{pqij}^{J}$ and the strain concentration tensor, it is necessary to identify the uniform matrix perturbation strain in terms of the average strain in the RVE. Recalling that $\bar{\varepsilon}_{ij} = \langle\varepsilon_{ij}\rangle$, and that the strain in the matrix is taken as the average strain in the RVE plus a perturbation, i.e. $\langle\varepsilon_{ij}^{N}\rangle = \bar{\varepsilon}_{ij} + \tilde{\varepsilon}_{ij}$, Eqn. 2.61b can be written as

$$\langle\varepsilon_{ij}\rangle = \bar{\varepsilon}_{ij} = c_N(\bar{\varepsilon}_{ij} + \tilde{\varepsilon}_{ij}) + \sum_{J=1}^{N-1} c_J \, {}^{MT}T_{ijpq}^{J}(\bar{\varepsilon}_{pq} + \tilde{\varepsilon}_{pq}) \tag{2.119}$$

which can be simplified as

$$\bar{\varepsilon}_{ij} = \left[c_N I_{ijkl} + \sum_{J=1}^{N-1} c_J \, {}^{MT}T_{ijkl}^{J}\right](\bar{\varepsilon}_{kl} + \tilde{\varepsilon}_{kl}) \tag{2.120}$$

Solving Eqn. 2.120 for the perturbation strain, which is equivalent to enforcing the

[26]Note that applying Eqn. 2.118 to the matrix phase, we observe that ${}^{MT}T_{ijkl}^{N}$ is identity by definition in the Mori-Tanaka method.

consistency condition, one obtains

$$\tilde{\varepsilon}_{kl} = \left\{ \left[c_N I_{ijkl} + \sum_{J=1}^{N-1} c_J \, {}^{MT}T^J_{ijkl} \right]^{-1} - I_{klij} \right\} \bar{\varepsilon}_{ij} \tag{2.121}$$

Substitution of Eqn. 2.121 into Eqn. 2.117 allows one to express the average strain in the J^{th} inhomogeneity in terms of the average strain in the RVE as

$$\varepsilon^J_{ij} = {}^{MT}T^J_{ijkl} \left[c_N I_{mnkl} + \sum_{J=1}^{N-1} c_J \, {}^{MT}T^J_{mnkl} \right]^{-1} \bar{\varepsilon}_{mn} \tag{2.122}$$

Therefore from the definition of the strain concentration tensor in Eqn. 2.64b, one observes that the concentration tensor is identified in the Mori-Tanaka method from Eqn. 2.122 as[27]

$${}^{MT}A^J_{ijmn} = {}^{MT}T^J_{ijkl} \left[c_N I_{mnkl} + \sum_{J=1}^{N-1} c_J \, {}^{MT}T^J_{mnkl} \right]^{-1} \tag{2.123}$$

The stress concentration tensor for the Mori-Tanaka method is obtained by application of constitutive relations to Eqn. 2.117 so that the stress in the J^{th} inhomogeneity is given by

$$\sigma^J_{ij} = L^J_{ijkl} \varepsilon^J_{kl} = L^J_{ijkl} \, {}^{MT}T^J_{klmn} (\bar{\varepsilon}_{mn} + \tilde{\varepsilon}_{mn}) \tag{2.124}$$

However, noting that $(\bar{\varepsilon}_{mn} + \tilde{\varepsilon}_{mn})$ denotes strain in the matrix, with the substitution of the constitutive relation for the compliance of the matrix into Eqn. 2.124 one can write the stress in the J^{th} inhomogeneity as

$$\sigma^J_{ij} = L^J_{ijkl} \, {}^{MT}T^J_{klmn} M^N_{mnpq} (\bar{\sigma}_{pq} + \tilde{\sigma}_{pq}) \tag{2.125}$$

One can define a tensor, ${}^{MT}P^J_{ijkl}$, relating the stress in the J^{th} inhomogeneity to

[27]Note that applying Eqn. 2.123 to the matrix phase, we observe that ${}^{MT}A^N_{ijkl}$ is identity by definition in the Mori-Tanaka method.

the uniform stress in the far field applied traction, i.e. σ_{ij}^{A} which in this case is the average stress in the RVE plus a perturbation, such that

$$\sigma_{ij}^{J} = {}^{MT}P_{ijkl}^{J}\sigma_{kl}^{A} = {}^{MT}P_{ijkl}^{J}(\bar{\sigma}_{kl} + \tilde{\sigma}_{kl}) \tag{2.126}$$

so therefore from Eqn. 2.125 one observes that

$${}^{MT}P_{ijpq}^{J} = L_{ijkl}^{J}\ {}^{MT}T_{klmn}^{J}M_{mnpq}^{N} \tag{2.127}$$

In comparing Eqn. 2.126 with the definition of the stress concentration tensor in Eqn. 2.64a it is again observed that ${}^{MT}P_{ijkl}^{J}$ is not equivalent to the stress concentration tensor, i.e. ${}^{MT}P_{ijkl}^{J} \neq {}^{MT}B_{ijkl}^{J}$. Again, in order to identify the relationship between ${}^{MT}P_{ijkl}^{J}$ and the stress concentration tensor, it is necessary to identify the uniform matrix perturbation stress in terms of the average stress in the RVE. Recalling that $\bar{\sigma}_{ij} = \langle\sigma_{ij}\rangle$, and that the stress in the matrix is taken as the average stress in the RVE plus a perturbation, i.e. $\langle\sigma_{ij}^{N}\rangle = \bar{\sigma}_{ij} + \tilde{\sigma}_{ij}$, Eqn. 2.61a can be written as

$$\langle\sigma_{ij}\rangle = \bar{\sigma}_{ij} = c_N(\bar{\sigma}_{ij} + \tilde{\sigma}_{ij}) + \sum_{J=1}^{N-1} c_J\ {}^{MT}P_{ijpq}^{J}(\bar{\sigma}_{pq} + \tilde{\sigma}_{pq}) \tag{2.128}$$

which can be simplified as

$$\bar{\sigma}_{ij} = \left[c_N I_{ijkl} + \sum_{J=1}^{N-1} c_J\ {}^{MT}P_{ijkl}^{J}\right](\bar{\sigma}_{kl} + \tilde{\sigma}_{kl}) \tag{2.129}$$

Solving Eqn. 2.129 for the perturbation stress, which is equivalent to enforcing the consistency condition, one obtains

$$\tilde{\sigma}_{kl} = \left\{\left[c_N I_{ijkl} + \sum_{J=1}^{N-1} c_J\ {}^{MT}P_{ijkl}^{J}\right]^{-1} - I_{klij}\right\}\bar{\sigma}_{ij} \tag{2.130}$$

Substitution of Eqn. 2.130 into Eqn. 2.126 allows one to express the average stress in

the J^{th} inhomogeneity in terms of the average stress in the RVE as

$$\sigma_{ij}^{J} = {}^{MT}P_{ijkl}^{J}\left[c_N I_{mnkl} + \sum_{J=1}^{N-1} c_J \, {}^{MT}P_{mnkl}^{J}\right]^{-1} \bar{\sigma}_{mn} \tag{2.131}$$

Therefore from the definition of the stress concentration tensor in Eqn. 2.64a, one observes that the concentration tensor is identified in the Mori-Tanaka method from Eqn. 2.131 as[28]

$${}^{MT}B_{ijmn}^{J} = {}^{MT}P_{ijkl}^{J}\left[c_N I_{mnkl} + \sum_{J=1}^{N-1} c_J \, {}^{MT}P_{mnkl}^{J}\right]^{-1} \tag{2.132}$$

b. The Mori-Tanaka Method for Thermal Conductivities

To calculate the heat intensity concentration tensor (or the heat flux concentration tensor) for homogeneous ellipsoidal inhomogeneities in a matrix, one can apply the thermal equivalent to Eshelby's equivalence principle by individually embedding each inhomogeneity into the matrix material subject to far field temperature or heat flux consistent with those applied to the boundary of the microscale RVE, which are reflective of the average macroscale heat flux/intensity, plus some perturbation which accounts for interactions (see Fig. 11).

Consider the J^{th} inhomogeneity embedded in an infinite body whose material properties are those of the matrix material (as shown in Figure 11), where the applied homogeneous temperature at infinity is reflective the homogeneous temperature applied at the boundary of the microscale RVE plus an unknown perturbation which accounts for interactions amongst the inhomogeneities, i.e. the uniform intensity in the applied temperature is $H_i^A = \bar{H}_i + \tilde{H}_i$ where it is recalled that $\bar{H}_i = \langle H_i \rangle$ and noted that the perturbation intensity is defined as $\tilde{H}_i \equiv \frac{1}{V_N}\int_{V_N} H_i^{\text{Total}} - \bar{H}_i \, dV$. Further, it

[28]Note that applying Eqn. 2.132 to the matrix phase, one observes that ${}^{MT}B_{ijkl}^{N}$ is identity by definition in the Mori-Tanaka method.

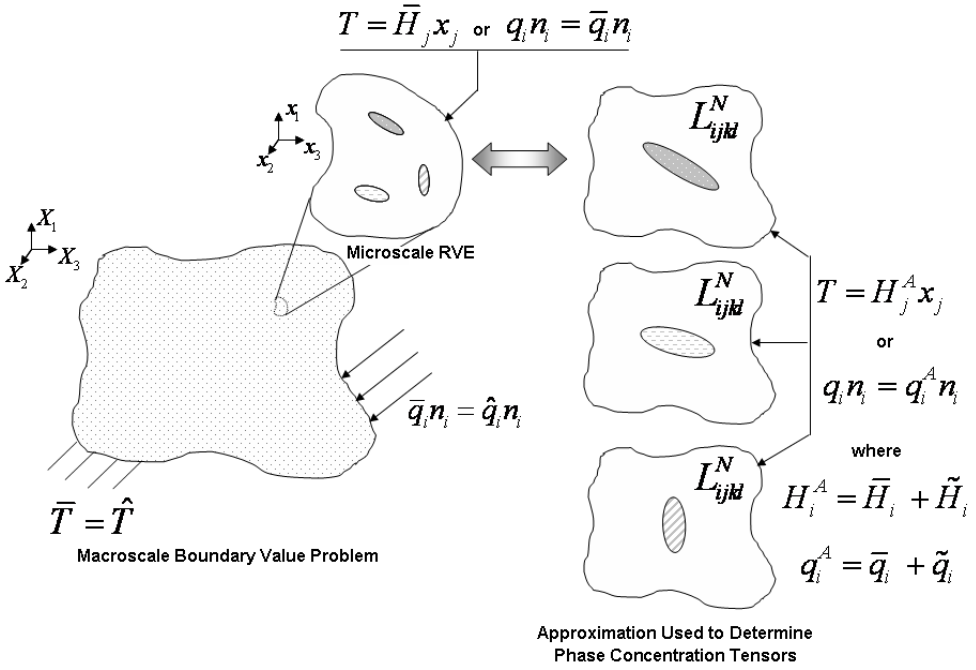

Fig. 11. Mori-Tanaka Approximation for Thermal Properties: the inhomogeneity is embedded in an infinite body whose material properties are those of the matrix material with far field homogeneous temperature applied which is consistent with the average heat intensity in the RVE plus a perturbation.

is noted again that the total intensity can be decomposed into two parts consisting of the intensity from the thermal gradient governed by Fourier's law and the intensity which results from the eigen thermal gradient.

From the equivalence principle, the heat flux in the J^{th} inhomogeneity is realted to the heat flux in an inclusion within the embedding material which is subject to an unknown eigen thermal gradient, and is therefore given as

$$q_i^J = k_{ij}^J(H_j^C + H_j^A) = k_{ij}^N(H_j^C + H_j^A - H_j^T) \tag{2.133}$$

where the thermal gradient in the inhomogeneity is $H_j^J = H_j^C + H_j^A$. Solving Eqn. 2.133 for the unknown eigen thermal gradient for the J^{th} inhomogeneity, H_j^T, one obtains

$$k_{ij}^J H_j^J = k_{ij}^N H_j^J - k_{ij}^N H_j^T \tag{2.134}$$

so that

$$k_{ij}^N H_j^T = (k_{ij}^N - k_{ij}^J)H_j^J \tag{2.135}$$

and thus one obtains the eigen thermal gradient as

$$H_i^T = \xi_{ij}^N(k_{jk}^N - k_{jk}^J)H_k^J \tag{2.136}$$

Since the thermal gradient in the inhomogeneity can be written as

$$H_k^J = H_k^C + \bar{H}_k + \tilde{H}_k \tag{2.137}$$

and using the thermal equivalent to the Eshelby solution[29], i.e. $H_i^C = S_{ij}H_j^T$, the

[29]From the Eshelby solution it is observed that the thermal gradient in the ellipsoidal inhomogeneity is uniform. It is also noted that the Eshelby tensor, S_{ij}, depends on the shape of the inclusion and the material properties of the material in which the inclusion is embedded, here the matrix material.

thermal gradient in the inhomogeneity becomes

$$H_i^J = S_{ij} H_j^T + \bar{H}_i + \tilde{H}_i \tag{2.138}$$

so that upon substitution of the eigen thermal gradient from Eqn. 2.136 into Eqn. 2.138 one obtains

$$H_i^J = S_{ij} \xi_{jk}^N (k_{kl}^N - k_{kl}^J) H_l^J + \bar{H}_i + \tilde{H}_i \tag{2.139}$$

which leads to

$$[I_{il} + S_{ij} \xi_{jk}^N (k_{kl}^J - k_{kl}^N)] H_l^J = (\bar{H}_i + \tilde{H}_i) \tag{2.140}$$

Thus, one may write the thermal gradient in the inhomogeneity in terms of the uniform intensity in the applied far field temperature as

$$H_l^J = [I_{il} + S_{ij} \xi_{jk}^N (k_{kl}^J - k_{kl}^N)]^{-1} (\bar{H}_i + \tilde{H}_i) \tag{2.141}$$

One can define a tensor, ${}^{MT}T_{ij}^J$, relating the thermal gradient in the J^{th} inhomogeneity to the uniform thermal gradient in the applied far field temperature, i.e. H_i^A which in this case the average thermal gradient in the RVE plus a perturbation, such that

$$H_l^J = {}^{MT}T_{li}^J H_i^A = {}^{MT}T_{li}^J (\bar{H}_i + \tilde{H}_i) \tag{2.142}$$

Therefore from Eqn. 2.141, one can identify the tensor ${}^{MT}T_{li}^J$ as being given by

$${}^{MT}T_{li}^J = [I_{il} + S_{ij} \xi_{jk}^N (k_{kl}^J - k_{kl}^N)]^{-1} \tag{2.143}$$

Though the intensity in the ellipsoidal inhomogeneity in the Mori-Tanaka method is again noted to be uniform, in comparing Eqn. 2.142 with the definition of the intensity concentration tensor in Eqn. 2.64d it is observed that, unlike the self-consistent method, ${}^{MT}T_{ij}^J$ is not equivalent to the intensity concentration tensor, i.e. ${}^{MT}T_{ij}^J \neq {}^{MT}A_{ij}^J$.

In order to identify the relationship between ${}^{MT}T_{ij}^{J}$ and the intensity concentration tensor, it is necessary to identify the uniform matrix perturbation intensity in terms of the average intensity in the RVE. Recalling that $\bar{H}_i = \langle H_i \rangle$, and that the intensity in the matrix is taken as the average intensity in the RVE plus a perturbation, i.e. $\langle H_i^N \rangle = \bar{H}_i + \tilde{H}_i$, Eqn. 2.61d can be written as

$$\langle H_i \rangle = \bar{H}_i = c_N(\bar{H}_i + \tilde{H}_i) + \sum_{J=1}^{N-1} c_J \, {}^{MT}T_{ij}^{J}(\bar{H}_j + \tilde{H}_j) \tag{2.144}$$

which can be simplified as

$$\bar{H}_i = \left[c_N I_{ij} + \sum_{J=1}^{N-1} c_J \, {}^{MT}T_{ij}^{J} \right] (\bar{H}_j + \tilde{H}_j) \tag{2.145}$$

Solving Eqn. 2.145 for the perturbation intensity, which is equivalent to enforcing the consistency condition, one obtains

$$\tilde{H}_j = \left\{ \left[c_N I_{ij} + \sum_{J=1}^{N-1} c_J \, {}^{MT}T_{ij}^{J} \right]^{-1} - I_{ji} \right\} \bar{H}_i \tag{2.146}$$

Substitution of Eqn. 2.146 into Eqn. 2.142 allows one to express the average intensity in the J^{th} inhomogeneity in terms of the average intensity in the RVE as

$$H_i^J = {}^{MT}T_{ij}^{J} \left[c_N I_{kj} + \sum_{J=1}^{N-1} c_J \, {}^{MT}T_{kj}^{J} \right]^{-1} \bar{H}_k \tag{2.147}$$

Therefore from the definition of the intensity concentration tensor in Eqn. 2.64d, one observes that the concentration tensor is identified in the Mori-Tanaka method from Eqn. 2.147 as[30]

$${}^{MT}A_{ij}^{J} = {}^{MT}T_{ij}^{J} \left[c_N I_{kj} + \sum_{J=1}^{N-1} c_J \, {}^{MT}T_{kj}^{J} \right]^{-1} \tag{2.148}$$

The flux concentration tensor for the Mori-Tanaka method is obtained by appli-

[30]Note that applying Eqn. 2.148 to the matrix phase, we observe that ${}^{MT}A_{ij}^{N}$ is identity by definition in the Mori-Tanaka method.

cation of constitutive relations to Eqn. 2.142 so that the flux in the J^{th} inhomogeneity is given by

$$q_i^J = k_{ij}^J H_j^J = k_{ij}^J \ {}^{MT}T_{jk}^J(\bar{H}_k + \tilde{H}_k) \tag{2.149}$$

However, noting that $(\bar{H}_k + \tilde{H}_k)$ denotes intensity in the matrix, with the substitution of the constitutive relation for the resistivity of the matrix into Eqn. 2.149 one can write the flux in the J^{th} inhomogeneity as

$$q_i^J = k_{ij}^J \ {}^{MT}T_{kl}^J \xi_{lm}^N(\bar{q}_m + \tilde{q}_m) \tag{2.150}$$

One can define a tensor, ${}^{MT}P_{ij}^J$, relating the flux in the J^{th} inhomogeneity to the uniform flux in the far field applied flux, i.e. q_i^A which in this case is the average flux in the RVE plus a perturbation, such that

$$q_i^J = \ {}^{MT}P_{ij}^J q_j^A = \ {}^{MT}P_{ij}^J(\bar{q}_j + \tilde{q}_j) \tag{2.151}$$

so therefore from Eqn. 2.150 one observes that

$${}^{MT}P_{il}^J = k_{ij}^J \ {}^{MT}T_{jk}^J \xi_{kl}^N \tag{2.152}$$

In comparing Eqn. 2.151 with the definition of the stress concentration tensor in Eqn. 2.64c it is again observed that ${}^{MT}P_{ij}^J$ is not equivalent to the flux concentration tensor, i.e. ${}^{MT}P_{ij}^J \neq \ {}^{MT}B_{ij}^J$. Again, in order to identify the relationship between ${}^{MT}P_{ij}^J$ and the flux concentration tensor, it is necessary to identify the uniform matrix perturbation flux in terms of the average flux in the RVE. Recalling that $\bar{q}_i = \langle q_i \rangle$, and that the flux in the matrix is taken as the average flux in the RVE plus a perturbation, i.e. $\langle q_i^N \rangle = \bar{q}_i + \tilde{q}_i$, Eqn. 2.61c can be written as

$$\langle q_i \rangle = \bar{q}_i = c_N(\bar{q}_i + \tilde{q}_i) + \sum_{J=1}^{N-1} c_J \ {}^{MT}P_{ij}^J(\bar{q}_j + \tilde{q}_j) \tag{2.153}$$

which can be simplified as

$$\bar{q}_i = \left[c_N I_{ij} + \sum_{J=1}^{N-1} c_J \, {}^{MT}P_{ij}^J \right] (\bar{q}_j + \tilde{q}_j) \tag{2.154}$$

Solving Eqn. 2.154 for the perturbation flux, which is equivalent to enforcing the consistency condition, one obtains

$$\tilde{q}_j = \left\{ \left[c_N I_{ij} + \sum_{J=1}^{N-1} c_J \, {}^{MT}P_{ij}^J \right]^{-1} - I_{ji} \right\} \bar{q}_i \tag{2.155}$$

Substitution of Eqn. 2.155 into Eqn. 2.151 allows one to express the average flux in the J^{th} inhomogeneity in terms of the average flux in the RVE as

$$q_i^J = {}^{MT}P_{ij}^J \left[c_N I_{kj} + \sum_{J=1}^{N-1} c_J \, {}^{MT}P_{kj}^J \right]^{-1} \bar{q}_k \tag{2.156}$$

Therefore from the definition of the flux concentration tensor in Eqn. 2.64c, one observes that the concentration tensor is identified in the Mori-Tanaka method from Eqn. 2.156 as[31]

$${}^{MT}B_{ik}^J = {}^{MT}P_{ij}^J \left[c_N I_{kj} + \sum_{J=1}^{N-1} c_J \, {}^{MT}P_{kj}^J \right]^{-1} \tag{2.157}$$

3. The Generalized Self-Consistent Method: Using Composite Spheres or Composite Cylinders

Both the self-consistent and Mori-Tanaka closed form approaches to approximating concentration tensors provided in the previous sections made use of the Eshelby solution in determining the field variables in the inhomogeneity, and thus are intended for homogeneous ellipsoidal inhomogeneities. However, the generalized self-consistent method, by imposing a matrix shell around the inhomogeneity in approximating the

[31]Note that applying Eqn. 2.157 to the matrix phase, one observes that ${}^{MT}B_{ij}^N$ is identity by definition in the Mori-Tanaka method.

concentration tensor, precludes the direct use of the Eshelby solution as the inhomogeneity and the matrix shell combined constitute an inhomogeneous inhomogeneity[32] within infinite effective material (see Figure 7(c)). Instead, in order to calculate the strain concentration tensor (or the stress concentration tensor) for homogeneous spheres or cylinders using the generalized self-consistent method, one can make use of closed form solutions for composite spheres or composite cylinders by individually embedding each inhomogeneity into the effective medium subject to far field displacements or tractions consistent with those applied to the boundary of the microscale RVE, which are reflective of the average macroscale strain/strain (see Fig. 12). The details of determining the concentration tensor from the generalized self-consistent composite cylinder solution will be given in Section E of Chapter III. Here it is simply noted that, from the composite spheres and composite cylinders solutions, the stress or strain states in the matrix shell and inhomogeneity can be determined, allowing for direct volume averaging in the determination of the components of the concentration tensor.

However, one question which immediately arises from the approximations in Figure 12 is how much matrix to associate with the inhomogeneity in constructing the composite sphere or cylinder assemblage. This amounts to identifying the volume fraction of the inhomogeneity within the matrix shell used in the generalized self-

[32]In general, should one wish to consider inhomogeneous inhomogeneities such as hollow and/or coated inhomogeneities, a different approach will be needed. One approach, referred to as the transfer matrix method [132, 133], has been applied wherein auxiliary problems such as a composite sphere or composite cylinder solution are employed in a two-step process to estimate the applied stress in the Mori-Tanaka method, and then to apply this stress to the composite cylinders assemblage in calculating the effective properties. Another two step approach [161] uses the composite cylinders method to first estimate the effective properties of the inhomogeneous inhomogeneity, and then applies the Mori-Tanaka as described above on this effective cylinder.

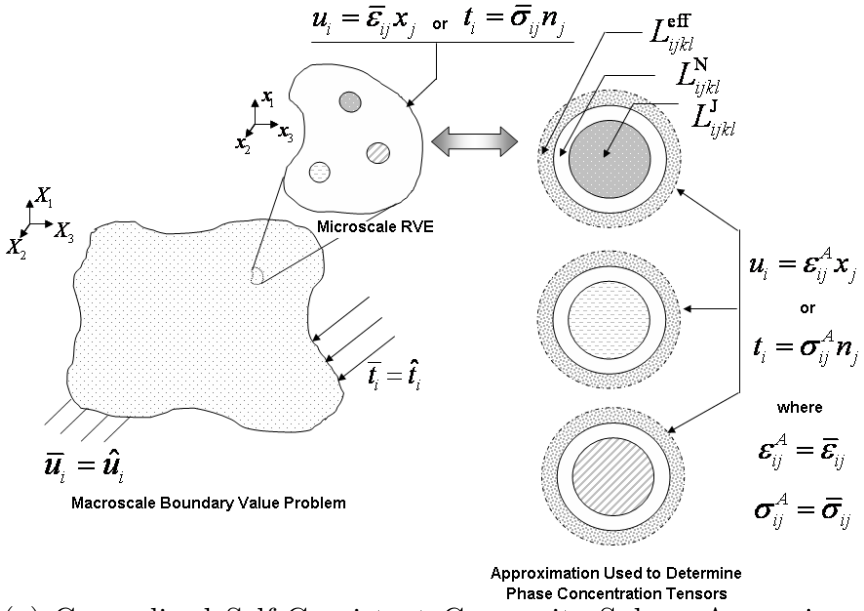

(a) Generalized Self-Consistent Composite Sphere Approximation

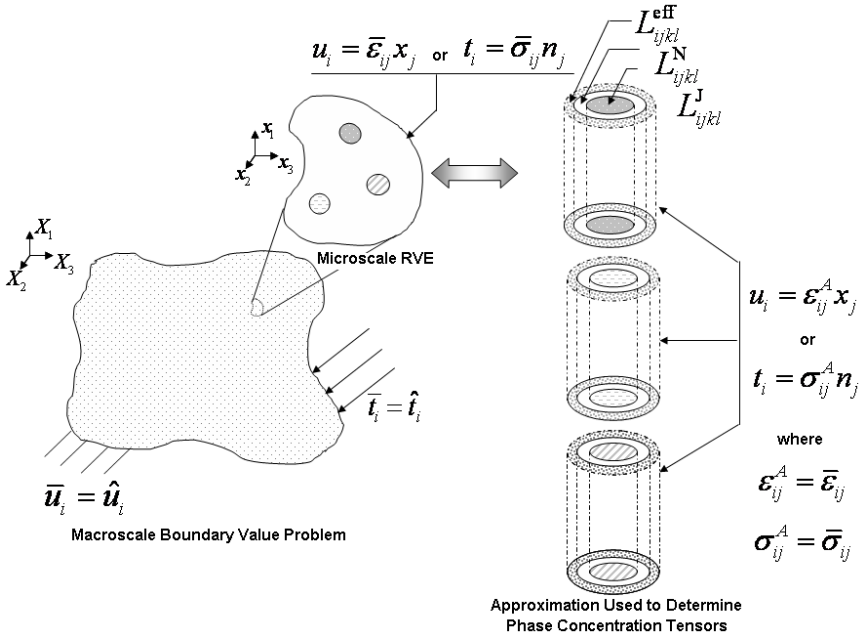

(b) Generalized Self-Consistent Composite Cylinder Approximation

Fig. 12. Generalized Self-Consistent Approximation: a composite sphere or composite cylinder assemblage consisting of the inhomogeneity embedded in the matrix and then the ensemble embedded in an infinite body whose material properties are those of the effective material with far field homogeneous displacement (or traction) applied which is consistent with the average strain (or stress) in the RVE.

consistent approximation, f_J, as

$$f_J = \frac{V_J}{V_N^* + V_J} \tag{2.158}$$

where V_N^* is the volume of the matrix shell in the generalized self-consistent approximation and is not necessarily equal to the total volume of the matrix in the microscale RVE, V_N. As such, it is observed that as $f_J \to 1$, the inhomogeneity is directly embedded in the effective material which is exactly the self-consistent method. As $f_J \to 0$, the inhomogeneity is embedded in a matrix shell of infinite thickness returning the dilute approximation. Miloh and Benveniste [186] suggest taking $f_J = c_J$ where c_J is the volume fraction of the inhomogeneity in the microscale RVE. This works well for the single type of inhomogeneity, but for multiple inhomogeneities, a counter argument can be constructed based on the consistency condition where each inhomogeneity is embedded in a matrix shell such that $f_J = 1 - c_N = \sum_{J=1}^{N-1} c_J$.

For example, consider a composite consisting aligned, well-dispersed fibers all with the same material properties embedded in a matrix material at a volume fraction of fibers of 0.2 and therefore a matrix volume fraction of 0.8. Applying the generalized self-consistent method to such a composite would naturally make use of a matrix shell with a volume fraction of 0.8, i.e. $f_1 = c_1 = 0.2$, where it is noted that a tessellation of the perfect hexagonal array representing such a dispersion would return a local volume fraction of fiber in each Voronoi polygon of 0.2.

Next consider the case where one quarter of the fibers from the previous case now have a different set of material properties. As such, the fiber volume fractions are 0.15 and 0.05, but the matrix volume fraction remains 0.8. If one were to apply the fiber volume fractions in constructing the generalized self-consistent approximation, i.e. taking $f_1 = c_1 = 0.15$ and $f_2 = c_2 = 0.05$, then each approximation would have a different volume fraction of matrix shell, i.e. 0.85 and 0.95, respectively. However,

the tessellation of such a dispersion would still yield local fiber volume fractions in each Voronoi polygon of 0.2 as the dispersion geometry has not changed. Further, if we consider the limit where the fiber properties approach one another, i.e. in the limit as we return to the previous case, we would observe an inconsistency in that some fibers were assigned more matrix than others, thereby changing the influence of those fibers on the effective properties calculated where clearly they should have equal influence.

If instead, we take a cue from the tessellation and impose consistency, that is to say, if we take $f_1 = f_2 = 1 - 0.15 - 0.05 = 0.8$, then we see that whether all fibers have the same properties or not, the amount of matrix shell provided is consistent with the dispersion of the fibers. This approach to assigning f_J will be adopted throughout the remainder of this work.

D. Orientational Averaging Methods

In order to consider composites containing inhomogeneities at distinct orientations (be they inhomogeneities with the same shape and properties or not), it is convenient to consider each orientation of a given inhomogeneity as a separate phase in a multiphase averaging approach. One such approach discussed in Christensen [198] for random orientations of single inhomogeneity types is to first obtain the effective properties as if the inhomogeneities were aligned. These effective properties then undergo the appropriate coordinate transformation from the aligned coordinate system to the global system and are then average over all possible orientations. This approach, which will be referred to as the rule of mixtures approach to orientational averaging, does not, however, account for the differences in interactions between inhomogeneities when they are aligned versus when they are oriented.

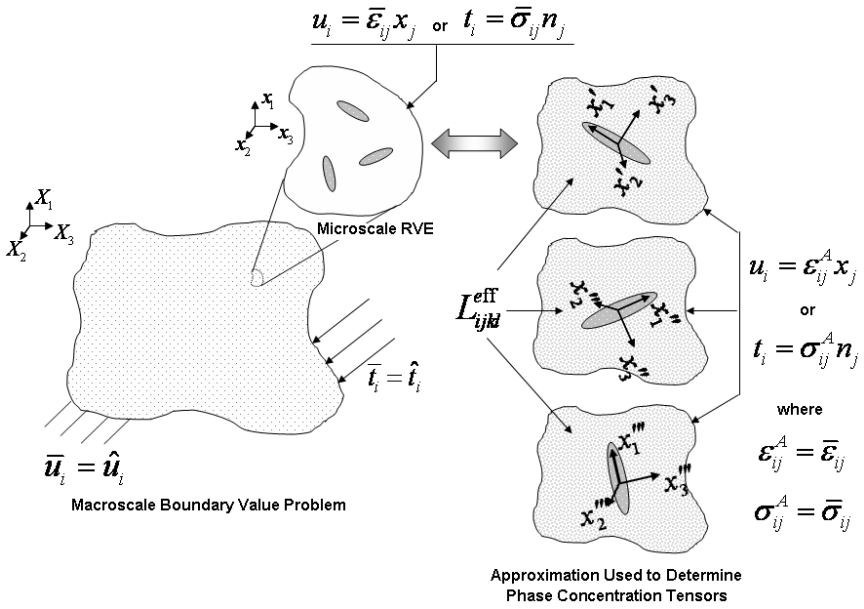

Fig. 13. Schematic representation a microscale RVE consisting of an inhomogeneity with a random distribution of orientations between the local inhomogeneity coordinate systems and that of the microscale RVE, and of the use of self-consistent method in determining the effective composite properties.

In an alternative approach [89, 208, 209], the interactions between the different orientations of the inhomogeneity are accounted for by determining the concentration tensor in the local inhomogeneity coordinate system, applying the appropriate coordinate transformation from the local inhomogeneity coordinate system to the microscale RVE coordinate system, and then properly imposing the consistency condition amongst concentration tensors obtained for the various orientations.

For example, consider a microscale RVE consisting of M orientations of a given inhomogeneity, as shown in Figure 13, so that including the matrix material, the total number of phases in the microscale RVE is $N = M + 1$.[33] Each orientation can be

[33]For a more illustrative example, see Appendix B.

defined by the angles φ_J, ψ_J which relate the local inhomogeneity orientation to the microscale RVE coordinate system by a change of basis which is determined from a series of single axis rotations, i.e. ${}^JQ_{ij} = {}^JQ^{\psi}_{ik}\,{}^JQ^{\varphi}_{kj}$ such that in engineering notation

$$\left[{}^JQ\right] = \begin{bmatrix} \cos(\varphi) & 0 & -\sin(\varphi) \\ \sin(\psi)\sin(\varphi) & \cos(\psi) & \sin(\psi)\cos(\varphi) \\ \cos(\psi)\sin(\varphi) & -\sin(\psi) & \cos(\psi)\cos(\varphi) \end{bmatrix} \tag{2.159}$$

The effective stiffness, for example, of the microscale RVE can therefore be obtained from Eqn. 2.71a. In order to denote the orientations associated with each phase the effective stiffness is written as

$$L^{\text{eff}}_{ijkl} = L^N_{ijkl} + \sum_{J=1}^{M} c_J(\varphi_J,\psi_J)(L^J_{ijmn}(\varphi_J,\psi_J) - L^N_{ijmn})A^J_{mnkl}(\varphi_J,\psi_J) \tag{2.160}$$

where $c_J(\varphi_J,\psi_J)$ is the volume fraction of a given orientation and where

$$L^J_{ijmn}(\varphi_J,\psi_J) = {}^JQ_{ip}\,{}^JQ_{jq}\tilde{L}_{pqrs}\,{}^JQ_{mr}\,{}^JQ_{ns} \tag{2.161a}$$

$$A^J_{ijmn}(\varphi_J,\psi_J) = {}^JQ_{ip}\,{}^JQ_{jq}\tilde{A}_{pqrs}\,{}^JQ_{mr}\,{}^JQ_{ns} \tag{2.161b}$$

$$c_J(\varphi,\psi) = w_J\bar{c} \tag{2.161c}$$

where the tilde denotes quantities expressed in the local inhomogeneity coordinate system and where w_J is the weight factor for the fraction of inhomogeneities with a given (φ_J,ψ_J) and $\bar{c}$ is the total volume fraction of the inhomogeneity irrespective of orientation. It is also noted that $\tilde{L}_{pqrs}$ and $\tilde{A}_{pqrs}$ have been expressed without a superscript J in order to emphasize that the only difference between the inhomogeneities in all of the phases is the orientation. As such, if one were to use the self-consistent method to approximate the concentration tensor, then one need only calculate $\tilde{A}_{pqrs}$ once using Eqn. 2.83.

It is noted that as $M \to \infty$, a continuous distribution of orientations over a unit sphere, $\rho(\varphi, \psi)$, can be obtained, and as such, one may write

$$L^{\text{eff}}_{ijkl} = L^{N}_{ijkl} + \frac{\int_0^{2\pi}\int_0^{\pi} \rho(\varphi,\psi)\bar{c}[L_{ijmn}(\varphi,\psi) - L^{N}_{ijmn}]A_{mnkl}(\varphi,\psi)\sin(\varphi)\; d\varphi\; d\psi}{\int_0^{2\pi}\int_0^{\pi} \rho(\varphi,\psi)\sin(\varphi)\; d\varphi\; d\psi} \quad (2.162)$$

where the lack of the subscript J on the angles denotes the continuous distribution of orientations as opposed to a discrete number of them. It is further noted that for a random distribution of orientations, each (φ, ψ) is equally likely and therefore $\rho(\varphi, \psi) = \rho_0$ and

$$L^{\text{eff}}_{ijkl} = L^{N}_{ijkl} + \frac{\bar{c}}{4\pi}\int_0^{2\pi}\int_0^{\pi} [L_{ijmn}(\varphi,\psi) - L^{N}_{ijmn}]A_{mnkl}(\varphi,\psi)\sin(\varphi)\; d\varphi\; d\psi \quad (2.163a)$$

$$M^{\text{eff}}_{ijkl} = M^{N}_{ijkl} + \frac{\bar{c}}{4\pi}\int_0^{2\pi}\int_0^{\pi} [M_{ijmn}(\varphi,\psi) - M^{N}_{ijmn}]B_{mnkl}(\varphi,\psi)\sin(\varphi)\; d\varphi\; d\psi \quad (2.163b)$$

$$k^{\text{eff}}_{ij} = k^{N}_{ij} + \frac{\bar{c}}{4\pi}\int_0^{2\pi}\int_0^{\pi} [k_{im}(\varphi,\psi) - k^{N}_{im}]A_{mj}(\varphi,\psi)\sin(\varphi)\; d\varphi\; d\psi \quad (2.163c)$$

$$\xi^{\text{eff}}_{ij} = \xi^{N}_{ij} + \frac{\bar{c}}{4\pi}\int_0^{2\pi}\int_0^{\pi} [\xi_{im}(\varphi,\psi) - \xi^{N}_{im}]B_{mj}(\varphi,\psi)\sin(\varphi)\; d\varphi\; d\psi \quad (2.163d)$$

resulting in effective properties for the composite which are isotropic [153, 209, 210].

It should be noted that when using the self-consistent and generalized self-consistent concentration tensor approximations, the consistency condition is automatically satisfied. However, when using the Mori-Tanaka approximation, one must use caution as the Mori-Tanaka consistency condition must be applied in the microscale RVE coordinate system. See Appendix C for more details.

E. Application of Interaction Energy for Effective Properties

As was previously noted, the theory of multiple scale expansion and the notion of energy equivalency between the microscale RVE and an effective homogeneous material, i.e. as in Eqn. 2.22, can be synonymous. It is further noted that, in some cases, for

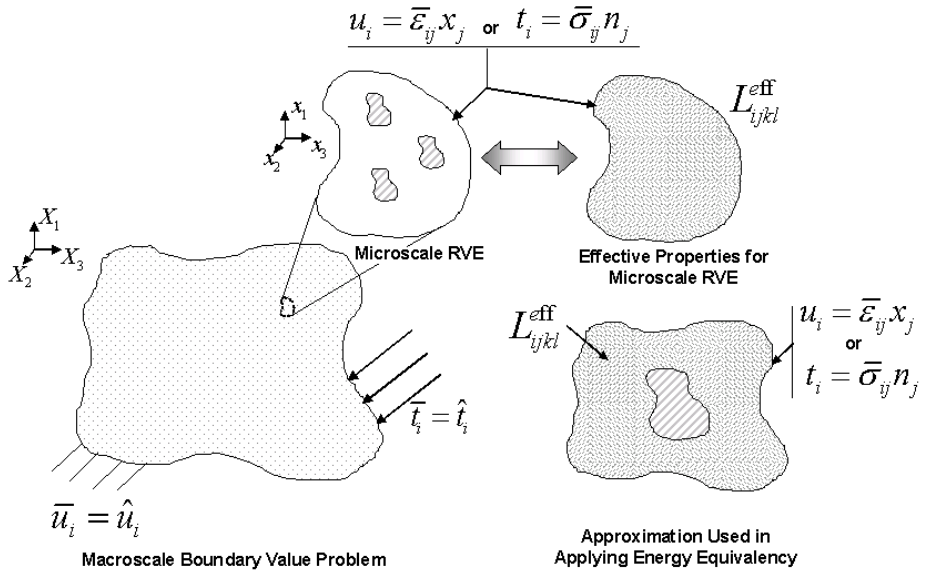

Fig. 14. Schematic representation of the energy equivalency between the microscale RVE and its effective material representation and identification of a single inhomogeneity approximation for calculating the RVE energy.

example in microscale RVEs consisting of a single type of inhomogeneity, the energy of the RVE be calculated using an approximation of the RVE as shown schematically in Figure 14. In such cases it is often convenient in the calculation of the volume averaged strain energy from the approximation of the microscale RVE to decompose the RVE energy, W^{RVE}, in terms of what is referred to as the interaction energy (see for example [198]) between the inhomogeneity and its surroundings, W^{int}, and the strain energy of the surrounding material in the approximation, measured in the absence of the inhomogeneity, W^0 (referred to as the homogeneous matrix energy), i.e.

$$W^{\text{RVE}} = W^{\text{int}} + W^0 \tag{2.164}$$

where the strain energy of the surrounding material using the definition in Eqn. 2.5 is given by

$$W^0 = \frac{1}{2}\langle \sigma_{ij}^0 \varepsilon_{ij}^0 \rangle \tag{2.165}$$

This decomposition is shown schematically for three approximations to the RVE energy, the dilute, the self-consistent and the generalized self-consistent approximations, in Figure 15. Thus, in what is referred to as the Eshelby formula[34], Eqn. 2.164 can be substituted into Eqn. 2.22 which can then be written as

$$W^{\text{eff}} = W^0 + W^{\text{int}} \tag{2.166}$$

It can be shown[35] that the interaction energy can be defined in terms of the surface tractions and displacements on the inhomogeneity and the tractions and displacements on an imaginary inhomogeneity boundary in the homogeneous surrounding material problem as

$$W^{\text{int}} = \frac{1}{V}\int_{S_i} \left(t_i u_i^0 - t_i^0 u_i\right) dS \tag{2.167}$$

where S_i is the surface of the inhomogeneity and where it should be noted that the expression given in Eqn. 2.167 is for applied average displacement, $\bar{u}_i$, on the boundary S. An analogous expression for the interaction energy for applied average traction, $\bar{t}_i$, on S is given by the negative of this equation.

It is noted from Figure 15, that in the dilute approach (Figure 15(a)), the inhomogeneity is embedded in the matrix so that the matrix constitutive properties are used for determining the homogeneous matrix strain energy and the interaction energy from Eqns. 2.165 and 2.167, respectively. In the self-consistent approximation in Figure 15(b), the inhomogeneity is instead embedded in the effective material so

[34]See for example [198].

[35]See for example [198].

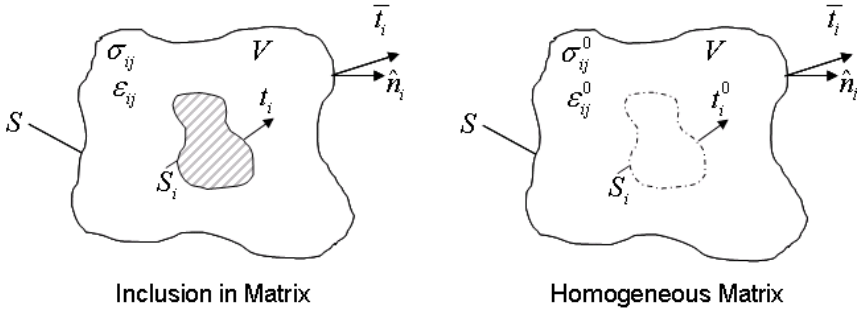

(a) Dilute Approach

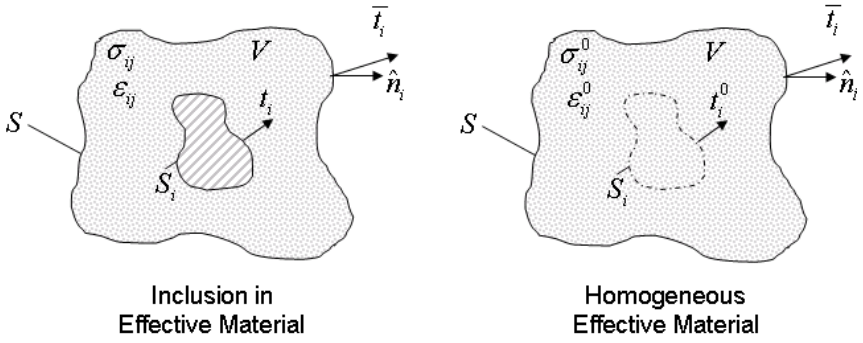

(b) Self-Consistent Approach

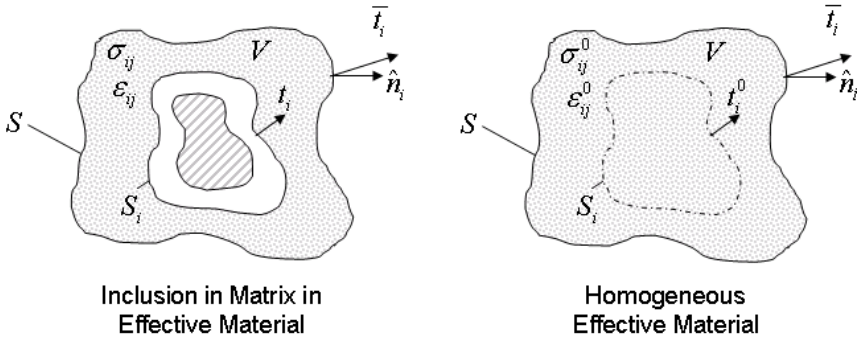

(c) Generalized Self-Consistent Approach

Fig. 15. Schematic representations of the decomposition of the strain energy into the interaction energy and the homogeneous matrix energy as applied in the dilute, self-consistent, and generalized self-consistent approximations.

that $\sigma_{ij}^0 = \sigma_{ij}^{\text{eff}}$ and $u_i^0 = u_i^{\text{eff}}$, and therefore $W^0 = W^{\text{eff}}$ and $t_i^0 = t_i^{\text{eff}}$ on S_i. As such, the Eshelby formula for the self-consistent method reduces to

$$W^{\text{int}} = \frac{1}{V} \int_{S_i} \left(t_i u_i^{\text{eff}} - t_i^{\text{eff}} u_i \right) dS = 0 \tag{2.168}$$

so that for the self-consistent method, the effective properties can be determined directly from the interaction energy using Eqn. 2.168. Similar to the self-consistent approximation, it is noted that the Eshelby formula in the generalized self-consistent approximation also reduces to Eqn. 2.168. The difference, however, is that the surface, S_i is no longer that of the inhomogeneity, but is instead the surface of a volume of matrix enveloping the inhomogeneity as shown in Figure 15(c), and thereby retains the load transfer between the matrix and the inclusion in the calculation of the interaction energy.

Finally, it is noted that many of the concepts presented in this chapter will be applied and/or discussed in great detail in the context of the generalized self-consistent composite cylinder method in Chapter III.

CHAPTER III

THE GENERALIZED SELF-CONSISTENT COMPOSITE CYLINDER METHOD

As the nanocomposite modeling approaches applied herein are centered on the generalized self-consistent composite cylinder method, a detailed description of the method is provided in this chapter. Originally developed for microscale RVEs of a single type of perhaps coated, high aspect ratio circular cylinder fibers, the method is extended here to account for multiple fiber types and orientations through the calculation of concentration tensor components. The chapter begins with a description of the multi-layered composite cylinders method for elastic properties which is followed by the multi-layered generalized self-consistent method for elastic properties. This is followed with a discussion of the development of graded interphase solutions for use in the generalized self-consistent method. The derivation of the multi-layered generalized self-consistent composite cylinders method for thermal and electrical conductivity is then provided, followed by a detailed description of how to obtain concentration tensors using the generalized self-consistent composite cylinders method and how these concentration tensors are used in orientational averaging. Finally the chapter closes with a few parametric studies and a brief description of how the generalized self-consistent model will be used applied in determining the effective elastic properties and conductivities of CNT-epoxy nanocomposites.

A. The Multi-Layered Composite Cylinders Method for Elastic Properties

In the discussion of the multi-layered and generalized self-consistent composite cylinders methods which follows, use of both energy equivalency and direct averaging methods will be in the determination of effective microscale RVE properties will be discussed. Each of these methods has their advantages and disadvantages and will be

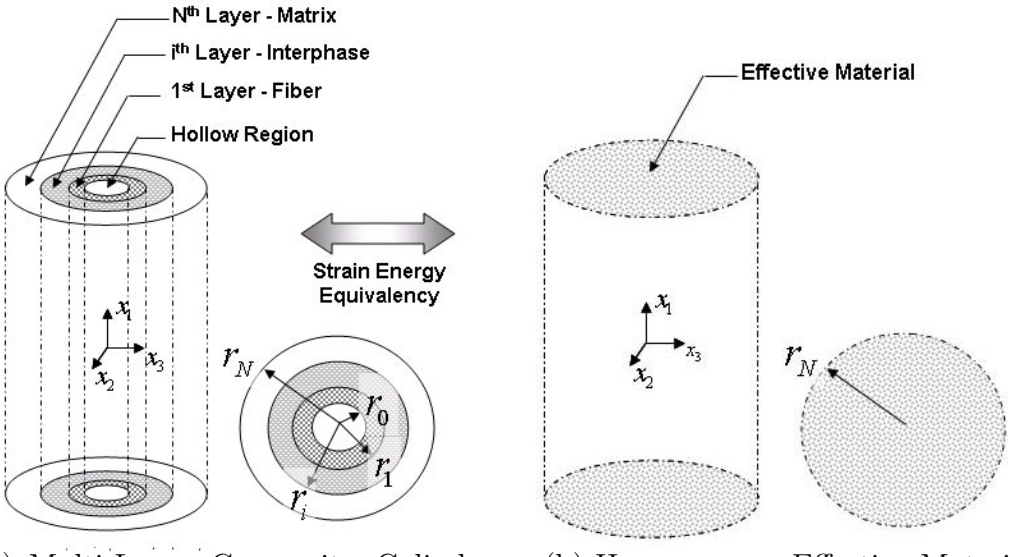

(a) Multi-Layer Composite Cylinder Assemblage for Coated Hollow Fiber (b) Homogeneous Effective Material

Fig. 16. General schematic representing the energy equivalency between a N-layer composite cylinder assemblage (16(a)) and its effective material representation (16(b)). It should also be noted that the tube axis is along the one-, or z-direction. The inner radius of the fiber is denoted as r_0, and the outer radius of the matrix is denoted as r_N, with r_1 denoting the fiber outer radius.

explored in the determination of the effective elastic properties of randomly oriented, graded interphase coated fiber composites as continuum level representations of carbon nanotube-polymer nanocomposites. What follows is a summary of the multi-layer composite cylinder method approach to modeling graded interphase regions similar to those provided by Jayaraman and Reifsnider [167] and by Jasiuk and Kouider [168].

As an example of the composite cylinder model, consider the composite cylinder assemblage shown in Figure 16(a) and the analogous homogeneous solid in Figure 16(b). Displacement fields which satisfy the equilibrium equations are assumed

for each layer of the composite cylinder assemblage and for the homogeneous solid.[1] The strains in each layer are determined from the displacement fields using the strain-displacement relations, with the layer stresses determined from the appropriate constitutive relation for each layer. The same is done for the homogeneous solid where the constitutive relations consist of the unknown effective properties of the composite. Sets of homogeneous boundary conditions consistent with the number of independent effective material properties are independently applied along with the appropriate interface matching conditions between the composite cylinder assemblage layers. For the effective elastic properties of the composite cylinder assemblage, five sets of boundary conditions are needed as the effective material response is transversely isotropic. In determining the effective elastic properties of aligned fiber composites using the composite cylinders method, the volume averaged strain energies of the composite cylinder assemblage, W, and of the effective homogeneous cylinder, $W^{(\text{eff})}$, are obtained from the volume average of the strain energy, and are set equal to one another.

The set of elasticity problems typically include assumed displacement fields consistent with determining 1) the in-plane bulk modulus (κ_{23}^{eff}), 2) the axial Young's modulus (E_1^{eff}), 3) the axial stiffness component (C_{1111}^{eff})[2], 4) the axial shear modulus (μ_{12}^{eff}), and 5) the in-plane shear modulus (μ_{23}^{eff}). A summary of the elasticity solutions for the boundary value problems identified in Figure 17 is provided here, followed by a discussion of methods for determining the effective properties from the elasticity solutions. It is noted that the assumed displacement fields applied in each of the

[1]Here it is assumed that each layer is a compatible phase in the reference configuration with no residual stresses or transformation strains and subject to small deformations so that continuity of tractions and displacements can applied across the layer boundaries.

[2]In order to be consistent with the notation of Hashin [158], C_{1111}^{eff} is used in place of L_{1111}^{eff}.

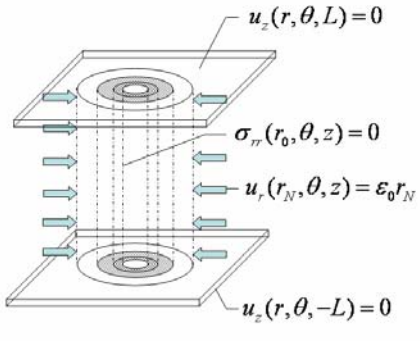

(a) In-plane Bulk Modulus, κ_{23}^{eff}

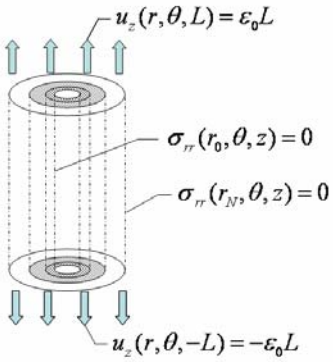

(b) Axial Young's Modulus, E_1^{eff}

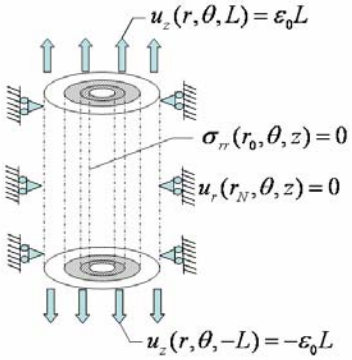

(c) Axial Stiffness Component, C_{1111}^{eff}

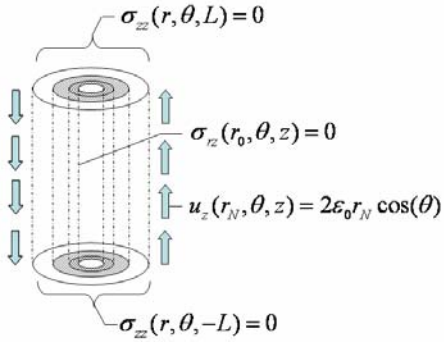

(d) Axial Shear Modulus, μ_{12}^{eff}

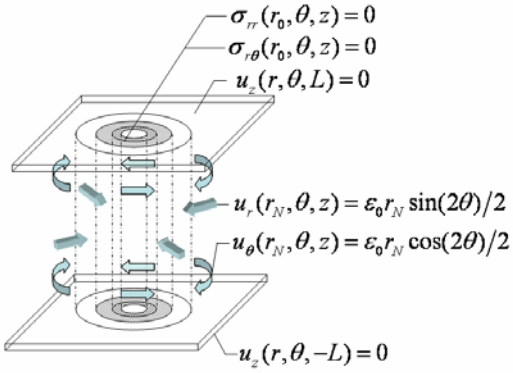

(e) In-plane Shear Modulus, μ_{23}^{eff}

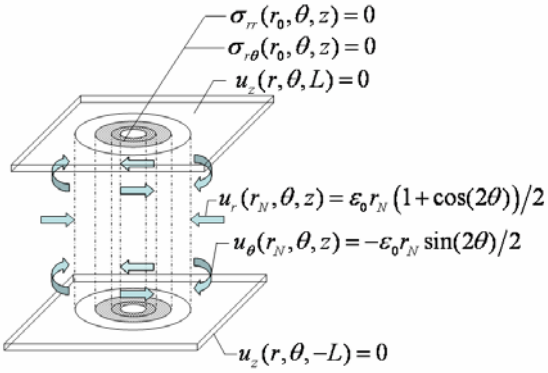

(f) A Transverse Extension Test

Fig. 17. Boundary value problems solved in the composite cylinder method.

boundary value problems are solutions to the equilibrium equations in cylindrical coordinates, i.e.

$$\begin{aligned}
&\frac{\partial \sigma_{rr}}{\partial r} + \frac{1}{r}\frac{\partial \sigma_{r\theta}}{\partial \theta} + \frac{\partial \sigma_{rz}}{\partial z} + \frac{1}{r}(\sigma_{rr} - \sigma_{\theta\theta}) = 0 \\
&\frac{\partial \sigma_{r\theta}}{\partial r} + \frac{1}{r}\frac{\partial \sigma_{\theta\theta}}{\partial \theta} + \frac{\partial \sigma_{\theta z}}{\partial z} + \frac{2}{r}\sigma_{r\theta} = 0 \\
&\frac{\partial \sigma_{rz}}{\partial r} + \frac{1}{r}\frac{\partial \sigma_{\theta z}}{\partial \theta} + \frac{\partial \sigma_{zz}}{\partial z} + \frac{1}{r}\sigma_{rz} = 0
\end{aligned} \tag{3.1}$$

where in obtaining these equations in terms of the displacement components it is noted for the present discussion that each phase of the composite cylinder assemblage is homogeneous.

1. Composite Cylinder Method for In-plane Bulk Modulus

a. Displacement, Strain, and Stress Fields

The in-plane, or plane strain bulk modulus, κ_{23}^{eff}, is determined through the application of the displacement field expressed in cylindrical coordinates in Eqn. 3.2 to each phase of the composite cylinder assemblage shown in Figure 16(a):

$$\begin{aligned}
u_r^i &= D_1^i r + D_2^i \frac{1}{r} \\
u_\theta^i &= 0 \qquad\qquad \text{for } r_{i-1} \le r \le r_i \\
u_z^i &= 0
\end{aligned} \tag{3.2}$$

where D_1^i and D_2^i are constants and i ranges from one to N where it is noted that r_N is dependent upon the desired volume fraction. It should also be noted that the displacement field satisfies equilibrium for isotropic and transversely isotropic layers so that the displacements in the homogeneous effective cylinder[3] of Figure 16(b) are

[3]See Sections D1 and D2 of Appendix D for the derivation of the displacement fields for homogeneous layers.

given by:

$$\begin{aligned} u_r^{\text{eff}} &= D_1^{\text{eff}} r + D_2^{\text{eff}} \frac{1}{r} \\ u_\theta^{\text{eff}} &= 0 \qquad\qquad\qquad \text{for } 0 \le r \le r_N \\ u_z^{\text{eff}} &= 0 \end{aligned} \tag{3.3}$$

These displacements are used to calculate first the strains and then the stresses. The non-zero strains in each layer of the composite cylinder assemblage are therefore given by:

$$\begin{aligned} \varepsilon_{rr}^i &= D_1^i - D_2^i \frac{1}{r^2} \\ \varepsilon_{\theta\theta}^i &= D_1^i + D_2^i \frac{1}{r^2} \end{aligned} \tag{3.4}$$

with the non-zero stresses for isotropic phases given by:

$$\begin{aligned} \sigma_{rr}^i &= 2D_1^i(\mu_i + \lambda_i) - 2\mu_i D_2^i \frac{1}{r^2} \\ \sigma_{\theta\theta}^i &= 2D_1^i(\mu_i + \lambda_i) + 2\mu_i D_2^i \frac{1}{r^2} \\ \sigma_{zz}^i &= 2\lambda_i D_1^i \end{aligned} \tag{3.5}$$

where μ_i and λ_i are the Lamé constants for the i^{th} isotropic phase. The boundary conditions consistent with an in-plane, or plane strain bulk test are applied to the composite cylinder assemblage as shown in Figure 17(a) and are given by (assuming hollow fiber):

$$\sigma_{rr}^1|_{r=r_0} = 0 \tag{3.6a}$$

$$u_r^N|_{r=r_N} = \varepsilon_0 r_N \tag{3.6b}$$

where Eqn. 3.6a corresponds to a traction free internal surface of the hollow cylinder and Eqn. 3.6b represents an applied displacement at the outer boundary consistent with ε_0 as the average radial strain in a homogeneous cylinder. In addition, the

continuity of displacement and traction conditions across internal phase boundaries given by:

$$u_r^j|_{r=r_j} = u_r^{j+1}|_{r=r_j} \tag{3.7a}$$

$$\sigma_{rr}^j|_{r=r_j} = \sigma_{rr}^{j+1}|_{r=r_j} \tag{3.7b}$$

where j ranges from one to $N-1$, the constants D_1^i and D_2^i are obtained for all phases of the composite cylinder assemblage. Note that for solid fibers, Equation 3.6a is replaced by the condition that $D_2^1 = 0$ (e.g., $D_2^{\text{eff}} = 0$ for the homogeneous effective material) which imposes the condition that the displacement field be bounded at the origin of solid fibers. Thus, the $2N$ unknown constants (D_1^i's and D_2^i's) are determined from the $2N$ boundary and matching condition equations. Solutions for the constants for $N = 2$ and $N = 3$ for the in-plane bulk modulus and for the other effective composite properties are provided in Appendix E.

b. Methods for Determining the Effective In-plane Bulk Modulus

With the displacements, strains and stresses for each case identified, the effective properties of the composite cylinder assemblage can be determined. Four methods for determining the effective properties are provided, each having advantages and disadvantages. The methods are based on the general micromechanics philosophies discussed in Chatper II. In the first method, the average stress and strain of the composite cylinder assemblage are used along with the definition of the effective property being determined (as in Eqn. 2.56). In the second method, the direct energy equivalency as in Eqn. 2.22 is applied using the average stress and strain of the composite cylinder assemblage and of the homogeneous effective material (Figures 4 and 16). The third and fourth methods presented make use of the interaction energy methods (Eqn. 2.164) described in Eqns. 2.167 and 2.168, respectively. Application

of each of these four methods is explicitly demonstrated in the determination of the in-plane bulk modulus, with the results for other properties briefly summarized.

- Method 1: Using Volume Averages and the Definition of the Engineering Property

The in-plane bulk modulus, κ_{23}^{eff}, is obtained by definition as:

$$\kappa_{23}^{\text{eff}} = \frac{\langle \sigma_{22}^{\text{comp}} \rangle}{2\langle \varepsilon_{22}^{\text{comp}} \rangle} \tag{3.8}$$

where the average stress and strain in Eqn. 3.8 are taken over the entire composite cylinder assemblage which includes the hollow region shown in Figure 16. As the internal surface is taken as traction-free in each of the composite cylinders assemblage, the stress in the hollow region can be taken as zero. However, the strain in the hollow region is nonzero and can be taken to be homogeneous and consistent with the strain at the internal surface (i.e., at r_0). This complication can be avoided, however, if the volume averages are instead expressed in terms of external surface tractions and displacements[4] by:

$$\kappa_{23}^{\text{eff}} = \frac{\sigma_{rr}^{N}|_{r=r_N}}{2\left(u_r^N|_{r=r_N}/r_N\right)} \tag{3.9}$$

For an isotropic matrix, the in-plane bulk modulus is then obtained in terms of the constants D_j^N as:

$$\kappa_{23}^{\text{eff}} = \frac{(\mu_N + \lambda_N) r_N^2 D_1^N - \mu_N D_2^N}{r_N^2 D_1^N + D_2^N} \tag{3.10}$$

From Eqn. 3.10, it is observed that the in-plane bulk modulus can be determined in terms of only two of the $2N$ displacement constants, and therefore encourages the use of techniques such as Cramer's rule to avoid solving potentially large algebraic systems of equations.

[4]See Appendix F.

- Method 2: Direct Strain Energy Equivalency

In the application of the direct strain energy equivalency of Eqn. 2.22 between the composite cylinder assemblage and the homogeneous effective material of Figure 16, the strain energy of the effective homogeneous material for the boundary conditions applied for the in-plane bulk test can be expressed as:

$$W^{\text{eff}} = 4\kappa_{23}^{\text{eff}}\varepsilon_0^2 \tag{3.11}$$

The volume averaged strain energy for the composite cylinder assemblage as given by Eqn. 2.17, can be expressed as separate volume integrals over each layer in the composite cylinder assemblage as:

$$W^{\text{RVE}} = \frac{1}{V}\left(\sum_{i=1}^{N}\int_{-L/2}^{L/2}\int_{r_{i-1}}^{r_i}\int_{0}^{2\pi}\sigma_{ij}^i\varepsilon_{ij}^i r\,d\theta\,dr\,dz\right) \tag{3.12}$$

where V is the total volume of the composite cylinder assemblage which includes the hollow region shown in Figure 16. However, it should be noted that the traction-free conditions on the internal surface of the composite cylinder assemblage means that the strain energy of the of hollow region is zero, and therefore does not appear in the summation in Eqn. 3.12. The effective in-plane bulk modulus is then obtained by solving Eqn. 2.22 for κ_{23}^{eff} and results in the following form in terms of the constants D_j^i:

$$\kappa_{23}^{\text{eff}} = \frac{1}{\chi_0}\sum_{i=1}^{N}\left(\chi_1^i(D_1^i)^2 + \chi_2^i(D_2^i)^2\right) \tag{3.13}$$

where the χ are constants which depend on layer geometries and layer elastic constants. For example, for $N = 2$ and isotropic layers, the χ are given by:

$$\begin{aligned}
\chi_0 &= r_0^2 r_1^2 r_2^4 \varepsilon_0^2 \\
\chi_1^1 &= r_0^2 r_1^2 r_2^2 (r_1^2 - r_0^2)(\mu_1 + \lambda_1) \\
\chi_2^1 &= r_2^2 (r_1^2 - r_0^2)\mu_1 \\
\chi_1^2 &= r_0^2 r_1^2 r_2^2 (r_2^2 - r_1^2)(\mu_2 + \lambda_2) \\
\chi_2^2 &= r_0^2 (r_2^2 - r_1^2)\mu_2
\end{aligned} \tag{3.14}$$

In this case, all of the constants in the displacement field must be determined in obtaining the effective in-plane bulk modulus.

- Method 3: Strain Energy Equivalency via Interaction Energy

In this method, the volume averaged strain energy is given in terms of the interaction energy defined on an internal surface of the composite cylinder assemblage and in terms of the volume averaged strain energy of the homogeneous matrix as shown in Figure 15(a). The strain energy of the composite is therefore given by Eqn. 2.164, where W^0 is the volume averaged strain energy of a homogeneous cylinder with material properties of the N^{th} layer and W^{int} is the interaction energy between the $N-1$ inner layers and the N^{th} layer. The strain energy of the composite is then taken to be equivalent to the strain energy of the effective material (Eqn. 2.22), and as such, this method involves two volume integrals over homogeneous cylinders and a surface integral in the composite cylinder assemblage, and therefore avoids integrating over each layer in the total volume.

The homogeneous matrix cylinder is assumed to have the same functional form of displacement field as the composite cylinder assemblage, i.e.,

$$\begin{aligned} u_r^0 &= D_1^0 r + D_2^0 \frac{1}{r} \\ u_\theta^0 &= 0 \qquad\qquad \text{for } 0 \le r \le r_N \\ u_z^0 &= 0 \end{aligned} \tag{3.15}$$

and is subjected to the same external boundary condition provided in Eqn. 3.6b, with Eqn. 3.6a replaced by the condition that the displacement be bounded at the origin (i.e., $D_2^0 = 0$). As such, it should be noted that $D_j^0 \neq D_j^N$, despite having the same material properties as the boundary conditions for the homogeneous cylinder and the N^{th} layer of the composite cylinder assemblage are different. From the displacement field, the strains and stresses of the homogeneous matrix cylinder are obtained and used to determine the homogeneous matrix volume averaged strain energy given by:

$$W^0 = \frac{1}{V}\left(\int_{-L/2}^{L/2}\int_0^{r_N}\int_0^{2\pi} \sigma_{ij}^0 \varepsilon_{ij}^0 r \, d\theta \, dr \, dz\right) \tag{3.16}$$

which for an isotropic matrix (i.e., N^{th} layer) reduces to $W^0 = 4\varepsilon_0^2(\mu_N + \lambda_N)$.

The interaction energy as defined in Eqn. 2.167, is taken over the surface S_i, taken to be the interface between the N^{th} and $(N-1)^{\text{th}}$ layer of the composite cylinder assemblage, and is an internal surface in the homogeneous matrix cylinder located where that phase boundary would have been. As such, the interaction energy can alternatively be expressed as:

$$\begin{aligned} W^{\text{int}} = \frac{1}{V}\int_{-L/2}^{L/2}\int_0^{2\pi} &[(\sigma_{rr}^N u_r^0 + \sigma_{r\theta}^N u_\theta^0 + \sigma_{rz}^N u_z^0) \\ &- (\sigma_{rr}^0 u_r^N + \sigma_{r\theta}^0 u_\theta^N + \sigma_{rz}^0 u_z^N)]_{r=r_{N-1}} \, r_{N-1} \, d\theta \, dz \end{aligned} \tag{3.17}$$

where it is noted that as a result of the imposition of continuity of tractions and displacements across phase boundaries in the composite cylinder assemblage, the N^{th} layer stresses and displacements of the composite cylinder assemblage have been used in place of the $(N-1)^{\text{th}}$ stresses and displacements in Eqn. 3.17.

For composite cylinder assemblages with isotropic N and $N-1$ layers, the in-plane bulk modulus is determined from solving Eqn. 2.164 and is given by:

$$\begin{aligned}\kappa_{23}^{\text{eff}} = \frac{1}{\varepsilon_0 r_N^2}[r_{N-1}^2(\mu_{N-1}+\lambda_{N-1}-\mu_N-\lambda_N)D_1^{N-1} \\ -(\mu_{N-1}+\mu_N+\lambda_N)D_2^{N-1}+\varepsilon_0 r_N^2(\mu_N+\lambda_N)]\end{aligned} \tag{3.18}$$

so that again, Cramer's Rule can again be used to solve for the two needed constants (D_1^{N-1} and D_2^{N-1}) as opposed to having to determine all of the $2N$ total constants in order to obtain explicit solutions for the in-plane bulk modulus.

- Method 4: Strain Energy Equivalency via Self-Consistent Interaction Energy

The fourth composite cylinder approach to determining the effective in-plane bulk modulus can be thought of as being similar to a generalized self-consistent approach. In this method, the homogeneous cylinder is taken to be the effective cylinder so that the generalized self-consistent equations provided in Eqns. 2.167 and and 2.168 are applied. However, this method is approximate in that it assumes that the interaction energy between the composite cylinder assemblage of Figure 16 and the effective cylinder is equal to zero on the composite cylinder assemblage surface at $r = r_N$. That is:

$$\begin{aligned}W^{\text{int}} = \int_{-L/2}^{L/2}\int_0^{2\pi}[(\sigma_{rr}^N u_r^{\text{eff}}+\sigma_{r\theta}^N u_\theta^{\text{eff}}+\sigma_{rz}^N u_z^{\text{eff}}) \\ -(\sigma_{rr}^{\text{eff}} u_r^N+\sigma_{r\theta}^{\text{eff}} u_\theta^N+\sigma_{rz}^{\text{eff}} u_z^N)]_{r=r_N} r_N\, d\theta\, dz = 0\end{aligned} \tag{3.19}$$

Table II. Summary of the resulting effective in-plane bulk modulus results for each of the four methods applied indicating the minimum number of displacement constants needing to be determined. Displacement constants for $N = 2$ and $N = 3$ composite cylinder assemblages can be found in Appendix E

.

Method	**No. Disp. Constants**	**Eqn.**	**In-plane Bulk Modulus**
Method 1	2	3.10	$\kappa_{23}^{\text{eff}} = \frac{(\mu_N+\lambda_N)r_N^2 D_1^N - \mu_N D_2^N}{r_N^2 D_1^N + D_2^N}$
Method 2	2N	3.13	$\kappa_{23}^{\text{eff}} = \frac{1}{\chi_0}\sum_{i=1}^{N}(\chi_1^i (D_1^i)^2 + \chi_2^i (D_2^i)^2)$
Method 3	2	3.18	$\kappa_{23}^{\text{eff}} = \frac{1}{\varepsilon_0 r_N^2}[r_{N-1}^2(\mu_{N-1}+\lambda_{N-1}-\mu_N-\lambda_N)D_1^{N-1}$ $-(\mu_{N-1}+\mu_N+\lambda_N)D_2^{N-1} + \varepsilon_0 r_N^2(\mu_N+\lambda_N)]$
Method 4	2	3.10	$\kappa_{23}^{\text{eff}} = \frac{(\mu_N+\lambda_N)r_N^2 D_1^N - \mu_N D_2^N}{r_N^2 D_1^N + D_2^N}$

Eqn. 3.19 is then solved for κ_{23}^{eff}, which for isotropic N^{th} layers produces an identical result to Eqn. 3.10, and therefore requires the solution of only two of the $2N$ displacement constants, D_1^N and D_2^N, which, because of the approximation of using the composite cylinder assemblage, do not contain effective material properties as they would have had the generalized self-consistent composite cylinder been used. Reasons why this is in fact a good approximation will be made clear in the subsequent discussion of the generalized self-consistent composite cylinders method. It is also of interest to point out that although the functional forms of the effective in-plane bulk modulus from each of the four methods may vary (see Table II), the numeric results obtained are in excellent agreement. The same is found to be true for the applicable methods in the remaining properties to be discussed.

2. Composite Cylinder Method for Axial Young's Modulus and Stiffness Component

a. Displacement, Strain, and Stress Fields

The displacement field applied to each phase of the composite cylinder assemblage to determine the axial Young's modulus (E_1^{eff}) is:

$$\begin{aligned} u_r^i &= D_1^i r + D_2^i \frac{1}{r} \\ u_\theta^i &= 0 \qquad\qquad \text{for } r_{i-1} \le r \le r_i \\ u_z^i &= \varepsilon_0 z \end{aligned} \tag{3.20}$$

The nonzero strains and stresses are therefore obtained as:

$$\begin{aligned} \varepsilon_{rr}^i &= D_1^i - D_2^i \frac{1}{r^2} \\ \varepsilon_{\theta\theta}^i &= D_1^i + D_2^i \frac{1}{r^2} \\ \varepsilon_{zz}^i &= \varepsilon_0 \end{aligned} \tag{3.21}$$

and (again assuming isotropic phases):

$$\begin{aligned} \sigma_{rr}^i &= 2D_1^i(\mu_i + \lambda_i) - 2\mu_i D_2^i \frac{1}{r^2} + \lambda_i \varepsilon_0 \\ \sigma_{\theta\theta}^i &= 2D_1^i(\mu_i + \lambda_i) + 2\mu_i D_2^i \frac{1}{r^2} + \lambda_i \varepsilon_0 \\ \sigma_{zz}^i &= 2\lambda_i D_1^i + (2\mu_i + \lambda_i)\varepsilon_0 \end{aligned} \tag{3.22}$$

respectively. The boundary conditions consistent with a uniaxial extension test (Figure 17(b)) are applied to the composite cylinder assemblage as (assuming hollow fiber):

$$\sigma_{rr}^1|_{r=r_0} = 0 \tag{3.23a}$$

$$\sigma_{rr}^N|_{r=r_N} = 0 \tag{3.23b}$$

The boundary condition in Eqn. 3.23a again corresponds to a zero-traction internal surface. The boundary condition in Eqn. 3.23b corresponds to a traction free external surface which allows for the Poisson's effect to take place. As the cylinder is under plane strain conditions, the axial extension corresponding the average axial strain in a homogeneous body is applied in z-component of the assumed displacement field of Eqn. 3.20. The matching conditions of continuity of tractions and displacements are identical to those identified in Eqn. 3.7 for determining the in-plane bulk modulus, thus allowing for the determination of the $2N$ unknown constants (D_1^i's and D_2^i's) from the $2N$ boundary and matching condition equations. The solutions for the displacement constants for $N = 2$ and $N = 3$ are provided in Appendix E.

The displacement field applied to each phase of the composite cylinder assemblage to determine the axial stiffness component (C_{1111}^{eff}) is identical to that used to determine the axial Young's modulus (Eqn. 3.20), and therefore, so too are the nonzero strain and stress components (Eqns. 3.21 and 3.22, respectively). In addition, the matching conditions across each phase boundary are also identical to those used for both the in-plane bulk modulus and axial Young's modulus (Eqn. 3.7). However, the boundary conditions applied are different (Figure 17(c)) and given by:

$$\sigma_{rr}^1|_{r=r_0} = 0 \tag{3.24a}$$

$$u_r^N|_{r=r_N} = 0 \tag{3.24b}$$

Eqn. 3.24a again corresponds to a traction-free internal surface, however, Eqn. 3.24b now corresponds to constraining the external surface of the composite cylinder assemblage and therefore disallowing the Poisson's effect. resulting in a set of $2N$ displacement constants different from the displacement constants determined in both the in-plane bulk and axial Young's modulus boundary value problems. The solutions

for the displacement constants for $N = 2$ and $N = 3$ are provided in Appendix E.

b. Methods for Determining Effective Axial Young's Modulus and Axial Stiffness Component

In the determination of the axial Young's modulus (E_1^{eff}) and stiffness component (C_{1111}^{eff}), only two of the four methods applied in determining the effective in-plane bulk modulus are applicable as a result of the exclusion of fiber end effects by using an infinitely long fiber assumption. Those two methods are methods one and two, the volume averaged property definition and direct energy equivalency approaches, respectively.

Using displacement field of Eqn. 3.20 and the definition of the axial Young's modulus, E_1^{eff} is obtained from the volume averages stress and strain of the composite cylinder assemblage by:

$$E_1^{\text{eff}} = \frac{\langle \sigma_{11} \rangle}{\langle \varepsilon_{11} \rangle} \tag{3.25}$$

where the volume averaged stress, $\langle \sigma_{zz} \rangle$, is given by:

$$\langle \sigma_{zz} \rangle = \frac{2\pi L}{\pi L r_2^2} \left[\sum_{i=1}^{2} \int_{r_{i-1}}^{r_i} \sigma_{zz}^{(i)} r \, dr \right] \tag{3.26}$$

where L is the arbitrary length of the composite cylinder assemblage and where it is noted that there is zero stress in the hollow region of the fiber. The volume averaged strain is similarly calculated as:

$$\langle \varepsilon_{zz} \rangle = \frac{2\pi L}{\pi L r_2^2} \left[\varepsilon_0 \frac{r_0^2}{2} + \sum_{i=1}^{2} \int_{r_{i-1}}^{r_i} \varepsilon_{zz}^{(i)} r \, dr \right] \tag{3.27}$$

where the additional term before the sum acknowledges the non-zero strains in the hollow of the fiber so that $\langle \varepsilon_{zz} \rangle = \varepsilon_0$ is maintained. It can be shown that for isotropic

layers, the effective axial Young's modulus can be expressed as[5]:

$$E_1^{\text{eff}} = \frac{\sum_{i=1}^{N}[(2\mu_i + \lambda_i)\varepsilon_0 + 2\lambda_i D_1^i](r_i^2 - r_{i-1}^2)}{\varepsilon_0 r_N^2} \tag{3.28}$$

Note that because the same displacement field is used for both the axial Young's modulus and stiffness component (i.e., Eqn. 3.20), and because of the similar definition of these two properties, i.e., $C_{11111}^{\text{eff}} = \langle\sigma_{11}\rangle/\langle\varepsilon_{11}\rangle$, the axial stiffness component obtained by definition has the same form as Eqn. 3.28, the only difference being in the values of the D_1^i as a result of the differences in the boundary conditions applied in Eqns. 3.23 and 3.24.

The application of the direct strain energy equivalency of Eqn. 2.22 between the composite cylinder assemblage and the homogeneous effective material of Figure 16 (method two), proceeds with the strain energy of the effective homogeneous material expressed as:

$$W^{\text{eff}} = E_1^{\text{eff}}\varepsilon_0^2 \tag{3.29}$$

The volume averaged strain energy for the composite cylinder assemblage as given by Eqn. 2.17, can be expressed as separate volume integrals over each layer in the composite cylinder assemblage as in Eqn. 3.12 so that effective axial Young's modulus is obtained as:

$$\begin{aligned} E_1^{\text{eff}} = \frac{1}{\varepsilon_0^2 r_N^2}\sum_{i=1}^{N}[(4(\mu_i + \lambda_i)(D_1^i)^2 + 4\lambda_i D_1^i \\ + \frac{4\mu_i}{r_i^2 r_{i-1}^2}(D_2^i)^2 + \varepsilon_0^2(2\mu_i + \lambda_i))(r_i^2 - r_{i-1}^2)] \end{aligned} \tag{3.30}$$

Again, the effective axial stiffness component obtained from the direct strain energy equivalency has the same form as Eqn. 3.30 with different values for the displacement field constants D_1^i and D_2^i.

[5]See Appendix F

3. Composite Cylinder Method for Axial Shear Modulus

a. Displacement, Stress and Strain Fields

The axial shear modulus, μ_{12}^{eff}, is determined through the application of the following displacement field expressed in cylindrical coordinates to each phase of the composite cylinder assemblage

$$\begin{aligned} u_r^i &= 0 \\ u_\theta^i &= 0 \qquad\qquad \text{for } r_{i-1} \le r \le r_i \\ u_z^i &= \left(D_1^i r + D_2^i \frac{1}{r} \right) \cos(\theta) \end{aligned} \tag{3.31}$$

The nonzero strains and stresses are therefore obtained as:

$$\begin{aligned} \varepsilon_{rz}^i &= \frac{1}{2} \left(D_1^i - D_2^i \frac{1}{r^2} \right) \cos(\theta) \\ \varepsilon_{\theta z}^i &= -\frac{1}{2} \left(D_1^i + D_2^i \frac{1}{r^2} \right) \sin(\theta) \end{aligned} \tag{3.32}$$

and (again assuming isotropic phases):

$$\begin{aligned} \sigma_{rz}^i &= \mu_i \left(D_1^i - D_2^i \frac{1}{r^2} \right) \cos(\theta) \\ \sigma_{\theta z}^i &= -\mu_i \left(D_1^i + D_2^i \frac{1}{r^2} \right) \sin(\theta) \end{aligned} \tag{3.33}$$

respectively. The boundary conditions consistent with an axial shear test (Figure 17(d)) are applied to the composite cylinder assemblage as (assuming hollow fiber):

$$\mu_1 \frac{\partial u_z^1}{\partial r}|_{r=r_0} = 0 \tag{3.34a}$$

$$u_z^N|_{r=r_N} = 2\varepsilon_0 r_N \cos(\theta) \tag{3.34b}$$

Eqn. 3.34a imposes that the internal surface be traction-free. The displacement imposed on the external surface in Eqn. 3.34b is consistent with the application of simple

shear. The matching conditions of continuity of tractions and displacements are again applied, but are different in form from those in the previous cases. They are given by:

$$u_z^j|_{r=r_j} = u_z^{j+1}|_{r=r_j} \tag{3.35a}$$

$$\mu_j \frac{\partial u_z^j}{\partial r}|_{r=r_j} = \mu_{j+1} \frac{\partial u_z^{j+1}}{\partial r}|_{r=r_j} \tag{3.35b}$$

where as before, j ranges from one to $N-1$, and again resulting in $2N$ equations to be solved for the $2N$ unknown constants in the displacement fields. The solutions for the displacement constants for $N=2$ and $N=3$ are provided in Appendix E.

b. Methods for Determining the Effective Axial Shear Modulus

Like the effective in-plane bulk modulus, the axial shear modulus (μ_{12}^{eff}) can be determined from each of the four methods presented. In the first method, the definition of the effective axial shear modulus in terms of average shear stress and strain can be alternatively expressed in a statement of equivalent surface tractions between the composite cylinder assemblage and the effective homogeneous cylinder[6], i.e.,

$$\mu_N \frac{\partial u_z^N}{\partial r}|_{r=r_N} = \mu_{12}^{\text{eff}} \frac{\partial u_z^{\text{eff}}}{\partial r}|_{r=r_N} \tag{3.36}$$

which for an isotropic N^{th} layer can be expressed in terms of the displacement constants as:

$$\mu_{12}^{\text{eff}} = \frac{\mu_N \left(D_1^N - D_2^N \frac{1}{r_N^2} \right)}{2\varepsilon_0} \tag{3.37}$$

so that, as was the case for the in-plane bulk modulus, only two of $2N$ composite cylinder displacement field constants need be determined in order to obtain the effective axial shear modulus.

[6]See Appendix F

Applying the direct energy equivalency between the composite cylinder assemblage and the effective material (Eqn. 2.22), volume averaged strain energy of the effective material from Eqn. 2.20 is observed to be given by:

$$W^{\text{eff}} = 4\mu_{12}^{\text{eff}}\varepsilon_0^2 \tag{3.38}$$

so that when equated to the volume averaged strain energy of the composite cylinder assemblage from Eqn. 3.12, the effective axial shear modulus is obtained in terms of the displacement field constants (assuming isotropic layers) as:

$$\mu_{12}^{\text{eff}} = \frac{1}{4\varepsilon_0^2 r_N^2}\sum_{i=1}^{N}\left[\mu_i\left(\left(r_i^2 - r_{i-1}^2\right)(D_1^i)^2 + \left(\frac{1}{r_{i-1}^2} - \frac{1}{r_i^2}\right)(D_2^i)^2\right)\right] \tag{3.39}$$

Similar applications of the interaction energy approaches of methods three and four result in expressions for the effective axial shear modulus of

$$\mu_{12}^{\text{eff}} = \mu_N - \frac{1}{2\varepsilon_0 r_N^2}\left(r_{N-1}^2(\mu_N - \mu_{N-1})D_1^{N-1} + (\mu_N + \mu_{N-1})D_2^{N-1}\right) \tag{3.40}$$

and

$$\mu_{12}^{\text{eff}} = \frac{\mu_N(D_1^N r_N^2 - D_2^N)}{D_1^N r_N^2 + D_2^N} \tag{3.41}$$

respectively, where it is noted that unlike the effective in-plane bulk modulus results, methods one and four for the axial shear modulus result in different expressions, though the numerical applications of both equations are again in excellent agreement.

4. Composite Cylinder Method for In-plane Shear Modulus

a. Displacement, Strain, and Stress Fields

The displacement field applied to the composite cylinders assemblage in order to determine the effective in-plane shear modulus is given by (for isotropic layers)[7]:

$$\begin{aligned} u_r^i &= \left[D_1^i r + D_2^i r^3 \left(\frac{\lambda_i}{3\mu_i + 2\lambda_i} \right) - D_3^i \frac{1}{r^3} + D_4^i \frac{1}{r} \left(\frac{2\mu_i + \lambda_i}{\mu_i} \right) \right] \sin(2\theta) \\ u_\theta^i &= \left[D_1^i r + D_2^i r^3 + D_3^i \frac{1}{r^3} + D_4^i \frac{1}{r} \right] \cos(2\theta) \\ u_z^i &= 0 \qquad\qquad \text{for } r_{i-1} \le r \le r_i \end{aligned} \tag{3.42}$$

The nonzero strains and stresses in the first N layers are obtained as:

$$\begin{aligned} \varepsilon_{rr}^i &= \left[D_1^i + 3 \left(\frac{\lambda_i}{3\mu_i + 2\lambda_i} \right) D_2^i r^2 \right] \sin(2\theta) \\ &\quad + \left[3 D_3^i \frac{1}{r^4} - \left(\frac{2\mu_i + \lambda_i}{\mu_i} \right) D_4^i \frac{1}{r^2} \right] \sin(2\theta) \\ \varepsilon_{\theta\theta}^i &= \left[-D_1^i + \left(\frac{\lambda_i}{3\mu_i + 2\lambda_i} - 2 \right) D_2^i r^2 \right] \sin(2\theta) \\ &\quad + \left[-3 D_3^i \frac{1}{r^4} + \left(\frac{2\mu_i + \lambda_i}{\mu_i} - 2 \right) D_4^i \frac{1}{r^2} \right] \sin(2\theta) \\ \varepsilon_{r\theta}^i &= \left[D_1^i + \left(\frac{\lambda_i}{3\mu_i + 2\lambda_i} + 1 \right) D_2^i r^2 \right] \cos(2\theta) \\ &\quad + \left[-3 D_3^i \frac{1}{r^4} + \left(\frac{2\mu_i + \lambda_i}{\mu_i} \right) D_4^i \frac{1}{r^2} \right] \cos(2\theta) \end{aligned} \tag{3.43}$$

[7]The following displacement field is derived from the method of plane harmonics which Hashin[158] simplified from Love's[211] representation See Section D3 of Appendix D for a summary of the derivation.

and

$$\begin{aligned}
\sigma^i_{rr} &= 2\mu_i \left\{ \left[D^i_1 + 3\left(\frac{\lambda_i}{3\mu_i + 2\lambda_i}\right) D^i_2 r^2 \right] \sin(2\theta) \right\} \\
&\quad + 2\mu_i \left\{ \left[3D^i_3 \frac{1}{r^4} - \left(\frac{2\mu_i + \lambda_i}{\mu_i}\right) D^i_4 \frac{1}{r^2} \right] \sin(2\theta) \right\} \\
&\quad + \lambda_i \left\{ \left[\left(\frac{4\lambda_i}{3\mu_i + 2\lambda_i} - 2\right) D^i_2 r^2 - 2D^i_4 \frac{1}{r^2} \right] \sin(2\theta) \right\} \\
\sigma^i_{\theta\theta} &= 2\mu_i \left\{ \left[-D^i_1 + \left(\frac{\lambda_i}{3\mu_i + 2\lambda_i} - 2\right) D^i_2 r^2 \right] \sin(2\theta) \right\} \\
&\quad + 2\mu_i \left\{ \left[-3D^i_3 \frac{1}{r^4} + \left(\frac{2\mu_i + \lambda_i}{\mu_i} - 2\right) D^i_4 \frac{1}{r^2} \right] \sin(2\theta) \right\} \\
&\quad + \lambda_i \left\{ \left[\left(\frac{4\lambda_i}{3\mu_i + 2\lambda_i} - 2\right) D^i_2 r^2 - 2D^i_4 \frac{1}{r^2} \right] \sin(2\theta) \right\} \\
\sigma^i_{zz} &= \lambda_i \left\{ \left[\left(\frac{4\lambda_i}{3\mu_i + 2\lambda_i} - 2\right) D^i_2 r^2 - 2D^i_4 \frac{1}{r^2} \right] \sin(2\theta) \right\} \\
\sigma^i_{r\theta} &= 2\mu_i \left[D^i_1 + \left(\frac{\lambda_i}{3\mu_i + 2\lambda_i} + 1\right) D^i_2 r^2 \right] \cos(2\theta) \\
&\quad + 2\mu_i \left[-3D^i_3 \frac{1}{r^4} + \left(\frac{2\mu_i + \lambda_i}{\mu_i}\right) D^i_4 \frac{1}{r^2} \right] \cos(2\theta)
\end{aligned} \tag{3.44}$$

The boundary conditions applied in order to determine the in-plane shear modulus (Figure 17(e)) are:

$$\sigma^1_{rr}|_{r=r_0} = 0 \tag{3.45a}$$

$$\sigma^1_{r\theta}|_{r=r_0} = 0 \tag{3.45b}$$

$$u^N_r|_{r=r_N} = \frac{1}{2}\varepsilon_0 r_N \sin 2\theta \tag{3.45c}$$

$$u^N_\theta|_{r=r_N} = \frac{1}{2}\varepsilon_0 r_N \cos 2\theta \tag{3.45d}$$

Eqns. 3.45a and 3.45b correspond to the zero traction condition on the internal surface of assemblage. Taken together, Eqns. 3.45c and 3.45d correspond to the application of pure shear in the plane of symmetry. The matching conditions of continuity of

tractions and displacements provide four additional equations and are given by:

$$u_r^j|_{r=r_j} = u_r^{j+1}|_{r=r_j} \tag{3.46a}$$

$$u_\theta^j|_{r=r_j} = u_\theta^{j+1}|_{r=r_j} \tag{3.46b}$$

$$\sigma_{rr}^j|_{r=r_j} = \sigma_{rr}^{j+1}|_{r=r_j} \tag{3.46c}$$

$$\sigma_{r\theta}^j|_{r=r_j} = \sigma_{r\theta}^{j+1}|_{r=r_j} \tag{3.46d}$$

where j ranges from one to $N-1$ (as N is the outermost layer). This leads to a system of $4N$ unknown constants determined from the $4N$ equations.

b. Methods for Determining the In-plane Shear Modulus

Any of the three energy methods for determining the effective properties can be used to try and determine the effective in-plane shear modulus. However, as observed by Hashin and Rosen [158] , such efforts would identify the upper bound on the effective in-plane shear modulus, with applied traction boundary conditions replacing Eqns. 3.45c and 3.45d resulting in a lower bound (the previous properties, i.e. κ_{23}^{eff}, E_1^{eff}, C_{1111}^{eff}, and μ_{12}^{eff}, produce coincident bounds for applied displacements and tractions). As such, the determination of the effective in-plane shear modulus can not be achieved via the composite cylinders method, therefore the effective in-plane shear modulus is instead obtained using the generalized self-consistent composite cylinders method.

5. Composite Cylinder Method for Additional Effective Properties

a. Axial Poisson's Ratio

The axial Poisson's ratio, ν_{12}^{eff}, can also be obtained from the composite cylinders method from a couple of different approaches. The first, and most direct approach, is

to use the definition of the axial Poisson's ratio in the application of the axial Young's modulus test (Eqns. 3.20 through 3.23), where the axial Poisson's ratio is defined as:

$$\nu_{12}^{\text{eff}} = -\frac{\langle \varepsilon_{22} \rangle}{\langle \varepsilon_{11} \rangle} \tag{3.47}$$

which corresponds to

$$\nu_{12} = \frac{-\langle \varepsilon_{rr} \rangle}{\langle \varepsilon_{zz} \rangle} \tag{3.48}$$

and which can alternatively be expressed in terms of the boundary quantities[8] as:

$$\nu_{12}^{\text{eff}} = -\frac{u_r^N|_{r=r_N}/r_N}{\varepsilon_0} \tag{3.49}$$

so that regardless of whether the N^{th} layer is isotropic or not, the effective axial Poisson's ratio can be determined from:

$$\nu_{12}^{\text{eff}} = -\frac{1}{\varepsilon_0}\left(D_1^N + D_2^N \frac{1}{r_N^2}\right) \tag{3.50}$$

This approach allows two independent effective composite properties to be determined from a single test, and can be used to determine a fifth independent effective property for the effective composite in place the determination of axial stiffness component.

It is of interest, however, to point out that the effective axial Poisson's ratio can not be obtained from an energy equivalency approach directly. The energy equivalency methods as applied to the axial Young's modulus displacement field have already been shown to yield one effective property, the axial Young's modulus as given in Eqn. 3.30. As such, if an energy equivalency approach is desired, the effective axial Poisson's ratio is then obtained as a dependent property from:

$$\nu_{12}^{\text{eff}} = \sqrt{\frac{C_{1111}^{\text{eff}} - E_1^{\text{eff}}}{4\kappa_{23}^{\text{eff}}}} \tag{3.51}$$

[8] See Appendix F

which can be shown to yield the same result as Eqn. 3.50.

b. Transverse Young's Modulus and Poisson's Ratio

Other dependent effective composite properties obtained from the composite cylinders method include the in-plane Young's modulus, E_2^{eff}, obtained as:

$$E_{22}^{\text{eff}} = \frac{4\mu_{23}^{\text{eff}}\kappa_{23}^{\text{eff}}}{\kappa_{23}^{\text{eff}} + \mu_{23}^{\text{eff}} + 4(\nu_{12}^{\text{eff}})^2\mu_{23}^{\text{eff}}\kappa_{23}^{\text{eff}}/E_{11}^{\text{eff}}} \tag{3.52}$$

and the in-plane Poisson's ratio, ν_{23}^{eff}, obtained as:

$$\nu_{23}^{\text{eff}} = \frac{\kappa_{23}^{\text{eff}} - \mu_{23}^{\text{eff}} - 4(\nu_{12}^{\text{eff}})^2\mu_{23}^{\text{eff}}\kappa_{23}^{\text{eff}}/E_{11}^{\text{eff}}}{\kappa_{23}^{\text{eff}} + \mu_{23}^{\text{eff}} + 4(\nu_{12}^{\text{eff}})^2\mu_{23}^{\text{eff}}\kappa_{23}^{\text{eff}}/E_{11}^{\text{eff}}} \tag{3.53}$$

However, as both properties depend on the effective in-plane shear modulus, the composite cylinders method again provides bounds on these properties. As such, the effective in-plane Young's modulus and Poisson's ratio are instead determined using the generalized self-consistent composite cylinders method.

c. Transverse Extension Test

The transverse extension test is an additional boundary value problem used in determining the stress concentration tensor components. It is based on the composite cylinder assemblage of Figure 16 and has a displacement field applied in each of the N layers given by (for isotropic layers):

$$u_r^i = \left[D_1^i\, r + D_2^i\, r^3 + D_3^i \frac{1}{r^3} + D_4^i \frac{1}{r}\right] \cos(2\,\theta) + D_5^i\, r + D_6^i \frac{1}{r} \tag{3.54a}$$

$$u_\theta^i = \left[-D_1^i\, r - D_2^i\, r^3 \left(\frac{(3\,\mu_i + 2\,\lambda_i)}{\lambda_i}\right) + D_3^i \frac{1}{r^3} - D_4^i \frac{1}{r}\left(\frac{\mu_i}{(2\,\mu_i + \lambda_i)}\right)\right] \sin(2\,\theta) \tag{3.54b}$$

$$u_z^i = 0 \tag{3.54c}$$

for $r_{i-1} \leq r \leq r_i$. It is noted that this displacement field is similar to a combination of the displacement fields used to in determining the in-plane bulk modulus (Eqn. 3.2) and the in-plane shear modulus (Eqn. 3.42), with the noted difference being the switching of the trigonometric functions relative to the in-plane shear modulus displacement field. From the displacement field in Eqn. 3.54, the nonzero strains and stresses are obtained as:

$$\varepsilon^i_{rr} = \frac{1}{r^4}\left[\left(D^i_1\, r^4 + 3\, D^i_2\, r^6 - 3\, D^i_3 - D^i_4\, r^2\right)\cos(2\,\theta) + D^i_5\, r^4 - D^i_6\, r^2\right] \tag{3.55a}$$

$$\begin{aligned}\varepsilon^i_{\theta\theta} = &-\left(\frac{1}{r^4\,\lambda_i\,(2\,\mu_i + \lambda_i)}\right)\{[D^i_1\, r^4\,(2\,\lambda_i\,\mu_i + {\lambda_i}^2) + D^i_2\, r^6\,(12\,{\mu_i}^2 + 12\,\mu_i\,\lambda_i + 3\,{\lambda_i}^2)\\ &- D^i_3\,(6\,\lambda_1\,\mu_1 + 3\,{\lambda_1}^2) - {\lambda_1}^2\, D^i_4\, r^2]\cos(2\,\theta) - (2\,\lambda_i\,\mu_i + {\lambda_i}^2)(D^i_5\, r^4 + D^i_6\, r^2)\}\end{aligned} \tag{3.55b}$$

$$\begin{aligned}\varepsilon^i_{r\theta} = &-\frac{1}{r^4\,\lambda_i\,(2\,\mu_i + \lambda_i)}[(2\,r^4\,\lambda_i\,\mu_i + r^4\,\lambda_i^2)D^i_1 + (9\,r^6\,\mu_i\,\lambda_i + 3\,r^6\,\lambda_i^2 + 6\,r^6\,\mu_i^2)D^i_2\\ &+ (3\,\lambda_i^2 + 6\,\lambda_i\,\mu_i)D^i_3 + (\lambda_i\,r^2\,\mu_i + \lambda_i^2\,r^2)D^i_4]\end{aligned} \tag{3.55c}$$

and

$$\begin{aligned}\sigma^i_{rr} = &\frac{2}{r^4\,(2\,\mu_i + \lambda_i)}\{[(2\,r^4\,\mu_i^2 + r^4\,\lambda_i\,\mu_i)D^i_1 - (3\,\lambda_i\,\mu_i + 6\,\mu_i^2)D^i_3\\ &- (2\,r^2\,\mu_i^2 + 2\,\lambda_i\,r^2\,\mu_i)D^i_4]\cos(2\,\theta) + (2\,r^4\,\mu_i^2 + 3\,r^4\,\lambda_i\,\mu_i + r^4\,\lambda_i^2)D^i_5\\ &- (2\,r^2\,\mu_i^2 + \lambda_i\,r^2\,\mu_i)D^i_6\}\end{aligned} \tag{3.56a}$$

$$\begin{aligned}\sigma^i_{\theta\theta} = &\frac{2}{\lambda_i\,r^4}\{[-r^4\,\lambda_i\,\mu_i D^i_1 - (6\,r^6\,\mu_i^2 + 6\,r^6\,\mu_i\,\lambda_i)D^i_2 + 3\,\mu_i\,\lambda_i D^i_3]\cos(2\,\theta)\\ &+ (r^4\,\lambda_i^2 + r^4\,\lambda_i\,\mu_i)D^i_5 + r^2\,\lambda_i\,\mu_i\,D^i_6\}\end{aligned} \tag{3.56b}$$

$$\begin{aligned}\sigma^i_{zz} = &\frac{2}{r^2\,(2\,\mu_i + \lambda_i)}\{[-(3\,r^4\,\lambda_i\,\mu_i + 6\,r^4\,\mu_i^2)D^i_2 - \lambda_i\,\mu_i\,D^i_4]\cos(2\,\theta)\\ &+ (2\,\lambda_i\,r^2\,\mu_i + \lambda_i^2\,r^2)D^i_5\}\end{aligned} \tag{3.56c}$$

$$\sigma^i_{r\theta} = -\frac{2\,\mu_i}{r^4\,\lambda_i\,(2\,\mu_i+\lambda_i)}[(2\,r^4\,\lambda_i\,\mu_i + r^4\,\lambda_i^2)D_1^i + (9\,r^6\,\mu_i\,\lambda_i + 3\,r^6\,\lambda_i^2 + 6\,r^6\,\mu_i^2)D_2^i$$
$$+ (3\,\lambda_i^2 + 6\,\lambda_i\,\mu_i)D_3^i + (\mu_i\,\lambda_i\,r^2 + r^2\,\lambda_i^2)D_4^i]\sin(2\,\theta) \tag{3.56d}$$

The boundary conditions applied in order in the transverse extension test (Figure 17(f)) are:

$$\sigma^1_{rr}|_{r=r_0} = 0 \tag{3.57a}$$

$$\sigma^1_{r\theta}|_{r=r_0} = 0 \tag{3.57b}$$

$$u^N_r|_{r=r_N} = \frac{r_N\varepsilon_0}{2}(1+\cos(2\,\theta)) \tag{3.57c}$$

$$u^N_\theta|_{r=r_N} = -\frac{r_N\varepsilon_0}{2}\sin(2\,\theta) \tag{3.57d}$$

Eqns. 3.57a and 3.57b correspond to the internal surface of the assemblage being traction-free. Eqns. 3.57c and 3.57d combined correspond to a homogeneous x_2 normal strain. The matching conditions of continuity of tractions and displacements involve four additional equations and are given by:

$$u^j_r|_{r=r_j} = u^{j+1}_r|_{r=r_j} \tag{3.58a}$$

$$u^j_\theta|_{r=r_j} = u^{j+1}_\theta|_{r=r_j} \tag{3.58b}$$

$$\sigma^j_{rr}|_{r=r_j} = \sigma^{j+1}_{rr}|_{r=r_j} \tag{3.58c}$$

$$\sigma^j_{r\theta}|_{r=r_j} = \sigma^{j+1}_{r\theta}|_{r=r_j} \tag{3.58d}$$

where j ranges from one to $(N-1)$. Application of the boundary and matching conditions results in $6N$ equations to solve for the $6N$ unknowns. The solutions for the displacement constants for $N=2$ are provided in Appendix E.

B. The Multi-Layered Generalized Self-Consistent Composite Cylinders Method for Elastic Properties

As an alternative to the bounds predicted for the in-plane shear modulus using the composite cylinders method, the approach taken for determining the effective in-plane shear modulus (μ_{23}^{eff}) involves the use of the generalized self-consistent composite cylinder of Christensen and Lo[159]. Here the entire composite cylinder assemblage in Figure 16(a) is is embedded in a $(N+1)^{th}$ layer whose material properties are the same as the material properties of the effective solid homogeneous material of Figure 16(b). This generalized self-consistent composite cylinder assemblage is shown in Figure 18. The effective in-plane shear modulus of the composite cylinder assemblage is determined through the use of the energy equivalence between the generalized self-consistent composite cylinder assemblage and a homogeneous solid effective cylinder.

1. Generalized Self-Consistent Composite Cylinder Method for In-plane Shear Modulus

a. Displacement, Strain and Stress Fields

The displacement field applied in the first N layers, i.e. $i \leq N$, of the generalized self-consistent composite cylinder assemblage in order to determine the effective in-plane shear modulus is given by Eqn. 3.42 (assuming isotropic layers). For the transversely isotropic effective material in the $(N+1)^{th}$ layer, the displacement field is given by:

$$\begin{aligned}
u_r^{N+1} &= -\left(\frac{r_{N+1}}{4\mu_{23}^{\text{eff}}}\right)\left[\frac{2r}{r_{N+1}} + D_3^{N+1}\frac{r_{N+1}^3}{r^3} + (\eta^{\text{eff}}+1)D_4^{N+1}\frac{r_{N+1}}{r}\right]\sin(2\theta) \\
u_\theta^{N+1} &= \left(\frac{r_{N+1}}{4\mu_{23}^{\text{eff}}}\right)\left[-\frac{2r}{r_{N+1}} + D_3^{N+1}\frac{r_{N+1}^3}{r^3} - (\eta^{\text{eff}}-1)D_4^{N+1}\frac{r_{N+1}}{r}\right]\cos(2\theta) \qquad (3.59) \\
u_z^{N+1} &= 0 \qquad \text{for } r_N \leq r \leq r_{N+1}
\end{aligned}$$

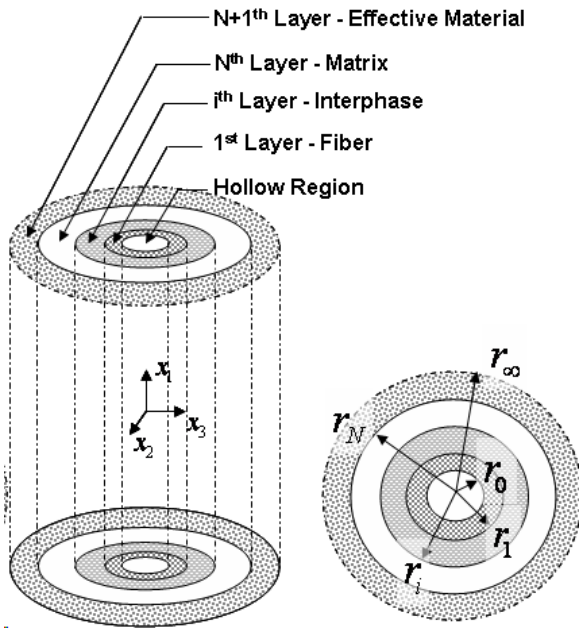

Fig. 18. General schematic of a N-layer generalized self-consistent composite cylinder assemblage. Here the composite cylinder assemblage of Figure 16(a) is seen to be enveloped by an additional layer (the $(N+1)^{\text{th}}$ layer) which can be taken as extending to infinity and to have the effective constitutive properties of the composite.

where it should be noted that $\eta^{\text{eff}} = 3 - 4\nu_{23}^{\text{eff}}$ and that ν_{23}^{eff} and μ_{23}^{eff} are the effective in-plane Poisson's ratio and shear modulus of the composite cylinder assemblage. The nonzero strains and stresses in the first N layers are again the same as those identified for the composite cylinder assemblage in Eqns. 3.43 and 3.44, respectively. For the $(N+1)^{\text{th}}$ layer, the strains and stresses are obtained as:

$$\begin{aligned}
\varepsilon_{rr}^{N+1} &= -\left[\frac{r_{N+1}}{4\mu_{23}^{\text{eff}}}\frac{2}{r_{N+1}} - 3D_3^{N+1}\frac{r_{N+1}^3}{r^4} - \left(\eta^{\text{eff}}+1\right)D_4^{N+1}\frac{r_{N+1}}{r^2}\right]\sin(2\theta) \\
\varepsilon_{\theta\theta}^{N+1} &= -\left[-\frac{r_{N+1}}{4\mu_{23}^{\text{eff}}}\frac{2}{r_{N+1}} + 3D_3^{N+1}\frac{r_{N+1}^3}{r^4} + \left(-\eta^{\text{eff}}+3\right)D_4^{N+1}\frac{r_{N+1}}{r^2}\right]\sin(2\theta) \\
\varepsilon_{r\theta}^{N+1} &= -\left[\frac{r_{N+1}}{4\mu_{23}^{\text{eff}}}\frac{2}{r_{N+1}} - 3D_3^{N+1}\frac{r_{N+1}^3}{r^4} + \left(\eta^{\text{eff}}+1\right)D_4^{N+1}\frac{r_{N+1}}{r^2}\right]\cos(2\theta)
\end{aligned} \tag{3.60}$$

and

$$\begin{aligned}
\sigma_{rr}^{N+1} &= \left(\kappa_{23}^{\text{eff}} + \mu_{23}^{\text{eff}}\right)\varepsilon_{rr}^{N+1} + \left(\kappa_{23}^{\text{eff}} - \mu_{23}^{\text{eff}}\right)\varepsilon_{\theta\theta}^{N+1} \\
\sigma_{\theta\theta}^{N+1} &= \left(\kappa_{23}^{\text{eff}} - \mu_{23}^{\text{eff}}\right)\varepsilon_{rr}^{N+1} + \left(\kappa_{23}^{\text{eff}} + \mu_{23}^{\text{eff}}\right)\varepsilon_{\theta\theta}^{N+1} \\
\sigma_{zz}^{N+1} &= \left(2\kappa_{23}^{\text{eff}}\nu_{12}^{\text{eff}}\right)\left(\varepsilon_{rr}^{N+1} + \varepsilon_{\theta\theta}^{N+1}\right) \\
\sigma_{r\theta}^{N+1} &= 2\mu_{23}^{\text{eff}}\varepsilon_{r\theta}^{N+1}
\end{aligned} \tag{3.61}$$

where ν_{12}^{eff} is the effective axial Poisson's ratio of the composite. The boundary and matching conditions applied in order to determine the in-plane shear modulus are similar to those provided for the composite cylinder assemblage in Eqns. 3.45 and 3.46; the only notable differences being that the displacement field for the generalized self-consistent composite cylinder in Eqn. 3.59 has already had the external boundary conditions applied to the $(N+1)^{\text{th}}$ layer (as noted by lack of D_1^{N+1} and D_2^{N+1} in Eqn 3.59), and that j ranges from one to N (as $N+1$ is the outermost layer). As observed from Eqn. 3.46, the effective properties contained in the $(N+1)^{\text{th}}$ layer displacement field in Eqn. 3.59 results in all of the $4N+2$ unknown constants determined from the $4N+2$ equations containing the effective properties of the composite.

The displacement constants for the $N = 2$ case are given in Appendix E where it is observed that there is a lengthy amount of algebra associated even with this the simplest of cases.

b. Method for Determining the Transverse Shear Modulus

Unlike the previous properties discussed, the in-plane shear modulus is obtained from the generalized self-consistent composite cylinder assemblage of Figure 18 using the generalized self-consistent method outlined in Eqns. 2.167 and 2.168. The internal surface, S_i, is taken to be between the N^{th} and $(N+1)^{\text{th}}$ layers of the generalized self consistent composite cylinder assemblage so that the interaction energy equation resulting from the strain energy equivalency (Eqn. 2.168) can be expressed as:

$$\int_0^{2\pi} \left[\sigma_{rr}^{N+1} u_r^{\text{eff}} + \sigma_{r\theta}^{N+1} u_\theta^{\text{eff}} - \left(\sigma_{rr}^{\text{eff}} u_r^{N+1} + \sigma_{r\theta}^{\text{eff}} u_\theta^{N+1}\right)\right]_{r=r_N} d\theta = 0 \tag{3.62}$$

where, by continuity of displacement and traction conditions of Eqns. 3.46c and 3.46d, the N^{th} stresses and displacements of the generalized self-consistent composite cylinder assemblage have been replaced by the $(N+1)^{\text{th}}$, and where the displacement field for the effective homogeneous material is given by:

$$\begin{aligned} u_r^{\text{eff}} &= \left(\frac{r_{N+1}}{4\mu_{23}^{\text{eff}}}\right)\left(\frac{2}{r_{N+1}} r\right)\sin(2\theta) \\ u_\theta^{\text{eff}} &= \left(\frac{-r_{N+1}}{4\mu_{23}^{\text{eff}}}\right)\left(-\frac{2}{r_{N+1}} r\right)\cos(2\theta) \qquad \text{for } 0 \le r \le r_{N+1} \\ u_z^{\text{eff}} &= 0 \end{aligned} \tag{3.63}$$

where it is noted that there are no displacement constants in Eqn. 3.63 like there are in Eqn. 3.59 for the $(N+1)^{\text{th}}$ layer as a result of the constraint that the displacement field in the effective homogeneous material be bounded at the origin. This emphasizes the point that despite having the same constitutive properties, displacement fields of

the $(N+1)^{\text{th}}$ layer and of the effective homogeneous material are different as was the case in the application of method three for the in-plane bulk modulus for the N^{th} layer and the homogeneous matrix material.

Substituting the displacements and stresses into Eqn. 3.62 leads to the condition that $(N+1)^{\text{th}}$ displacement field constant D_4^{N+1} (Eqn. 3.59) should be identically zero. As a result of solving the system of the boundary and matching conditions for the generalized self-consistent composite cylinder assembalge, D_4^{N+1} is in terms of all of the geometric and constitutive parameters of the generalized self-consistent composite cylinder assemblage (i.e., the r_i, the μ_i and λ_i, and the effective properties μ_{23}^{eff}). Thus, μ_{23}^{eff} is then obtained by setting:

$$D_4^{N+1} = 0 \tag{3.64}$$

and solving for μ_{23}^{eff}. It should be noted that the algebra involved in obtaining D_4^{N+1}, and indeed the other displacement field constants in the generalized self-consistent composite cylinders assemblage for in-plane shear conditions, in terms of the unknown effective properties is quite intensive (see Appendix E and as such, Cramer's rule is recommended in order to solve only for the needed expression of D_4^{N+1}.

It is also of interest to point out that the displacement field for the $(N+1)^{\text{th}}$ layer of the generalized self-consistent composite cylinder assemblage provided in Eqn. 3.59 does not initially satisfy equilibrium. However, when D_4^{N+1} is observed to be zero in order to satisfy the interaction energy being zero (Eqn. 3.64), the equilibrium equation for the $(N+1)^{\text{th}}$ is satisfied as well. For comparison purposes, the displacement field

for the $(N+1)^{\text{th}}$ layer which does satisfy equilibrium a priori is given by

$$\begin{aligned} u_r^{N+1} &= \left(\varepsilon_0 r - D_3^{N+1} r^{-3} + \frac{\left(\mu_{23}^{\text{eff}} + \kappa_{23}^{\text{eff}}\right)}{\mu_{23}^{\text{eff}}} D_4^{N+1} r^{-1} \right) \sin(2\theta) \\ u_\theta^{N+1} &= \left(\varepsilon_0 r + D_3^{N+1} r^{-3} + D_4^{N+1} r^{-1} \right) \cos(2\theta) \\ u_z^{N+1} &= 0 \qquad\qquad \text{for } r_N \leq r \leq r_{N+1} \end{aligned} \tag{3.65}$$

As an alternative approach, one could use the displacement field in Eqn. 3.65 in place of the displacement field in Eqn. 3.59 for the $(N+1)^{\text{th}}$ layer of the generalized self-consistent composite cylinder assemblage. However, the approach to obtaining the effective properties would be different, perhaps using the direct energy equivalency as opposed to the interaction energy, and may therefore require the solution of all of the displacement constants.

Finally, it is noted that the in-plane shear modulus obtained from Eqn. 3.64 is the same for both displacement and traction boundary conditions (noting the different form of Eqn. 3.62 for traction boundary conditions). As such, one could obtain the effective elastic properties of the fiber reinforced composites using a combination of the composite cylinders and generalized self-consistent composite cylinder methods, and many have [165, 166, 168].

2. Generalized Self-Consistent Composite Cylinder Method for In-plane Bulk Modulus, Axial Young's Modulus, Axial Stiffness Component, and Axial Shear Modulus

As described above, the composite cylinders method consists of a combination of the use of the composite cylinder assemblage of Figure 16 and the generalized self-consistent composite cylinder assemblage of Figure 18 in determining the effective composite properties; an observation particularly poignant for the dependent prop-

erties provided in Eqns. 3.52 and 3.53. However in addition to the effective in-plane shear modulus, μ_{23}^{eff}, the generalized self-consistent composite cylinder assemblage can in fact be used in a unified approach to determine the other independent effective composite properties, i.e., the in-plane bulk modulus (κ_{23}^{eff}), the axial Young's modulus (E_1^{eff}), the axial stiffness component (C_{1111}^{eff}), and the axial shear modulus (μ_{12}^{eff}).

In fact, the functional form for the displacement field in the composite cylinders method for each of these properties is the same for $(N+1)^{\text{th}}$ layer (with D_j^i replaced by D_j^{N+1}), with the external boundary conditions shifted to the $(N+1)^{\text{th}}$ layer surface at r_{N+1} and the matching conditions between the N^{th} and the $(N+1)^{\text{th}}$ layers enforced. In these cases, the preferred methods for determining the effective properties are the energy equivalency approaches (Methods 2 and 3), as the boundary for the $(N+1)^{\text{th}}$ layer can be taken to be at infinity.

For example, application of the general energy equivalency ($W^{\text{eff}} = W^{\text{RVE}}$) for the axial Young's modulus (for N isotropic layers) results in

$$\begin{aligned} E_1^{\text{eff}}\varepsilon_0^2 = {} & \frac{1}{r_{N+1}^2}\sum_{i=1}^{N}\left[(r_i^2 - r_{i-1}^2)\left(4(\mu_i+\lambda_i)(D_1^i)^2 + 4\varepsilon_0\lambda_i D_1^i + (2\mu_i+\lambda_i)\varepsilon_0^2\right)\right] \\ & + \frac{1}{r_{N+1}^2}\sum_{i=1}^{N}\left[\frac{(r_i^2 - r_{i-1}^2)}{r_i^2 r_{i-1}^2}\left(4\mu_i(D_2^i)^2\right)\right] + \frac{4\mu_{23}^{\text{eff}}(r_{N+1}^2 - r_N^2)}{r_{N+1}^4 r_N^2}(D_2^{N+1})^2 \\ & + \frac{r_{N+1}^2 - r_N^2}{r_{N+1}^2}[4\kappa_{23}^{\text{eff}}(D_1^{N+1})^2 + 8\kappa_{23}^{\text{eff}}\nu_{12}^{\text{eff}}\varepsilon_0 D_1^{N+1} + (E_1^{\text{eff}} + 4\kappa_{23}^{\text{eff}}(\nu_{12}^{\text{eff}})^2)\varepsilon_0^2] \end{aligned} \tag{3.66}$$

where it is noted from Eqn. 3.66 that not only are some of the properties coupled (E_1^{eff} depending on κ_{23}^{eff} and ν_{12}^{eff}), but they are also nonlinear. Recall, that as discussed in the determination of the in-plane shear modulus, the generalized self-consistent approach results in the displacement constants in each layer of the generalized self-consistent composite cylinder assemblage being functions of the effective properties (i.e., the D_j^i depend on κ_{23}^{eff}), and in Eqn. 3.66, these displacement constants are squared and

in some cases are directly multiplying the effective properties. As such, an iterative technique is applied in the simultaneous solution of the effective composite properties in the unified generalized self-consistent composite cylinders method.

It is of interest to note, however, that this simultaneous iterative solution leads to effective properties which are in very good agreement with the effective composite properties obtained from the composite cylinder method as previously discussed (i.e., E_1^{eff} obtained from the simultaneous iterative solution of Eqn. 3.66 agrees with the results of Eqns. 3.28 and 3.30 to within 0.001% difference). This should in fact be the case as the results for the bounds on all but the effective in-plane shear modulus obtained from the composite cylinders solutions by Hashin and Rosen [158] were coincident. As such, from this point on when referring to the generalized self-consistent composite cylinder method, it will be understood that for the axial Young's modulus and stiffness component, the in-plane bulk modulus, and the axial shear modulus, the composite cylinders solution is used while for the in-plane shear modulus, the generalized self-consistent composite cylinder solution is used. It is also noted that it is this good agreement between the composite cylinders and generalized self-consistent composite cylinders approaches which makes the approximate method provided in Method 4 a good approximation.

C. Generalized Self-Consistent Composite Cylinders Method with Continuous Graded Interphase Regions

Further attempts at more accurately representing the interphase region could take the form of a continuous gradation in properties. The solution for such a region necessitates the identification of a solution for the displacement field in the graded interphase region as the equilibrium equations contain additional terms as compared

to the piecewise constant interphases. Exact solutions for the displacement field, if attainable depend on the functional form of the graded interphase properties. Once the displacement field satisfying the equilibrium equation is obtained, the remainder of the composite cylinder approach remains unchanged, i.e., the volume averaged strain energy of the composite cylinder assemblage is equated to that of the homogeneous solid. As such, here we provide only the needed displacement fields for use in the generalized self-consistent composite cylinders method. A summary of the derivation of the displacement field similar to the one provided by Jayaraman and Reifsnider [167] is provided for the in-plane bulk modulus.

First, we note in general, that, if the displacement field and material properties in a continuum are spatially varying, that the strain-displacement relations and constitutive relations of Eqns. 2.7 and 2.8, respectively remain unchanged. However, assuming that there are no body forces or inertial effects, recall that the equilibrium equation in Eqn. 2.6 can be expressed as

$$C_{ijkl,j}\,\varepsilon_{kl} + C_{ijkl}\,\varepsilon_{kl,j} = 0 \tag{3.67}$$

where for non-functionally graded materials, $C_{ijkl,j}$ is identically zero so that for isotropic materials, and by using the strain-displacement relations, Eqn. 3.67 reduces to the familiar Lamé-Navier equations. For functionally graded materials, Eqn. 3.67 indicates that displacement field solutions will be dependent on the functional form of the material property gradation.

For example, consider the case where the displacement field in cylindrical coordinates has only a nonzero radial component which is assumed to be a function of r only, i.e. $u_r = U_r(r)$, as in the in-plane bulk test of Eqn. 3.2. The nonzero strain

components are therefore given by

$$\begin{aligned} \varepsilon_{rr} &= \frac{\partial u_r}{\partial r} = \frac{d U_r}{d r} \\ \varepsilon_{\theta\theta} &= \frac{1}{r}\frac{\partial u_\theta}{\partial \theta} + \frac{u_r}{r} = \frac{1}{r}U_r \end{aligned} \tag{3.68}$$

where U_r is the unknown radial displacement component function. The nonzero stresses for an isotropic material symmetry are therefore given by

$$\begin{aligned} \sigma_{rr} &= (2\mu + \lambda)\frac{d U_r}{d r} + \lambda\frac{1}{r}U_r \\ \sigma_{\theta\theta} &= (2\mu + \lambda)\frac{1}{r}U_r + \lambda\frac{d U_r}{d r} \\ \sigma_{zz} &= \lambda\left(\frac{d U_r}{d r} + \frac{1}{r}U_r\right) \end{aligned} \tag{3.69}$$

where, though appearing identical to the equations used in determining the functional form of the stress field in Eqn. 3.5, the difference is that in Eqn. 3.69, μ and λ are not constant. In fact, if μ and λ are taken to be functions of r, then the equilibrium equations in cylindrical coordinates, i.e. Eqn. 3.1, reduce to

$$\left(2\frac{d\mu}{d r} + \frac{d\lambda}{d r}\right)\frac{dU_r}{d r} + \frac{d\lambda}{d r}\frac{1}{r}U_r + (2\mu + \lambda)\left[\frac{d^2U_r}{d r^2} + \frac{1}{r}\frac{dU_r}{d r} - \frac{1}{r^2}U_r\right] = 0 \tag{3.70}$$

Further, if the Young's modulus is taken to be a function of r and the Poisson's ratio a constant, the derivatives of the Lamé constants can be expressed as

$$\frac{d\mu}{d r} = \frac{1}{2(1+\nu)}\frac{dE}{d r} \tag{3.71a}$$

$$\frac{d\lambda}{d r} = \frac{\nu}{(1+\nu)(1-2\nu)}\frac{dE}{d r} \tag{3.71b}$$

so that the nontrivial equilibrium equation becomes

$$\frac{dE}{d r}\frac{dU_r}{d r} + \frac{\nu}{1-\nu}\frac{dE}{d r}\frac{1}{r}U_r + E\frac{d^2U_r}{dr^2} + \frac{E}{r}\frac{dU_r}{d r} - \frac{E}{r^2}U_r = 0 \tag{3.72}$$

It should be noted that $E(r)$ is considered to be a known functional variation of

the Young's modulus so that the only unknown in Eqn. 3.72 is $U_r(r)$. Assuming that the functional form of $E(r)$ can be represented by a polynomial series, i.e., that $E(r) = \sum_{p=m}^{n} \xi_p \, r^p$, we obtain from Eqn. 3.72 the following differential equation for U_r:

$$\frac{d^2U_r}{d\,r^2} + \left(\frac{\sum_{p=m}^{n} (p+1)\,\xi_p \, r^{(p-1)}}{\sum_{p=m}^{n} \xi_p \, r^p} \right) \frac{dU_r}{d\,r} + \left(\frac{\sum_{p=m}^{n} \left(\frac{p\,\nu}{1-\nu} - 1 \right) \xi_p \, r^{(p-2)}}{\sum_{p=m}^{n} \xi_p \, r^p} \right) U_r = 0 \quad (3.73)$$

where the ξ_p are constants and where m and n are real numbers. For reasons which will be discussed below, attempts at obtaining analytic solutions for $U_r(r)$ for $m \neq n$ were unsuccessful. However, for $m = n$, i.e., for $E(r)$ equal to any monomial, the differential equation in Eqn. 3.73 reduces to:

$$\frac{d^2U_r}{d\,r^2} + (n+1)\,\frac{1}{r}\,\frac{dU_r}{d\,r} + \left(\frac{n\,\nu}{1-\nu} - 1 \right) \frac{1}{r^2}\,U_r = 0 \quad (3.74)$$

which has an exact solution given by:

$$U_r(r) = c_1\, r^{\left(\frac{1}{2}\,\left(\frac{n - n\,\nu + \gamma}{\nu - 1} \right) \right)} + c_2\, r^{\left(\frac{1}{2}\,\left(\frac{n - n\,\nu - \gamma}{\nu - 1} \right) \right)} \quad (3.75)$$

where c_1 and c_2 are integration constants to be determined by the boundary and/or matching conditions and where

$$\gamma = \sqrt{(\nu - 1)[\nu(n+2)^2 - (n^2+4)]} \quad (3.76)$$

Note that for Poisson's ratios between -1 and 0.5 that γ is real, with $\gamma = 0$ only when $\nu = 0.5$ and $n = 2$. Note also that for n = 0 the radial displacement function provided in Eqn 3.2 for the in-plane bulk test is obtained, i.e., $u_r(r) = c_1\, r + c_2\, r^{-1}$. In fact, it is the substitution of this radial displacement summed with the radial displacement of Eqn. 3.75 for $n \neq 0$ into Eqn. 3.73 which produces a residual and indicates the

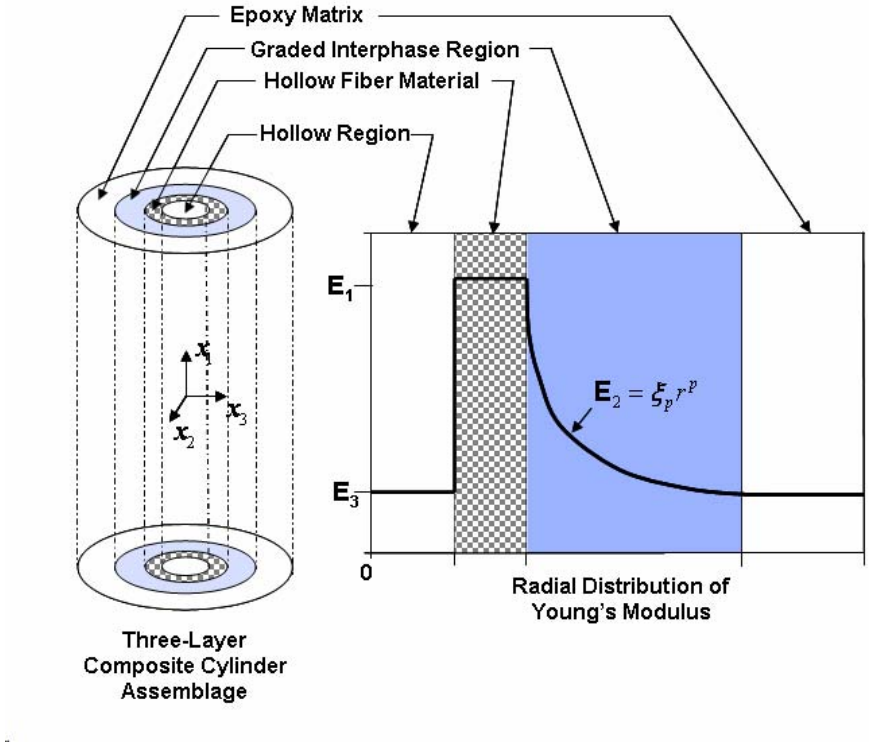

Fig. 19. General schematic of a three layer composite cylinder assemblage where the interphase region (layer two) consists of a functionally graded material.

need for approximate or series solutions[167–169] for such variations of $E(r)$. The same is true for the sum of any two values for n.

For example, in determining the effective in-plane bulk modulus for a three layer composite cylinder assemblage like the one shown in Figure 19, i.e., $N = 3$, Eqn. 3.2 is used to define the displacement field in layers one and three, with the displacement field for layer 2 given by Eqn. 3.75 with $u_\theta^2 = u_z^2 = 0$ assuming for layer two that $E_2(r) = \xi_n\, r^n$ and ν_2 is a constant. As such, the nonzero strains and stresses in layers one and three are given by Eqns. 3.4 and 3.5, respectively. For the graded interphase

layer, the nonzero strains and stresses are given by:

$$\begin{aligned} \varepsilon_{rr}^{2} &= c_1 \varrho_1 r^{\varrho_1 - 1} + c_2 \varrho_2 r^{\varrho_2 - 1} \\ \varepsilon_{\theta\theta}^{2} &= c_1 r^{\varrho_1 - 1} + c_2 r^{\varrho_2 - 1} \end{aligned} \tag{3.77}$$

and

$$\begin{aligned} \sigma_{rr}^{2} &= \frac{\xi_n \, r^n}{(1+\nu_2)(1-2\nu_2)} \left[c_1 r^{\varrho_1 - 1} \left((1-\nu_2)\varrho_1 + \nu_2 \right) + c_2 r^{\varrho_2 - 1} \left((1-\nu_2)\varrho_2 + \nu_2 \right) \right] \\ \sigma_{\theta\theta}^{2} &= \frac{\xi_n \, r^n}{(1+\nu_2)(1-2\nu_2)} \left[c_1 r^{\varrho_1 - 1} \left((1-\nu_2) + \nu_2 \varrho_1 \right) + c_2 r^{\varrho_2 - 1} \left((1-\nu_2) + \nu_2 \varrho_2 \right) \right] \\ \sigma_{zz}^{2} &= \frac{\nu_2 \, \xi_n \, r^n}{(1+\nu_2)(1-2\nu_2)} \left[c_1 r^{\varrho_1 - 1} \left(\varrho_1 + 1 \right) + c_2 r^{\varrho_2 - 1} \left(\varrho_2 + 1 \right) \right] \end{aligned} \tag{3.78}$$

respectively, where ϱ_1 and ϱ_2 are given by:

$$\begin{aligned} \varrho_1 &= \frac{1}{2} \left(\frac{n - n\,\nu_2 + \gamma_2}{\nu_2 - 1} \right) \\ \varrho_2 &= \frac{1}{2} \left(\frac{n - n\,\nu_2 - \gamma_2}{\nu_2 - 1} \right) \end{aligned} \tag{3.79}$$

where n is any real number and where γ_2 is given by Eqn. 3.76 with ν replaced by ν_2. The displacement field constants, D_1^1, D_2^1, c_1, c_2, D_1^3, and D_2^3 are determined from the same set of boundary and matching conditions provided in Eqns. 3.6 and 3.7, respectively, and are provided in Section E3 of Appendix E. The effective in-plane bulk modulus is then determined by any one of the four methods provided in Eqns. 3.8, 3.12, 3.17, and 3.19, where it should be noted that the functional forms of Eqns. 3.10, 3.13, and 3.18 where the effective in-plane bulk modulus is provided in terms of the displacement field constants must be suitably adjusted to account for the influence of the graded interphase. The equilibrium equations for the remaining independent effective properties result in displacement fields provided in Appendix G

D. The Multi-Layered Generalized Self-Consistent Composite Cylinders Method for Conductivities

From the electrical and thermal equilibrium equations, Eqns. 2.36 and 2.51, respectively, and assuming homogeneous orthotropic materials, in cylindrical coordinates we may write

$$\check{\sigma}_{rr}\frac{\partial^2\phi}{\partial r^2}+\check{\sigma}_{\theta\theta}\left(\frac{1}{r^2}\frac{\partial^2\phi}{\partial\theta^2}+\frac{1}{r}\frac{\partial\phi}{\partial r}\right)+\check{\sigma}_{zz}\frac{\partial^2\phi}{\partial z^2}=0 \tag{3.80a}$$

$$k_{rr}\frac{\partial^2\phi}{\partial r^2}+k_{\theta\theta}\left(\frac{1}{r^2}\frac{\partial^2\phi}{\partial\theta^2}+\frac{1}{r}\frac{\partial\phi}{\partial r}\right)+k_{zz}\frac{\partial^2\phi}{\partial z^2}=0 \tag{3.80b}$$

As these equations are of the same form, we will continue the discussion using the electrical equations. Therefore, if one further assumes that the material is transversely isotropic ($\check{\sigma}_{rr}=\check{\sigma}_{\theta\theta}=\check{\sigma}_T$ and $\check{\sigma}_{zz}=\check{\sigma}_A$) and considers the cases of conduction in the axial direction ($\phi=\phi(z)$) and transverse conduction ($\phi=\phi(x)\Rightarrow\phi=\phi(r,\theta)$), Eqn. 3.80a reduces to

$$\check{\sigma}_A\frac{\partial^2\phi}{\partial z^2}=0 \tag{3.81}$$

and, assuming the potential is separable, i.e. $\phi(r,\theta)=\Gamma(r)\Upsilon(\theta)$,

$$\check{\sigma}_T\frac{\partial^2\Gamma}{\partial r^2}\Upsilon+\check{\sigma}_T\left(\frac{1}{r^2}\frac{\partial^2\Upsilon}{\partial\theta^2}\Gamma+\frac{1}{r}\frac{\partial\Gamma}{\partial r}\Upsilon\right)=0 \tag{3.82}$$

respectively. Eqns. 3.81 and 3.82 have solutions

$$\phi=Az+B \tag{3.83}$$

and

$$\phi=\left(Ar+\frac{1}{r}B\right)\cos(\theta) \tag{3.84}$$

respectively, where A and B are constants to be determined from boundary and/or interface conditions. These solutions will be applicable in both homogeneous cylinders and in each phase of the composite cylinders assemblages.

1. Generalized Self-Consistent Composite Cylinders Method for Axial Conductivity

As with the elastic properties, the composite cylinder method establishes an energy equivalency between an effective homogeneous material and a composite cylinder assemblage consisting of N concentric circular cylinders, as was shown schematically in Figure 16

In order to determine the effective axial conductivity, the homogeneous cylinder (Figure 16(b)) is taken to have the potential

$$\phi^{(\text{eff})} = D_1^{(\text{eff})} z + D_2^{(\text{eff})} \tag{3.85}$$

and is subject to the boundary conditions

$$\phi^{(\text{eff})}(z = -\frac{L}{2}) = \phi_0 \tag{3.86a}$$

$$\phi^{(\text{eff})}(z = \frac{L}{2}) = \phi_0 + \Delta\phi \tag{3.86b}$$

resulting in

$$D_1^{(\text{eff})} = \frac{\Delta\phi}{L} \tag{3.87a}$$

$$D_2^{(\text{eff})} = \phi_0 + \frac{\Delta\phi}{2} \tag{3.87b}$$

Thus the nonzero electric field component in the effective homogeneous material is determined to be

$$E_z^{(\text{eff})} = -\frac{\Delta\phi}{L} \tag{3.88}$$

so that the nonzero flux component is then given by

$$J_z^{(\text{eff})} = -\check{\sigma}_A \frac{\Delta\phi}{L} \tag{3.89}$$

and finally the energy density as defined in Eqn. 2.39a is used to obtain the total

volume averaged energy of the effective homogeneous cylinder as

$$W^{(\text{eff})} = \langle w^{(\text{eff})} \rangle = \frac{\check{\sigma}_A}{2} \left(\frac{\Delta\phi}{L} \right)^2 \tag{3.90}$$

The composite cylinder assemblage is used to determine the effective axial conductivity consists of N concentric cylinders or phases (Figure 16(a)), each of which is assumed to have isotropic material symmetry and has a potential of the form

$$\phi^{(i)} = D_1^{(i)} z + D_2^{(i)} \qquad \text{for } r_{i-1} \leq r \leq r_i \tag{3.91}$$

where i ranges from one to N, and where $r_0 \neq 0$ denotes a hollow fiber. Thus the nonzero electric field component in each phase is determined to be

$$E_z^{(i)} = -D_1^{(i)} \tag{3.92}$$

so that the nonzero flux component is then given by

$$J_z^{(i)} = -\check{\sigma}^{(i)} D_1^{(i)} \tag{3.93}$$

and finally the energy density of each phase is identified as

$$w^{(i)} = \frac{1}{2} \sigma^{(i)} \left(D_1^{(i)} \right)^2 \tag{3.94}$$

is used to obtain the total volume averaged energy of the composite cylinder assemblage as

$$W^{(\text{comp})} = \frac{1}{V} \left(\sum_{i=1}^{N} \int_{V_i} w^{(i)} dV \right) = \frac{1}{2r_N^2} \sum_{i=1}^{N} \check{\sigma}^{(i)} \left(D_1^{(i)} \right)^2 (r_i^2 - r_{i-1}^2) \tag{3.95}$$

The composite cylinder assemblage is subjected to the same boundary conditions as provided in Eqn. 3.86, and, since there is no radial flux component, the interface conditions are automatically satisfied so that the phase constants can be easily expressed

as

$$D_1^{(i)} = \frac{\Delta\phi}{L} \tag{3.96a}$$

$$D_2^{(i)} = \phi_0 + \frac{\Delta\phi}{2} \tag{3.96b}$$

Thus, the energy equivalency between the effective homogeneous cylinder and the composite cylinder assemblage yields that the effective axial conductivity of the composite is given by

$$\check{\sigma}_A = \sum_{i=1}^{N} \check{\sigma}^{(i)} \frac{(r_i^2 - r_{i-1}^2)}{r_N^2} \tag{3.97}$$

which is the rule of mixtures.

2. Generalized Self-Consistent Composite Cylinders Method for Transverse Conductivity

In order to determine the effective transverse conductivity, the homogeneous cylinder is taken to have the potential

$$\phi^{(\text{eff})} = \left(D_1^{(\text{eff})} r + \frac{1}{r} D_2^{(\text{eff})} \right) \cos(\theta) \tag{3.98}$$

However, as the potential must be bounded at the origin, $D_2^{(\text{eff})}$ must be identically zero so that the homogeneous cylinder is subject to the lone boundary condition of

$$\phi^{(\text{eff})}(r = r_N, \theta) = E_0 r_n \cos(\theta) \tag{3.99}$$

resulting in

$$D_1^{(\text{eff})} = E_0 \tag{3.100a}$$

$$D_2^{(\text{eff})} = 0 \tag{3.100b}$$

Thus the nonzero electric field components in the effective homogeneous material are determined to be

$$E_r^{(\text{eff})} = -E_0 \cos(\theta) \tag{3.101a}$$

$$E_\theta^{(\text{eff})} = E_0 \sin(\theta) \tag{3.101b}$$

so that the nonzero flux components are then given by

$$J_r^{(\text{eff})} = -\check{\sigma}_T E_0 \cos(\theta) \tag{3.102a}$$

$$J_\theta^{(\text{eff})} = \check{\sigma}_T E_0 \sin(\theta) \tag{3.102b}$$

and finally the total energy is obtained as

$$W^{(\text{eff})} = \langle w^{(\text{eff})} \rangle = \frac{\check{\sigma}_T}{2} E_0^2 \tag{3.103}$$

The composite cylinder assemblage used to determine the effective transverse conductivity consists of N concentric cylinders or phases, each of which is assumed to have isotropic material symmetry and has a potential of the form

$$\phi^{(i)} = \left(D_1^{(i)} r + \frac{1}{r} D_2^{(i)} \right) \cos(\theta) \qquad \text{for } r_{i-1} \leq r \leq r_i \tag{3.104}$$

where i ranges from one to N, and where $r_0 \neq 0$ denotes a hollow fiber. Thus the nonzero electric field components in each phase are determined to be

$$E_r^{(i)} = -\left(D_1^{(i)} - \frac{1}{r^2} D_2^{(i)} \right) \cos(\theta) \tag{3.105a}$$

$$E_\theta^{(i)} = \left(D_1^{(i)} + \frac{1}{r^2} D_2^{(i)} \right) \sin(\theta) \tag{3.105b}$$

so that the nonzero flux components are then given by

$$J_r^{(i)} = -\check{\sigma}^{(i)} \left(D_1^{(i)} - \frac{1}{r^2} D_2^{(i)} \right) \cos(\theta) \tag{3.106a}$$

$$J_\theta^{(i)} = \breve{\sigma}^{(i)} \left(D_1^{(i)} + \frac{1}{r^2} D_2^{(i)} \right) \sin(\theta) \tag{3.106b}$$

and finally the energy density in each phase is identified as

$$w^{(i)} = \frac{\breve{\sigma}^{(i)}}{2} \left(\left(D_1^{(i)} - \frac{1}{r^2} D_2^{(i)} \right)^2 \cos^2(\theta) + \left(D_1^{(i)} + \frac{1}{r^2} D_2^{(i)} \right)^2 \sin^2(\theta) \right) \tag{3.107}$$

which is used to obtain the total volume averaged energy of the composite cylinder assemblage as

$$W^{(\text{comp})} = \frac{1}{2r_N^2} \sum_{i=1}^{N} \breve{\sigma}^{(i)} \left[\left(D_1^{(i)} \right)^2 (r_i^2 - r_{i-1}^2) - \left(D_2^{(i)} \right)^2 \left(\frac{1}{r_i^2} - \frac{1}{r_{i-1}^2} \right) \right] \tag{3.108}$$

Thus, applying the energy equivalency of Eqn. 2.22, the effective transverse conductivity is then given by

$$\breve{\sigma}_T = \frac{1}{r_N^2 E_0^2} \sum_{i=1}^{N} \breve{\sigma}^{(i)} \left[\left(D_1^{(i)} \right)^2 (r_i^2 - r_{i-1}^2) - \left(D_2^{(i)} \right)^2 \left(\frac{1}{r_i^2} - \frac{1}{r_{i-1}^2} \right) \right] \tag{3.109}$$

In order to determine the constants $D_1^{(i)}$ and $D_2^{(i)}$ in Eqn. 3.109, the boundary conditions are applied as

$$\phi^{(N)}(r = r_n, \theta) = E_0 r_N \cos(\theta) \tag{3.110a}$$

$$J_r^{(1)}(r = r_0, \theta) = 0 \tag{3.110b}$$

where Eqn. 3.110a corresponds to an electric field transverse to the composite cylinder assemblage axis in the x_2 direction, and Eqn. 3.110b corresponds to a no flux through the hollow condition. In addition, the interface conditions representative of continuity of potential and flux are applied as

$$\phi^{(j)}(r = r_j, \theta) = \phi^{(j+1)}(r = r_j, \theta) \tag{3.111a}$$

$$J_r^{(j)}(r = r_j, \theta) = J_r^{(j+1)}(r = r_j, \theta) \tag{3.111b}$$

where j ranges from one to $N-1$. The resulting system of algebraic equations is solved to yield the final expression for the transverse conductivity from Eqn. 3.109.

Upon closer inspection of the potential, fields, and fluxes for the transverse conductivities, Eqns. 3.104, 3.105 and 3.106, respectively, as well as of the boundary and matching conditions of Eqns. 3.110 and 3.111, it is observed that transverse conductivity is mathematically analogous to the axial shear modulus (Eqns. 3.31, 3.32, 3.33, 3.34 and 3.35) as originally observed by Hashin [179], where the potential corresponds to the displacement, the field to the strain, and the flux to the stress. Further, it can be shown that this analogy remains applicable when considering graded interphase regions, i.e. solutions to Eqn. 2.35, so that the effective conductivities of graded interphase regions need not be presented here again. Thus, for both the axial conductivity and the transverse conductivity, the application of both field and flux boundary conditions results in coincident bounds and therefore, the application of the composite cylinder and the generalized self-consistent composite cylinder methods yield identical results.

E. Concentration Tensor Approximation Using the Generalized Self-Consistent Composite Cylinder Method

1. Stress Concentration Tensor Approximation

As with determining the effective properties via th multi-layer generalized self-consistent composite cylinders method, the procedure for determining the concentration tensor requires the solution of five elasticity boundary value problems leading to a system of equations to determine the stress concentration tensor components. This system of equations comes from the definition of the stress concentration tensor provided in

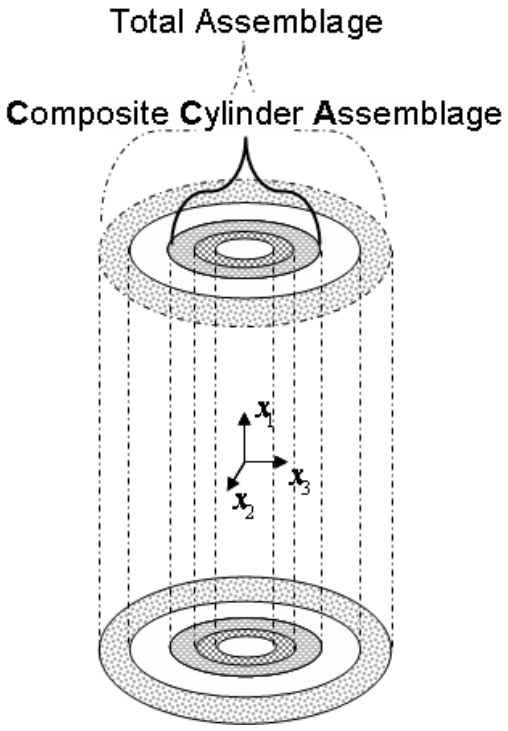

Fig. 20. Schematic identifying Composite Cylinder Assemblage and the Total Assemblage used in determining the components of the concentration tensor from the generalized self-consistent method.

Eqn. 2.64a and expressed here as

$$\langle \sigma_{ij}^{\mathrm{CCA}} \rangle = B_{ijkl} \langle \sigma_{kl}^{\mathrm{Total}} \rangle \tag{3.112}$$

where $\langle \sigma_{kl}^{\mathrm{Total}} \rangle$ refers to the volume average of the stress over the entire assemblage (i.e, over all N layers) and $\langle \sigma_{ij}^{\mathrm{CCA}} \rangle$ refers to the volume average of the stress over just the fiber and interphase layers of the composite cylinder assemblage (i.e., over all layers up through the $(N-1)^{\mathrm{th}}$) as shown schematically in Figure 20. Here it is noted that because the multi-phase effective compliance in Eqn. 2.68b is most conveniently applied in Cartesian coordinates, the stresses averaged in Eqn. 3.112 are the composite

cylinder assemblage stress components expressed in Cartesian coordinates, i.e.,

$$\begin{aligned}
\sigma^i_{11} &= \sigma^i_{zz} \\
\sigma^i_{22} &= \sigma^i_{rr}\cos^2(\theta) - 2\sigma^i_{r\theta}\cos(\theta)\sin(\theta) + \sigma^i_{\theta\theta}\sin^2(\theta) \\
\sigma^i_{33} &= \sigma^i_{rr}\cos^2(\theta) + 2\sigma^i_{r\theta}\cos(\theta)\sin(\theta) + \sigma^i_{\theta\theta}\sin^2(\theta) \\
\sigma^i_{23} &= \sigma^i_{rr}\cos(\theta)\sin(\theta) + \sigma^i_{r\theta}(\cos^2(\theta) - \sin^2(\theta)) - \sigma^i_{\theta\theta}\cos(\theta)\sin(\theta) \\
\sigma^i_{13} &= \sigma^i_{rz}\sin(\theta) + \sigma^i_{\theta z}\cos(\theta) \\
\sigma^i_{12} &= \sigma^i_{rz}\cos(\theta) - \sigma^i_{\theta z}\sin(\theta)
\end{aligned} \tag{3.113}$$

Eqn. 3.112 can therefore be expressed in indicial notation as

$$\langle \sigma^{\text{CCA}}_{ij} \rangle = B_{ijkl} \langle \sigma^{\text{Total}}_{kl} \rangle \tag{3.114}$$

or in engineering notation

$$\langle \sigma^{\text{CCA}}_{I} \rangle = B_{IJ} \langle \sigma^{\text{Total}}_{J} \rangle \tag{3.115}$$

where I and J range from one to six, and where the subscripts of Eqn. 3.114 are related to those of Eqn. 3.115 as $11 \Rightarrow 1$, $22 \Rightarrow 2$, $33 \Rightarrow 3$, $23 \Rightarrow 4$, $13 \Rightarrow 5$, and $12 \Rightarrow 6$. Thus the volume averaged stresses of Eqn. 3.115 can expressed as[9]

$$\langle \sigma^{\text{CCA}}_{I} \rangle = \frac{1}{\pi r^2_{N-1} L} \sum_{i=1}^{N-1} \int_{-L/2}^{L/2} \int_0^{2\pi} \int_{r_{i-1}}^{r_i} \sigma^i_I r \; dr \; d\theta \; dz \tag{3.116}$$

and

$$\langle \sigma^{\text{Total}}_{J} \rangle = \frac{1}{\pi r^2_{N} L} \sum_{i=1}^{N} \int_{-L/2}^{L/2} \int_0^{2\pi} \int_{r_{i-1}}^{r_i} \sigma^i_J r \; dr \; d\theta \; dz \tag{3.117}$$

It is of interest to note that the volume averages of Eqns. 3.116 and 3.117 are over the entire subvolume and volume, respectively, including the hollow region of the com-

[9]While we have chosen to use Cartesian components of the stress tensor, those components are still expressed in terms of r, θ, and z so that the integration over the composite cylinder can be more conveniently carried out.

posite cylinder assemblage. However, because the internal surface of the composite cylinder assemblage is traction free, the stress in the hollow region is taken to be zero and hence, there is no integral term from zero to r_0. In determining the strain concentration tensor, however, the displacement at the boundary should be used to extend an appropriate strain field into the hollow region as in some cases the strain should be taken to be non-zero (e.g., the ε_{zz} component of strain is non-zero in the hollow region for the axial Young's modulus displacement field).

From each displacement field applied in the multi-layer composite cylinders method, the stresses in each layer are calculated and averaged resulting in a set of six equations containing components of the stress concentration tensor to be determined. The combination of these sets of equations results in a total of 36 equations to solve for the 36 components (B_{IJ}) of the stress concentration tensor. However, due to the symmetry conditions, i.e., as the effective material is expected to transversely isotropic, it can be shown that $\langle\sigma_5^{\text{CCA}}\rangle = \langle\sigma_6^{\text{CCA}}\rangle$ and $\langle\sigma_5^{\text{Total}}\rangle = \langle\sigma_6^{\text{Total}}\rangle$, the number of equations and unknowns can be reduced to 30 equations and 30 unknowns.

The six equations obtained from the displacement field applied in the in-plane bulk modulus test (Eqn. 3.2) contain 18 of the unknown stress concentration tensor components and can be expressed as

$$\begin{aligned}
\langle\sigma_1^{\text{CCA}}\rangle &= B_{11}\langle\sigma_1^{\text{Total}}\rangle + B_{12}\langle\sigma_2^{\text{Total}}\rangle + B_{13}\langle\sigma_3^{\text{Total}}\rangle \\
\langle\sigma_2^{\text{CCA}}\rangle &= B_{21}\langle\sigma_1^{\text{Total}}\rangle + B_{22}\langle\sigma_2^{\text{Total}}\rangle + B_{23}\langle\sigma_3^{\text{Total}}\rangle \\
\langle\sigma_3^{\text{CCA}}\rangle &= B_{31}\langle\sigma_1^{\text{Total}}\rangle + B_{32}\langle\sigma_2^{\text{Total}}\rangle + B_{33}\langle\sigma_3^{\text{Total}}\rangle \\
0 &= B_{41}\langle\sigma_1^{\text{Total}}\rangle + B_{42}\langle\sigma_2^{\text{Total}}\rangle + B_{43}\langle\sigma_3^{\text{Total}}\rangle \\
0 &= B_{51}\langle\sigma_1^{\text{Total}}\rangle + B_{52}\langle\sigma_2^{\text{Total}}\rangle + B_{53}\langle\sigma_3^{\text{Total}}\rangle \\
0 &= B_{61}\langle\sigma_1^{\text{Total}}\rangle + B_{62}\langle\sigma_2^{\text{Total}}\rangle + B_{63}\langle\sigma_3^{\text{Total}}\rangle
\end{aligned} \tag{3.118}$$

where it should be noted that B_{IJ} is not necessarily equal to B_{JI}. The displacement field applied in determining the axial Young's modulus and the axial stiffness component (Eqn. 3.20) produce 12 additional equations of the same form as Eqn. 3.118, the differences being in the values of the volume averaged stresses as a result of the different boundary conditions applied. This would seem to constitute a solvable subset of 18 equations and 18 unknowns, however, the sets of equations produced by the in-plane bulk modulus test (κ_{23}) and the axial stiffness component (C_{11}) are *not* linearly independent, and therefore an additional composite cylinder boundary value problem, the transverse extension test as described in Section A, is needed. The transverse extension test results in six equations of the same form as given in Eqn. 3.118 and therefore provides a third set of equations to solve the 18 equation, 18 unknown subset of the stress concentration tensor component system. For example, in order to determine the B_{11}, B_{12}, and B_{13} stress concentration tensor components, the volume averaged stresses from the axial Young's modulus, the in-plane bulk modulus, and the transverse extension tests constitute a subset of equations given by

$$\begin{aligned}
&\text{Axial Young's Modulus:} && \langle\sigma_1^{\text{CCA}}\rangle = B_{11}\langle\sigma_1^{\text{Total}}\rangle + B_{12}\langle\sigma_2^{\text{Total}}\rangle + B_{13}\langle\sigma_3^{\text{Total}}\rangle \\
&\text{In-plane Bulk Modulus:} && \langle\sigma_1^{\text{CCA}}\rangle = B_{11}\langle\sigma_1^{\text{Total}}\rangle + B_{12}\langle\sigma_2^{\text{Total}}\rangle + B_{13}\langle\sigma_3^{\text{Total}}\rangle \\
&\text{Transverse Extension:} && \langle\sigma_1^{\text{CCA}}\rangle = B_{11}\langle\sigma_1^{\text{Total}}\rangle + B_{12}\langle\sigma_2^{\text{Total}}\rangle + B_{13}\langle\sigma_3^{\text{Total}}\rangle
\end{aligned} \tag{3.119}$$

Five similar subsets are obtained from Eqn. 3.118 in order to obtain the B_{2J}, B_{3J}, B_{4J}, B_{5J} and B_{6J} for J from one to three.

From the displacement field applied in the axial shear modulus test (Eqn. 3.31) the six equations obtained contain 6 additional unknown stress concentration tensor

components and can be expressed as

$$\begin{aligned} 0 &= B_{16}\langle\sigma_6^{\text{Total}}\rangle \\ 0 &= B_{26}\langle\sigma_6^{\text{Total}}\rangle \\ 0 &= B_{36}\langle\sigma_6^{\text{Total}}\rangle \\ 0 &= B_{46}\langle\sigma_6^{\text{Total}}\rangle \\ 0 &= B_{56}\langle\sigma_6^{\text{Total}}\rangle \\ \langle\sigma_6^{\text{CCA}}\rangle &= B_{66}\langle\sigma_6^{\text{Total}}\rangle \end{aligned} \tag{3.120}$$

where it is again noted that the fifth column of the stress concentration tensor matrix is analogous to the sixth by material and geometric symmetry considerations such that $B_{55} = B_{66}$ and $B_{I5} = 0$.

The final column of components of the matrix representation of the stress concentration tensor is obtained from the solving of the displacement fields in Eqns. 3.42 and 3.59 and results in equations of the form

$$\begin{aligned} 0 &= B_{14}\langle\sigma_4^{\text{Total}}\rangle \\ 0 &= B_{24}\langle\sigma_4^{\text{Total}}\rangle \\ 0 &= B_{34}\langle\sigma_4^{\text{Total}}\rangle \\ \langle\sigma_4^{\text{CCA}}\rangle &= B_{44}\langle\sigma_4^{\text{Total}}\rangle \\ 0 &= B_{54}\langle\sigma_4^{\text{Total}}\rangle \\ 0 &= B_{64}\langle\sigma_4^{\text{Total}}\rangle \end{aligned} \tag{3.121}$$

where it is noted that the composite cylinder assemblage used in determining the volume averaged stresses is the generalized self-consistent composite cylinder assemblage. However, the volume averages used in determining the stress concentration

tensor remain unchanged and are therefore taken over $(N-1)^{\text{th}}$ and N^{th} layers as indicated in Eqns. 3.116 and 3.117, respectively. As such, the $(N+1)^{\text{th}}$ layer is not included in the volume averages. However, the presence of the $(N+1)^{\text{th}}$ layer does enter into the stress concentration tensor component solution through the matching conditions between N^{th} and $(N+1)^{\text{th}}$ layers.

As a precursor to using the stress concentration tensor for the composite cylinder assemblage in determining the effective properties of composites, a comparison between the non-zero components of the stress concentration tensor for a no interphase case as obtained by the composite cylinders method and by using the values provided in a Mori-Tanaka approach is provided in Table III. Here we note that there is good agreement between the composite cylinders and Mori-Tanaka approaches out to four significant figures for most stress concentration tensor components, with only minor discrepancies between stress concentration tensor components which are more directly associated with the transverse direction. These results are consistent with observations made for similar composites where the composite cylinders and Mori-Tanaka results where shown to nearly coincide, with deviations most notable in the transverse properties [161]. With only minor differences in the stress concentration tensor components, the use of the generalized self-consistent composite cylinders method to determine stress concentration tensors is validated for use in coated and/or hollow fiber composites.

2. Flux Concentration Tensor Approximation

As with determining the effective conductivities via th multi-layer composite cylinders method, the procedure for determining the concentration tensor requires the solution of two boundary value problems leading to a system of equations to determine the flux concentration tensor components. This system of equations comes from the definition

Table III. Comparison of non zero stress concentration tensor components at 5% volume fraction for a composite cylinder assemblage with no interphase regions as obtained by the generalized self-consistent composite cylinders method and by using a Mori-Tanaka approach.

Stress Concentration Tensor Component	**Composite Cylinders**	**Mori-Tanaka**
B_{11}	19.75	19.75
$B_{12} = B_{13}$	-7.044	-7.044
$B_{22} = B_{33}$	1.473	1.423
$B_{21} = B_{31}$	-2.106E-03	-2.106E-03
$B_{23} = B_{32}$	-2.472E-01	-1.967E-01
B_{44}	1.623	1.620
$B_{55} = B_{66}$	1.903	1.903

of the flux concentration tensor provided in Eqn. 2.64c and expressed here as

$$\langle \mathbf{J}^{\mathrm{CCA}} \rangle = \mathbf{B} \langle \mathbf{J}^{\mathrm{Total}} \rangle \tag{3.122}$$

where $\langle \mathbf{J}^{\mathrm{Total}} \rangle$ refers to the volume average of the flux over the entire assemblage (i.e, over all N layers) and $\langle \mathbf{J}^{\mathrm{CCA}} \rangle$ refers to the volume average of the flux over just the fiber and interphase layer(s) of the composite cylinder assemblage (i.e., over all layers up through the $(N-1)^{\mathrm{th}}$). Here it is noted that because the multi-phase effective resistivity in Eqn. 2.68d is most conveniently applied in Cartesian coordinates, the fluxes averaged in Eqn. 3.122 are the composite cylinder assemblage flux components expressed in Cartesian coordinates, i.e.,

$$\begin{aligned} J_1^{(i)} &= J_z^{(i)} \\ J_2^{(i)} &= J_r^{(i)} \cos(\theta) - J_\theta^{(i)} \sin(\theta) \\ J_3^{(i)} &= J_r^{(i)} \sin(\theta) + J_\theta^{(i)} \cos(\theta) \end{aligned} \tag{3.123}$$

Eqn. 3.122 can therefore be expressed in indicial notation as

$$\langle J_i^{\mathrm{CCA}} \rangle = B_{ij} \langle J_j^{\mathrm{Total}} \rangle \tag{3.124}$$

Thus the volume averaged stresses of Eqn. 3.124 can expressed as[10]

$$\langle J_i^{\mathrm{CCA}} \rangle = \frac{1}{\pi r_{N-1}^2 L} \sum_{j=1}^{N-1} \int_{-L/2}^{L/2} \int_0^{2\pi} \int_{r_{j-1}}^{r_j} J_i^{(j)} r \; dr \; d\theta \; dz \tag{3.125}$$

and

$$\langle J_i^{\mathrm{Total}} \rangle = \frac{1}{\pi r_N^2 L} \sum_{j=1}^{N} \int_{-L/2}^{L/2} \int_0^{2\pi} \int_{r_{j-1}}^{r_j} J_i^{(j)} r \; dr \; d\theta \; dz \tag{3.126}$$

[10]While we have chosen to use Cartesian components of the flux vector, those components are still expressed in terms of r, θ, and z so that the integration over the composite cylinder can be more conveniently carried out.

It is of interest to note that the volume averages of Eqns. 3.125 and 3.126 are over the entire subvolume and volume, respectively, including the hollow region of the composite cylinder assemblage. However, because the internal surface of the composite cylinder assemblage has a no flux condition imposed, the flux in the hollow region is taken to be zero and hence, there is no integral term from zero to r_0 [11].

From each potential field applied in the multi-layer composite cylinders method, the fluxes in each layer are calculated and averaged resulting in a set of three equations containing the components of the stress concentration tensor to be determined. The combination of these sets of equations results in a total of 9 equations to solve for the 9 components (B_{ij}) of the flux concentration tensor. However, due to the symmetry conditions, i.e., as the effective material is expected to transversely isotropic, it can be shown that $\langle J_2^{\mathrm{CCA}} \rangle = \langle J_3^{\mathrm{CCA}} \rangle$ and $\langle J_2^{\mathrm{Total}} \rangle = \langle J_3^{\mathrm{Total}} \rangle$, the number of equations and unknowns can be reduced to 6 equations and 6 unknowns.

The three equations obtained from the potential applied in the axial conductivity test (Eqn. 3.91) contain three of the unknown flux concentration tensor components and can be expressed as

$$\begin{aligned} \langle J_1^{\mathrm{CCA}} \rangle &= B_{11} \langle J_1^{\mathrm{Total}} \rangle \\ 0 &= B_{21} \langle J_1^{\mathrm{Total}} \rangle \\ 0 &= B_{31} \langle J_1^{\mathrm{Total}} \rangle \end{aligned} \tag{3.127}$$

From the potential applied in the transverse conductivity test (Eqn. 3.104) the three equations obtained contain three additional unknown flux concentration tensor

[11] In determining the field concentration tensor, the potential at the boundary should be used to extend an appropriate field into the hollow region as in some cases the field should be taken to be non-zero (e.g., the E_z component of strain is non-zero in the hollow region for the axial conductivity potential field).

components and can be expressed as

$$\begin{aligned} 0 &= B_{12}\langle J_2^{\text{Total}}\rangle \\ \langle J_2^{\text{CCA}}\rangle &= B_{22}\langle J_2^{\text{Total}}\rangle \\ 0 &= B_{32}\langle J_2^{\text{Total}}\rangle \end{aligned} \tag{3.128}$$

where it is again noted that the second column of the flux concentration tensor matrix is analogous to the third by material and geometric symmetry considerations such that $B_{33} = B_{22}$, $B_{13} = B_{12}$, and $B_{23} = B_{32}$.

Again, it is noted that by the mathematical analogy between the electrical and thermal conductivity equilibrium equations, that the concentration tensors obtained here for the electric flux are equally applicable to the heat flux.

3. Application of Generalized Self-Consistent Composite Cylinders Concentration Tensor Towards Obtaining Effective Properties

Having the stress (or flux) concentration tensor is the key to allowing one to determine the effective compliance of composites containing multiple types of coated fibers and of composites containing partially aligned or randomly oriented coated fibers via the general averaging. However, it is important to note, as illustrated in Eqn. 3.129a (or Eqn. 3.129b), that even for a single type of aligned coated fiber (Figure 21) , it is also necessary to identify the compliance (or resistivity) of the inner portion of the composite cylinder assemblage consisting of the fiber and any interphase regions, i.e. M_{ijkl}^{CCA} (or $\check{\rho}_{ij}^{\text{CCA}}$) so that c_f is the volume fraction of the inner portion of the composite cylinder assemblage as a whole, i.e. $c_f = r_{N-1}^2/r_N^2$.

$$M_{ijkl} = M_{ijkl}^N + c_f(M_{ijmn}^{\text{CCA}} - M_{ijmn}^N)B_{mnkl} \tag{3.129a}$$

$$\check{\rho}_{ij}^{\text{eff}} = \check{\rho}_{ij}^N + c_f(\check{\rho}_{ik}^{\text{CCA}} - \check{\rho}_{ik}^N)B_{kj} \tag{3.129b}$$

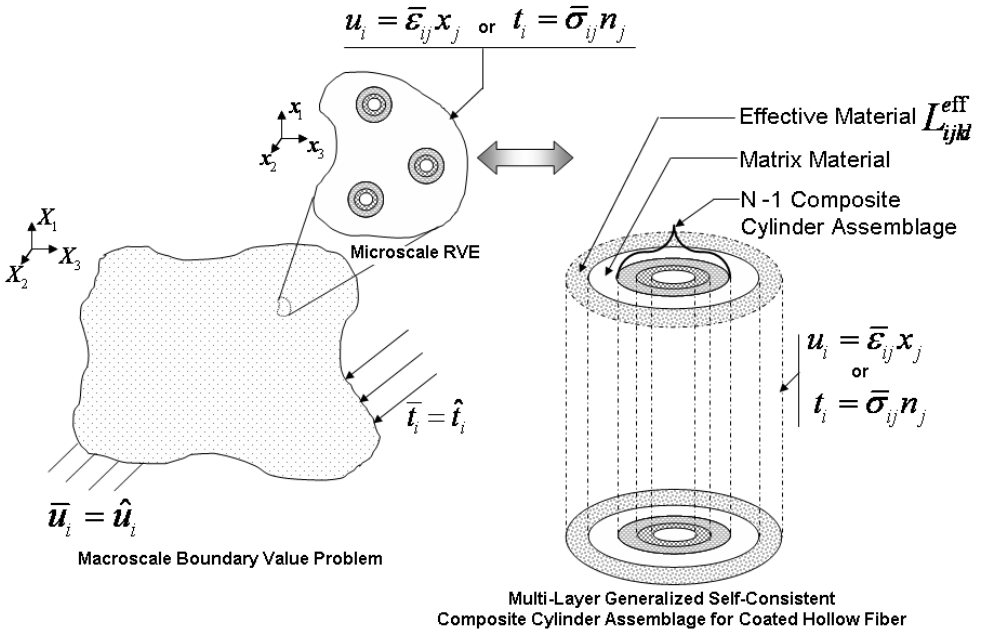

Fig. 21. Schematic representation of using the generalized self-consistent composite cylinders method for determining concentration tensors in a non-Eshelby approach for a composite containing a single type of coated, hollow, aligned inhomogeneities.

One way of obtaining M_{ijkl}^{CCA} is to calculate the effective properties of the composite cylinder assemblage using any of the methods provided in Section A at a volume fraction referred to as the critical volume fraction. If the volume fraction of the first layer within a composite cylinder assemblage like the one shown in Figure 16 is given by $v_f = r_1^2/r_{\text{out}}^2$ where r_{out} is the outer radius of the assemblage, then as this volume fraction increases, the outer radius contracts.[12] When $r_{\text{out}} = r_{N-1}$, then $v_f = \hat{v}_f = r_1^2/r_{N-1}^2$ and there is essentially no matrix material remaining so that the effective properties obtained correspond to just the first layer plus the interphase regions and can therefore be taken as the effective properties of the $(N-1)^{\text{th}}$ composite cylinder assemblage denoted by M_{ijkl}^{CCA} in Eqn. 3.129a. This compliance can be expressed in engineering notation as

$$\left[M_{IJ}^{\text{CCA}}\right]^{-1} = \begin{bmatrix} (E_1^{\text{eff}} + 4(\nu_{12}^{\text{eff}})^2\kappa_{23}^{\text{eff}}) & (2\kappa_{23}^{\text{eff}}\nu_{12}^{\text{eff}}) & (2\kappa_{23}^{\text{eff}}\nu_{12}^{\text{eff}}) & 0 & 0 & 0 \\ (2\kappa_{23}^{\text{eff}}\nu_{12}^{\text{eff}}) & (\mu_{23}^{\text{eff}} + \kappa_{23}^{\text{eff}}) & (-\mu_{23}^{\text{eff}} + \kappa_{23}^{\text{eff}}) & 0 & 0 & 0 \\ (2\kappa_{23}^{\text{eff}}\nu_{12}^{\text{eff}}) & (-\mu_{23}^{\text{eff}} + \kappa_{23}^{\text{eff}}) & (\mu_{23}^{\text{eff}} + \kappa_{23}^{\text{eff}}) & 0 & 0 & 0 \\ 0 & 0 & 0 & 2\mu_{23}^{\text{eff}} & 0 & 0 \\ 0 & 0 & 0 & 0 & 2\mu_{12}^{\text{eff}} & 0 \\ 0 & 0 & 0 & 0 & 0 & 2\mu_{12}^{\text{eff}} \end{bmatrix} \tag{3.130}$$

where the effective properties are obtained at the critical volume fraction, i.e. $\kappa_{23}^{\text{eff}} = \kappa_{23}^{\text{eff}}|_{v_f=\hat{v}_f}$. It should be noted that, as should be expected, using Eqn. 3.129a to determine the effective properties of aligned composite cylinder assemblages of single type yields identical effective properties as those obtained directly from the generalized self-consistent composite cylinder method. One can then use B_{ijkl} and M_{ijkl}^{CCA} in Eqn. 3.129a (or use B_{ij} and $\check{\rho}_{ij}^{\text{CCA}}$ in Eqn. 3.129b) to study a range of volume fractions

[12] If there are no interphase regions, then $c_f = v_f$.

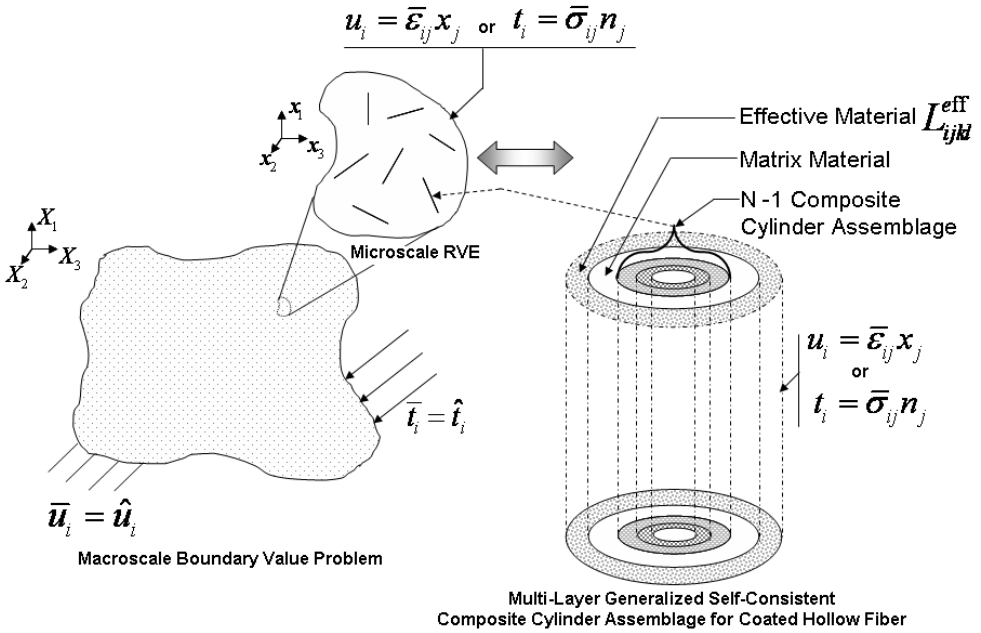

Fig. 22. Schematic representation of using the generalized self-consistent composite cylinders method for determining concentration tensors in a non-Eshelby approach for a composite containing a single type of coated, hollow, randomly oriented inhomogeneities.

of aligned coated fibers of a single type, or using Eqn. 2.68b (or Eqn. 2.68d) to determine the effective properties with multiple types of fibers(different inhomogeneity, different interphase(s), some hollow some not, etc.) or other inclusion geometries to determine the effective properties of multi-phase composites.

Further, for composites containing randomly oriented coated and/or hollow fiber composites (Figure 22) , one can apply the methods developed in Section D of Chapter II and using B_{ijkl} and M^{CCA}_{ijkl} in Eqn. 2.163b (or use B_{ij} and $\check{\rho}^{\mathrm{CCA}}_{ij}$) to obtain the effective properties, i.e.

$$M^{\mathrm{eff}}_{ijkl} = M^{N}_{ijkl} + \frac{c_f}{4\pi}\int_0^{2\pi}\int_0^{\pi}\{(M^{\mathrm{CCA}}_{ijmn}(\varphi,\psi) - M^{N}_{ijmn})B_{mnkl}(\varphi,\psi)\}\sin(\varphi)d\varphi\, d\psi \tag{3.131a}$$

$$\check{\rho}_{ij}^{\text{eff}} = \check{\rho}_{ij}^{N} + \frac{c_f}{4\pi}\int_0^{2\pi}\int_0^{\pi}\{(\check{\rho}_{ik}^{\text{CCA}}(\varphi,\psi) - \check{\rho}_{ik}^{N})B_{kj}(\varphi,\psi)\}\sin(\varphi)d\varphi\, d\psi \qquad (3.131b)$$

where it is noted that $\bar{c} = c_f$.

Finally, it is noted that the effective stiffness (or conductivity) is then obtained by taking the inverse of the compliance, i.e. $L_{ijkl}^{\text{eff}} = (M_{klij}^{\text{eff}})^{-1}$ (or $\check{\sigma}_{ij}^{\text{eff}} = (\check{\rho}_{ji}^{\text{eff}})^{-1}$).

In the following chapters the generalized self-consistent composite cylinders method will be employed in a variety of approaches towards determining the effective elastic properties and electrical and thermal conductivities of carbon nanotube-polymer nanocomposites. In much of this work, the carbon nanotubes are modeled as high aspect ratio, straight, randomly oriented composite cylinder assemblages as shown schematically in Figure 22. In general, the composite cylinder assemblages will consist of the carbon nanotube surrounded by interphase layer(s), embedded in the matrix, and finally surrounded by the effective medium. As such, the following chapters will refer back to this chapter and to Chapter II as needed.

CHAPTER IV

EFFECTIVE ELASTIC PROPERTIES OF NANOCOMPOSITES

In the present work, Mori-Tanaka, self-consistent, and the generalized self-consistent composite cylinders analytic micromechanics approaches in addition to finite element based computation micromechanics approaches are employed in modeling the effective elastic properties of CNT reinforced composites such as the one seen in Figures 3 and 23. The effects of interphase regions as observed in Figure 3(b), such as can result due to functionalization and polymer wrapping, on the effective elastic properties are also investigated using a multi-layer composite cylinders and computational micromechanics approaches. In the largest scale image in Figure 23, clusters of CNTs can be seen dispersed throughout a polymer matrix. Subsequent images at smaller scales show that within each cluster, bundles of CNTs having diameters on the order of 50 nm are observed to have a high degree of alignment. As such, clustering of CNTs in a polymer matrix is modeled herein in the context of aligned CNT bundles using a tessellation procedure to quantify clustering and both analytic and computational micromechanics approaches to assess the impact of clustering.

In order to model CNT composites several assumptions are made. The first simplification made is to assume that the carbon nanotubes are perfectly bonded to the matrix (or interphase). By this it is meant that there can be no discontinuities in displacement field when crossing the boundary between polymer and carbon nanotubes. This assumption is implicit to all micromechanics techniques which have not been appropriated modified so as to relax this assumption (e.g. composite cylinders, generalized self-consistent, and Mori-Tanaka). A second simplification is that of assuming that all carbon nanotubes are without any curvature (i.e. that they are straight nanotubes). Next, it is assumed for the time being that the nanotubes within

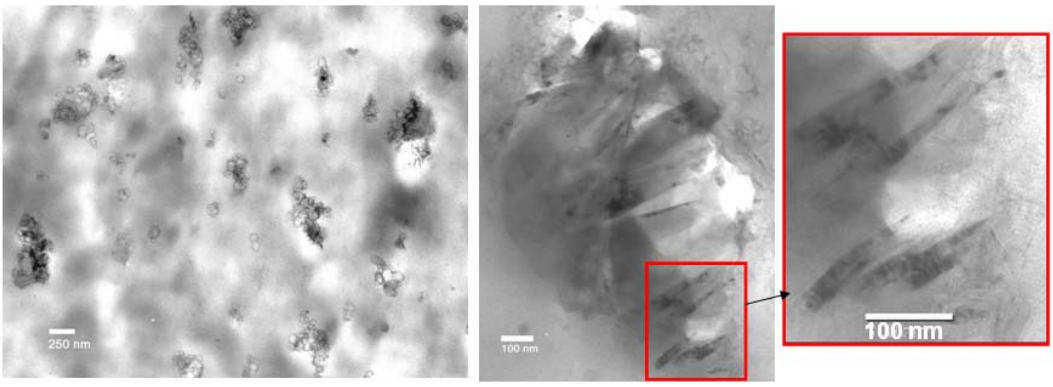

Fig. 23. TEM images depicting clustering and alignment of CNT bundles in a polymer matrix. The images were taken using a JEOL 1200 EX TEM operating at an accelerating voltage of 100kV at Texas A&M University by P. Thakre. Here the polymer matrix was polypropylene.

the composite are well aligned. At present, full scale alignment is difficult to obtain for actual composites throughout the entire sample. However, using Figures 3(a) and 23 as motivation, one can consider this assumption akin to analyzing a single cluster of bundles within the composite. Finally, it is assumed that the CNTs contain no defects or residual catalyst, and that the CNTs are sufficiently long (having aspect ratios on the order of 1000) so as to ignore end effects. It is also noted that all materials, matrix, CNTs, and any interphase region(s), are assumed to be isotropic linear elastic, and subject to small deformations.

For modeling purposes, the composite in Figures 3 and 23 has been idealized as shown in Figure 24(a) to a composite containing randomly oriented aligned clustered bundles of straight high aspect ratio CNTs. Effective elastic properties can be derived by first determining the effective properties of the clustered bundles as represented by the representative volume element (RVE) shown in Figure 24(b). In Figure 24(b), individual CNTs within the bundle can be seen with varying types and

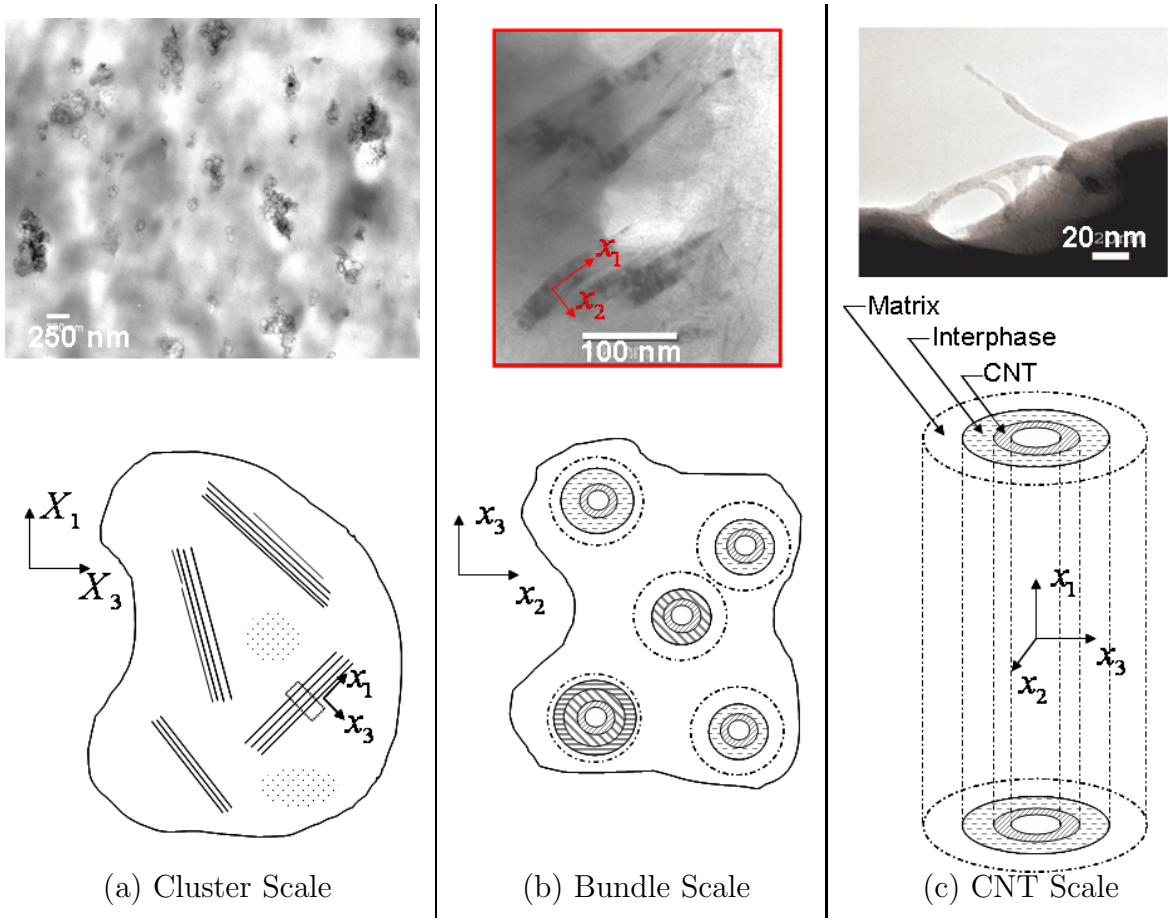

(a) Cluster Scale (b) Bundle Scale (c) CNT Scale

Fig. 24. Schematic representation of assumed simplifications for CNT-polymer composite modeling. 24(a) TEM and schematic of randomly clusters of bundles of CNTs. 24(b) TEM and schematic of an aligned bundle with M distinct CNT-interphase arrangements (here M=4 as two CNTs are identical). 24(c) TEM and schematic of a CNT with an interphase region (i.e. N=3 for the in the generalized self-consistent composite cylinder method).

number of interphase regions. The effective properties and concentration tensors of each individual CNT surrounded by its interphase regions can be determined using a multi-layer generalized self-consistent composite cylinders approach as discussed in Chapter III for arrangements like the one shown in Figure 24(c). Each unique effective CNT arrangement constitutes a separate phase to be used in a multi-phase averaging approach (see Chapter II) applied to the clustered bundle of Figure 24(b). Finally, effective elastic properties for the composite as whole can be obtained again from a multi-phase micromechanics approach where each orientation of every distinct effective bundle constitutes a separate phase (see Section D of Chapter II).

The remainder of this chapter proceeds as follows. First, the composite cylinders method is used to estimate effective CNT properties. Next, the Mori-Tanaka, self-consistent, and generalized self-consistent composite cylinder methods are used to obtain effective elastic properties for aligned, well-dispersed CNTs. Results for the effective elastic properties of aligned, well-dispersed CNTs with interphase regions obtained using both the generalized self-consistent composite cylinders method and computational micromechanics follows. This in turn is followed by analytic and computational micromechanics approaches towards estimating the effective elastic properties of aligned, clustered CNTs both with and without interphase regions. Finally, the effective elastic properties obtained using the micromechanics approaches described herein are compared to measured data from the literature for randomly oriented CNT-polymer nanocomposites.

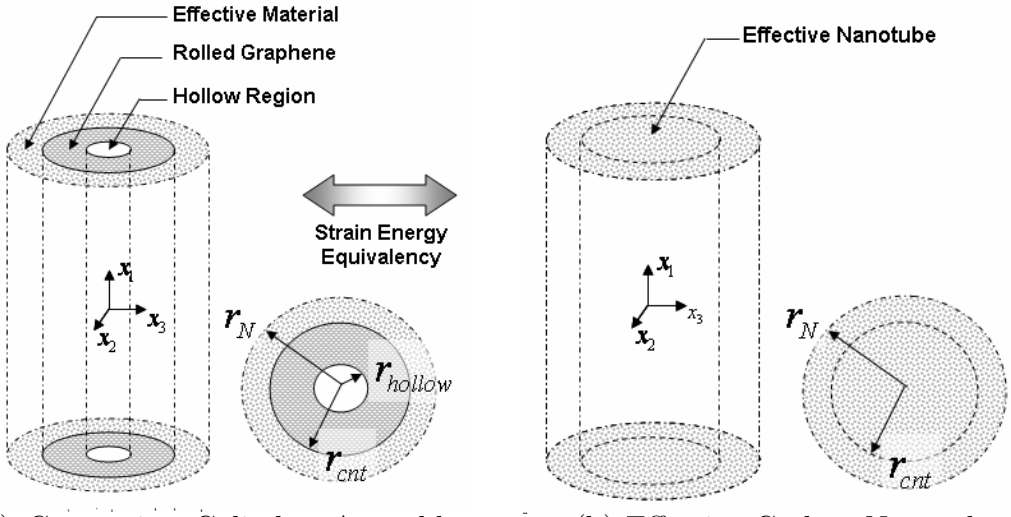

(a) Composite Cylinder Assemblage for Carbon Nanotubes (b) Effective Carbon Nanotube

Fig. 25. Schematic representation of the application of an $N = 1$ generalized self-consistent composite cylinders method in determining effective carbon nanotube properties.

A. Use of the Generalized Self-Consistent Method to Estimate Carbon Nanotube Properties

In order to be able to properly compare results for CNT-polymer nanocomposites from the generalized self-consistent composite cylinder model with results from Mori-Tanaka and self-consistent approaches, it is necessary to obtain an effective nanotube, i.e. a solid cylinder with transversely isotropic effective properties, for which an Eshelby tensor can be defined. This is accomplished through the application of the generalized self-consistent composite cylinders method for a $N = 1$ composite cylinder assemblage as shown schematically in Figure 25. With the number of layers set equal to one, the effective properties obtained correspond to the hollow CNT with no

surrounding interphases or matrix[1].

In implementing the generalized self-consistent composite cylinders method towards determining effective nanotube properties, several assumptions have to be made. The first set of such assumptions pertain to the specific geometry of the nanotube, and the second set, to the elastic properties of the tube. The geometric information needed in order to apply the generalized self-consistent composite cylinder method consists of the inner and outer radii of the CNT, thereby introducing the thickness of the CNT as a length scale in the formulation. Using electron microscopy, the outer radius of single and multi-walled carbon nanotubes can be discerned, with some [6] reporting typical values for single wall carbon nanotubes between 0.5 and 20 nm. In order to put this radius range into perspective, the standard notation for CNT identification (see for example the summary provided by Terrones [4]) provided in Figure 26 is used to calculate the radii of both zigzag and armchair CNTs provided in Table IV. Taking the bonding distance between carbon atoms as 0.144 nm, it is observed that a zigzag nanotube with radius between 0.5 and 20 nm can have between 13 and 500 carbon atoms around it's circumference while for armchair nanotubes, this range of radii would correspond to between 16 and 600 carbon atoms around the circumference.

While the outer radius is somewhat discernible using electron microscopy, estimates of the thickness of a single-walled carbon nanotube are a subject of much debate. As shown in Figures 27 and 28, values for CNT thicknesses[2] applied in es-

[1]Results for the $N = 1$ composite cylinder assemblage representing the CNT are analogous to the results that would be obtained for a graphene sheet with cylindrical voids. Computational micromechanics techniques discussed in Section B will demonstrate that the effective properties obtained for CNTs via the this method can be used to as reasonable input properties for the Mori-Tanaka and self-consistent methods.

[2]See Appendix A for the tabularized data used in constructing Figures 27 and 28

Table IV. Comparison of zigzag and armchair CNT radii.

	Zigzag radius (n,0)		Armchair (n,n)	
n	circumference (nm)	radius (nm)	circumference (nm)	radius (nm)
5	1.247	0.198	2.160	0.344
10	2.494	0.397	4.320	0.688
11	2.744	0.437	4.752	0.756
12	2.993	0.476	5.184	0.825
13	3.242	0.516	5.616	0.894
15	3.741	0.595	6.480	1.031
20	4.988	0.794	8.640	1.375
21	5.238	0.834	9.072	1.444
22	5.487	0.873	9.504	1.513
25	6.235	0.992	10.800	1.719
30	7.482	1.191	12.960	2.063
50	12.471	1.985	21.600	3.438
100	24.942	3.970	43.200	6.875
200	49.883	7.939	86.400	13.751
300	74.825	11.909	129.600	20.626
500	124.708	19.848	216.000	34.377

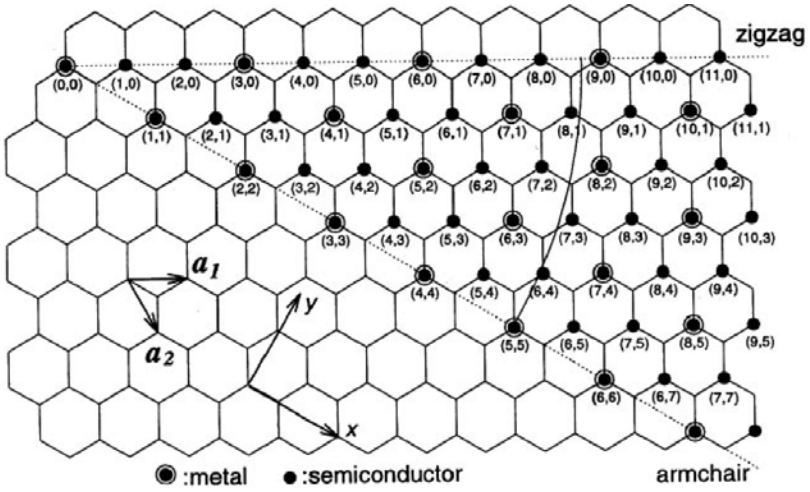

Fig. 26. Diagram for identification of CNT type as armchair, zigzag, or chiral.[4]

timating CNT (Axial) Young's modulus from both modeling results and measured data have ranged between 0.06 and 0.95 nm [92, 97, 212, 213]. However, as the radius of carbon atom is noted to be 0.17nm, and as the interlayer spacing of graphite and multi-walled carbon nanotubes is often observed to be 0.34 nm (i.e. the carbon atom diameter), many have opted to employ 0.34 nm for the single wall carbon nanotube thickness. In order to proceed with calculation of the effective properties of a single wall carbon nanotube using the generalized self-consistent composite cylinder model, geometric data indicated by Ruoff et al.[9, 214–216] was employed; namely, an outer radius of 0.85 nm and a thickness of 0.34 nm. Thus the volume fraction of the hollow region of the nanotube is given by $c_h = r^2_{hollow}/r^2_{cnt}$, where r_{hollow} is the inner radius of the CNT and r_{cnt} the outer, and is determined to have a value of $c_h = 0.36$.

In addition to identifying aspects of the geometry of the nanotube, it is necessary to also identify the material properties of the nanotube. Here it is presumed that the interior of the nanotube is ideally hollow in that it has zero stiffness. The nanotube itself is presumed to have isotropic properties corresponding to those of graphite in

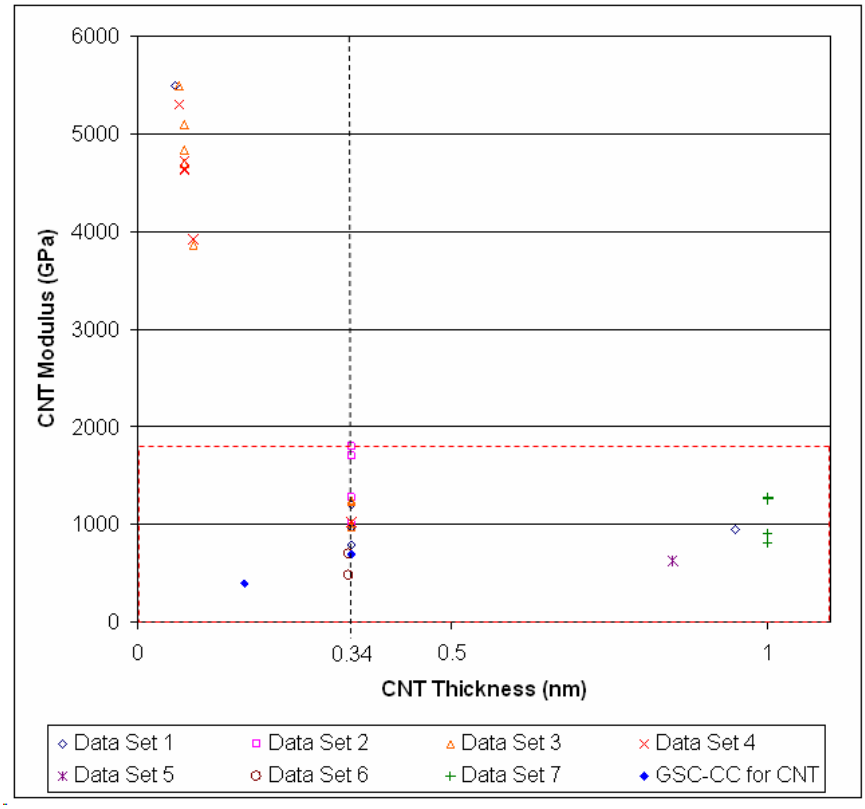

Fig. 27. Estimated Young's modulus of carbon nanotubes as a function of CNT thickness. The data presented here indicates a generally accepted value for CNT thickness of 0.34 nm. Data points are take from the following sources in the literature: Data Set 1 [97], Data Set 2 [97], Data Set 3 [213], Data Set 4 [213], Data Set 5 [212], Data Set 6 [92], Data Set 7 [25]. It is noted that the values provided for Data Set 7 are for multi-walled carbon nanotubes, and that no thickness was provided. They are placed at 1 simply demonstrate some of the values of Young's modulus obtained for MWCNTs in comparison to SWCNTs. Also provided in the figure are the results for the axial Young's modulus of the effective nanotube for two different CNT thicknesses (GSC-CC for CNT), both with CNT radii of 0.85 nm.

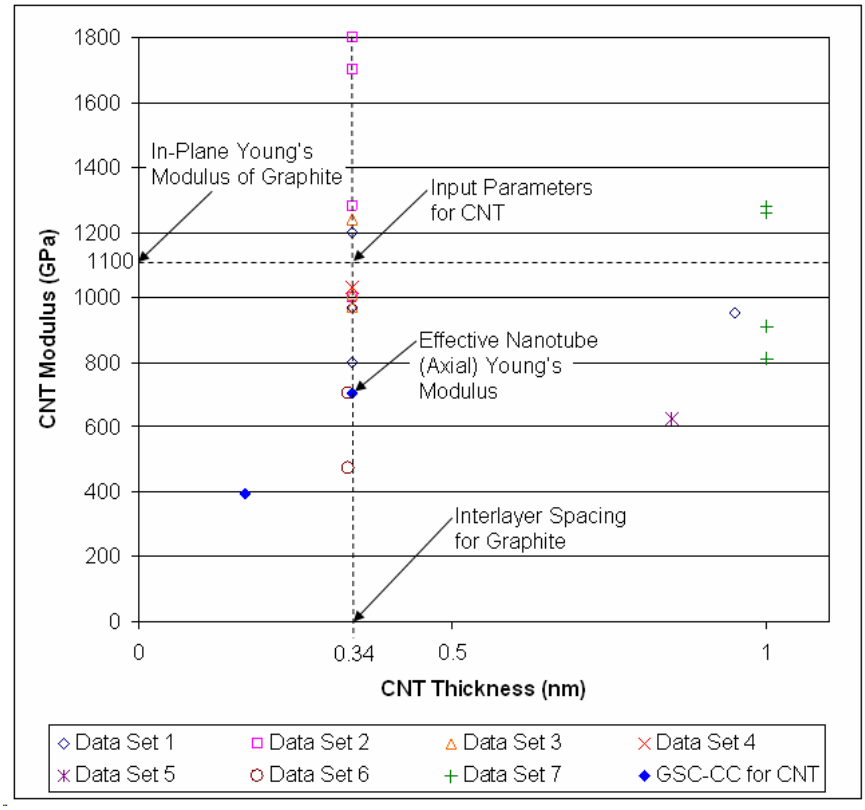

Fig. 28. Subset of the values of the estimated Young's modulus of carbon nanotubes as a function of CNT thickness. This subset of the values provided in Figure 27 denotes both the generally accepted CNT thickness and the value for the in-plane Young's modulus of graphite, both of which are used as CNT input parameters in the present study.

the plane of a graphene sheet, i.e. a Young's of 1100 GPa and Poisson's ratio of 0.14 [2, 217]. This assumption is reasonable given the relative similarity between graphene sheets and nanotubes, however, it should be noted that material properties for nanotubes obtained from a wide variety of lower length scale calculations ranging from quantum mechanics to molecular dynamics or from measured data, a sampling of which is provided in Figures 27 and 28, could readily be substituted in place of graphene. Large variance in the values obtained from both simulations and measurements shown in Figures 27 and 28 lead to the selection of the value applied.

The resulting axial Young's modulus, E_1, of the effective nanotube using these identified parameters for the CNT in generalized self-consistent composite cylinder method (Eqn. 3.28) are also provided in Figures 27 and 28 and are shown to be within the acceptable range of CNT values. Similarly, in-plane bulk modulus, κ_{23}, the axial shear modulus, μ_{12}, the in-plane shear modulus, μ_{23}, and the axial Poisson's ratio, ν_{12}, are obtained from Eqns. 3.10, 3.37, 3.64, and 3.50, respectively, all with $N = 1$. The resulting effective nanotube properties are provided in Table V, where the transverse Young's modulus, E_2 obtained from Eqn. 3.52, is also provided. The effective CNT properties for a nanotube having half of the desired thickness are also provided in Table V to illustrate the significant influence of the choice of thickness.

In order to further illustrate the influence of the two significant geometric parameters on the effective CNT properties, two parametric studies are provided (Figures 29 and 30). In the first, the radius of the CNT, r_{cnt}, is increased while the thickness remains constant at 0.34 nm.[3] This corresponds to sweeping through different values

[3]The input elastic constants corresponding to graphite also remain constant as the material properties of the annulus of the nanotube are not changing. This is reasonable given the assumption of an undisturbed graphene lattice. It is also in agreement with the observations of Lu [217] who observed nearly identical properties for the annulus of the nanotube for CNTs with the same thickness (0.34 nm) but varying radii using a lattice dynamics model.

Table V. Values for the elastic properties of effective CNTs as obtained using the generalized self-consistent composite cylinder method. In both cases, the radius of the CNT is taken to be 0.85 nm, and the properties of the nanotube are taken to be those of graphene sheets (E = 1100 GPa and ν = 0.14). Thicknesses provided correspond to the interlayer spacing of graphene sheets in graphite and half of that value.

Effective Property	Thickness 0.34 nm	Thickness 0.17 nm
E_1 (GPa)	704	396
E_2 (GPa)	396	47.5
μ_{12} (GPa)	227	106
μ_{23} (GPa)	106	13.1
κ_{23} (GPa)	286	128
ν_{12}	0.14	0.14

of the CNT identifiers, n, as provided in Table IV. The resulting effective CNT axial and transverse Young's moduli are provided in Figure 29. There it is observed that from an initially nearly equal axial and transverse Young's moduli for what would be a (5,5) armchair nanotube, both moduli decrease rapidly, but at different rates. For example, for the values corresponding to a (15,15) armchair nanotube, the transverse Young's modulus is less than half (37%) the value of the axial Young's modulus, and for a (30,30) armchair nanotube, is less than a tenth (7%) of the axial Young's modulus value. This is while the axial Young's modulus has decreased by 55% and 30%, respectively, relative to the (5,5) armchair nanotube value. Also noted in Figure 29 are the values for the effective CNT axial and transverse Young's moduli identified in order to consistently compare modeling results for nanocomposites in the subsequent sections.

In the second illustrative example, the CNT radius is increased by increments of 0.34 nm while the radius of the hollow interior, r_{hollow} is held fixed at 0.51 nm. This is representative of the estimation of effective CNT axial and transverse Young's moduli for multi-walled carbon nanotubes, with each increment of 0.34 nm corresponding to an additional wall. The results for the effective CNT properties are provided in Figure 30 where it is observed that as the number of walls is increased, the effective CNT axial and transverse Young's moduli approach one another, nearly converging at 17 walls with a Young's modulus nearly equal to that of the input graphite modulus for the nanotube annulus, which is also within the range of values for MWCNT Young's modulus provided in Data Set 7 [25].[4] Here it is cautioned that while results for the axial Young's modulus provided in Figure 30 are reliable, the results for the transverse

[4]In reference [25], the outer radius of the MWCNTs was provided, but not the number of walls or the inner radius. As such, the Young's modulus data was placed in Figure 30 at 17 walls using an assumed inner radius of 0.51 nm.

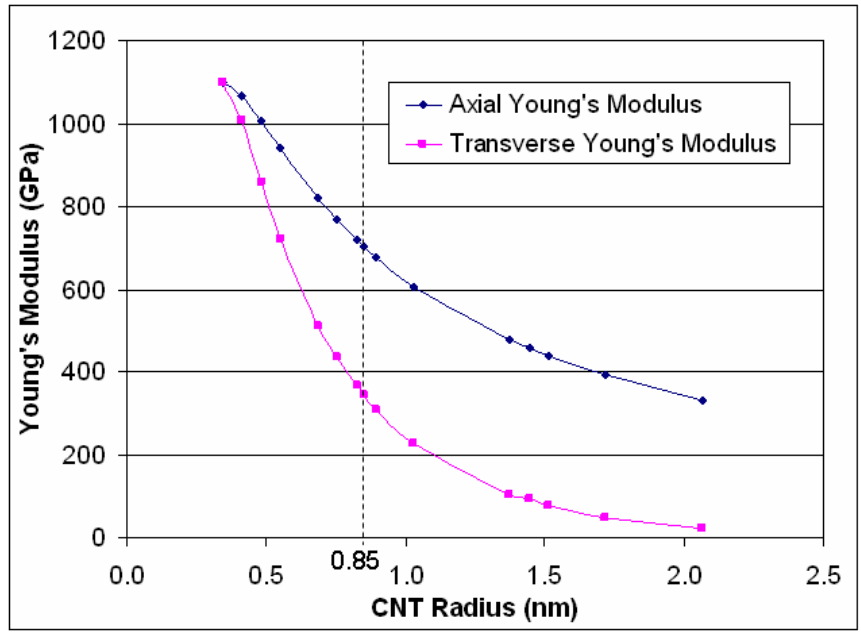

Fig. 29. Observation on the influence of CNT radius on effective CNT axial and transverse Young's moduli estimated using the generalized self-consistent composite cylinders method. It is noted that the CNT outer radius, r_{cnt}, is varied while holding the thickness of 0.34 nm constant (therefore the inner radius, r_{hollow} is not constant).

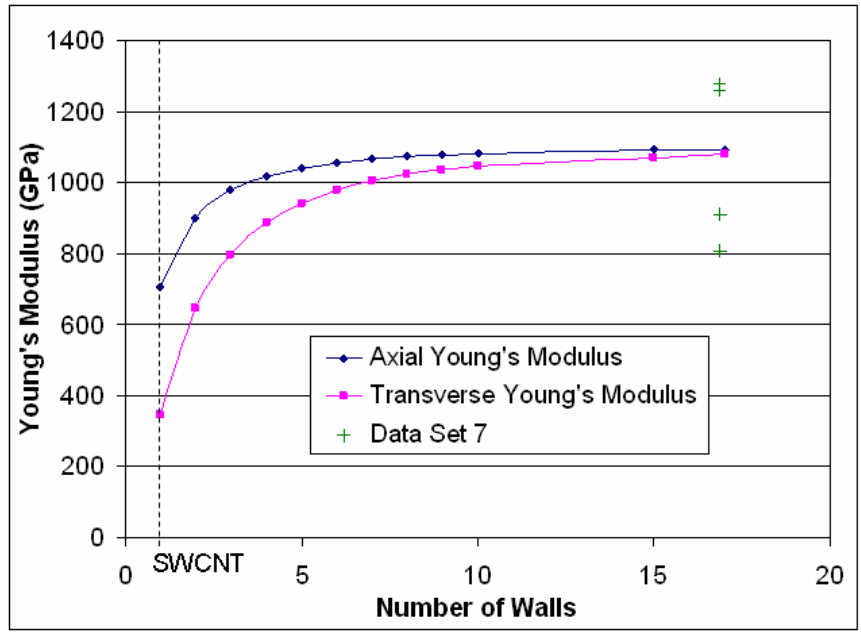

Fig. 30. Observation on the influence of CNT thickness on effective CNT axial and transverse Young's moduli estimated using the generalized self-consistent composite cylinders method. The effective CNT axial and transverse Young's moduli for CNTs are provided as a function of the number of walls for a MWCNTs. Here the CNT inner radius is held constant while additional layers of the thickness of 0.34 nm are added (therefore the outer radius is not constant). For comparison purposes, Data Set 7 [25] is included as the data is for multi-walled carbon nanotubes.

Young's modulus provided do not take into consideration any interlayer discontinuity in traction or displacement which may effect the estimated value. Finally, it is noted that both illustrative examples in Figures 29 and 30 correspond to varying the volume fraction of the hollow region in the nanotube, c_h. However, the physical reasons for these different volume fractions drives the preceding discussion and the resulting conclusions which can be made in comparing subsequent nanocomposite modeling results with measured data.

B. Effective Elastic Properties of Aligned CNT Composites

The effective elastic properties of CNT-epoxy nanocomposites with aligned, well-dispersed CNTs are obtained using the generalized self-consistent composite cylinder model, and compared with results from the proper application of the Mori-Tanaka and self-consistent models as shown schematically in Figure 31. Here a hollow, $N = 2$ composite cylinder assemblage consisting of a single wall carbon nanotube and the matrix material is used to obtain the effective axial Young's modulus, E_1^{eff} (Eqn. 3.28), in-plane bulk modulus, κ_{23}^{eff} (Eqn. 3.10), the axial shear modulus, μ_{12}^{eff} (Eqn. 3.37), the in-plane shear modulus, μ_{23}^{eff} (Eqn. 3.64), and the axial Poisson's ratio, ν_{12}^{eff} (Eqn. 3.50), of the nanocomposite, with the transverse Young's modulus, E_2^{eff} obtained from Eqn. 3.52. The nanotube geometric and material parameters remain the same as previously identified, i.e., an inner radius of $r_0 = 0.51$ nm, an outer radius of $r_1 = 0.85$ nm, with a Young's modulus and Poisson's ratio for the nanotube annulus of $E = 1100$ GPa and $\nu = 0.14$. The matrix material properties are chosen to reflect the elastic properties of epoxy (in this case EPON 862 $E = 3.07$ GPa and $\nu = 0.3$)[5] at room temperature (well below Tg).

[5]Measured values for Young's modulus of epoxies can vary between 2.03-3.91 GPa [33, 36, 49, 218–220]. However, relative to the nanotube Young's modulus, this

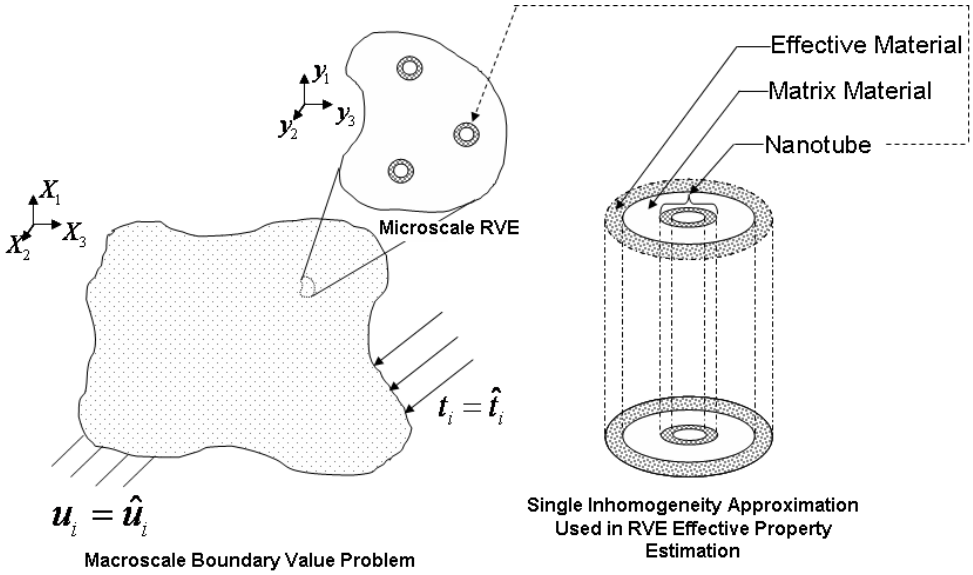

(a) Generalized Self-Consistent Composite Cylinder Model

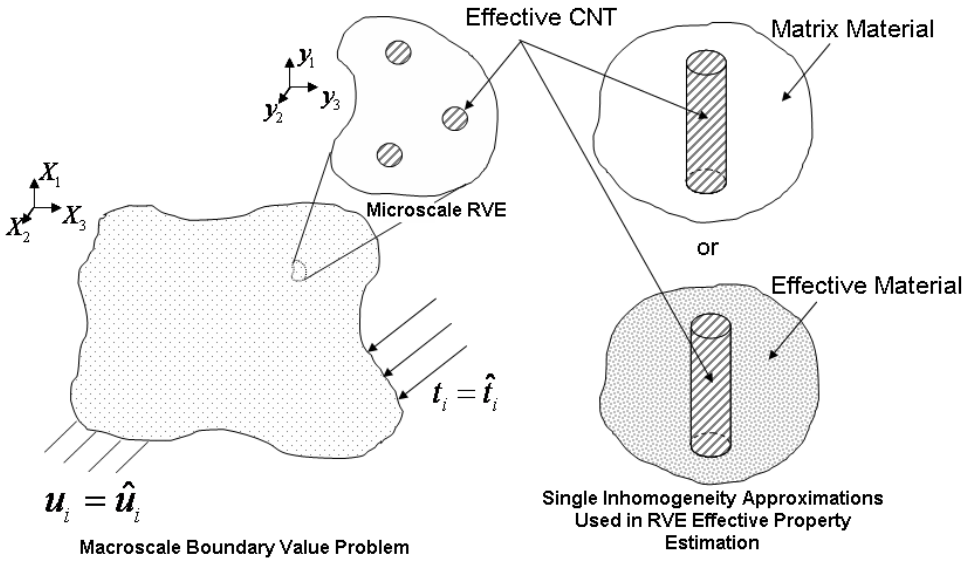

(b) Mori-Tanaka and Self-Consistent Models

Fig. 31. Schematic representation of the application of the generalized self-consistent composite cylinders, the Mori-Tanaka, and the self-consistent models for aligned, well-dispersed CNT nanocomposites. 31(a) depicts the $N = 2$ composite cylinder assemblage applied. 31(b) depicts the use of the effective CNT properties in applying the Mori-Tanaka and self-consistent approximations.

For the Mori-Tanaka and self-consistent models, the effective nanocomposite properties are obtained from Eqn. 2.71a (also for $N = 2$) where the strain concentration tensors are approximated using Eqns. 2.123 and 2.83, respectively, where the Eshelby tensor corresponds to an infinitely long circular cylinder embedded in an isotropic and transversely isotropic material, respectively (see for example pgs. 80 and 141 of reference [221]). In both cases, the effective CNT properties provided in Table V are used to construct the stiffness tensor for the inhomogeneity ($\mathbf{L}^1$) for use in determining the effective nanocomposite stiffness ($\mathbf{L}^{\text{eff}}$) by using the elastic constant relationships for transversely isotropic materials, i.e. $L^1_{1111} = E_1 + 4\nu_{12}^2\kappa_{23}$, $L^1_{1122} = 2\kappa_{23}\nu_{12}$, $L^1_{2222} = \mu_{23} + \kappa_{23}$, $L^1_{2233} = -\mu_{23} + \kappa_{23}$, and $L^1_{1212} = \mu_{12}$ [198], and it is noted that the CNT volume fraction within the matrix is identified for the composite cylinder assemblage and the Mori-Tanaka and self-consistent methods as $v_f = c_1 = r_1^2/r_2^2$.

Figure 32 provides a comparison of the results obtained for nanocomposites with aligned, well-dispersed CNTs using the generalized self-consistent composite cylinders (CC) method with results from both the Mori-Tanaka (CC/MT) and self-consistent (CC/SC) methods. Figure 32(a) demonstrates, as expected, that all three methods return the rule of mixtures for the effective axial Young's modulus, E_1^{eff}. However, for the remaining effective composite properties, the CC and CC/MT provide similar results whereas the CC/SC shows large differences relative to the other two methods, particularly at volume fractions greater then 60% as shown in Figure 32(b) for E_2^{eff}. Moreover, this difference becomes more pronounced with increasing CNT volume fraction as the CC and CC/MT approaches demonstrate a higher degree of matrix dominance than does the CC/SC. It is noted that by matrix dominance it is meant

---

variance makes little difference. The value selected was near the middle of this range and was taken from [36].

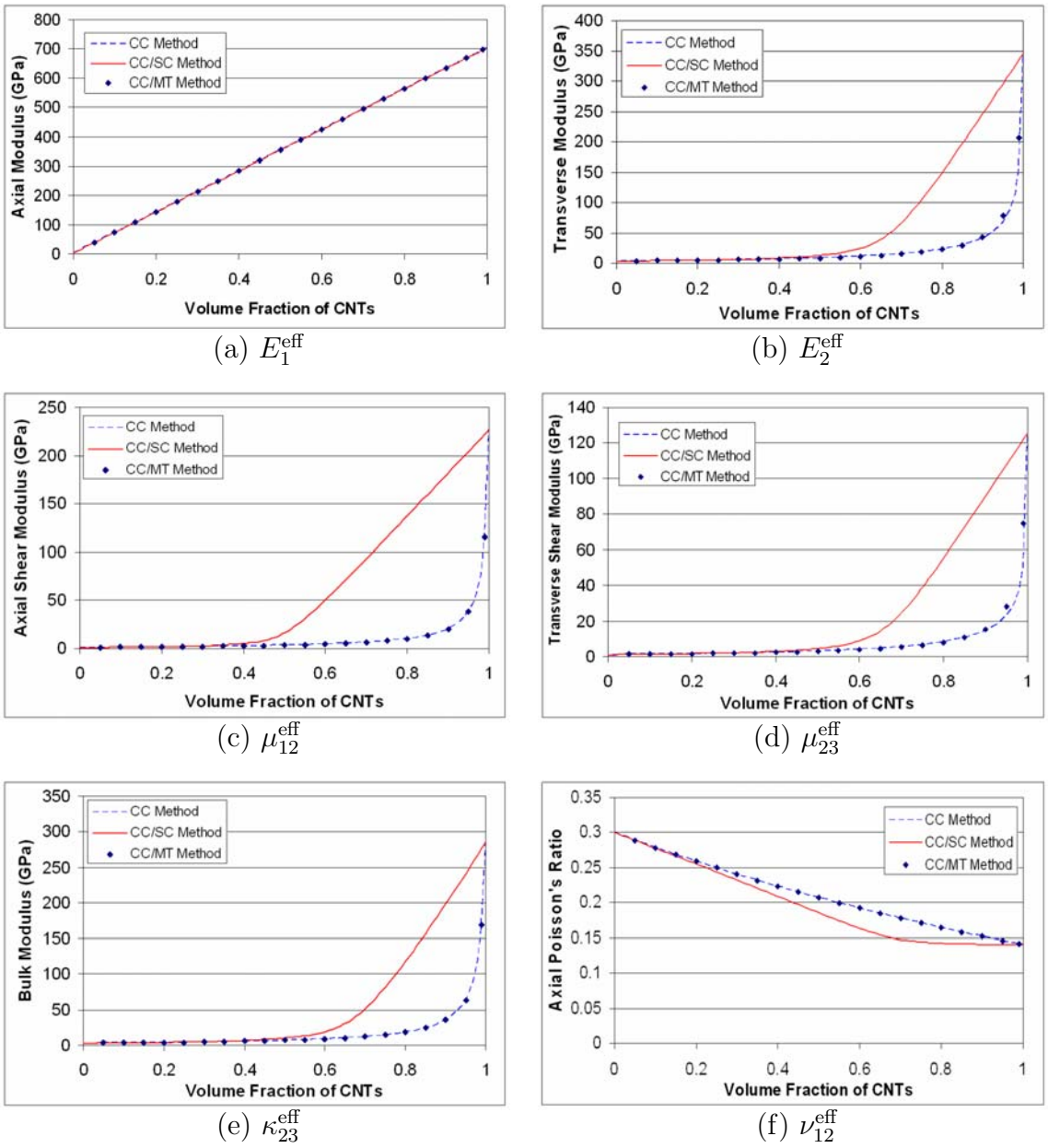

(a) E_1^{eff} (b) E_2^{eff}

(c) μ_{12}^{eff} (d) μ_{23}^{eff}

(e) κ_{23}^{eff} (f) ν_{12}^{eff}

Fig. 32. Effective properties for nanocomposites consisting of aligned, well-dispersed CNTs in epoxy using the generalized self-consistent composite cylinders, Mori-Tanaka, and self-consistent methods. For convenience the three methods are labeled CC, CC/SC, and CC/MT, respectively, where the CC in the self-consistent and Mori-Tanaka methods serves as a reminder that these results were obtained using effective CNTs as input.

that the effective properties obtained are much closer to the matrix properties at high volume fractions and therefore well below a weighted average of the input properties such as the rule of mixtures. The effective μ_{12}^{eff}, μ_{23}^{eff}, and κ_{23}^{eff} elastic moduli display similar matrix dominated behavior as observed for E_2^{eff}. The degree of matrix dominance is attributed [161] to the large differences between the matrix and nanotube properties. As a simple explanation, it is noted that in determining the axial Young's modulus, the plane strain assumptions associated with the high aspect ratio of the nanotube result in the extensional load being applied to both the matrix and the nanotube. However, in determining transverse properties like the in-plane bulk modulus, the applied displacements must be transmitted through the compliant matrix before reaching the much stiffer nanotube so that most of the strain observed would occur in the matrix.

It is also noted that the effective properties reported in Figure 32 are for the full range of volume fractions in order to demonstrate that all three methods return the matrix properties at zero volume fraction, and the effective CNT properties at a volume fraction of one. However, there is a limit on the highest attainable volume fraction as all of the nanotubes in the composite are assumed to be of the same size, i.e. the maximum packing volume fraction for identically sized aligned fibers which is 0.90. Further, it is noted that the current attainable volume fractions for CNT-epoxy nanocomposites are less than 0.10.[6] However, at these volume fractions

[6]Higher volume fraction comparisons with experimental data are not presently possible as currently it is difficult to make epoxy composites with volume fractions of CNTs much higher than 10% due to the large increase in viscosity of the liquid polymer with the introduction of CNTs. This point is emphasized if one considers the ideal case of having well-dispersed and well-aligned CNTs in a matrix material. At 1% volume fraction, CNTs would have an average center-to-center separation of 17nm while at 10% volume fraction, the center-to-center separation would be 5.4nm (based on tessellation and polygon to sphere conversion of the regular hexagonal array of CNTs). For the cross-linked thermoset epoxy matrix used in the present study, such a small spacing may be the source of the large viscosity increases, as for noncross-

all three methods yield nearly identical results, with increases in the axial Young's modulus of 2300% and a more modest value in the transverse Young's modulus of 30% relative to the matrix at a volume fraction of 0.10. It is also of interest to note that good agreement between the Mori-Tanaka and generalized self-consistent methods at nearly all volume fractions is consistent with the 5% volume fraction comparison of stress concentration tensor components provided in Table III, where it is noted that the comparison is in fact for effective CNTs.

Effective properties for nanocomposites consisting of aligned, well-dispersed CNTs in an epoxy matrix obtained from the generalized self-consistent composite cylinders method are also compared with computational micromechanics results obtained from finite element analysis (FEA). The FEA results were obtained using the actual hollow CNT geometry with the isotropic properties of graphene, as previously discussed, with CNTs arranged in a regular hexagonal array, shown in Figure 33, which is subject to periodic boundary conditions on all six sides. The regular hexagonal array is known to produce effective properties which are transversely isotropic, as expected to be the case for random distributions of fibers in the transverse plane [141, 222]. The large representative volume element (RVE) chosen for the numerical examples is not the smallest for a perfect hexagonal array, but was chosen so as to be consistent with the clustering studies presented herein. In addition, the same arrangement but with using solid transversely isotropic cylinders with effective CNT properties as provided in Table V in what could be termed a CC/FEA method was studied. Further details concerning the finite element simulation are provided in Appendix H.

Finite element results for the effective elastic properties of hollow and effective fiber FEA representations for the well-dispersed case are provided in Figure 34. Also

---

linked systems, such as polystyrene, CNT volume fractions of up to 50% have been obtained [47], though mechanical properties were not the focus.

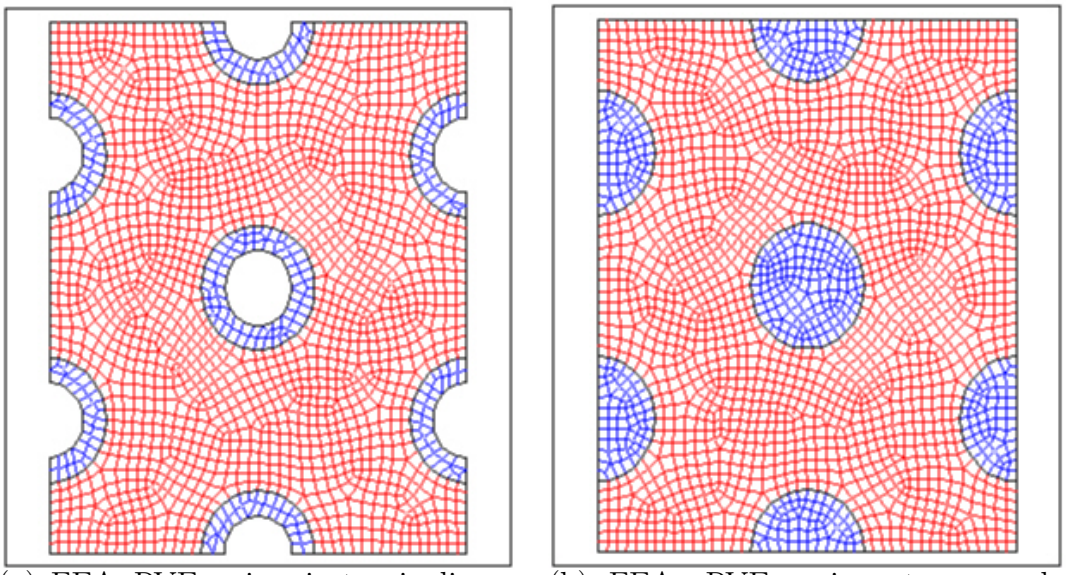

(a) FEA RVE using isotropic linear elastic CNTs

(b) FEA RVE using transversely isotropic linear elastic effective CNTs

Fig. 33. FEA RVE's used to generate effective composite properties.

included in the figures are the effective properties obtained using the generalized self-consistent composite cylinders method (which by Figure 32 also implies comparison with CC/MT results) where it is noted that the in-plane Poisson's ratio, ν_{23}^{eff}, is obtained from Eqn. 3.53.[7]

As shown in Figure 34(a), the effective axial modulus, E_1^{eff}, for both finite element representations and for the composite cylinders solution compare very favorably throughout the complete range of volume fractions. As is expected to be the case for fibrous composites, the effective elastic axial modulus is well approximated by a linear function of volume fraction between the fiber and matrix stiffnesses (i.e., rule of

[7]It is noted that certain effective properties are obtained directly using either the analytic or computational micromechanics approach, but calculated for the other approach. For example, the transverse Young's modulus, E_2^{eff}, is a property which is directly obtained from the six tests in the finite element approach, but is calculated from the other five properties in the generalized self-consistent composite cylinders approach. Conversely, the in-plane bulk modulus, κ_{23}^{eff}, can be directly obtained in the composite cylinders approach, but is calculated from the other five engineering properties in the finite element approach.

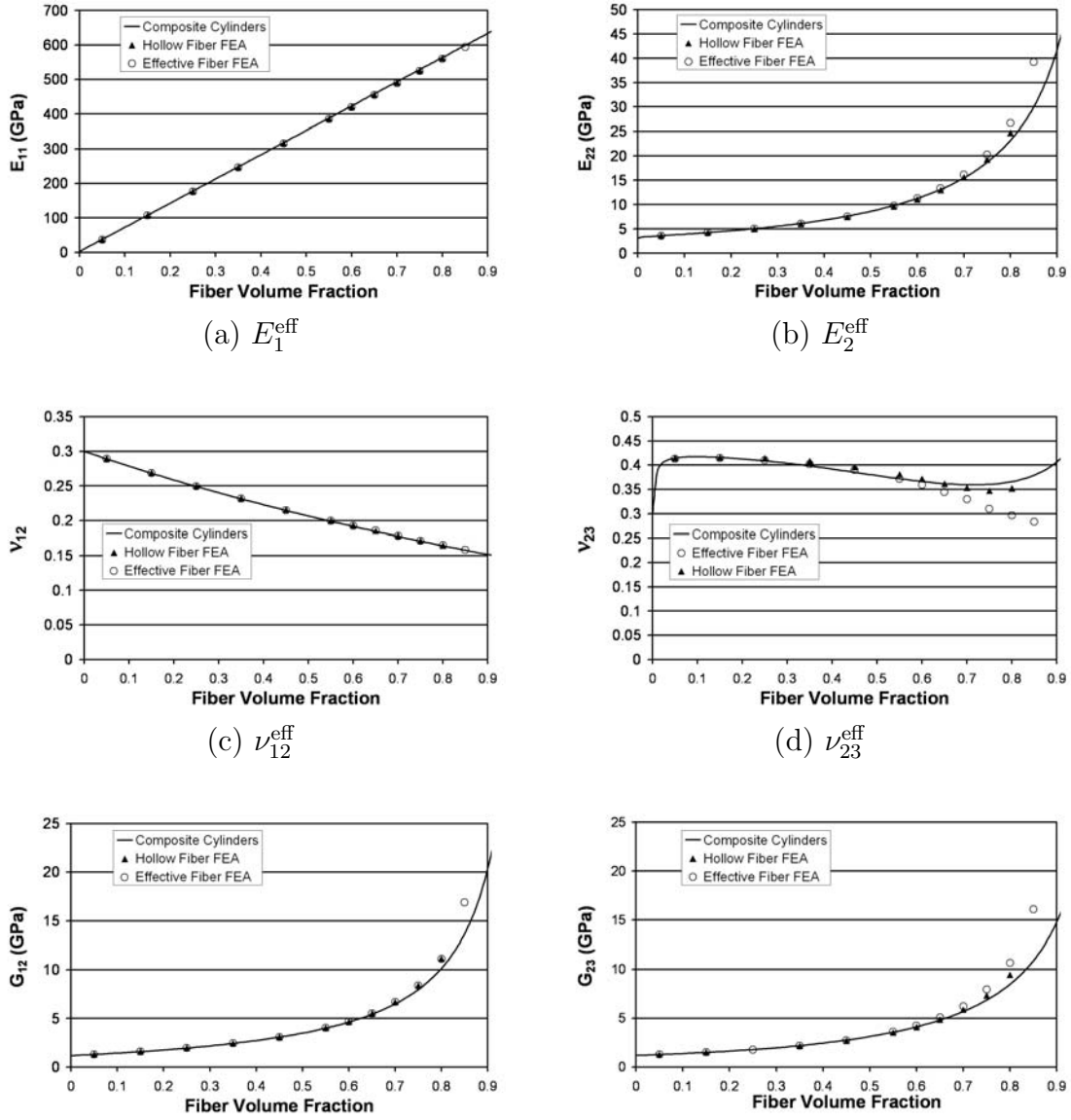

(a) E_1^{eff} (b) E_2^{eff}

(c) ν_{12}^{eff} (d) ν_{23}^{eff}

(e) μ_{12}^{eff} (f) μ_{23}^{eff}

Fig. 34. Effective properties for nanocomposites consisting of aligned, well-dispersed CNTs in epoxy using the generalized self-consistent composite cylinders and finite element computational micromechanics methods.

mixtures). Figure 34(b) provides the effective transverse modulus, E_2^{eff}, where again good agreement between both of the finite element representations and the composite cylinders solution is observed for fiber volume fractions less than 60%. At fiber volume fractions greater than 60%, increasing differences (though slight as compared to differences with the CC/SC results in Figure 32) in effective E_2^{eff} are seen, with the effective fiber FEA representation demonstrating the largest effective stiffness followed by the hollow fiber FEA representation and then the generalized self-consistent composite cylinder solution. The difference in effective transverse modulus between the effective fiber FEA representation and the composite cylinder solution is noted to be of the order of 15% at a fiber volume fraction of 80%.

Similar trends are observed in the Poisson's ratios. That is, for the effective axial Poisson's ratio, ν_{12}^{eff} shown in Figure 34(c), all solutions compare favorably throughout the complete range of volume fractions. However, for the in-plane Poisson's ratio, ν_{23}^{eff}, observable differences between the results from the two computational and the analytic solution methods again begin around 60% fiber volume fraction as shown Figure 34(d). Of particular note in Figure 34(d) is the more pronounced difference between the hollow and effective fiber FEA representations at high volume fractions. Here the effective fiber FEA representation does not adequately account for the zero-stiffness hollow region of the fiber which has increasing influence in the transverse properties at high fiber volume fractions.

Whereas the effective moduli and Poisson's ratios displayed dissimilar trends compared to one another (i.e., E_1^{eff} vs. E_2^{eff} and ν_{12}^{eff} vs. ν_{23}^{eff}), the effective shear moduli, μ_{12}^{eff} and μ_{23}^{eff}, results shown in Figures 34(e) and 34(f), respectively, are quite similar. Both shear moduli show initially good agreement between all three solution approaches up to 60% fiber volume fraction, and both show differences in effective shear moduli at larger fiber volume fractions. In fact, both effective shear moduli

plots demonstrate a similar increase in effective property with increasing fiber volume fraction as that observed for the effective transverse modulus in Figure 34(b), where the increase in effective property is relatively small initially before increasing rapidly after 60% fiber volume fraction. As such, compared to the effective axial Young's modulus and Poisson's ratio, which show an almost rule of mixtures change in effective property with increasing fiber volume fraction, the axial shear modulus, μ_{12}^{eff}, is observed to be much more sensitive to the compliant nature of the matrix material. Though the shear moduli show similar trends, the effective μ_{12}^{eff} results are larger in value and show less difference between solution methods at high fiber volume fractions than do the effective μ_{23}^{eff} results due to the reinforcing effect of the fibers being aligned in the 1-direction.

Reasons for the differences in the effective elastic properties observed in Figure 34 can best be understood by examining the associated stress distributions. Stress distribution contour plots for the well-dispersed, effective CNT finite element representation results are provided in Figure 35 for fiber volume fractions of 20% and 70% ($c_f = 0.2$ and 0.7). In both cases, the applied average strain, $\overline{\varepsilon}_{ij}$, is 1%, and the stress distributions have been plotted with a single contrast value used for each element, consistent with the under-integrated, mean quadrature 8-node brick element employed.

In Figure 35(a), stress contours of axial stress, σ_{11}, as a result of applied average axial strain, $\overline{\varepsilon}_{11}$, indicate that the effective fibers carry the majority of the load at all volume fractions. In fact, the stress level in the effective fibers and in the matrix remain constant at all volume fractions so that as the fiber volume fraction is increased, the average stress in the composite is proportionally increased resulting in the good agreement with the rule of mixtures response previously noted for the axial Young's modulus, E_1^{eff}. In contrast, Figures 35(b) and 35(c), which provide the

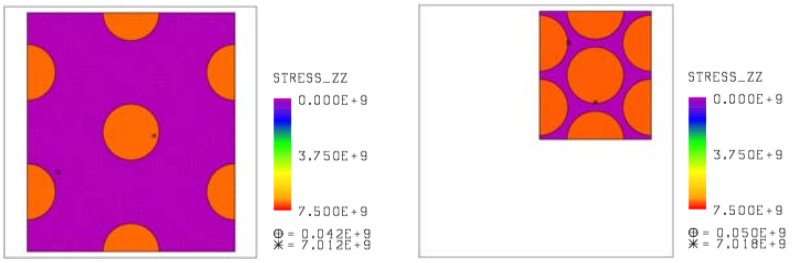

$c_f = 0.2$ $c_f = 0.7$

(a)

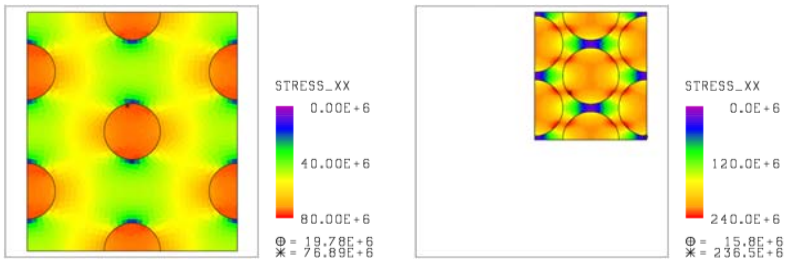

$c_f = 0.2$ $c_f = 0.7$

(b)

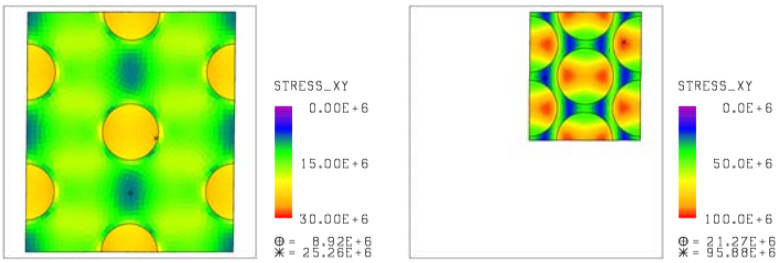

$c_f = 0.2$ $c_f = 0.7$

(c)

Fig. 35. Effective CNT FEA stress distribution contour plots for volume fractions of 20 and 70%. The contour plots are obtained at applied average strains of 1%. Note that the x_2-direction is positive to the right and the x_3-direction is positive towards the top (x_1 is out of the page). 35(a) Normal stress σ_{11} due to applied normal strain $\overline{\varepsilon}_{11}$ using a 0-7.5 GPa scale for each c_f; 35(b) Normal stress σ_{22} due to applied normal strain $\overline{\varepsilon}_{22}$ using scales of 0-80 and 0-240 MPa for $c_f = 0.2$ and 0.7, respectively; 35(c) Shear stress σ_{23} due to applied shear strain $\overline{\gamma}_{23}$ using scales of 0-30 and 0-100 MPa for $c_f = 0.2$ and 0.7, respectively.

stress contours associated with the determination of the transverse Young's modulus, E_2^{eff}, and the in-plane shear modulus, μ_{23}^{eff}, respectively, show an increasing amount of effective fiber interaction with increasing fiber volume fraction, as indicated by the increased stress state in both the fibers and the matrix at 70% volume fraction. It is this increase in the local stress state in and around the effective fiber which results in an increase in the average stress state, and which is also believed to explain the difference between the finite element and composite cylinders solutions for effective elastic properties at high volume fractions.

It can also be noted in Figures 35(b) and 35(c) that, at high volume fractions, the stress in the fiber is not only augmented, but becomes increasingly non-uniform. This has important consequences for previous modeling efforts wherein effective CNT representations have been used in conjunction with the Mori-Tanaka and self-consistent methods (i.e. the CC/MT and CC/SC results). Unlike the composite cylinders approach, the Mori-Tanaka and self-consistent micromechanics methods make use of the Eshelby tensor [131], therefore are assuming a uniform stress state in the fibers. Thus, at high fiber volume fractions, use of the Mori-Tanaka or self-consistent techniques for CNT reinforced composites may be increasingly less accurate approaches.

Finally, it is noted that the stresses induced in the hollow CNT FEA representation, although not shown, are much higher than those for the effective CNT FEA representation. This is to be expected due to the higher stiffness of the hollow fiber and its corresponding smaller volume of load-carrying material. This increased stress in the hollow fiber also results in an increase in the stress state in the surrounding matrix material. However these increases in the stress state are not sufficiently high so as to counteract the contribution of the zero-stress regions of the hollow fibers such that the average stress in the hollow CNT FEA representation is in fact lower than the average stress in the effective CNT FEA representation. Thus, the difference in effec-

tive properties observed between the hollow and effective CNT FEA representations at high fiber volume fractions is confirmed to be a result of the effective CNT FEA representation's inability to accurately account for the hollow region. However, for physically obtainable CNT-epoxy composite volume fractions which are less than 10% and certainly much less than 60%, either hollow or effective fiber FEA representations can be used.

C. Effective Elastic Properties of Aligned CNT Composites with Interphase Regions

The presence of interphase regions in CNT-polymer nanocomposites, such as shown in Figure 24(c), has been suggested by many to play a significant role in the effective properties of nanocomposites. In unfunctionalized CNT nanocomposites, this interphase region is thought to be the result of having perturbed matrix due to nanotube interaction with the polymer chains of the matrix (polymer chains are noted to entangle with carbon nanotubes to some degree producing a relatively large region [compared to the radius of the nanotube] wherein the polymer mobility has been reduced thereby increasing it's stiffness)[12, 223]. In functionalized CNT nanocomposites, the size of the interphase region and its effect on the matrix can vary greatly depending on the type of functionalization, some being intended to improve dispersion and others to improve adhesion. For CNTs and for CNTs with interphase regions it is believed that the generalized self-consistent composite cylinders method can be used to obtain the components of the concentration tensors.[8] Concentration tensors for CNTs with different functionalizations can then be obtained and averaged together to get the effective properties for epoxies containing a mixture of CNT types. Here

[8]Here it is assumed that the interphase is a compatible phase in the reference configuration with no residual stresses or transformation strains and subject to small deformations so that continuity of tractions and displacements can applied across the CNT-interphase and interphase-matrix boundaries.

however, for illustrative purposes, we consider a nanocomposite having aligned CNTs with a single type of interphase region, the properties of which are chosen to reflect varying degrees of interaction between CNTs and the polymer matrix as a result of the differing types of functionalization or lack thereof.

While experimental and computational evidence has been obtained for the existence of an interphase region between CNTs and polymer matrices [38, 224], the exact size and material properties of such interphase regions are still an active area of discussion in the research community [119, 224]. As such, interphase regions of various sizes and stiffnesses are used in a parametric study in the present discussion. However, in each case, the interphase regions around the individual CNTs of the respective RVEs are taken to be of the same size and stiffness so that the composite consists of identical high-stiffness CNTs with identical interphase regions embedded in the matrix, as shown schematically in Figure 21, so that N is equal to three in the application of the generalized self-consistent composite cylinders method in determining the effective elastic properties of the nanocomposite (Eqns. 3.10, 3.28, 3.37, 3.50, 3.52, and 3.64).

It is also noted that the inclusion of an interphase region constitutes the introduction of a length parameter, in addition to those length parameter introduced by having hollow CNTs, which for nanocomposites is quite significant as the CNT radius and interphase thickness can be of the same order of magnitude. Motivated by the chemistry of the functionalization process [33, 49], the interphase thickness, once identified, is taken as not varying with changes in CNT radius[9] Thus, for a given CNT

[9]By having the thickness fixed for a given functionalization and independent of CNT radius, it is noted that the influence of the interphase on CNTs with a large radius will be smaller than the influence of the same interphase region on CNTs with smaller radii. Thus, the constant thickness of the interphase region produces effective elastic properties which do not necessarily scale with fiber (CNT) geometry.

radius, as CNT volume fraction is increased for a given RVE, so too is the interphase volume fraction.

The constant thickness of the interphase with increasing volume fraction has additional consequences for the generalized self-consistent composites cylinders method in the form of a critical CNT volume fraction, v_f^*, for which the generalized self-consistent composites cylinders method undergoes a transition. The critical CNT volume fraction is determined as a result of the maximum packing fraction based on the interphase outer radius (i.e., where the interphase regions of adjacent CNTs come into contact), and can be substantially lower than the maximum CNT volume fraction of $v_f = 0.90$. Below the critical volume fraction, i.e. $v_f < v_f^*$, the composite cylinders assemblage consists of three layers, the CNT, the interphase, and the matrix as shown in Figure 36(a). Here the outer radius of the composite cylinder assemblage, r_{out}, is equivalent to the outer radius of the matrix phase, r_N, and is determined by the volume fraction by $r = r_1/\sqrt{v_f}$, where r_1 is the CNT outer radius. As the volume fraction is increased, the amount of matrix material is reduced up to volume fraction identified as the critical volume fraction, v_f^* defined as $v_f^* = r_1^2/r_2^2$. At this volume fraction, the matrix has been consumed such that the outer radius of the composite cylinder, r_{out} is now equal to the outer radius of the interphase region, r_2, as shown in Figure 36(b). At volume fractions larger than the critical volume fraction, Figure 36(c), the outer radius is now less than the outer radius of the interphase region. This is equivalent to saying that the matrix material has been replaced by the interphase resulting in a $N = 2$ composite cylinder assemblage consisting of the CNT and the interphase.[10]

[10]Strictly speaking for same sized fibers with a given interphase thickness, like for example in finite element calculations, there remains a small amount of matrix between the points of contact of the interphase regions of adjacent fibers. As the volume fraction is increased, this small amount of matrix is consumed until there is no

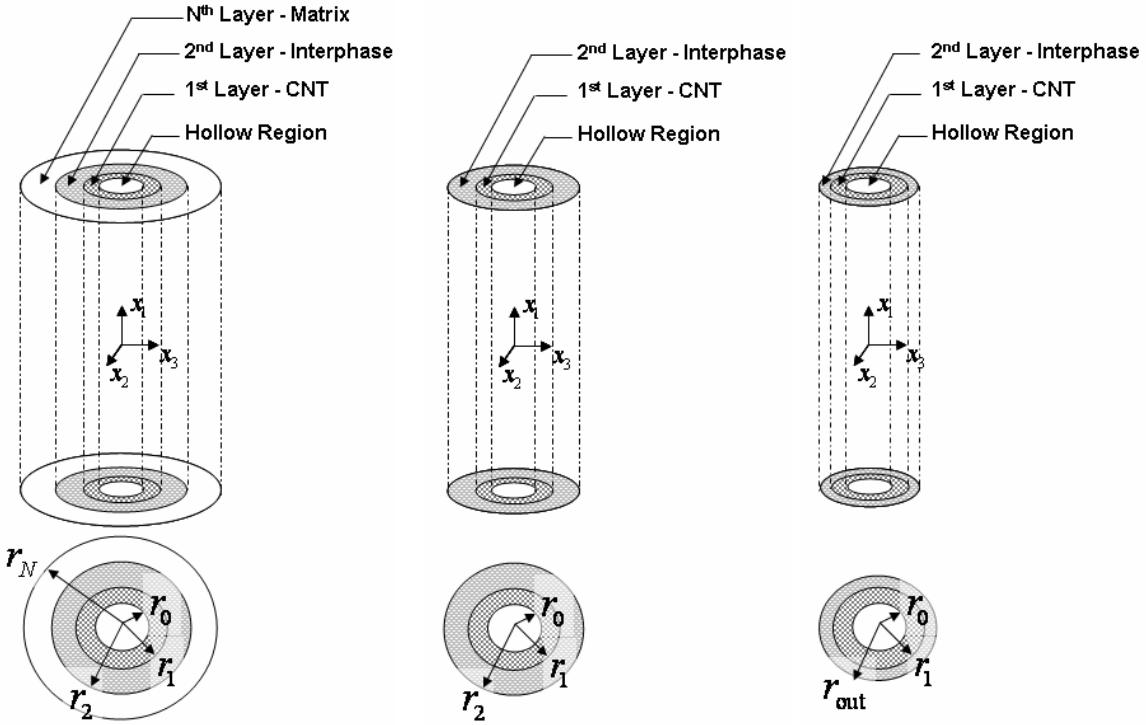

(a) $N = 3$ Composite Cylinder Assemblage Below Critical Volume Fraction

(b) $N = 3/N = 2$ Composite Cylinder Assemblage at Critical Volume Fraction

(c) $N = 2$ Composite Cylinder Assemblage Above Critical Volume Fraction

Fig. 36. Schematic representation of the transition from an $N = 3$ to an $N = 2$ composite cylinder assemblage at the critical volume fraction. Figure 36(a) $N = 3$ Composite cylinder assemblage below the critical volume fraction, i.e. $v_f < v_f^*$, so that $r_{\text{out}} = r_N = r_1/\sqrt{v_f}$. Figure 36(b) $N = 3/N = 2$ Composite cylinder assemblage at the critical volume fraction, i.e. $v_f = v_f^*$, so that $r_{\text{out}} = r_N = r_2 = r_1/\sqrt{v_f^*}$. Figure 36(c) $N = 2$ Composite cylinder assemblage above the critical volume fraction, i.e. $v_f > v_f^*$, so that $r_2 > r_{\text{out}} = r_1/\sqrt{v_f}$.

Parametric studies using the generalized self-consistent composite cylinder method on the effects of having interphases with elastic modulus ranging from one tenth that of the matrix to ten times the matrix modulus, and with thicknesses from half of a CNT radius to four times a CNT radius are provided in Figure 37. Here only the nanocomposite effective transverse Young's modulus, E_2^{eff}, results are provided as the impact of the interphase regions on the axial Young's modulus and Poisson's ratio, E_1^{eff} and ν_{12}^{eff} were found to be negligible, and the results for shear moduli and the in-plane bulk modulus, μ_{12}^{eff}, μ_{23}^{eff}, and κ_{23}^{eff} were observed to yield identical trends as shown for E_2^{eff}. Also it is noted that thin interphase regions are taken to be indicative of shorter range perturbations in the matrix perhaps due to a lack of functionalization or the use of functional groups which are short or not well entangled into to the host polymer while thick interphase regions reflect just the opposite, i.e. functional groups which entangle well into the host polymer, perhaps even bonding to the polymer at multiple sites. Likewise, compliant interphase regions are taken to represent less than perfect adhesion of the CNT or the interphase region to the surrounding matrix, perhaps a result of functionalization intended for dispersion, while interphase regions with stiffnesses greater than polymer stiffness denote functionalizations which have a strong interaction with the polymer perhaps the result of functional groups intended to improve adhesion.

Noticeable in Figures 37(a), 37(b), and 37(c) is a sharp change in the effective properties at directly attributed to the transition between the $N = 3$ composite cylinder assemblage to the $N = 2$ assemblage at the critical volume fractions of 0.04,

---

matrix remaining. From geometric considerations, this occurs at $r_{\text{out}} = 2r_2(1-\sqrt{3}/3)$ and therefore corresponds to a volume fraction of $v_f = 1.3995\ v_f^*$. For the generalized self-consistent composite cylinder assemblage, the approximation considers a single fiber and its matrix as embedded in the effective medium which accounts for this residual matrix material.

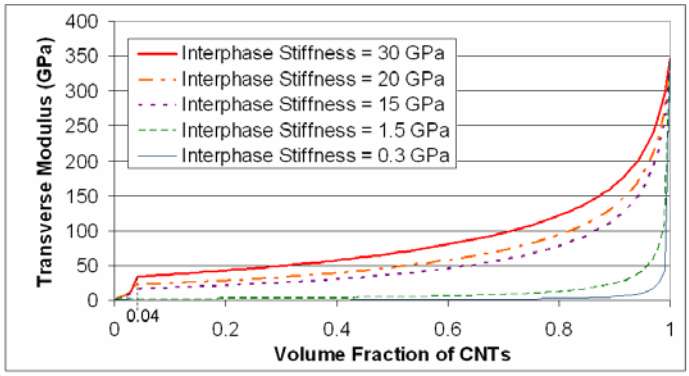

(a) Interphase thickness of Four CNT radii, $r_2 = (1+4)r_1$.

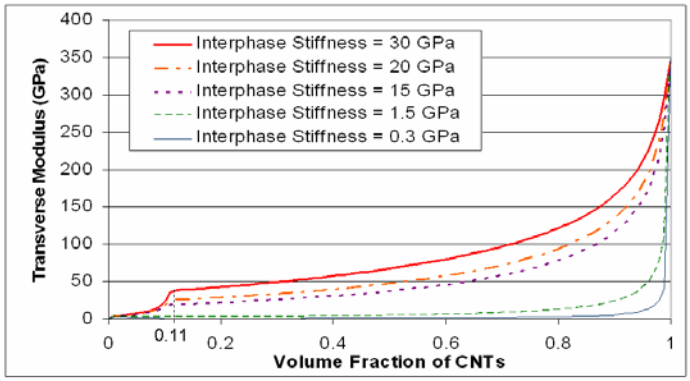

(b) Interphase thickness of Two CNT radii, $r_2 = (1+2)r_1$.

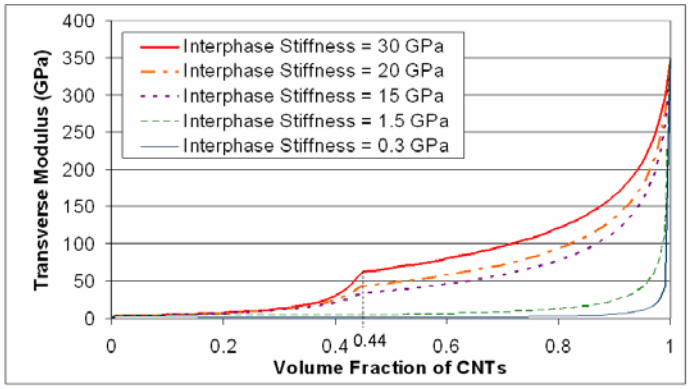

(c) Interphase thickness of Half of the CNT radius, $r_2 = (1+0.5)r_1$.

Fig. 37. Parametric study on the effects of interphase thickness and stiffness on the effective transverse Young's modulus of nanocomposites consisting of aligned, well-dispersed, interphase coated CNTs using the generalized self-consistent composite cylinders method. Identified on the plots are the critical volume fractions where there $N = 3$ composite cylinder assemblage transitions to a $N = 2$ assemblage.

0.11, and 0.44, respectively. It is observed that large interphase thicknesses correspond to effective property transitions at small volume fraction, 4% volume fraction for an interphase whose thickness is four times the radius of the CNT, as shown in Figure 37(a). In contrast, small interphase thicknesses cause effective property transitions at larger volume fraction, 44% for a thickness of half of a CNT radius, as seen in Figure 37(c). Also observed, while a nearly three orders of magnitude difference between the matrix and CNTs exists, an interphase stiffness of only five times that of the matrix is enough to significantly improve the nanocomposite's effective properties. Similarly, an interphase whose stiffness is only half that of the matrix can significantly degrade the nanocomposite's effective properties. It is noted that the $N = 2$ above the critical volume fraction are similar to the $N = 2$ results in Figure 32(b) in that the nanocomposite transverse Young's modulus is matrix dominated, but by the new matrix material which is the interphase.

The results of the parametric study of the effects of interphase regions of various stiffnesses on the effective transverse Young's modulus, E_2^{eff}, for the case of well-dispersed fibers are also shown in Figure 38 for a range of volume fractions corresponding to the current processing abilities for nanocomposites and for an interphase thickness of 1.7 nm (i.e., equal to twice the fiber outer radius selected based on Figure 23) using both computational micromechanics and the generalized self-consistent composite cylinder method. Interphase stiffnesses of 1/2, 1, 5, and 10 times the stiffness of the matrix (i.e., $E = 1.5$, 3, 15, and 30 GPa with $\nu = 0.3$) are used and the effective transverse modulus is obtained for volume fractions up to the limit volume fraction for the composite cylinders solution (i.e., a volume fraction of 11%). As presented in Figure 38, both the finite element simulations and the composite cylinders solution are in excellent agreement and indicate large differences in effective modulus relative to the no-interphase case. In fact, to obtain an equivalent value for the effec-

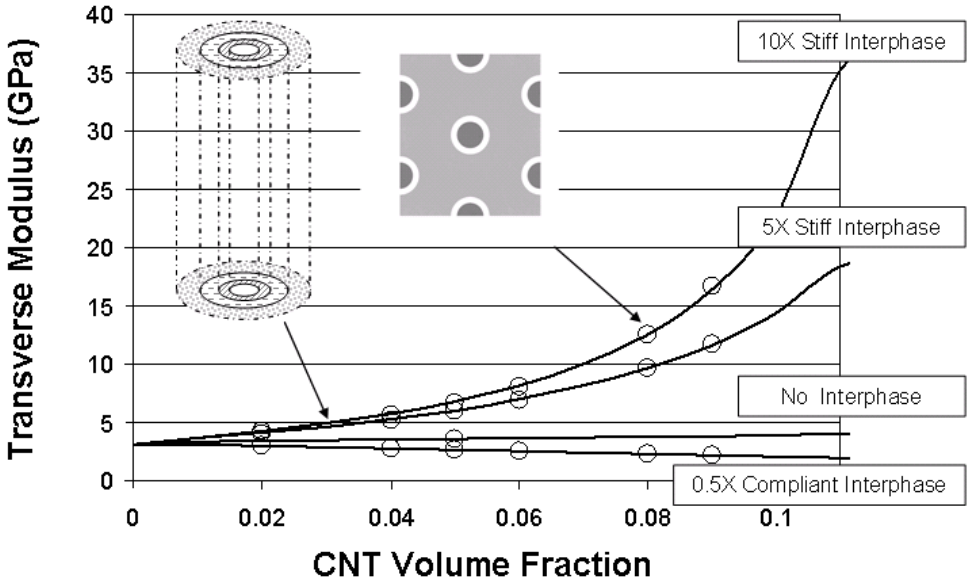

Fig. 38. Comparison between FEA and generalized self-consistent composite cylinder results in observing the effects of interphase stiffness on the transverse Young's modulus of nanocomposite containing aligned, well-dispersed CNTs. Results using three different interphase stiffnesses (1.5, 15, and 30 GPa) are shown along with the previous results with no interphase region. Results are for an interphase thickness of 1.7 nm, or twice the fiber radius, making the limit volume fraction for the composite cylinders solution to be 11%. Solid lines denote generalized self-consistent composite cylinder method results with circles denoting the results of finite element simulations. The inset of the FEA mesh corresponds to a volume fraction of $v_f = 0.08$.

tive transverse modulus as calculated for the 30 GPa interphase at 9% CNT volume fraction, a CNT volume fraction of 60% in the no-interphase case would be required. At that same volume fraction, the 1.5 GPa interphase results in a 44% decrease in the effective transverse modulus. Thus, it is observed that the effective properties associated with the transverse directions can be greatly impacted by the presence of an interphase region at volume fractions corresponding to current processing abilities, particularly if that interphase region is a compliant interphase and therefore representative of poor load transfer from the matrix to the CNT.

D. Effective Elastic Properties of Aligned CNT Composites with Clustering

It has been observed that, due to van der Waals forces, CNTs have a tendency to bundle or cluster together making it quite difficult to produce well dispersed CNT reinforced composites [12, 32], see for example Figure 23. As such, it may be necessary to incorporate the effects of clustering in the prediction of effective elastic properties. Here, the focus is on a cluster of aligned CNTs forming a bundle as shown in the RVE in Figure 24(b). In an analytic micromechanics approach towards capturing the effects of clustering within a bundle of CNTs, a Dirichlet tessellation is used to quantify the degree of clustering by assigning to each CNT in the bundle a local volume fraction. This local volume fraction is used to identify the amount of matrix used in a given generalized self-consistent composite cylinder model used to determine the stress concentration tensor for a given local volume fraction. These stress concentration tensors are used along with the effective CNT properties in a multiphase averaging method (Eqn. 2.71b) to determine the effective elastic properties of clustered bundles of CNTs. Given the good agreement observed between the stress concentration tensors determined for CNTs using both the generalized self-consistent

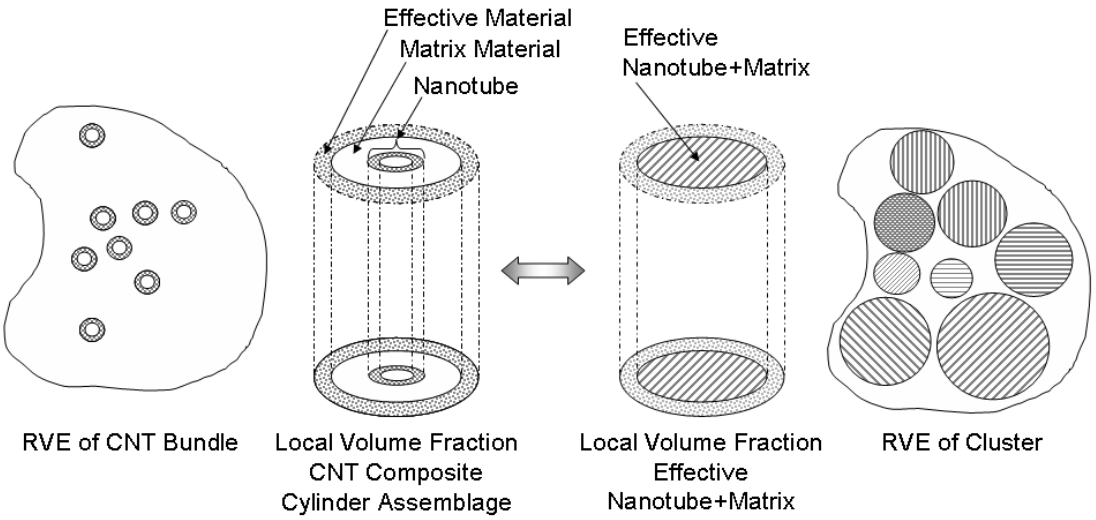

Fig. 39. Schematic diagram of how clustering is incorporated into calculating effective composite properties.

composite cylinder method and the Mori-Tanaka method (see Table III), this method is equivalent to determining the effective local effective CNT+matrix properties and applying a multi-phase Mori-Tanaka approach as shown schematically in Figure 39. As it is more expedient, analytic micromechanics results for the effects of clustering on the effective properties of CNT composites provided here are obtained using this combined generalized self-consistent composite cylinder, Mori-Tanaka method.

Many research efforts have used tessellation techniques to identify what constitutes a clustered arrangement as well as to delineate different amounts of clustering [148–153]. The Dirichlet tessellation procedure used herein to obtain the local volume fractions is a well established geometric technique for obtaining the minimum area polygons encompassing a given set of seed points, which for the present work denotes the set of CNT centers [148]. The procedure involves the connecting of seed points to all other seed points by a straight line, the perpendicular bisectors of which are

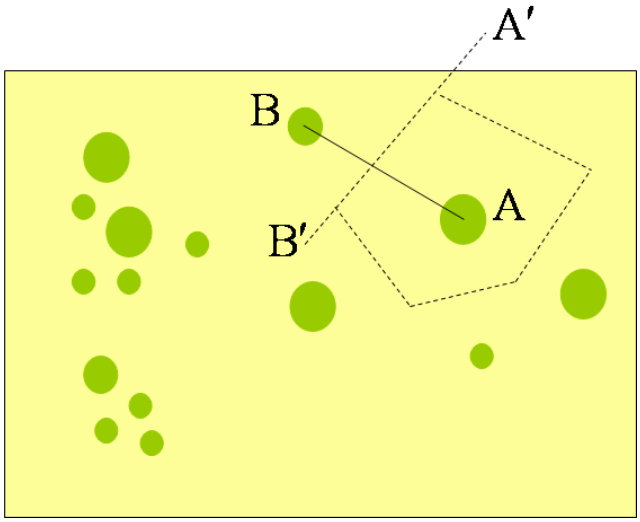

Fig. 40. Voronoi tessellation procedure diagram.

constructed and used to identify the polygonal boundaries[11], as shown schematically in Figure 40. Thus, regions in the composite where CNT center density is quite high (clustered regions) will produce small polygons and regions where the CNT center density is low will produce larger polygons as shown in Figure 41. Note that applying the tessellation routine for the hexagonal arrangement of CNTs which represents well dispersed CNT composites would produce identically sized polygons whose local volume fraction would be identically equal to the global volume fraction. This corresponds to having a distribution of local volume fractions represented by the Dirac function and is indicative of the arrangement not being clustered. In contrast, if there are significant numbers of both small and large polygons, then a bimodal distribu-

[11]The step-by-step method can be described as follows: 1) seed point coordinate locations are established (A and B in Figure 40), 2) seed points are connected to all other seed points by a straight line (solid line AB in Figure 40), 3) the perpendicular bisectors of the seed connecting lines are constructed (dashed line A'B' in Figure 40), 4) the collection of perpendicular bisector lines surrounding a seed point are selected (dashed lines surrounding A in Figure 40).

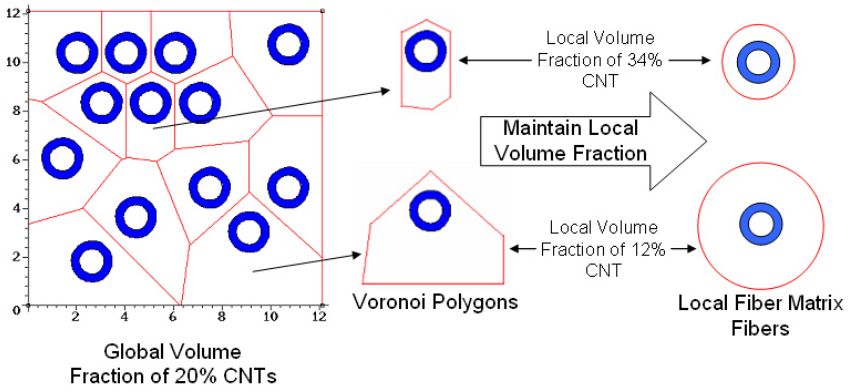

Fig. 41. Schematic demonstrating how Voronoi polygons obtained from the Dirichlet tessellation are used to identify local volume fractions and composite cylinder assemblages.

tion in polygon size will occur indicating the existence of bimodal clustering in the composite.

It is also noted that the inclusion of clustering constitutes the introduction of additional length parameters, in addition to those length parameters introduced by having hollow CNTs and/or interphase regions. However, as with the hollow region effects, the clustering effects scale with inhomogeneity size, i.e. whether microns or nanometers are the dimensions of interest, the proportional effects of the hollow region and clustering remain the same. In contrast, the length parameters introduced as a result of having interphase regions, as noted above, are based on specific nanoscale interactions and hence do not scale with the dimensions of interest, i.e. the interphase thickness remains on the order of nanometers whether the inhomogeneity has dimensions of nanometers or microns.

For clustered arrangements of aligned CNTs one can readily identify three distinct volume fractions. The first is the global volume fraction, c_{global}, as expressed in Eqn. (4.1) where N_{CNT} is the number of CNTs, A_{CNT} is the area of a CNT based

solely on its outer radius (all having the same outer radius), and A_{RVE} is the total area of the bundle RVE.[12] This is the volume fraction of the total CNT volume (including the hollow regions) in the matrix relative to the total volume of the bundle RVE. Second is the volume fraction of each CNT within its associated matrix expressed in Eqn. (4.2) and referred to as the local volume fraction, c_{local}. It is the volume fraction directly obtained from the tessellation results with A_i referring to the area of the polygon used to define the amount of associated matrix with the i^{th} CNT. This volume fraction corresponds to the volume fraction of the CNT within the composite cylinder assemblage, i.e. v_f. The third volume fraction is used to denote the overall volume fraction of the of a given local volume fraction, and as such, is referred to as the global-local volume fraction, $c_{\text{global/local}}$ as given by Eqn. (4.3), where n_J is the number of times a given local volume fraction occurs as a result of the tessellation, i.e. the number of polygons with same area, A_J. The global-local volume fractions are the volume fractions used in the multi-phase averaging method with the $c_{\text{global/local}}$ values equal to the c_J values in Eqn. 2.71b for each distinct local volume fraction up to P distinct local volume fractions so that J in Eqn. 2.71b ranges from 1 to $P+1$.

$$c_{\text{global}} = \left(\frac{N_{\text{CNT}} A_{\text{CNT}}}{A_{\text{RVE}}} \right) \tag{4.1}$$

$$c_{\text{local}} = \left(\frac{A_{\text{CNT}}}{A_i} \right) \tag{4.2}$$

$$c_{\text{global/local}} = \left(\frac{n_J A_J}{A_{\text{RVE}}} \right) \tag{4.3}$$

It should be noted that under the current assumptions, all of the CNTs are the same size and as such, polygons of the same area (but perhaps different shapes) will produce identical local volume fractions. However, if this were not the case, then CNTs of

[12]The volume fraction is given in terms of area as the length along the CNT axis is the same for the entire bundle RVE.

different sizes could produce the same local volume fractions with different polygon sizes.

In order to construct the composite cylinder assemblage for each local volume fraction, each polygonal area is calculated and set equal to the area of a circle of unknown radius. The radius of the circle is then determined, and the circle is set to be concentric with the CNT which it encompasses. Thus, the local volume fraction is obtained as the ratio of the squares of the radius of the CNT to that of the circle encompassing the fiber, thereby maintaining the volume fraction of the CNT within the polygon. This process is depicted graphically in Figure 41.

This technique has been applied to several test cases involving a range from thirteen to twenty-five identical CNTs in the absence of interphase effects embedded in the polymer matrix. Here the CNTs were arranged within the matrix in such manner so as to introduce clustering. As would be expected, it was observed that the clustered nanocomposite's axial Young's modulus was unaffected by clustering, and as such, only the transverse Young's modulus results are provided (recall that the other effective properties follow the same trend as E_2^{eff} and thus are not reported). Figure 42 provides the tessellation results for the distributions of local volume fractions of five test cases[13] at 10% global volume fraction of CNTs. The four CNT arrangements are shown as insets in Figure 42. Also shown in the figure is the distribution of local volume fraction obtained from the regular hexagonal array where it is noted that indeed all CNTs have the same local volume fraction which is also equal to the global volume fraction. Case B is identified as the most clustered mesh having a distribution in local volume fraction which is bimodal and widely separated as one set of local

[13]There are many different possible arrangements of fibers in an RVE that can be used to represent clustering, of which those chosen for the present work are only a small subset.

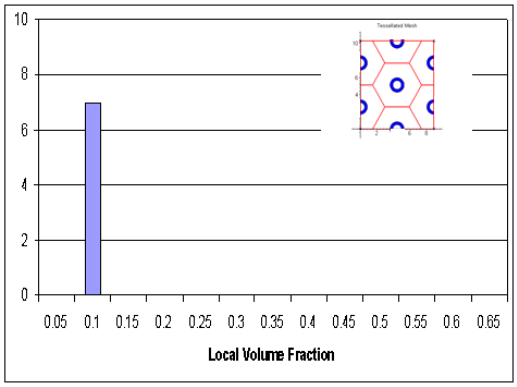

(a) Well-Dispersed Case

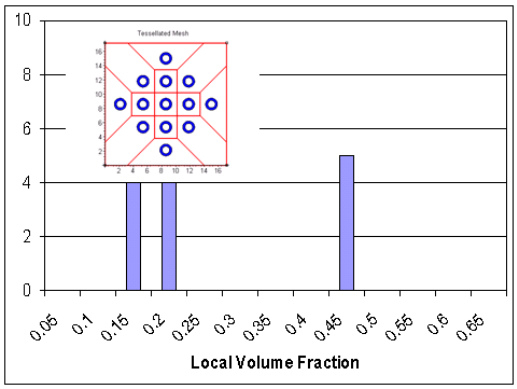

(b) Case A: 0.064% Increase

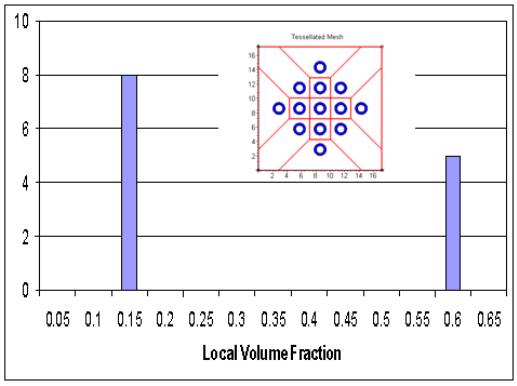

(c) Case B: 0.106% Increase

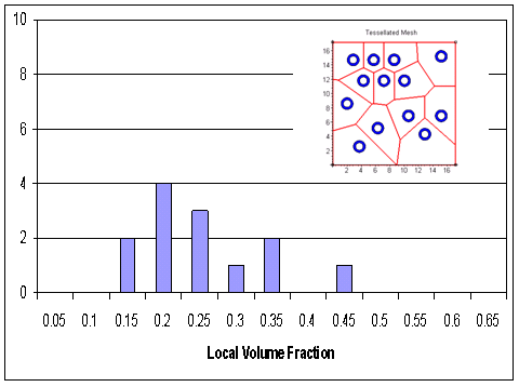

(d) Case C: 0.027% Increase

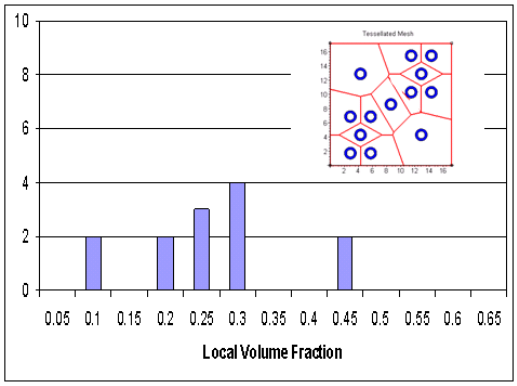

(e) Case D: 0.050% Increase

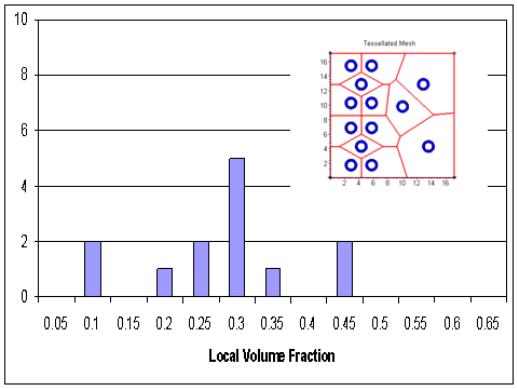

(f) Case E: 0.059% Increase

Fig. 42. Distribution in local volume fraction of well-dispersed and clustered arrangement of aligned CNTs at 10% global volume fraction. Insets denote the CNT arrangements studied. Percent differences relative to the well-dispersed CNT distribution value of E_2^{eff} are also provided.

volume fractions is significantly lower than the other set. Case A is also observed to be a significantly clustered arrangement, although less so than Case B. Cases C, D, and E are also observed to differ greatly from the well-dispersed case, though it is difficult to identify which of these three is the more clustered arrangement.

Also noted in Figure 42 are the percent differences in transverse Young's moduli of each clustered arrangement relative to the well-dispersed case. Consistent with the observation that Case B is the most clustered arrangement, the transverse Young's modulus for Case B is noted to have the largest percent difference. However, the value is a paltry 0.106%. Case A, identified as the second most clustered arrangement also yields the second largest percent difference with a value of 0.064%. The remaining cases in order of decreasing percent differences are Case E, D, and C with values of 0.059, 0.050, and 0.027%, respectively, which also corresponds to the order of decreasing average local volume fraction of the distribution and standard deviation. Thus, the effect of clustering on the effective transverse Young's modulus observed via analytic micromechanics does seem consistent with the distribution of local volume fractions, but the impact is too small to draw any conclusions from. As such, computational micromechanics techniques are applied to identical arrangements of CNTs.

For the clustered arrangements of CNTs, the computational representative volume elements, like the one denoted by the dashed lines in Figure 43(b), contain several dispersed effective CNTs, some of which are in closer proximity than others. Also shown in Figure 43 are interphase regions surrounding the fibers which are assumed to be of uniform size and stiffness and are perfectly bonded to both the CNTs and the matrix. As was the done for the well-dispersed case, the equilibrium equations are numerically solved using FEA, subject to periodic boundary conditions for the clustered arrangements (See Appendix H). Additional clustered arrangements stud-

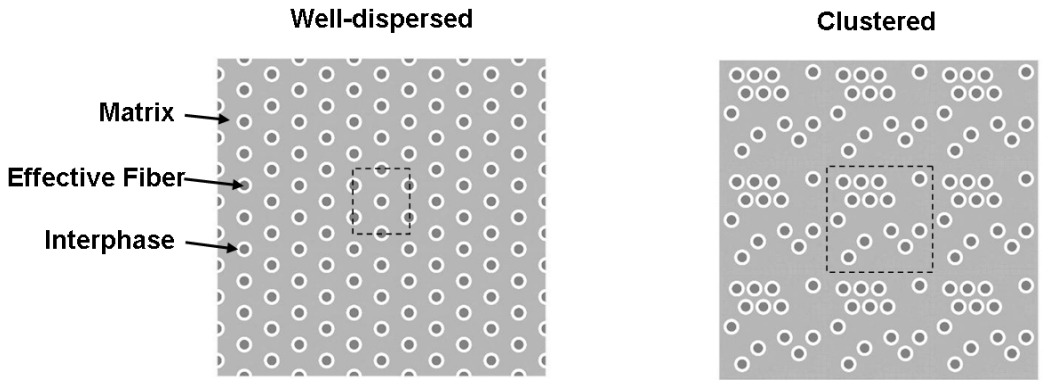

(a) Well-Dispersed CNTs (b) Clustered CNTs

Fig. 43. Schematic of effective CNT-interphase-polymer matrix FEA representations. 43(a) The well-dispersed case (perfect hexagonal array). 43(b) A clustered case (Case C). Both schematics are plotted using the same geometrical scale and both correspond to 10% volume fraction of effective CNTs and 10% volume fraction of interphase regions. Dashed lines denote the computational representative volume elements for each case.

ied are identified in Figures 42(b), 42(c), 42(e) and 42(f), all consisting of deviations from the perfect hexagonal array (Figure 43(a)).[14] As was previously noted for the well-dispersed case (identified as PH in the subsequent results), the results reported in the present work are for clustered arrangements having fiber and interphase volume fractions of 10%, with the interphase regions having stiffnesses of either 0.1, 1, or 10 times that of the matrix, with the 1X cases being indicative of clustered arrangements with no interphase regions.

Computational micromechanics results of the effective nanocomposite transverse

[14]It should also be noted that any deviation from the perfect hexagonal arrangement could result in effective properties which are not transversely isotropic. As such, it is necessary to perform all six numerical simulations previously discussed to determine the complete set of effective orthotropic engineering elastic constants. Due in large part to the periodic boundary conditions applied, the effective properties of the clustered arrangements studied herein remain very nearly transversely isotropic.

Young's modulus for well-dispersed and clustered cases both with and without interphase regions is provided in Figure 44. The column identified as PH (i.e., for the perfect hexagonal arrangement) in Figure 44 summarizes the results of an additional computational micromechanics comparison of the effects of interphase regions on the effective transverse Young's modulus for the well-dispersed case at a specific CNT volume fraction of 10%. From Figure 44, direct comparison of the stiff and compliant interphases relative to the no-interphase case can be readily discerned. In this case, the effect of the 0.1X interphase is to lower the effective transverse modulus by 34% relative to the well-dispersed, no-interphase case, whereas the effect of the 10X interphase increases the effective transverse modulus by 15%.

The effects of clustering without the effects of an interphase region on the effective transverse modulus can be assessed by comparing the 1X well-dispersed result in the PH column with the 1X results in columns A through E in Figure 44. Such a comparison demonstrates that there is hardly any difference in the effective transverse modulus relative to the well-dispersed solution for the clustered arrangements considered. Case B, which is identified as the most clustered arrangement as measured by the distribution of local volume fractions obtained via Dirichlet tessellation, shows a slightly larger increase in effective transverse modulus relative to the well-dispersed case than do the other clustering cases. However, all demonstrate small increases in effective transverse modulus on the order of 3% or less. While this value is small, it is nearly 30 times the percent difference observed using the analytic micromechanics approach to clustering.

The increase in effective transverse modulus as a result of the clustering effect observed in the 1X cases of Figure 44 can be explained by examining Figures 45(a) and 45(b), which provide the σ_{22} stress distribution contour plots for the well-dispersed and clustered Case C 1X interphase cases at 10% effective CNT

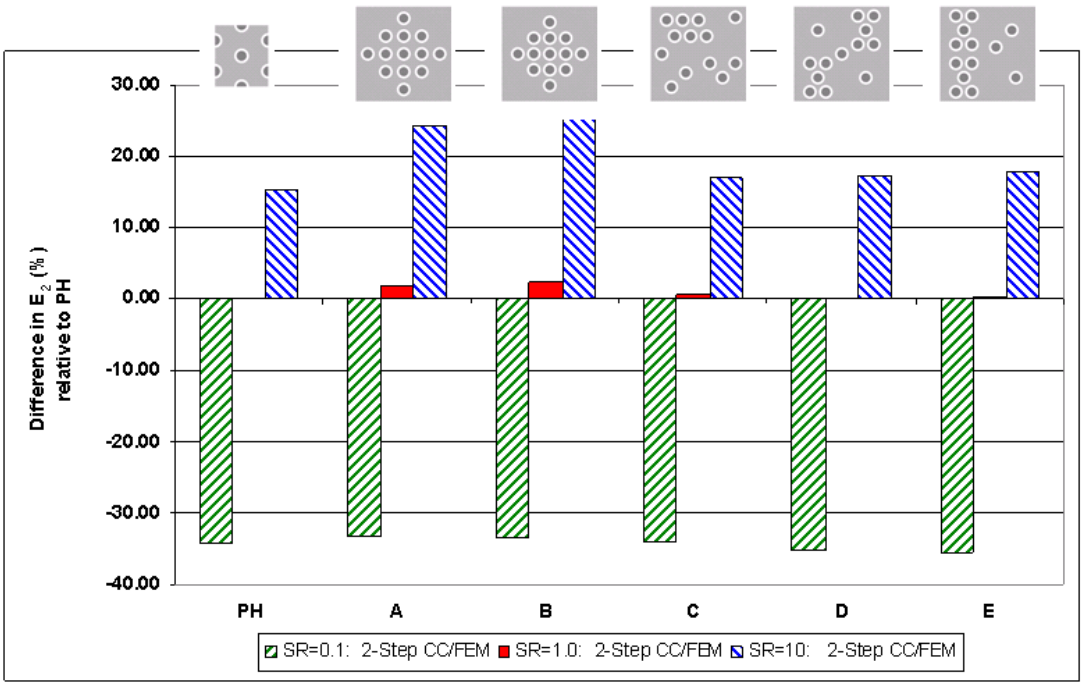

Fig. 44. Summary of the computational micromechanics results for the independent and combined effects of clustering and interphase regions on the effective transverse Young's modulus of nanocomposites. Both the CNT and interphase volume fractions are set at 10% for all cases with interphase stiffnesses 0.1, 1.0 (i.e., no interphase), and 10.0 times that of the matrix. The results in the column denoted PH correspond to well-dispersed CNTs, and those in the columns A-E to clustered CNT arrangements, as pictured by the schematics above the result columns.

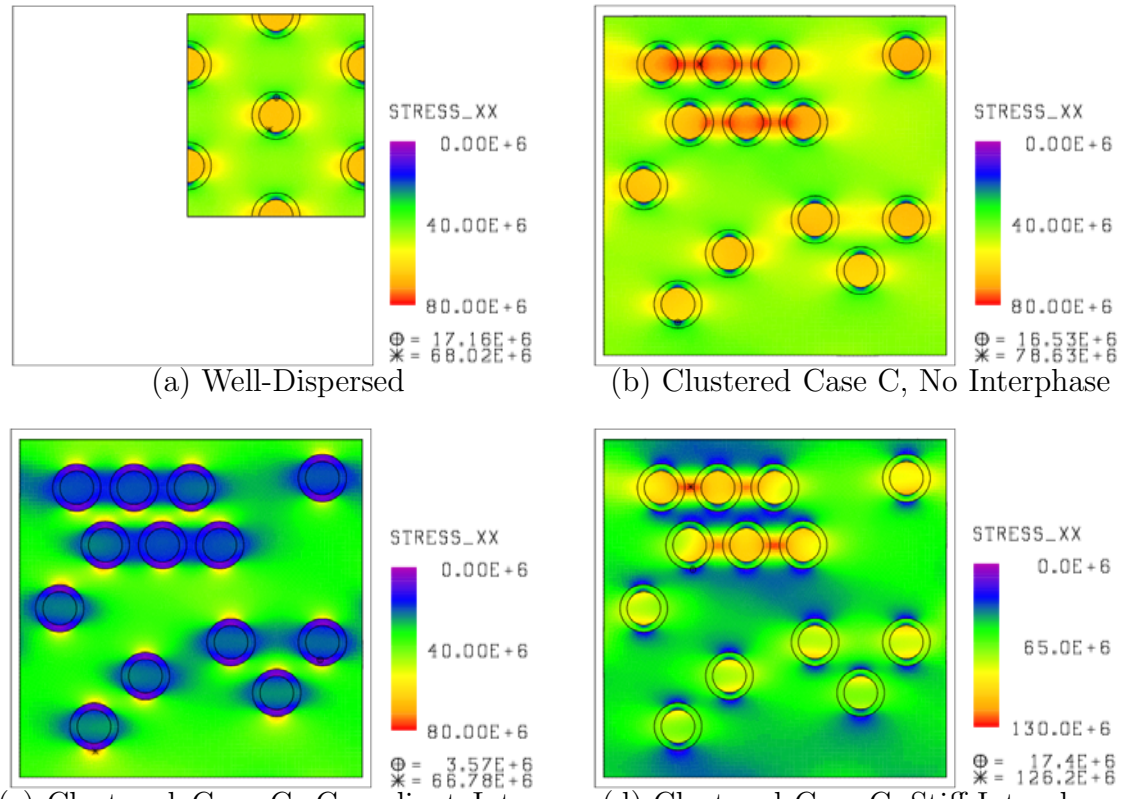

(a) Well-Dispersed

(b) Clustered Case C, No Interphase

(c) Clustered Case C, Compliant Interphase

(d) Clustered Case C, Stiff Interphase

Fig. 45. Stress distribution contour plots of the resulting normal stress σ_{22} from an applied average strain $\overline{\varepsilon}_{22}$ of 1% for 10% effective CNT and interphase volume fractions and for various interphase stiffnesses. 45(a) 1X PH well-dispersed arrangement (0-80 MPa scale); 45(b) 1X Case C clustered arrangement (0-80 MPa scale); 45(c) 0.1X Case C clustered arrangement (0-80 MPa scale); 45(d) 10X Case C clustered arrangement (0-130 MPa scale).

volume fraction for an applied average transverse strain, $\overline{\varepsilon}_{22}$, of 1%. The effective CNTs in the cluster of fibers in the upper left corner of Figure 45(b) demonstrate an increased stress state in the effective CNTs and surrounding matrix relative to the effective CNTs in the well-dispersed case as a result of the interactions between effective fibers in close proximity. However, this localized increase in the stress state results in a peak stress value of 78 MPa, only 10 MPa larger than the peak stress in the well-dispersed 1X case, and hence, only a marginal increase in the effective transverse modulus. It is also believed that it is this localized stress which the analytic micromechanics clustering approach does not accurately capture as the method is based strictly on the local volume fraction, and therefore, does not retain nearest neighbor proximity information in converting Vornoi polygons to composite cylinder assemblages as shown in Figure 41.

The combined effects of including clustering and interphase regions on the effective nanocomposite transverse Young's modulus, E_2^{eff}, are also presented in Figure 44, denoted by the 10X and 0.1X labels. From Figure 44, it is observed that the combined effects of clustering and interphase regions differ overall depending on the interphase stiffness. For the 0.1X well-dispersed (PH) and clustered cases (A-E), a uniform decrease in the effective transverse Young's modulus of approximately 33-36% relative to the 1X well-dispersed case is observed. This indicates that the nanocomposite is interphase dominated in that, regardless of the degree of clustering, it is the compliant interphase regions which are the main contributor to the reduction in effective transverse Young's modulus. For the 10X well-dispersed and clustered cases, the increase in transverse Young's modulus ranges from 15% for the well-dispersed case up to 25% for the most clustered case, Case B. Thus, for the 10X cases, there is a measurable interaction between clustering and interphase effects which causes larger increases in the effective transverse Young's modulus than either effect independently.

Reasons for the different trends in the effective transverse modulus results observed between the 0.1X and 10X clustered arrangements can again be better understood by examining the σ_{22} stress contour plots provided in Figures45(c) and 45(d) for the 0.1X and 10X Case C cases, respectively. In Figure 45(c), the compliant nature of the interphase results in almost no stress being transferred to the effective CNT, which explains why clustering has relatively little effect on the effective transverse Young's modulus for the compliant interphase cases. Figure 45(d), however, shows that the stiff interphase leads to large increases in stress in the effective CNTs and in the matrix as compared to both the well-dispersed and clustered, no-interphase cases. These elevated stresses, which are especially large for effective CNTs in close proximity, in turn lead to significant increases in the effective transverse modulus. These strong interactions among clustered effective CNTs produce a peak stress in the 10X clustered case shown which is 60% larger than the peak stress in the 1X clustered case, resulting in the noted coupling between interphase and clustering effects (note the different scale bar for Figure 45(d)). This again points to the large impact that the interphase regions can have on the effective properties associated with the transverse direction in representing various degrees of load transfer.

A summary of the effects of clustering and interphase regions on the other effective engineering moduli is provided in Table VI, where it is observed that the effective axial modulus is not affected by the clustering in the transverse plane. The "Average Effect" column in Table VI provides the nominal magnitude of the interphase effect for the studied well-dispersed and clustered arrangements and with the "Variation with Clustering" column stating how much variation with clustering arrangement there is for each property (E_1^{eff}, E_2^{eff}, ν_{12}^{eff}, ν_{23}^{eff}, μ_{12}^{eff}, and μ_{23}^{eff}). For example, for the 0.1X interphase stiffness, the effect of including the interphase region on μ_{12}^{eff} is large (approximately a 34% decrease), but nearly the same magnitude for all CNT

Table VI. Summary of the combined and independent effects of clustering and interphase regions on the effective engineering properties for composites with 10% CNT and 10% interphase region volume fractions. The average effect is the is the average percent difference of the studied cases PH, A, B, C, D, and E relative to the 1X PH case (i.e., the well-dispersed, no-interphase case). The effect variation with clustering is the difference between the highest and lowest percentage changes also relative to the 1X PH case.

Property	0.1X interphase		1X (no interphase)	10X interphase	
	Average Effect (%)	Variation w/ Clustering (%)	Variation w/ Clustering (%)	Average Effect (%)	Variation w/ Clustering (%)
E_1^{eff}	-0.48	0.10	0.10	3.75	0.10
E_2^{eff}	-34.36	2.24	2.33	19.49	10.35
ν_{12}^{eff}	3.74	0.79	0.96	-0.53	1.87
ν_{23}^{eff}	-6.42	5.06	3.17	-7.01	11.63
μ_{12}^{eff}	-34.35	1.97	1.96	19.95	7.78
μ_{23}^{eff}	-36.20	2.95	2.24	14.20	8.38

arrangements (less than 2% variation). Consistent with the observations made for the effective transverse modulus, it is observed in general that for the compliant interphase regions, there is less variation in the effective engineering properties with clustering than for the stiff interphase regions with clustering. As a result of the more significant influence of interphase regions, the focus of subsequent modeling efforts will be on accurate representation of the interphase regions in nanocomposites.

E. Effective Elastic Properties of Composites with Randomly Oriented CNTs and Comparison with Measured Data

As alignment of the CNTs within nanocomposites remains a processing challenge, the effects of random orientation of CNTs and interphase coated CNTs within the epoxy matrix are considered. By considering each orientation of a CNT as a separate phase, aligned with its own local coordinate system, the expression of the stiffness tensor and concentration tensor are obtained in the local coordinate system as described in Section E of Chapter III and then rotated to the global coordinate system. The effective properties are then obtained by averaging over all possible orientations, i.e., phases, as in Eqn. 2.163b and are observed to be isotropic, despite the transverse isotropy of the CNTs. However, with the concentration tensors determined in a non-Eshelby approach directly from the composite cylinders solutions, the random orientation averaging can take place without using the Mori-Tanaka method, and thereby allow for a more direct accounting for the presence of interphase regions.

To demonstrate the impact of random orientation, the effective properties of nanocomposites with randomly oriented non-clustered CNTs, such as in Figure 24(a) but where CNTs are not clustered into bundles, are compared to aligned non-clustered results (see Figure 22). To isolate the effects of random orientation, identical CNTs

with no interphase regions were considered. The effective nanocomposite Young's modulus obtained from the randomly orientation equation is provided in Figure 46, as are the effective axial and transverse Young's moduli for aligned CNT nanocomposites. As can be seen in Figure 46(a), without fiber alignment, one can not as readily take advantage of the high modulus of the CNTs, even at what would by processing standards be very large volume fractions. Figure 46(b) indicates that, at volume fractions currently able to be processed, the Young's modulus of nanocomposites with randomly oriented CNTs at a volume fraction of 10% is 290% larger than the transverse Young's modulus. In contrast, the axial Young's modulus at that same volume fraction is 375% larger than the randomly oriented CNT value.

Thus, it would appear that the two of the most important considerations in nanocomposite modeling would be to capture the effects of random orientation of the CNTs and to capture the effects of interphase regions. As such, Figure 47 provides the effective Young's modulus of nanocomposites containing randomly oriented, interphase coated CNTs as predicted using the generalized self-consistent composite cylinder method in comparison to the values of for the Young's modulus obtained from characterizations efforts published in the literature for both pristine and functionalized CNT-epoxy nanocomposites.[15] Modeling results are provided for seven sets of input parameters. These input parameter sets are identified in Tables VII and VIII, and are intended to reflect the uncertainty in the range of input parameters and therefore to provide reasonably bounds for modeling results. The input parameter set identified as the Base Case corresponds to the previously identified values for CNT elastic properties, radius and thickness assumed in all of the modeling results provided

[15]Some data from the literature as well as the modeling results were converted from the reported volume fraction to weight fraction (and then percent) using $1.8 g/cm^3$ for the density of CNTs and $1.175 g/cm^3$ for the density of epoxy as identified in reference [21].

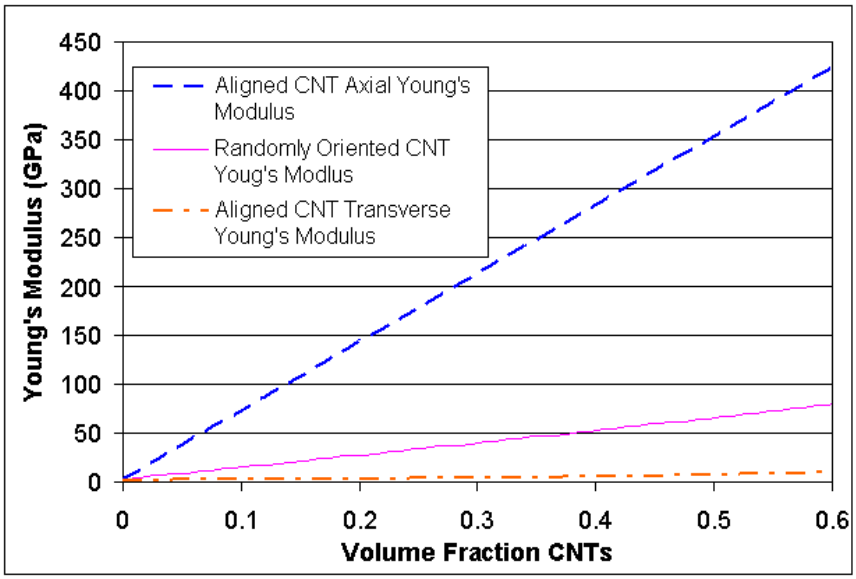

(a) Large Range of Volume Fractions

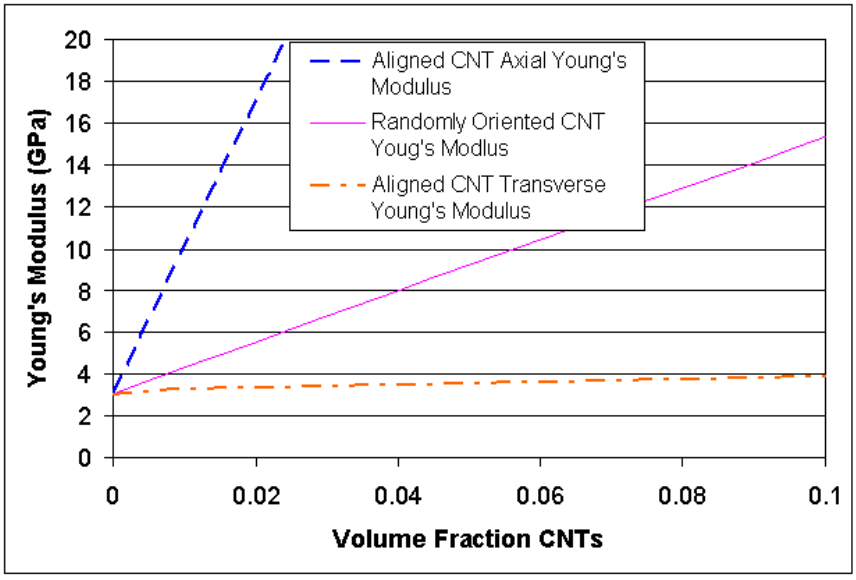

(b) Current Fabrication Volume Fractions

Fig. 46. Comparison of the effective Young's moduli of nanocomposites containing randomly oriented CNTs with nanocomposites containing aligned CNTs using the generalized self-consistent composite cylinder method.

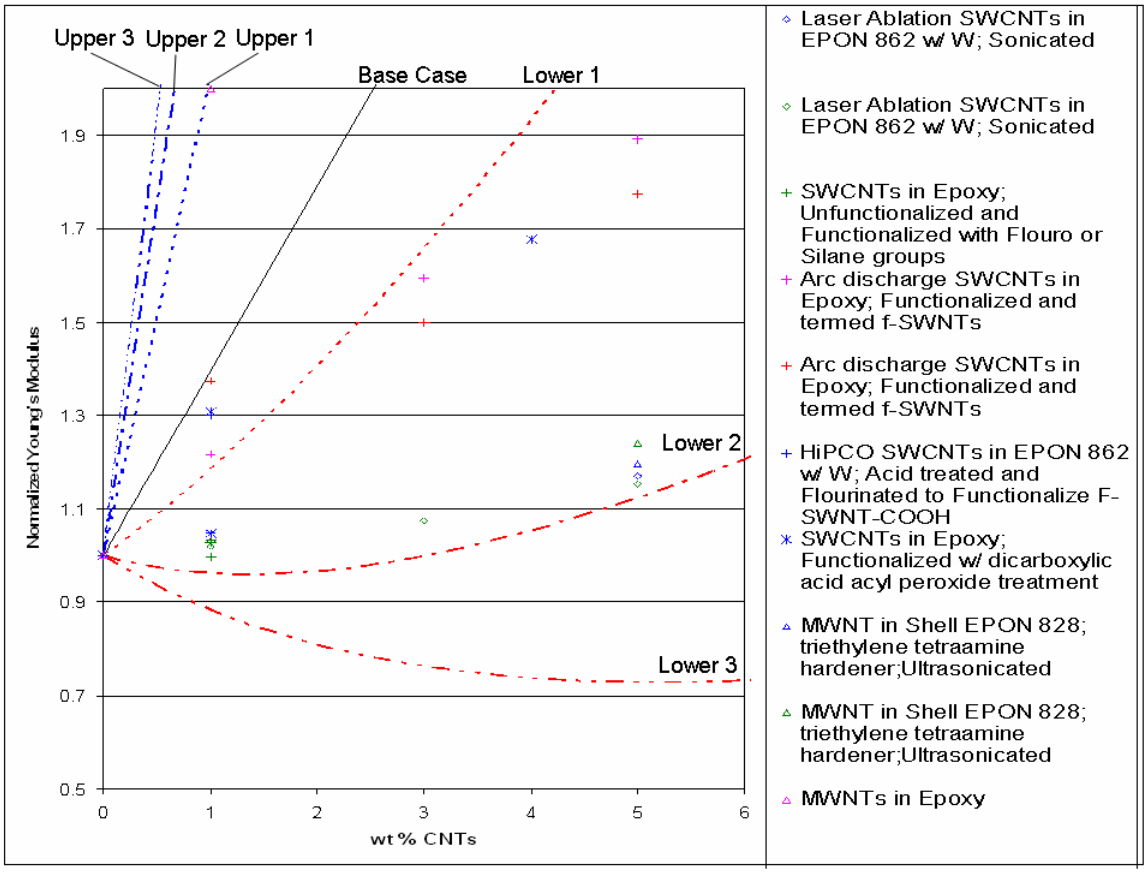

Fig. 47. Comparison of experimental data for epoxy nanocomposites from the literature with model predictions for randomly oriented carbon nanotubes with and without interphase regions. Comparisons are made between the base case which consists of non-interphase coated CNTs and three upper and lower bounds based on uncertainty in the input parameters. Details for the input parameters for the seven modeling cases are provided in Tables VII and VIII. Data from the literature comes from the following sources (in order as listed in legend): [219], [219], [225, 226], [220], [220], [33], [49], [36], [36], and [51] (Repeated entries denote slight differences in measurement or processing approaches.).

Table VII. Input parameters used in establishing upper bounds on generalized self-consistent composite cylinders modeling results of nanocomposites containing randomly oriented CNTs with and without interphase regions for use in comparison with measured data from the literature. E, ν, and t are the Young's moduli, Poisson's ratio and thickness, respectively.

	Base Case	Upper 1	Upper 2	Upper 3
E_{CNT} (GPa)	1100	1100	1800	1800
ν_{CNT}	0.14	0.14	0.14	0.14
t_{CNT} (nm)	0.34	0.34	0.34	Solid
E_{Int} (GPa)	N/A	$E_{\mathrm{CNT}} \rightarrow E_N$	$E_{\mathrm{CNT}} \rightarrow E_N$	$E_{\mathrm{CNT}} \rightarrow E_N$
ν_{Int}	N/A	0.34	0.34	0.34
t_{Int} (nm)	N/A	2.95	2.95	2.95
E_N (GPa)	2.026	2.026	2.026	2.026
ν_N	0.34	0.34	0.34	0.34

Table VIII. Input parameters used in establishing lower bounds on generalized self-consistent composite cylinders modeling results of nanocomposites containing randomly oriented CNTs with and without interphase regions for use in comparison with measured data from the literature. E, ν, and t are the Young's moduli, Poisson's ratio and thickness, respectively.

	Base Case	Lower 1	Lower 2	Lower 3
E_{CNT} (GPa)	1100	1100	475	475
ν_{CNT}	0.14	0.14	0.14	0.14
t_{CNT} (nm)	0.34	0.34	0.34	2x0.077
E_{Int} (GPa)	N/A	$0.1E_N$	$0.1E_N$	$0.1E_N$
ν_{Int}	N/A	0.34	0.34	0.34
t_{Int} (nm)	N/A	2.95	2.95	2.95
E_N (GPa)	2.026	2.026	2.026	2.026
ν_N	0.34	0.34	0.34	0.34

in this chapter. The Upper 1 and Lower 1 input parameters correspond to uncertainty in the interphase stiffness assuming an interphase thickness of three and half CNT radii. For the upper bound, the interphase is taken to have a continuous, power law gradation in properties from the CNT stiffness at the CNT-interphase interface down to the epoxy stiffness at the interphase-matrix interface (i.e., $E(r) = 555E9\ r^{-4.20}$). For the lower bound, the interphase was taken to have a constant stiffness of one tenth of the matrix stiffness. The Upper 2 and Lower 2 correspond to uncertainty in the CNT stiffness. These input parameter sets use the same interphase properties as the previous set, with the only difference being that the CNT stiffness is taken to be 1800 GPa (based on thermal vibration measurement from reference [97]) for the upper bound and 475 GPa (based on modified Cauchy-Born rule modeling from reference [92]) for the lower bound. Finally, the Upper 3 and Lower 3 parameter sets correspond to further uncertainty in the CNT thickness. Retaining the input parameters from the previous case for the interphase properties and the CNT stiffness, the CNT in the upper bound case is considered to be solid while the CNT in the lower bound case is taken to have a thickness corresponding to diameter of a carbon atom [227].

As a result of the variance in neat epoxy input data, the results are presented in Figure 47 as normalized by their respective neat epoxy values. In looking at the Base Case of randomly oriented CNTs with no interphase regions, it is observed that the model results over predict the Young's modulus for all but one data set (the set from reference [51] for MWCNTs), consistent with the observation of poor load transfer in CNT-epoxy nanocomposites. In fact, aside from this data set, it is observed that measured data from the literature can be grouped into two categories, functionalized CNT results and results for pristine and ultrasonicated CNTs. The functionalized CNT nanocomposite results show an average increases in Young's modulus relative

to the epoxy matrix of 29, 54, and 83%, at 1, 3, and 5 weight percent, respectively, while the pristine/ultrasonicated CNT nanocomposite results show smaller increases of 2.5, 7, and 18% at those same weight percents.[16] While the Base Case results over predict both groupings of data, the model predictions are closer to the functionalized CNT nanocomposite results with estimated increases relative to the matrix Young's modulus of 38, 120, and 200%, at weight percents of 1, 3, and 5%, respectively. This seems to indicate that the functionalization does appear to be improving load transfer, but that it is not yet equivalent to a perfect bonding assumption.

In comparing the first set of bounds corresponding to the variance in interphase stiffness with the same measured data in Figure 47, it is observed that the lower bound model results corresponding to a compliant interphase correlates well with the functionalized CNT nanocomposite grouping of measured data with increases in Young's modulus relative to the matrix Young's modulus of 6.7, 66, and 120% at weight percents of 1, 3, and 5%. However, it should be noted that this does not necessarily indicate that the input parameters used in obtaining the model values for this lower bound are in fact the actual values of the interphase properties as further measurements or multiscale modeling efforts will are needed to better identify this information. What this does indicate is that a compliant interphase is capable of representing the effects of functionalization on the Young's modulus of nanocomposites, and that functionalization, while improving load transfer, has yet to achieve a load transfer consistent with the perfect bonding assumptions of most micromechanics models. Interestingly, the upper bound, corresponding to a gradation in properties

[16]It is noted that these are substantial improvements relative to a compliant Young's modulus. However, compared to the axial Young's modulus values that could be obtained with the presumed CNT Young's modulus of 1100 GPa (i.e., 225, 680, and 1240% increases at 1, 3, and 5% weight), these improvements are relatively small.

from the CNT value down to the matrix value, captures well the 1% weight data point from reference [51] for MWCNTs, though it is not yet clear why in general this data set behaves so differently from the others provided in the figure.

Also of note in Figure 47, the second set of bounds, corresponding to uncertainty in the CNT stiffness, yields a good correlation between the lower bound and the pristine/ultrasonicated CNT nanocomposite grouping of the measured data, with the measured data lying just above the lower bound results. For the lower bound, percent differences in Young's moduli relative to the matrix value of -4, 0.1, and 12% at 1, 3, and 5% weight, respectively, were obtained in comparison with the 2.5, 7, and 18% differences obtained for the pristine/ultrasonicated grouping of data. This seems to indicate that, perhaps due to the presence of defects due to processing or perhaps due to the ultrasonication, the CNT stiffness may not be as high as is often reported. In addition, it is noted that the lower bound results retained the interphase properties from the previous case, which seems to also indicate that may be prudent to include interphase regions to account for van der Waals interaction even in unfunctionalized CNT nanocomposites.

Finally, it is noted that all of the measured data in the literature falls between the third set of bounds which correspond to perceived maximum and minimum values in CNT thickness and stiffness and interphase thickness. However the range of values covered by this swath is quite large, spanning from -13 to 200% difference relative to the matrix Young's modulus at 1% weight and growing from -24 to 570% and -28 to 975% difference at 3 and 5% weight, respectively. Such large ranges in potential nanocomposite elastic properties point to the need for further model refinements, perhaps through multiscale modeling efforts , and to the need for improved experimental techniques capable of probing for nanoscale properties.

CHAPTER V

EFFECTIVE ELECTRICAL CONDUCTIVITY OF NANOCOMPOSITES

Measured values of the electrical conductivity of carbon nanotube-epoxy nanocomposites have identified two unique features. The first feature is that the percolation limit is often observed to occur prior to the limits estimated by contact percolation theories [21, 54, 55], as well as at volume fractions much lower than some of the measured percolation volume fractions obtained from attempts to make conducting polymers using micron sized graphite particles or polymer blends with doped conducting polymers [228, 229].[1] The second feature is that the percolation limit identified is often preceded by an additional percolation-like effect. Both of these features are illustrated in the experimentally measured results taken from the literature provided in Figure 48.[2] The four data sets provided in Figure 48 correspond to measured values reported by Sandler et al. [54] for ultrasonicated multi-walled carbon nanotubes in epoxy, by Gojny et al. [53] for single-walled carbon nanotubes dispersed in the epoxy matrix by a three-roll mill (mini-calander), by Allaoui et al. [51] for multi-walled carbon nanotubes dispersed in a methanol solution and homogenized into the epoxy matrix, and by Martin et al. [21] for multi-walled nanotubes dispersed into the epoxy by high shear mixing.

---

[1]Nakamura et al. [228]produced graphite filled elastomers using graphite flakes, needles and spherical micron-sized particles. They measured a percolation volume fraction 0.2 for the needle and spheres and percolation volume fraction of 0.06 for the graphite flakes which had a surface area approximately 40 times that of the needles and spheres. Yang et al. [229] identified a percolation weight percent of 3.2% for polyacrylonitrile (PAN) with dispersed 20-50 nm sized particles of the conducting polymer polyaniline (PANI) doped with dodecylbenzene sulfonic acid (DBSA).

[2]Most of the data was provided in percent weight and converted to volume fraction (v_f) from weight fraction w_f by $v_f = -w_f\rho_2/(-\rho - 1 + w_f\rho_1 - w_f\rho_2)$ where ρ_1 is the density of carbon nanotubes (taken as 1.8 g/cm^3 [21]) and ρ_2 then density of the epoxy (taken as 1.175 g/cm^3 [21]).

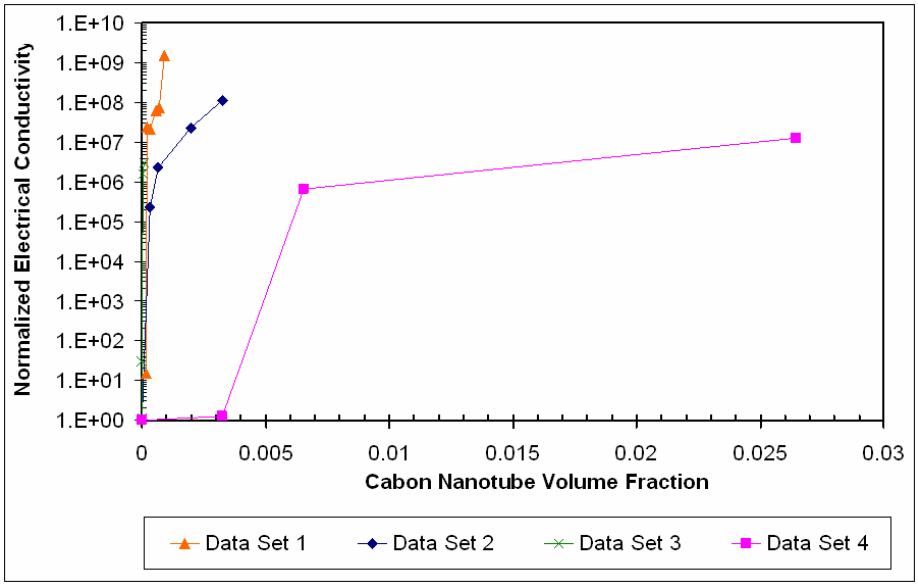

(a)

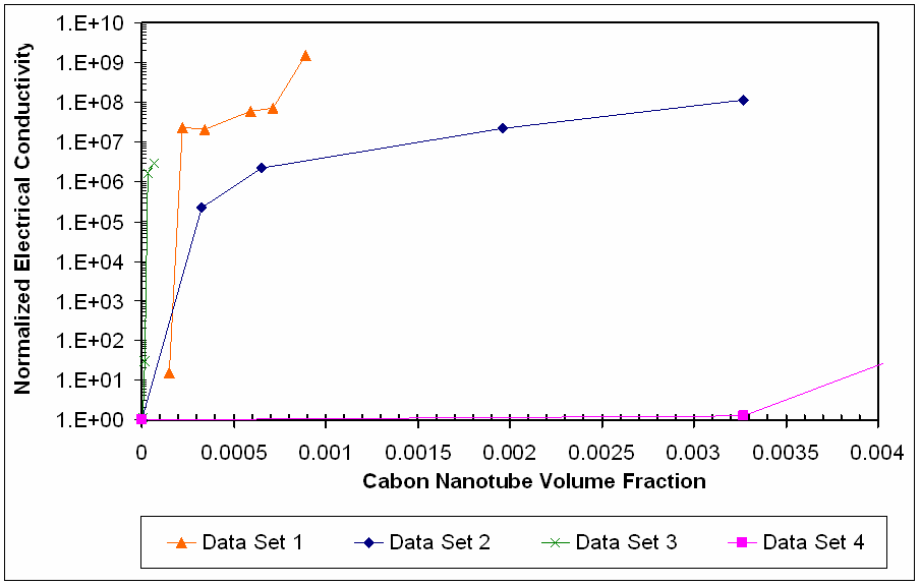

(b)

Fig. 48. Survey of experimentally measured values of carbon nanotube-epoxy nanocomposite electrical conductivity from the literature demonstrating two subcritical percolation limit behavior. Data Set 1 corresponds to reference [54], Data Set 2 to reference [53], Data Set 3 to reference [21], and Data Set 4 to reference [51]. All of the data provided is normalized by their respective matrix conductivities. Figure 48(a) displays the full range of the data taken from the literature while Figure 48(b) provides a subset of that range in order to better observe the two subcritical percolation limits for Data Sets 1, 2 and 3.

From Figure 48(a), it is observed that all of the data sets provided achieve percolation below the lower value of the range of geometric (contact) percolation limits provided via computational approaches of a volume fraction of 0.007, and from Figure 48(b), it is observed that three of the data sets reach a final percolation at volume fractions below even the lower end of the analytic estimates of a volume fraction for forming a percolated network of 0.0008. Of particular note, Data Set 1 shows an initial percolation limit at a volume fraction of 0.0002 with an increase in conductivity of nearly six orders of magnitude, followed by a brief plateau, and finally, a second percolation behavior at a volume fraction of 0.00075 with an additional three orders of magnitude increase.

Nine order of magnitude increase in conductivity may not be surprising to some as it is only a fraction of the 13 or more orders of magnitude separating the electrical conductivity of metallic carbon nanotubes, estimated to be between 150 and 200,000 S/cm [27, 59, 230], and that of some polymers, which is measured to be on the order of 10^{-12} S/cm [53]. However, assuming that, as was the case for aligned, well-dispersed CNTs as noted in Chapter IV, the ideal dispersion would result in a local volume fraction equivalent to a Dirac distribution, then the amount of polymer separating CNTs at such low volume fractions would be significant. For example, a volume fraction of 0.0002 would correspond to an ideal CNT separation of 118 nm ($\sim$ 110 nm if considering finite CNT lengths of 1 μm), with a volume fraction of 0.00075 corresponding to an ideal CNT separation of 60 nm ($\sim$ 58.6 nm for finite CNT lengths)[3] These distances may seem small, however, Lesiak et al. [231] have

[3]For infinitely long CNTs, the separation distance is estimated from composite cylinder assemblage volume fraction of CNT ($v_f = r_{\text{CNT}}^2/r_N^2$), which is then doubled and from which twice the CNT radius (0.85 nm) is subtracted. For the finite length estimate, the volume fraction is instead calculated from the ratio of the CNT of length, L, embedded in a matrix of thickness, t, in both the radial direction and in the z-direction.

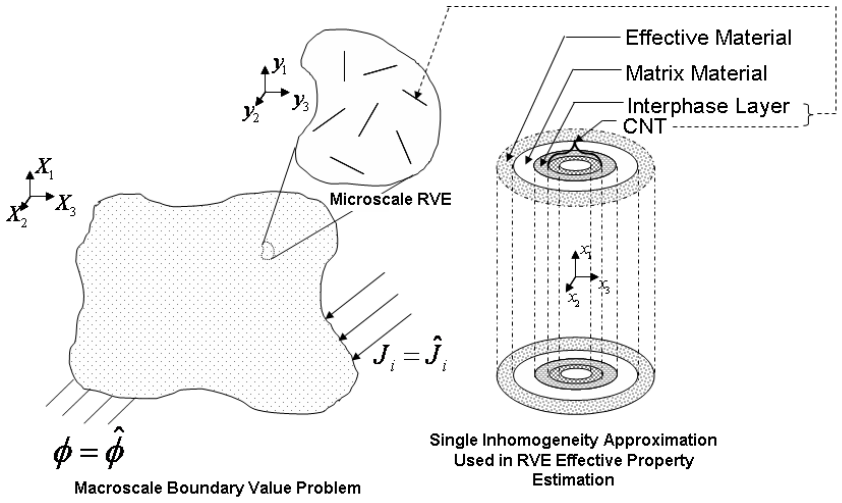

Fig. 49. Schematic representation of the application of the generalized self-consistent composite cylinders approximation for randomly oriented, well-dispersed CNT nanocomposites in determining effective electrical conductivity.

reported electron mean free paths in polyaniline (PANI), which is considered to be a conducting polymer, of 0.1 to 10 nm. Thus, for non-conducting polymers, these separation distances are large compared to the mean free path of electrons, indicating that there may be sufficient polymer present to insulate CNTs in an ideal dispersion.

Here an attempt is made to understand the observed subcritical, double percolation behavior of CNT-polymer nanocomposites using the generalized self-consistent composite cylinders method for randomly oriented, well-dispersed[4] CNTs both with and without interphase regions (see for example Figure 49) as described in Chapter III using Eqn. 2.163d (with ξ_{ij} replaced by $\check{\rho}_{ij}$ as a result of the noted mathematical analogy between electrical and thermal conductivity/resistivity). As was the case

[4]By well-dispersed it is meant that the CNTs have the ideal distribution, and therefore are fully encompassed by the polymer matrix, i.e. there is no direct CNT-CNT contact. As such, the model is not intended to capture contact percolation, but instead is for non-contact percolation behavior.

for the elastic properties reported in the previous chapter, the CNTs are assumed to be straight and defect free with a sufficiently high aspect ratio so as to consider the CNTs as infinitely long, again with outer radius of 0.85 nm and a thickness of 0.34 nm. While it is noted that CNTs may be either semiconducting or metallic depending on the chiral angle[5] as illustrated in Figure 26, here it is assumed that the volume fractions of CNTs reported in the subsequent results correspond to the metallic CNTs.[6] As such, the CNT conductivity is taken from the average of the range of metallic CNT conductivities reported by Ebbesen et al. [27] as 1000 S/cm.

Given the even larger discrepancy between the CNT and polymer properties (i.e., 13 orders of magnitude difference in conductivities as compared to 3 orders of magnitude for the Young's modulus), parametric studies on the effect of CNT:matrix conductivity ratio, CF, on the effective conductivities of nanocomposites containing randomly oriented CNTs are provided in Figure 50. The CNT:matrix conductivity ratio is taken from 10 (corresponding to a very conductive matrix as the CNT conductivity is considered fixed at 1000 S/cm) to a value of 10^{14}, representative of the disparity in conductivity between non-conducting polymers and carbon nanotubes. It is noted that beyond a ratio of 10^3 there is little impact of increased CNT:matrix conductivity on the effective nanocomposite conductivity. In fact, out to volume fractions as large as 0.6, the effective nanocomposite response for the CNT:matrix ratios between 10^3 and 10^{14} is only a factor of 5 increase relative to the matrix, indicating that initial expectations of extremely large increases at low volume fractions (e.g.,

[5]The elastic properties have been noted to be independent of chiral angle.

[6]This assumption amounts to assuming that a processing method can preferentially produce a given chirality, or that the semiconducting CNTs are at most as conductive the polymer in which they are embedded at voltages lower than the band gap. It was noted by Odom et al. [232], that some had reported that laser vaporization and arc discharge production of SWCNTs had produced predominantly metallic (10,10) armchair CNTs, but from their results, that no one chirality dominated.

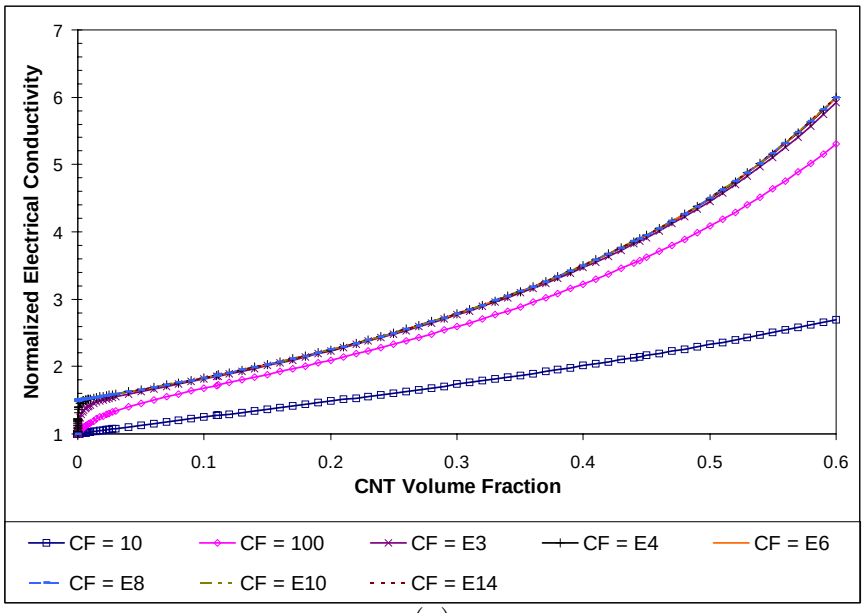

(a)

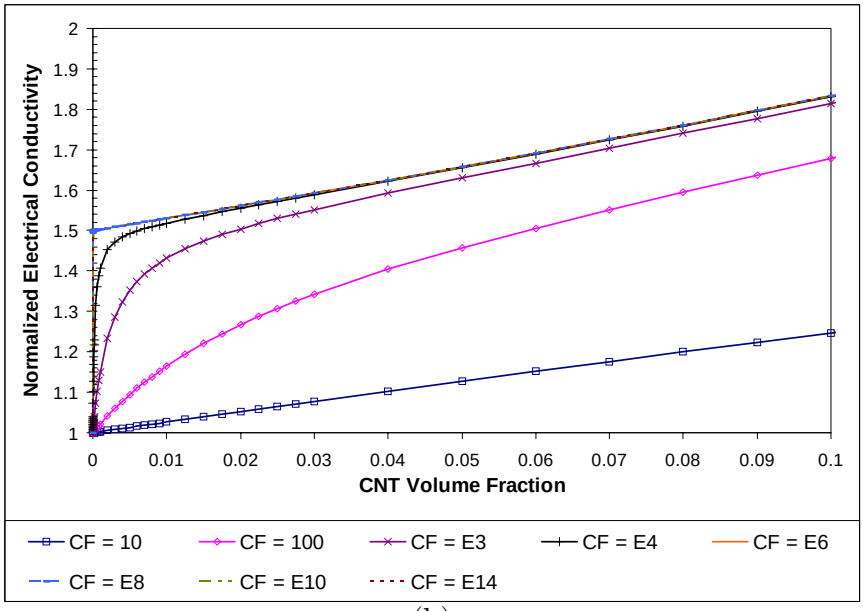

(b)

Fig. 50. Parametric study on the effect of CNT:matrix conductivity ratio, CF, on the effective electrical conductivity of randomly oriented composite cylinder assemblages. The CNT conductivity was taken as 1000 S/cm, with CNT inner and outer radius of 0.51 and 0.85 nm, respectively. Values for effective conductivities are reported as normalized relative to the matrix conductivity. Figure 50(a) effective conductivity out to a volume fraction of 0.6. Figure 50(b) effective conductivity out to a volume fraction of 0.1 demonstrating effect of the CNT:matrix conductivity ratio on the initial increase in conductivity at very low volume fractions.

rule of mixtures estimates could be as high as 12 orders of magnitude at 1% volume fraction) strictly due to the large conductivity of CNTs may be unrealistic.[7] It is also interesting to note that even the changes in the initial conductivity observed in Figure 50(b) are saturated when considering CNT conductivities six orders of magnitude larger than the matrix. This indicates that the assumption of CNT conductivity of 1000 S/cm, which is nearer to the lower end of the range of reported CNT conductivities, is sufficiently large so as to represent metallic CNTs in non-conducting polymer matrices even at low CNT volume fractions. Perhaps more importantly, this also indicates that to obtain dramatic increases in effective nanocomposite conductivity of nearly five orders of magnitude or more, the introduction of an interphase layer will be necessary.

Making a similar assumption as was the case with the elastic properties that the disturbance of the polymer structure near the CNT surface may alter the properties of the CNT, an interphase region of perturbed polymer is assumed to envelope the CNTs in the nanocomposite. A parametric study on the effects of this interphase's thickness, as measured by the interphase:CNT thickness ratio, TF = $t_{\text{Int}}/r_{\text{CNT}}$ where t_{Int} is the interphase thickness, and on the interphase:matrix conductivity ratio, ICF, on the effective electrical conductivity of randomly interphase coated CNTs is shown in Figure 51. To better illustrate the effects of the interphase region, the CNT:matrix conductivity ratio was selected as E4. Interphases thickness ratios of 1/2, 1, and 2 times the CNT radius are provided (based on the arguments provided in Chapter IV), with interphase conductivity factors of 10, 100, and 1000 times the matrix value. From Figure 51(a) an immediate impact of the interphase is observed with the sharp,

[7]Sandler et al. [55] expressed disappointment at obtaining 0.002 S/cm at a weight fraction of 0.01: "...the relatively low maximum conductivity observed. The value of about 2 S/m for a loading fraction of 1 wt% of nanotubes, is orders of magnitude lower than the expected intrinsic nanotube conductivity."

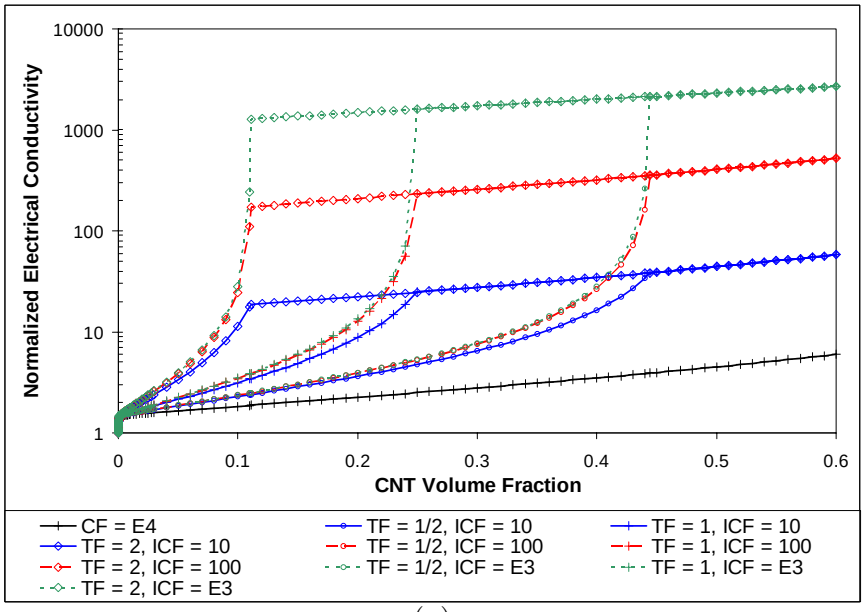

(a)

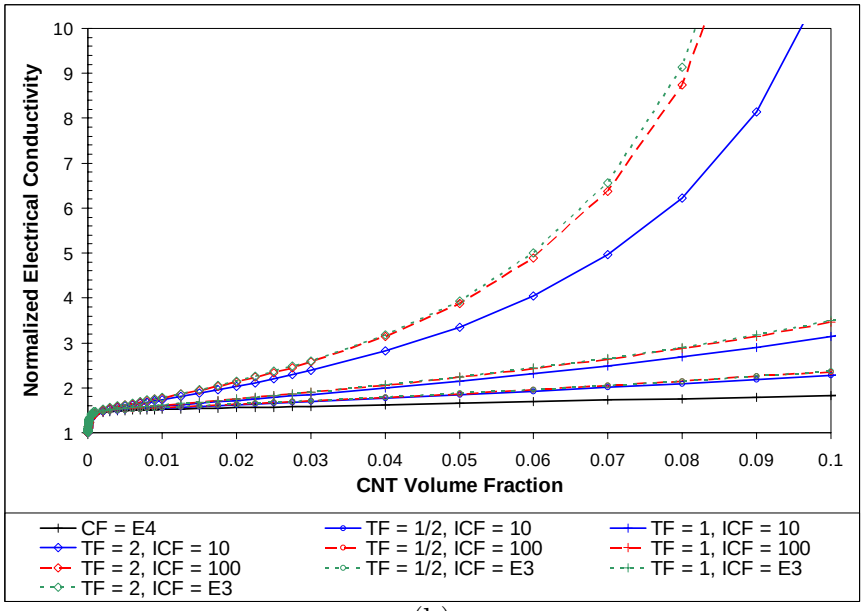

(b)

Fig. 51. Parametric study on the effects of interphase thickness as measured by the interphase:CNT thickness ratio, TF = $t_{\text{Int}}/r_{\text{CNT}}$ where t_{Int} is the interphase thickness, and on the interphase:matrix conductivity ratio, ICF, on the effective electrical conductivity of randomly oriented, $N = 3$ composite cylinder assemblages. To better illustrate the effects of the interphase region, the CNT:matrix conductivity ratio was selected as E4. Figure 51(a) Log-plot of effective conductivity out to a volume fraction of 0.6. Figure 51(b) effect conductivity out to a volume fraction of 0.1 demonstrating the effects of interphase thickness and conductivity on the initial increase in conductivity at very low volume fractions.

orders of magnitude increases in the effective conductivity preceding a secondary plateau. The effect of the interphase thickness is observed to dictate where this sharp increase occurs, with the magnitude of the interphase conductivity controlling the behavior after the sharp increase. The reasons for this, which are discussed in detail in Chapter IV and shown schematically in Figure 36, are associated with the volume fraction of the matrix in a $N = 3$ composite cylinder assemblage decreasing with increasing CNT volume fraction to the point where the CNT is instead embedded in just the interphase, i.e., a $N = 2$ composite cylinder assemblage.

Thus, the sharp increase in the effective conductivity in Figure 51 is seen as a result of the increasing influence of the interphase region as the matrix is steadily consumed with increasing CNT volume fraction. The effective conductivity asymptotically approaches the effective interphase-CNT value as the critical volume fraction is approached. After the critical volume fraction is surpassed, the effective composite response is that of the 2-phase CNT-interphase composite. As noted previously, the effect of the interphase thickness is to shift the critical volume fraction. The thicker the interphase region, the lower the critical volume fraction, and hence, where the 2-phase composite response is intercepted. This allows one to have some control over the initial slope of the 3-phase conductivity as shown in Figure 51(b). Note that the 2-phase results will exhibit the same behavior as observed in Figure 50 so that the composite is expected to be dominated by the new matrix material, and hence, further large increases in effective conductivity would not occur without additional interphase regions.

Further, it allows one to assess whether or not it is reasonable to expect that an interphase region due the perturbed structure of the polymer can reasonably account for the large increases in CNT-polymer nanocomposites as observed in Figure 48. First, recall that the separation distances identified in the ideal dispersion for the

volume fractions at which percolation behavior is observed were on the order of 60 to 100 nm. While it is unclear if the polymer structure may be significantly disturbed over such a distance in general, certainly such distances are inconsistent with interphase thickness observed in Figure 3(b) where the interphase thickness is observed to be much less than 20 nm. Second, recall that the amount of increase in conductivity of the interphase relative to the matrix needed to explain the measured data is on the order of 6 or more orders of magnitude. Such large changes in polymer conductivity due to structural influences may be unreasonable. Thus, while there is likely an interphase region due to the disturbance of the polymer structure in the presence of the interphase region as noted by Smith et al. [71], such an interphase region does not sufficiently explain the large increases in conductivity observed in the measured data below the contact percolation limit.

Many [42, 59, 71, 75] have instead indicated that the dominant mechanism which might explain the observed electrical conductivity measurements of nanocomposites is the nanoscale effect of electron hopping between nanotubes within the polymer. This hopping of electrons can occur intra-tube or from one nanotube to another, and is dependent on separation distance between the tubes (or parts of the same tube) and the material in between them.

While there appears to be some consensus that electron hopping governs CNT-polymer nanocomposite conductivity, how the conductivity is impacted remains a point of debate. Some [59, 75] have indicated that the electron hopping mechanism is a source of resistance in CNT-polymer nanocomposites while others [42, 71] have indicated it to be a source of increased conductivity. However, in light of Figure 50, it is believed that the electron hopping mechanism is in fact a source of increased conductivity, allowing the formation of conductive networks prior to nanotube contact, and that efforts to explain the hopping mechanism as a source of resistance are perhaps

a product of expecting a rule of mixtures effective nanocomposite conductivity.

As nanoscale effects such as electron hopping are not generally included in continuum models for effective conductivity, the generalized self-consistent composite cylinders model is employed to incorporate the electron hopping mechanism through the incorporation of interphase layers of increased conductivity representing the increased likelihood of electron hopping as the volume fraction of nanotubes is increased, and hence, the tube-tube distance decreased. In applying this model, it is necessary to identify both the interphase(s) conductivity and thickness. Estimates corresponding to a conductivity for such an interphase region are difficult to obtain, however, estimates of the thickness may be obtained from observations in the literature. Some [42, 75] have estimated that for the electron hopping mechanism to be activated, CNTs must be no more than 5 nm apart, while others [233, 234] have provided estimates from 26 to 80 nm.[8] As from Figure 51 it was observed that interphase thickness governs where percolation behavior is observed, it is noted that values of 5, 26, and 80 nm correspond to critical volume fractions of 0.065, 0.0037, and 0.00044, respectively, which are close to the percolation volume fractions identified for Data Set 1 in Figure 48. As such, Data Set 1 will be used in order to identify potential values for the interphase in a generalized self-consistent composite cylinder model for randomly oriented CNTs in an epoxy matrix as shown in Figure 52.

In order to provide perspective, it is first noted that the results for a 2-phase generalized self-consistent composite cylinders model corresponding to randomly oriented CNTs in the polymer matrix with no interphase region are provided in Figure 52. Here it is observed that the resulting effective nanocomposite response was matrix dominated, not even able to intercept the first data point of the data set. The reason for

[8]The value of 80 nm taken from reference [234], though not for CNTs, is provided as example of electron hopping ranges in general.

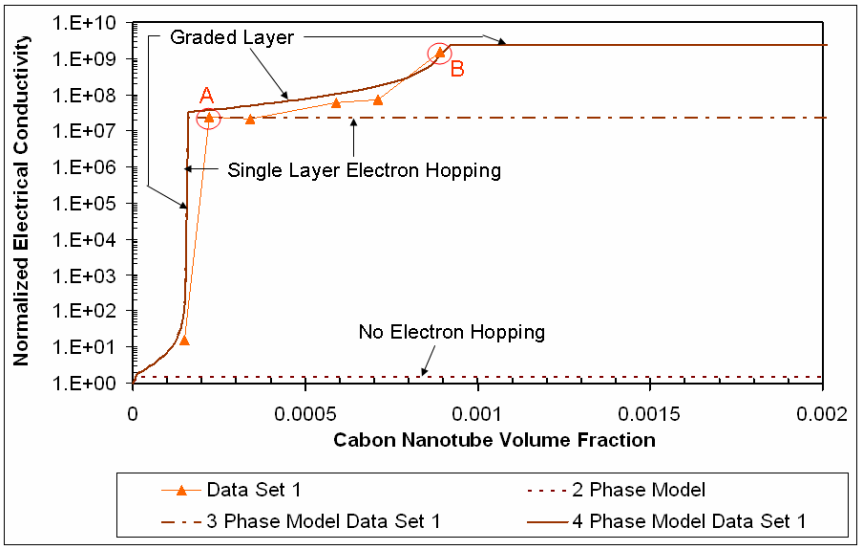

Fig. 52. Comparison of randomly oriented 2-, 3-, and 4-phase composite cylinders models with experimentally measured values from Data Set 1 [54]. Point A is used to calibrate 3- and 4-phase models by indicating an interphase conductivity corresponding to an approximately 8 order of magnitude increase in conductivity relative to matrix and by indicating a total interphase thickness of 68 nm. Point B is used to further calibrate the 4-phase model by indicating a second interphase conductivity corresponding to an approximately 10 order of magnitude increase in conductivity relative to matrix and by indicating the second interphase thickness of 27 nm.

this two fold. The first reason being the assumption that the nanotubes are so well dispersed, that at such a low volume fraction, each nanotube is completely wet by the surrounding polymer matrix, and therefore unable to make direct contact with one another to establish a direct connection percolation path. As was observed in the parametric studies, this can be directly attributed to the large disparity between the conductivities of the nanotube and the matrix, a nearly 15 order of magnitude difference. The second reason for the matrix dominant behavior is the lack of inclusion of nanoscale effects such as the electron hopping.

The next set of results of note correspond to a 3-phase composite cylinder model consisting of the nanotube, an interphase layer, and the matrix. The interphase layer is introduced into the composite cylinder assemblage with a conductivity which is augmented relative to the matrix conductivity in order to reflect the increased likelihood of electrons hopping from one nanotube to the next as they are brought into closer proximity with increasing volume fraction. The thickness of the interphase layer is determined by the location of the jump in the data set at a volume fraction of approximately 0.00015 (just prior to Point A), which is then the critical volume fraction for the 3-phase model, corresponding to a CNT separation of 137 nm. The second parameter, the interphase conductivity, is determined by the value of the first data point after the jump (Point A) so that once the matrix is consumed, the remaining 2-phase model will fit the first data point. As seen in Figure 52, the 3-phase portion of the model captures well the initial percolation behavior and reduces to a 2-phase model at the desired volume fraction. However, the 2-phase portion of this model subsequently only captures well the first data point of the second percolation behavior (.i.e., the data point which was used to calibrate the conductivity of the interphase), and the second data point thereafter. The remaining three data points are not well modeled with this 3-phase model, indicating the need for yet another inter-

phase layer to capture the secondary percolation event. Though a direct correlation is not herein made, one could view the combination of the two interphase regions in a 4-phase model as a means for modeling the increase probability of electron hopping as nanotubes are brought into increasingly closer proximity. [9]

The 4-phase generalized self-consistent composite cylinder model, consisting of the nanotube, two distinct interphase layers, and the matrix, is observed in Figure 52 to provide a much more accurate correlation to Data Set 1. In the 4-phase model, the total interphase thickness is now defined by the initial jump in the data set at a volume fraction of 0.00015 (just prior to Point A), corresponding to the 137 nm of separation between CNTs. The interphase layer closest to the nanotube, which will have the larger conductivity of the two interphase regions as determined by the second percolation event conductivity, has a thickness determined by the second percolation volume fraction in the data at a volume fraction of 0.0009 (at Point B corresponding to a CNT separation of 55 nm), thus constraining the two interphase thickness parameters and leading to two critical volume fractions. The second interphase layer retains the conductivity of the lone interphase layer from the 3-phase composite cylinder model. Thus, in comparing the 3- and 4-phase composite cylinder model configurations, it is as if the additional interphase is obtained by taking the portion of the 3-phase composite cylinder model closest to the nanotube and augmenting its conductivity. The resulting 4-phase model thus retains the ability to capture the effective conductivity prior to the initial percolation limit (as a saturation effect was observed in the parametric studies), then transitions after the first critical volume fraction to a 3-phase portion of the model consisting of the nanotube and the two interphase layers,

[9] If one were to obtain a continuous curve for the probability of electron hopping with respect to nanotube separation, this curve could be fit with an increasing number of interphase regions or use a graded interphase region.

Table IX. Geometry and electrical conductivities applied in the 2-, 3- and 4-phase composite cylinder models. All geometry data provided in nm and conductivities in S/cm. The radius of the carbon nanotube is taken to be $r_{\text{cnt}} = 0.85$ nm with a thickness of 0.34 nm in which the conductivity is taken to be $\sigma_{\text{cnt}} = 1\text{E}3$ S/cm The radius of the matrix phase (prior to being consumed) is given by $r_N = r_{\text{cnt}}/\sqrt{c_f}$

	2-Phase		**3-Phase D1**		**4-Phase D1**		**4-Phase D4**	
	r_i	σ_i	r_i	σ_i	r_i	σ_i	r_i	σ_i
Phase 1	r_{cnt}	σ_{cnt}	r_{cnt}	σ_{cnt}	r_{cnt}	σ_{cnt}	r_{cnt}	σ_{cnt}
Phase 2	r_N	$3.3\text{E}-12$	69.1	$5\text{E}-5$	28.3	$5\text{E}-3$	4.9	$5\text{E}-3$
Phase 3	-	-	r_N	$3.3\text{E}-12$	69.1	$5\text{E}-5$	13.4	$3\text{E}-3$
Phase 4	-	-	-	-	r_N	$3.3\text{E}-12$	r_N	$3\text{E}-10$

and finally transitions to a 2-phase portion after the second critical volume fraction consisting of the nanotube and the inner most interphase layer (as depicted by the arrows in Figure 52). The resulting 4-phase model thus captures well the measured conductivity values in Data Set 1, capturing the secondary percolation and predicting nanocomposite conductivities in good agreement with data points prior to Point A and between Points A and B. The thickness and conductivity parameters used in each of these models is provided in Table IX.

As a result of the relatively good agreement between Data Sets 1 through 3, the 4-phase composite cylinder model can be taken as a representative of all three data sets. Data Set 4, however, demonstrates a drastically different response, perhaps due to some unidentified processing difference. Taking the same approach as was done for Data Set 1, a 4-phase generalized self-consistent composite cylinder model with good correlation to Data Set 4 is shown in Figure 53, the interphase parameters of which

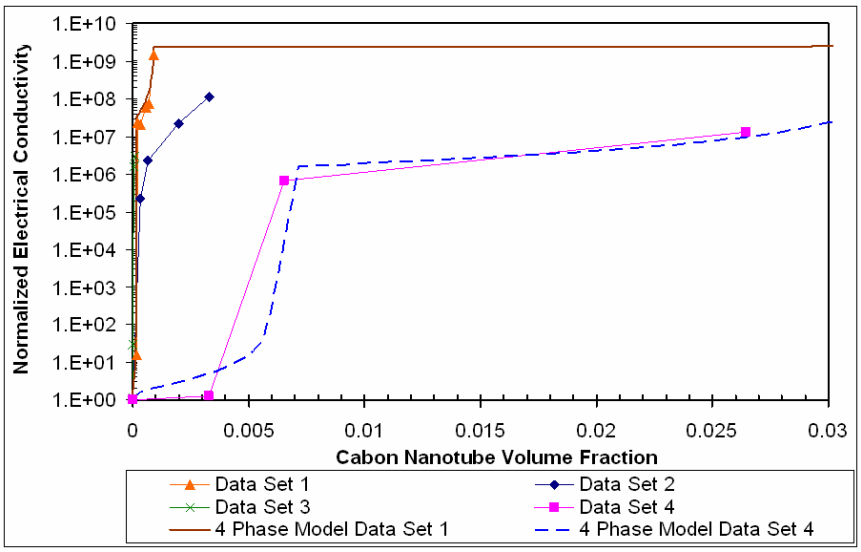

Fig. 53. Comparison of randomly oriented 4-phase composite cylinders model fits with experimentally measured values from the literature. Data Set 1 corresponds to [54], Data Set 2 to [53], Data Set 3 to [21], and Data Set 4 to [51].

are also provided in Table IX. The two 4-phase generalized self-consistent composite cylinders models together can be used to provide a range of values for the interphase thicknesses and conductivities. While the initial increase in conductivities for both 4-phase models is observed to be seven orders of magnitude, the total interphase thickness is seen to have a range 10 - 70 nm. It is not yet clear if such a range reflects differences in processing or mechanisms, or could be correlated to do so. However, it is of interest to note that the thickness of first interphase layer for 4-phase model that correlates with Data Set 4 is comparable to the value identified as the requisite distance for electron hopping in reference [42] for single walled carbon nanotubes in PMMA. Thus, the generalized self-consistent composite cylinders model may be a useful tool in modeling the nanoscale effects leading to percolation-like effects prior to the onset of contact percolation.

For example, if the generalized self-consistent composite cylinder model with suf-

ficiently accurate representations of the electron hopping mechanism using interphase regions is established, the increase in conductivity at given volume fraction for an ideal distribution of CNTs provided by such a model could then be used to assess how well dispersed CNTs are in a sample measured in the lab. Nanocomposites which demonstrate percolation behavior at volume fractions lower than predicted for the ideal dispersion would correspond to poor dispersions of CNTs while sample with percolation behaviors closer to the ideal case would correspond to better dispersions. Here it is noted, however, that the generalized self-consistent composite cylinder model will need to also be calibrated for the effects of differing functionalizations, bearing in mind that some functionalizations are intended to improve dispersion while others are intended to improve bonding, thus pointing to the competing roles of functionalization in meeting the demands of nanocomposites in terms of elastic and electrical properties, both of which can be modeled using the generalized self-consistent composite cylinder model.[10]

[10]It has been argued that the functionalization of nanotubes can lead to a distinct region of altered polymer surrounding the nanotubes [53, 161]. The effect of such interphase layers on the mechanical properties of nanotube-epoxy nanocomposites has been examined with the composite cylinder solutions by [161] and in Chapter IV. It is noted that the interphase layers for mechanical and electrical properties may be of different size, number and functionality as a result of the different mechanisms between the two properties.

CHAPTER VI

EFFECTIVE THERMAL CONDUCTIVITY OF NANOCOMPOSITES

Measured values from the literature [72–76] for the thermal conductivity of carbon nanotube-polymer matrix composites at different volume fractions of carbon nanotubes are provided in Figure 54, normalized by their respective matrix conductivities.[1] Some of the measured values come from work by Song and Youn [72] for nanocomposites consisting of single-walled carbon nanotubes in epoxy. Additional data comes from work by Bryning et al. [73] for nanocomposites consisting DMF treated and surfactant dispersed, respectively, HiPCO carbon nanotubes in epoxy. For these three sets of data it is of interest to note the large differences between measured values for CNTs dispersed in the same matrix, believed to be due to differences in processing methods. Data points taken from Winey et al. [74] are the average of several measurements from also from Winey et al. [75] for single-walled carbon nanotubes in PMMA. Data from the work by Xu et al. [76] is for nanocomposites consisting of single-walled carbon nanotubes in PVDF. Also included in Figure 54 are the often cited and modeled results from Choi et al. [235] for suspensions of CNTs in a synthetic poly (α-olefin) oil. It is of interest to note that the data from Choi et al. demonstrates the largest increases in thermal conductivity with increasing CNT volume fraction.

It is also noted from Figure 54 that, despite the large disparity in thermal conductivity between CNTs (250-6600 W/mK [82, 235–237]) and polymers (0.175-0.225 W/mK [73–76]), and despite the mathematical analogy between the governing differ-

[1]Some of the data in the literature was provided in wt. % and converted to volume fraction by $v_f = w_f\rho_{poly}/(\rho_{cnt} - w_f\rho_{cnt} + w_f\rho_{poly})$ where w_f is the weight fraction, ρ_{cnt} the density of carbon nanotubes (taken as 1.8 g/cm^3) and ρ_{poly} the density of the polymer matrix (nominally assumed to be 1.175 g/cm^3).

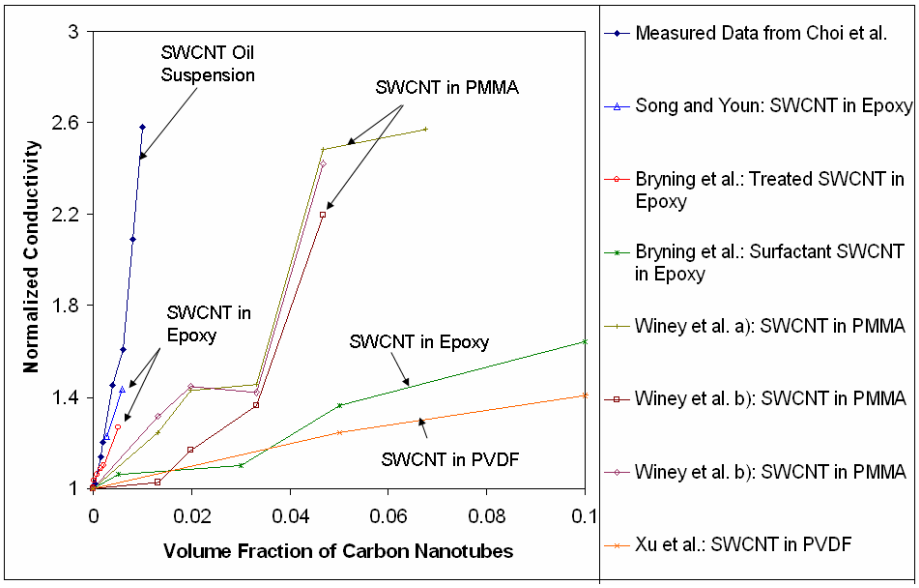

Fig. 54. Sampling of available data in the literature for the thermal conductivity of carbon nanotube-polymer composites normalized by the matrix conductivity. Measured values from Choi et al. [235] are for a suspension of single-walled carbon nanotubes in a synthetic poly (α-olefin) oil. Song and Youn [72] measurements are for single-walled carbon nanotubes in epoxy. Bryning et al. [73] measurements are for DMF treated and surfactant dispersed, respectively, HiPCO carbon nanotubes in epoxy. Winey et al. a) [74] is the average of several measurements from Winey et al. b) [75] for single-walled carbon nanotubes in PMMA. Xu et al. [76] measurements are for single-walled carbon nanotubes in PVDF.

ential equations for thermal and electrical conductivity, that the thermal conductivity data does not demonstrate the percolation behavior observed in the electrical conductivity data. This is a result of the difference in nanoscale effects between the two properties. The electrical conductivity of nanocomposites was identified to be governed by an electron hopping mechanism which acted to increase conductivity (see Chapter V). However, for the thermal conductivity of CNT nanocomposites, many [73, 75, 77, 79, 82, 85, 123] have identified the presence of an interface thermal resistance, often referred to as the Kapitza resistance [238–240], as the nanoscale phenomenon which governs conductivity. The Kapitza resistance is identified as being the result of a large impedance of thermal phonons across an interface due to acoustic mismatch between materials. It is defined in terms of a temperature difference across an interface of area, A, and the total heat flux across the interface, Q, by

$$R_{\text{Kap}} = \frac{A \triangle T}{Q} \tag{6.1}$$

and is traditionally measured for solid-liquid interfaces to better control thermal exchange conditions, but is applicable to solid-solid interfaces.

As it is difficult to directly probe the interface between carbon nanotubes and the polymers in which they are embedded in the lab, some [78, 79] have used molecular dynamics simulations to estimate the interfacial thermal resistance. Based on temperature decay times on the order of tens of picoseconds, such efforts have yielded estimates for the interfacial thermal resistance on the order of 10^{-8} $\text{m}^2\text{K/W}$. Using molecular dynamics estimates of the interfacial thermal resistance as a starting point, many [73, 79, 81–84] have used effective medium approaches (EMA) [85] in parametric studies to theoretically assess the potential impact of the interfacial thermal resistance on effective nanocomposite thermal conductivity. In an alternative approach, Chen et al. [90] introduced the interfacial thermal resistance in the form

of a jump factor [241] in conjunction with a Mori-Tanaka approach [127, 189, 242] for randomly oriented, well-dispersed solid isotropic nanotubes to theoretically investigate the potential impact of the interface thermal resistance.

In the present work, the generalized self-consistent composite cylinders method is employed to predict the effective thermal conductivity (see Chapter III) of nanocomposites consisting of randomly oriented CNTs in a polymer matrix. As was the case in predicting the effective elastic properties and electrical conductivities of nanocomposites in the previous chapters, the CNTs are taken to be straight, defect-free, and of sufficiently high aspect ratio so as to be considered infinitely long. Further, it is noted that unlike the electrical properties of CNTs, the thermal properties of CNTs are not dependent on chiral angle [122] so that the volume fraction of CNTs reported corresponds to the total volume fraction for all chiral angles. As was similarly done for the electrical properties of CNT-polymer nanocomposites, the nanoscale effects, which for thermal conductivity stem from the Kapitza resistance, are incorporated into the micromechanics model through the inclusion of an interphase region, as shown schematically in Figure 55.

Before assessing the influence of the Kapitza resistance on the effective thermal conductivity of CNT-polymer nanocomposites, it is of interest to first note the resulting micromechanics predictions of the effective thermal conductivity of such nanocomposites under the ideal assumption of perfect heat transfer across the CNT-polymer interface typically reflected in continuity of heat flux and temperature assumptions. As such, generalized self-consistent composite cylinder model results for the effective thermal conductivity of nanocomposites containing randomly oriented CNTs (i.e. an $N = 2$ composite cylinder assemblage with $k_{11}^{(1)} = k_{22}^{(1)} = k_{33}^{(1)} = k^{\text{CNT}} = 2000$ W/mK, $r_1 = 0.85$ nm, and nanotube thickness of $t_{\text{CNT}} = 0.34$ nm embedded in an epoxy matrix ($k_{11}^{(2)} = k_{22}^{(2)} = k_{33}^{(2)} = k^M = 0.16725$ W/mK) are provided in Figure 56. The

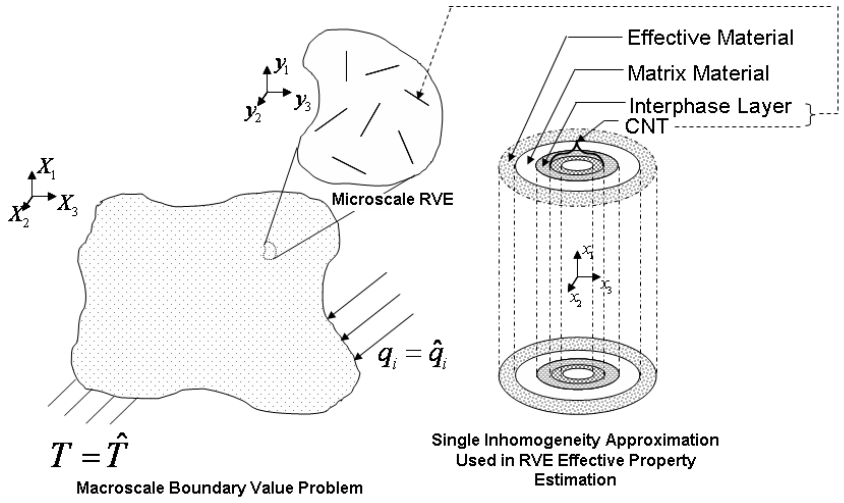

Fig. 55. Schematic representation of the application of the generalized self-consistent composite cylinders approximation for randomly oriented, well-dispersed CNT nanocomposites in determining effective thermal conductivity.

resulting thermal conductivities are normalized by the matrix thermal conductivity.

Also provided in the figure are the results obtained from a Maxwell-Garnett Effective Medium Approach (MG-EMA) employed by Nan et al. [77, 82] and a Mori-Tanaka approach [127, 189, 242] employed by Chen et al. [90], both of which treat the CNTs as randomly oriented isotropic solid cylinders. It is noted that, for these cases, which do not include the effects of interfacial thermal resistance, the MG-EMA and Mori-Tanaka approaches yield identical results and predict an effective nanocomposite thermal conductivity which is orders of magnitude larger than the results obtained from the generalized self-consistent composite cylinder method employed herein. Upon closer inspection of the theory behind the MG-EMA (see for example [243], it is found that the MG-EMA and Mori-Tanaka methods are based on the same philosophy of using single inclusions embedded in an infinite matrix material subject to a perturbation in the thermal gradient to obtain effective thermal

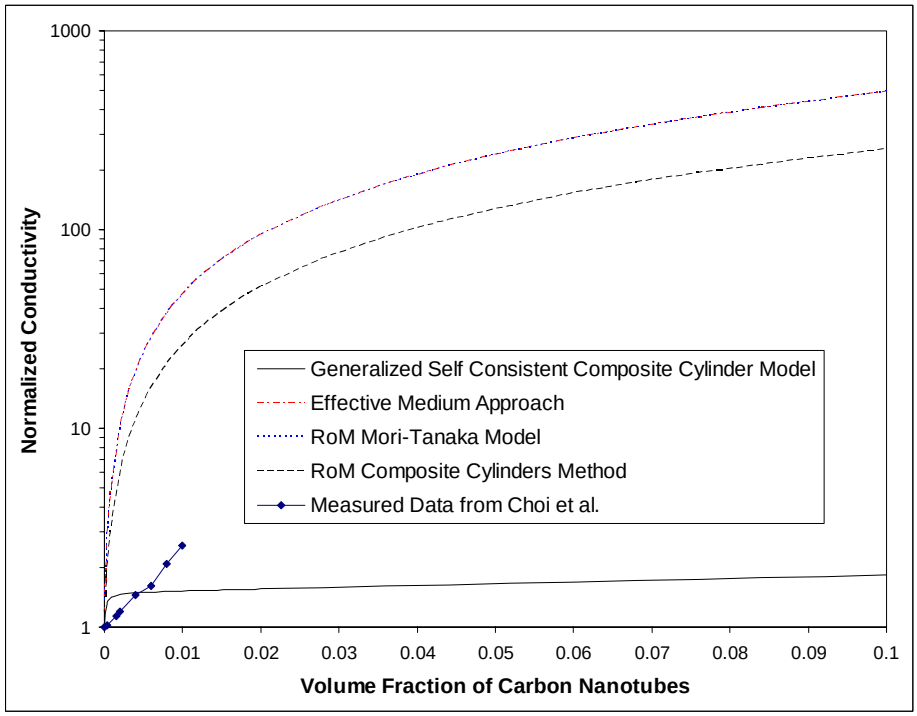

Fig. 56. Initial comparison of micromechanics modeling approaches for the effective thermal conductivity of CNT nanocomposites with the experimental data obtained by Choi et al. [235]. Comparisons are made between the Effective Medium Approach (Maxwell-Garnett) method used by Nan et al. [77, 82], the Mori-Tanaka method as used by Chen et al. [90] and the generalized self-consistent composite cylinders model employed herein illustrating the difference between a rule of mixtures approach to orientational averaging (the two former) versus accounting for interactions in the orientational averaging (the latter). A final comparison is made to a fourth micromechancis approach in which a composite cylinders model is used to obtain an effective nanotube which is then averaged over all orientations using a rule of mixtures.

conductivities through the definition of the thermal Eshelby tensors, and that both methods account for random orientations of inclusions in exactly the same manner. As such, it is not surprising that both methods yield identical results. The natural question then is why are these two methods providing such different results from the generalized self-consistent composite cylinders method employed herein.

One possible explanation for the differences in the results was thought to be the treatment of CNTs as solid isotropic cylinders in the MG-EMA and Mori-Tanaka methods versus the inclusion of the hollow region of the CNT in the generalized self-consistent composite cylinder method. As such, as was similarly done for the elastic properties, the composite cylinder method was used to identify an effective solid cylinder having transversely isotropic properties based on the hollow cylinder geometry used in the generalized self-consistent composite cylinder method. The effective transversely isotropic solid cylinder was then used in the Mori-Tanaka method as applied by Chen et al. [90] to yield the curve identified as *RoM Composite Cylinder Method* in Figure 56. There it is noted that accounting for the hollow nature alone does not explain the differences observed between the MG-EMA and Mori-Tanaka methods and the generalized self-consistent composite cylinder method.

Instead, the large differences between these methods stems from the manner in which the effects of random orientation are accounted for. In the MG-EMA and Mori-Tanaka methods as employed by Nan et al. [77, 82] and Chen et al. [90], respectively, the effects of random orientation are accounted for in such a way that the concentration tensor in Eqn. 3.131b would be the identity tensor. As such, these approaches reduce to a rule of mixtures approach towards averaging all orientations. In contrast, the generalized self-consistent composite cylinder method employed herein accounts for interactions between the various orientations of CNTs in a self-consistent manner and therefore results in a concentration tensor which is not the identity tensor.

Further, though not shown in Figure 56, it is noted that using the effective transversely isotropic cylinder for the CNT in a Mori-Tanaka method which also accounts for interactions in a consistent manner (as opposed to the rule of mixtures)[2] yields nearly identical results to the generalized self-consistent composite cylinder method, as was similarly observed for the elastic properties in Chapter IV. However, it is interesting to note that for the elastic properties, both rule of mixtures approaches and consistent approaches for accounting for the effects of random orientation yield nearly identical results, seemingly indicating a sensitivity of orientational averaging to tensor order.

It is also of interest to note that included in Figure 56 are the measured data for the thermal conductivity of a suspension of CNTs in a synthetic poly (α-olefin) oil obtained by Choi et al. [235]. This data has been used by both Nan et al. [77, 82] and Chen et al. [90] to demonstrate that micromechanics methods over predict experimental measurements, and was previously noted in Figure 54 to demonstrate the largest increases in thermal conductivity with increasing CNT volume fraction of all of the measured data provided. However, from Figure 56 it is noted the generalized self-consistent composite cylinders model results are of the same order of magnitude as the data from Choi et al. In order to provide a clearer assessment of the initial generalized self-consistent composite cylinders model results with the measured data, Figure 57 provides the model predictions from Figure 56 on the scale of mea-

[2]It is noted that the Mori-Tanaka method applied in reference [90] follows from the work of Hatta and Taya [189]. However, differences in averaging for random orientation between the work of Hatta and Taya and the Mori-Tanaka description provided in Chapter II of the present work lead to different estimates for the two Mori-Tanaka approaches. The Mori-Tanaka method for random orientation as described in Chapter II is noted to provided nearly identical results to the generalized self-consistent composite cylinders method as was similarly noted for the mechanical properties. As such, the results from Hatta and Taya will be referred to as the *RoM Mori-Tanaka Model*.

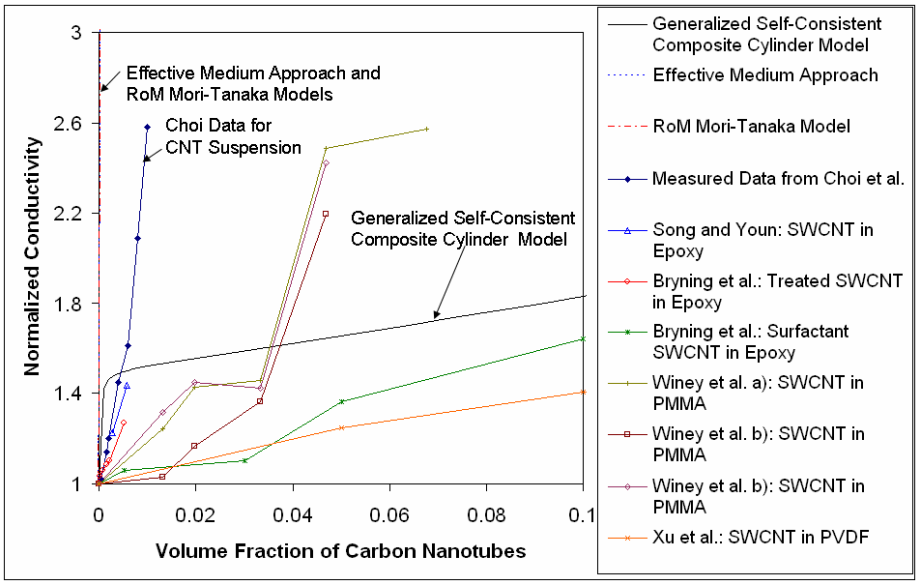

Fig. 57. Sampling of available data in the literature for the thermal conductivity of carbon nanotube-polymer composites normalized by the matrix conductivity and compared with MG-EMA, RoM Mori-Tanaka, and generalized self-consistent composite cylinder micromechanics models assuming perfect heat transfer across the CNT-matrix interface.

sured data from Figure 54. While the rule of mixtures approaches to accounting for random orientation over predict all of of the composite data, accounting for the interactions amongst the randomly oriented CNTs in a consistent manner as is done in the generalized self-consistent composite cylinders method is observed to be much closer to the measured data, but also over predicts all of the low volume fraction measurements before undergoing a transition at a volume fraction of 0.004 where the increase in effective thermal conductivity with increasing nanotube volume fraction slows dramatically.

As it was believed that the source of the difference between the theoretical predictions of the effective medium approach and the measured data the was the Kapitza

resistance [77, 82], this effect was introduced into the effective medium approach through a proportional scaling of the axial, k_{11}^C, and transverse, $k_{22}^C = k_{33}^C$, conductivities of the CNTs [82]. For example, the axial conductivity of the CNTs was modified by

$$k_{11}^C = \frac{k^{\mathrm{CNT}}}{1 + \dfrac{2a_{\mathrm{Kap}}}{L}\dfrac{k^{\mathrm{CNT}}}{k^M}} \tag{6.2}$$

where L is the CNT length and a_{Kap} is the Kapitza radius given by $a_{\mathrm{Kap}} = R_{\mathrm{Kap}}k^M$ where R_{Kap} is the Kapitza resistance. Similarly, the transverse conductivity was modified by

$$k_{22}^C = \frac{k^{\mathrm{CNT}}}{1 + \dfrac{2a_{\mathrm{Kap}}}{d}\dfrac{k^{\mathrm{CNT}}}{k^M}} \tag{6.3}$$

where d is the diameter of the CNTs, so that the effective conductivity of the nanocomposite was given by

$$\frac{k^{\mathrm{eff}}}{k^M} = \frac{3 + c_f(\varrho_x + \varrho_z)}{3 - c_f\varrho_x} \tag{6.4}$$

where

$$\varrho_x = \frac{2(k_{22}^C - k^M)}{k_{22}^C + k^M} \tag{6.5a}$$

$$\varrho_z = k_{11}^C/k^M - 1 \tag{6.5b}$$

By varying the nanotube aspect ratio, initial nanotube conductivity, and the Kapitza resistance values, EMA predictions of this type can obtain good agreement with a given set of measured data. For example, using a Kapitza resistance of 8×10^{-8} m^{2}K/W, Nan et al. [82] applied EMA and varied the nanotube diameter for a fixed aspect ratio of 2000, obtaining good agreement with the data from Choi et al. [235] with a diameter of 15 nm (and therefore length of 30 μm). In contrast, Bryning et al. [73] applied EMA and varied the Kapitza resistance, obtaining good agreement with their measured data using a Kapitza resistance of 2.6×10^{-8} m^{2}K/W and nan-

otube diameter and length of 1.1 nm and 167 nm, respectively, or an aspect ratio of 150. While both efforts used Kapitza resistances of the order estimated by MD simulations, the large disparities in CNT properties needed to obtain good agreement with the measured data coupled with the rule of mixtures approach to orientational averaging are points of concern.

In contrast, Chen et al. [90] introduced the Kapitza resistance in the form of a jump factor, J_{ij}, [241] defined as

$$\frac{1}{V_{\mathrm{CNT}}}\int_{\Gamma}(T^{\mathrm{CNT}}-T^{M})n_i\,ds \equiv J_{ij}H_j^0 \tag{6.6}$$

where T is the temperature and n_i is the unit outer normal of the surface Γ between the CNT and the matrix, and where

$$k^M\frac{\partial T^M}{\partial n} = k^{\mathrm{CNT}}\frac{\partial T^{\mathrm{CNT}}}{\partial n} = \beta(T^M - T^{\mathrm{CNT}})\mid_{\Gamma} \tag{6.7}$$

where β is Kapitza conductivity ($\beta = 1/R_{\mathrm{Kap}}$). The jump factor in Eqn. 6.6 is then multiplied by the volume fraction of the CNTs and thermal conductivity of the matrix, averaged over all orientations, and subtracted from the Mori-Tanaka method using the rule of mixtures approach to orientational averaging. While this method does not rely on the scaling of the CNT conductivity or geometry, it was observed by Chen et al. [90] that the Kapitza resistance over a wide range values had little impact on the effective thermal conductivity of the nanocomposite as the jump factor only accounted for the thermal resistance along the lateral surface of the nanotubes. Instead, it was argued that the thermal transport across the tube ends played a larger role which was demonstrated through the introduction of anisotropy in the nanotube conductivity by taking the axial conductivity of the nanotube as different mean values of the isotropic nanotube and matrix conductivities.

In the present work, the Kapitza resistance is introduced into the nanocomposite

composite cylinder assemblage as a thin interphase region enveloping the nanotube. The thickness of the interphase region is arbitrarily set to a value less than 1% the radius of the nanotube (i.e., thickness, $t_{\text{Kap}} = 0.005\, r_{\text{CNT}}$ so that $r_{\text{Kap}} = r_{\text{CNT}} + t_{\text{Kap}}$). The conductivity of the interphase region is taken to be isotropic (i.e., $k_{11}^{(2)} = k_{22}^{(2)} = k_{33}^{(2)} = k^{\text{Kap}}$), with the value of the conductivity determined from the conservation of energy condition that

$$Q^{(\text{CNT})}|_{r=r_{\text{CNT}}} = \int_{-L/2}^{L/2}\int_{0}^{2\pi} \beta(T^{(\text{CNT})}|_{r=r_{\text{CNT}}} - T^{(M)}|_{r=r_{\text{Kap}}}) r_{\text{CNT}} d\theta dz = Q^{(M)}|_{r=r_{\text{Kap}}} \tag{6.8}$$

where the $T^{(i)}$ are the temperatures given by analogy from Eqn. 3.104 and where the total heat fluxes, $Q^{(i)}$, are given by

$$Q^{(i)}|_{r=r_i} = \int_{-L/2}^{L/2}\int_{0}^{2\pi} q_r|_{r=r_i} r_i d\theta dz \tag{6.9}$$

The parameter β is the inverse of the interface thermal resistance (i.e. the Kapitza resistance) analogous to a convection constant, and is used to determine the conductivity of the thin interphase layer representing the interface thermal resistance. From the continuity conditions in Eqn. 3.111 applied at $r_1 = r_{\text{CNT}}$ (the CNT-Kapitza layer interface) and $r_2 = r_{\text{Kap}}$ (the Kapitza layer-matrix interface), Eqn. 6.8 can be written as

$$Q^{(\text{Kap})}|_{r=r_{\text{CNT}}} = Q^{(\text{Kap})}|_{r=r_{\text{Kap}}} = \int_{-L/2}^{L/2}\int_{0}^{2\pi} \beta(T^{(\text{Kap})}|_{r=r_{\text{CNT}}} - T^{(\text{Kap})}|_{r=r_{\text{Kap}}}) r_{\text{CNT}} d\theta dz \tag{6.10}$$

allowing the conductivity of the interphase layer representing the interface thermal resistance to be given by

$$k^{\text{Kap}} = \frac{\beta\left[D_1^{(\text{Kap})}\left(r_{\text{CNT}} - r_{\text{Kap}}\right) + D_2^{(\text{Kap})}\left(\frac{1}{r_{\text{CNT}}} - \frac{1}{r_{\text{Kap}}}\right)\right]}{\left(D_1^{(\text{Kap})} - \frac{1}{r_{\text{CNT}}^2} D_2^{(\text{Kap})}\right)} \tag{6.11}$$

where the constants $D_1^{(\mathrm{Kap})}$ and $D_2^{(\mathrm{Kap})}$ are determined from the application of the boundary and continuity conditions in Eqns. 3.110 and 3.111 to the composite cylinder assemblage. The resulting simplified expression for the Kapitza layer conductivity is then given as

$$k^{\mathrm{Kap}} = \frac{\beta k^{\mathrm{CNT}} t_{\mathrm{CNT}} t_{\mathrm{Kap}} \gamma_1}{\gamma_2 t_{\mathrm{Kap}}^2 \beta + \gamma_3 t_{\mathrm{CNT}} k^{\mathrm{CNT}}} \tag{6.12}$$

where

$$\begin{aligned} \gamma_1 &= (t_{\mathrm{CNT}} - 2r_{\mathrm{CNT}})(2r_{\mathrm{CNT}} + t_{\mathrm{Kap}}) \\ \gamma_2 &= 2r_{\mathrm{CNT}}^2 - 2r_{\mathrm{CNT}} t_{\mathrm{CNT}} + t_{\mathrm{CNT}}^2 \\ \gamma_3 &= (2t_{\mathrm{CNT}} - 4r_{\mathrm{CNT}})(t_{\mathrm{Kap}} + r_{\mathrm{CNT}}) \end{aligned} \tag{6.13}$$

As only of the $Q^{(i)}$ conditions in Eqn. 6.10 is needed to determine the conductivity of the Kapitza layer, the other is used to evaluate the error associated with a chosen thickness of the Kapitza layer. In the results which follow, the thickness of the interphase region is set to a value less than 1% the radius of the nanotube, e.g. $t_{\mathrm{Kap}} = .005 \times r_{\mathrm{CNT}}$ which results in an evaluated error of one one-thousandth of a percent.

The resulting predictions of the nanocomposite thermal conductivity for an $N = 3$ (CNT-Kapitza layer-matrix) generalized self-consistent composite cylinder model for randomly oriented CNTs in a polymer matrix are provided in Figure 58 for a range of values of the Kapitza conductivity, β. Also shown in the figure are data from Choi eat al. [235], representative of the upper range of the CNT nanocomposite data, and from Winey et al. [74], representative of the average behavior for CNT nanocomposites. It is observed that the inclusion of the Kapitza layer does not effect the initial predicted thermal conductivities, leaving the initial slope unchanged. Instead, the effect of the Kapitza layer is to change the rate at which the

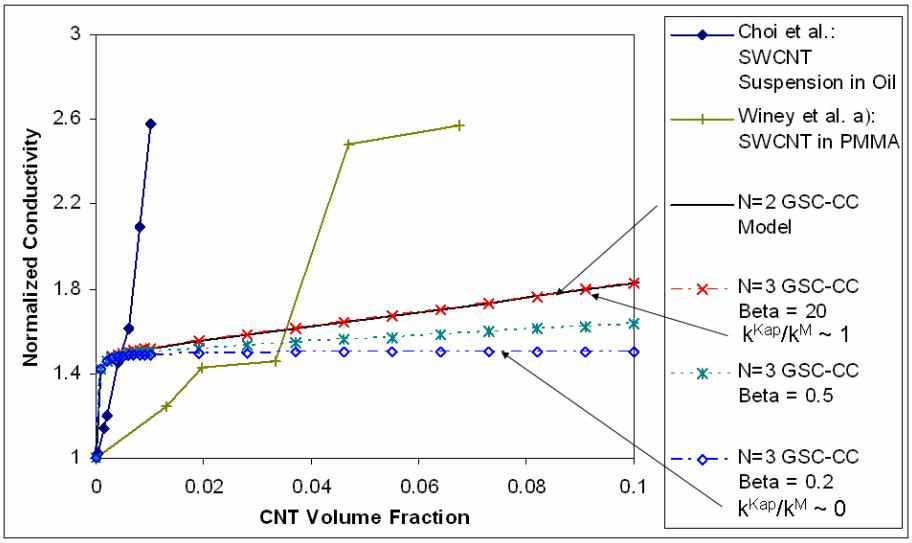

Fig. 58. Comparison of $N = 3$ (CNT-Kapitza layer-matrix) generalized self-consistent composite cylinder model for nanocomposites with randomly oriented CNTs including the interface thermal resistance to measured data in the literature. Comparisons are made with data from Winey et al. [74] representing the average nanocomposite thermal conductivity and from Choi et al. [235] representing the upper range of nanocomposite thermal conductivity. Generalized self-consistent composite cylinder model results for different values of the interface thermal resistance as measured by the parameter β demonstrate the range interface behavior from perfectly conducting, and therefore equivalent to the $N = 2$ perfectly conducting interface results, to perfectly insulating.

thermal conductivity increases with increasing CNT volume fraction following the initial sharp increase at low volume fractions. In addition, it is observed that a β value of 20 W/m^{2}K is sufficiently large enough so as to represent the perfect interface condition, with the results obtained being nearly identical to those obtained with the $N = 2$ generalized self-consistent composite cylinder model. This corresponds to the ratio of the Kapitza layer conductivity to that of the matrix having approached a value of one, and is indicative of a perfectly conducting interface. As the value of β decreases (i.e. as the Kapitza resistance becomes larger), the rate of increase in conductivity with increasing CNT volume fraction of the predicted results decreases. It is further observed that at a β value of 0.2 W/m^{2}K, the rate of increase in conductivity with increasing CNT volume fraction is essentially zero, with further decreases in β providing nearly identical predictions of effective thermal conductivities. This indicates that the ratio of the Kapitza conductivity layer to that of the matrix has approached a value near zero, indicative of being a perfectly insulating interface. Thus, the entire range of influence for the Kapitza conductivity as modeled here essentially spans three orders of magnitude and does not correct the over prediction of measured data. It is also of interest to note that using values for the Kapitza resistance reported from atomistic modeling [78, 79] efforts would result in a β value of 12×10^6 W/m^{2}K, which far exceeds the value of β representing a perfectly insulating using the generalized self-consistent composite cylinder model.

However, it is recalled that it was noted by Chen et al. [90] that the jump parameter used to capture the effects of the Kapitza resistance did not have a significant impact on the predicted effective thermal conductivities as it did not account for the tube end transport. While the generalized self-consistent composite cylinder model results do indicate a larger impact of the Kapitza resistance than the model used by Chen et al. [90], end effects associated with the Kapitza resistance are also not

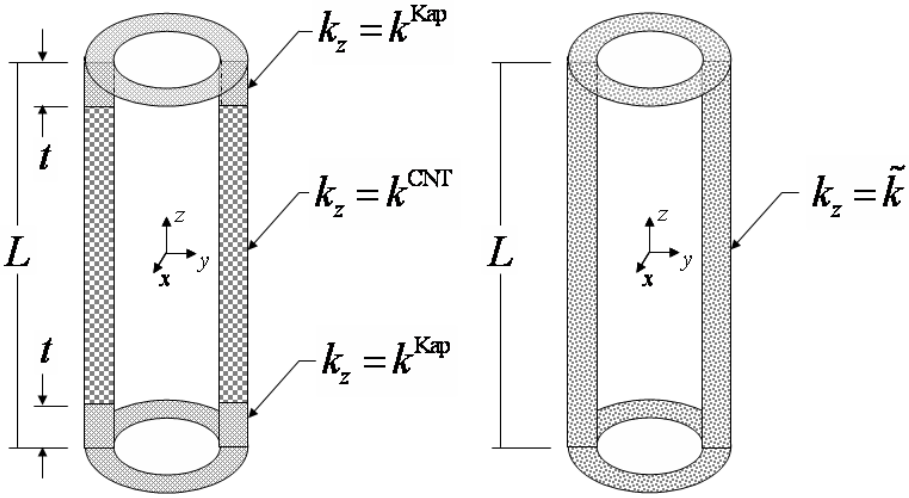

Fig. 59. Schematic representation of how the Kapitza layer conductivity is used to introduce anisotropy into the nanotube conductivity.

included, and portions of the measured data remain largely over predicted. As such, a simple model is used to effectively account for the interface thermal resistance end effects.

As a result of modeling the carbon nanotubes with high aspect ratio composite cylinder assemblages, the transfer of heat from the ends of the nanotube to the polymer matrix are ignored. As such, incorporating the interface thermal resistance as a thin interphase region does not reflect the inclusion of the interface thermal resistance at the nanotube ends. A simple model for including such effects is instead applied in which the nanotube axial conductivity, $k_{11}^{(1)} = k^{\mathrm{CNT}}$, is replaced by an effective value, $k_{11}^{(1)} = \tilde{k}$, determined from the simple series model shown in Figure 59. Looking at a θ cross section of the nanotube (see Figure 59), the lengthwise ends of the nanotube are replaced by regions with conductivity equal to that determined for the Kapitza layer interphase, k^{Kap}, and with the same thickness, $t = t_{\mathrm{Kap}}$. Applying the general solution for the axial heat flow potential (Eqn. 3.83) for each phase in this column

we obtain

$$T^{(2a)} = D_1^{(2a)} z + D_2^{(2a)} \qquad \text{for } -\frac{L}{2} \leq z \leq -\frac{L}{2} + t \tag{6.14a}$$

$$T^{(1)} = D_1^{(1)} z + D_2^{(1)} \qquad \text{for } -\frac{L}{2} + t \leq z \leq \frac{L}{2} - t \tag{6.14b}$$

$$T^{(2b)} = D_1^{(2b)} z + D_2^{(2b)} \qquad \text{for } \frac{L}{2} - t \leq z \leq \frac{L}{2} \tag{6.14c}$$

where t is the thickness of the interface thermal resistance interphase layer and L is the length of the nanotube. The constants $D_1^{(i)}$ and $D_2^{(i)}$ are determined from the boundary and matching conditions given by

$$T^{(2a)}|_{z=-\frac{L}{2}} = \hat{T}_1 \tag{6.15a}$$

$$T^{(2b)}|_{z=\frac{L}{2}} = \hat{T}_2 \tag{6.15b}$$

$$T^{(2a)}|_{z=-\frac{L}{2}+t} = T^{(1)}|_{z=-\frac{L}{2}+t} \tag{6.15c}$$

$$q_z^{(2a)}|_{z=-\frac{L}{2}+t} = q_z^{(1)}|_{z=-\frac{L}{2}+t} \tag{6.15d}$$

$$T^{(2b)}|_{z=\frac{L}{2}-t} = T^{(1)}|_{z=\frac{L}{2}-t} \tag{6.15e}$$

$$q_z^{(2b)}|_{z=\frac{L}{2}-t} = q_z^{(1)}|_{z=\frac{L}{2}-t} \tag{6.15f}$$

The cross section is then taken as equivalent to a homogeneous cross section with axial conductivity $\tilde{k}$ and with axial heat flow potential given by

$$T^{(*)} = D_1^{(*)} z + D_2^{(*)} \qquad \text{for } -\frac{L}{2} \leq z \leq \frac{L}{2} \tag{6.16}$$

where the constants $D_1^{(*)}$ and $D_2^{(*)}$ are determined through application of the boundary conditions identical to those applied in Eqns. 6.15a and 6.15b. Equating the thermal energies, an expression for the effective axial conductivity of the nanotube as

$$\tilde{k} = \frac{2k^{\mathrm{Kap}}(D_1^{(2a)})^2 t + k^{\mathrm{CNT}}(D_1^{(1)})^2 (L - 2t)}{(D_1^{(*)})^2 L} \tag{6.17}$$

where k^{Kap} is the conductivity of the interface thermal resistance interphase layer determined from Eqn. 6.11 and k^{CNT} is the original nanotube conductivity. Substituting the values for the constants into Eqn. 6.17, the expression for the effective axial conductivity of the nanotube can be expressed as

$$\tilde{k} = \frac{k^{\mathrm{CNT}} k^{\mathrm{Kap}} L}{k^{\mathrm{CNT}} 2t + k^{\mathrm{Kap}}(L - 2t)} \tag{6.18}$$

It is of interest to note from Eqn. 6.18 that as the Kapitza layer thickness goes to zero, that $\tilde{k}$ returns the nanotube conductivity. Further, as k^{Kap} goes to zero, $\tilde{k}$ goes to zero indicative of the Kapitza layer being a perfect insulator. Finally, if k^{Kap} goes to infinity, then $\tilde{k} = k^{\mathrm{CNT}} \dfrac{L}{L - 2t}$ which means that for small thicknesses, $\tilde{k}$ approaches k^{CNT} returning the perfect interface assumption. It is finally noted that though the axial conductivity of the nanotube is reduced to account for the end of effects associated with the interfacial thermal resistance ($k_{11}^{(1)} = \tilde{k}$), the transverse conductivity of the nanotubes remains unchanged, i.e., $k_{22}^{(1)} = k_{33}^{(1)} = k^{\mathrm{CNT}}$, as the effects of the interfacial thermal resistance in the transverse direction are accounted for by the interphase conductivity of the Kapitza layer, k^{Kap}.

A reexamination of the effects of the effects of the interfacial thermal resistance using the $N = 3$ (CNT-Kapitza layer-matrix) generalized self-consistent composite cylinder model, this time including the end effects associated with the Kapitza layer, are provided in Figure 60 for a range of β values, with the corresponding values for the interface thermal resistance interphase conductivity and effective nanotube axial conductivity provided in Table X. It is again observed that a β value of 20 W/m^{2}K is sufficiently large enough so as to represent the perfect interface condition, with the results for this case being nearly identical to those of the $N = 2$ composite cylinder model, so that again using the values for the Kapitza conductivity reported from MD simulations would constitute a perfect interface. This is again because the value of

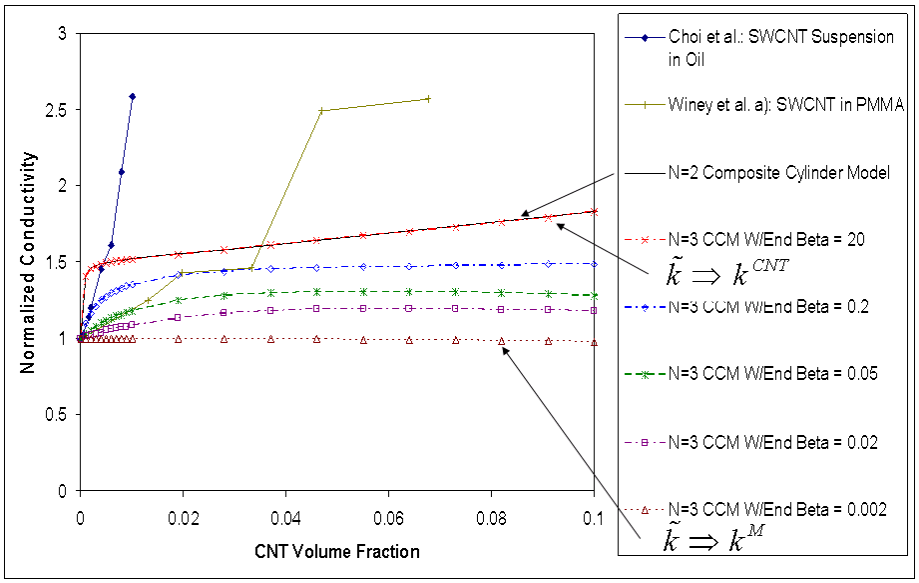

Fig. 60. Comparison of $N = 3$ (CNT-Kapitza layer-matrix) generalized self-consistent composite cylinder model including interface thermal resistance end effects to measured data in the literature. Comparisons are made with data from Winey et al. [74] representing the average nanocomposite thermal conductivity and from Choi et al. [235] representing the upper range of nanocomposite thermal conductivity. Generalized self-consistent composite cylinder model results for different values of the interface thermal resistance as measured by the parameter β demonstrate the range interface behavior from perfectly conducting, and therefore equivalent to the $N = 2$ results, to nearly insulating.

Table X. Values for β and the corresponding interface thermal resistance interphase conductivity, k^{Kap} given by Eqn. 6.11, and effective nanotube axial conductivity, $\tilde{k}$ given by Eqn. 6.18, for the $N = 3$ generalized self-consistent composite cylinder model for both lateral and end effects of interface thermal resistance. Note that transverse conductivity of the nanotube remains unchanged, i.e., $k_{22}^{(1)} = k_{33}^{(1)} = k^{\text{CNT}}$.

β W/m^{2}K	k^{Kap} W/mK	$\tilde{k}$ W/mK
$\beta = 20$	$9.97\ 10^{-2}$	1665
$\beta = 0.2$	$9.97\ 10^{-4}$	94.97
$\beta = 0.05$	$2.49\ 10^{-4}$	24.62
$\beta = 0.02$	$9.97\ 10^{-5}$	9.92
$\beta = 0.002$	$9.97\ 10^{-6}$	0.996

the Kapitza layer conductivity, k^{Kap} given in Table X, is nearly equal to the matrix value of 0.16725 W/mK, and further, the effective axial conductivity of the nanotube, $\tilde{k}$ in Table X is nearly equal to the CNT value of $k^{\text{CNT}} = 2000$ W/mK. However, with decreasing β it is observed that the inclusion of the interface end effects changes the predicted effective thermal conductivity throughout the entire range of volume fractions, removing the initial sharp increase in conductivity at low volume fractions. In fact, a β value of 0.2W/m^{2}K is no longer observed as the saturation limit; this occurs at much lower β values. For example, at a β value of 0.002 W/m^{2}K, where k^{Kap} is orders of magnitude below the matrix value while $\tilde{k}$ is on the order of the matrix conductivity, the results begin to reflect the effective conductivity of a porous media. As such, further reductions in β lead to the opposite type of matrix dominance associated with porosity where the matrix is far more conductive than the other constituents. Thus, it is noted that the combined effects the lateral and end effects

of the interfacial thermal resistance can have a significant impact on nanocomposite thermal conductivity.[3]

It is further noted that a β value of 0.2 W/m^{2}K is observed to capture well the initial portion of the data from Choi et al. [235] while a β value of 0.05 W/m^{2}K is observed to capture well the initial portion of the data from Winey et al. [74]. As the two data sets correspond to different matrix materials, it is reasonable to expect that the interface thermal resistance may be different, reflecting the varying degree of phonon scattering at the nanotube-matrix interface. However, neither β value models well the full range of measured data with increasing nanotube volume fraction. This may be due to changes in polymer morphology due to the interaction of the polymer chains with nanotube leading to differences in the polymer conductivity adjacent to the nanotube surface.[4] Such effects are considered in the present model through the inclusion of matrix interphase regions.

TEM images have previously been used in Chapter IV to justify the inclusion of a matrix interphase region in the micromechanics modeling of CNT-polymer nanocomposites elastic properties. Variations in polymer density distributions surrounding

[3]It was observed in Figure 58 that the effects of an isotropic interphase layer representing the interfacial thermal resistance were unable to reduce the effective conductivity below the results provided for $\beta = 0.2$ W/m^{2}K. However, it is observed in Figure 60 that the introduction of anisotropy into the nanotube conductivity through the reduction of the axial conductivity can achieve values below the results provided for $\beta = 0.2$ W/m^{2}K. One may therefore ask is it possible for the anisotropy to reside in Kapitza layer and achieve the same effect. The answer is no as in Figure 58 it is the very large axial conductivity of the nanotube as compared to the matrix which constrains the lower bound of the effective thermal conductivity. While anisotropy in the Kapitza layer could be introduced, the Kapitza layer conductivity for a β value of 0.2 W/m^{2}K is already well below the matrix conductivity. As the effective axial conductivity of the composite cylinder assemblage is governed by a rule of mixtures, further reductions in the β parameter for a given thickness will not cause significant reductions in axial conductivity of the composite cylinder assemblage.

[4]It has been noted that the increases in polymer molecular weight and crosslink density lead to increases in polymer conductivity and other properties [244]

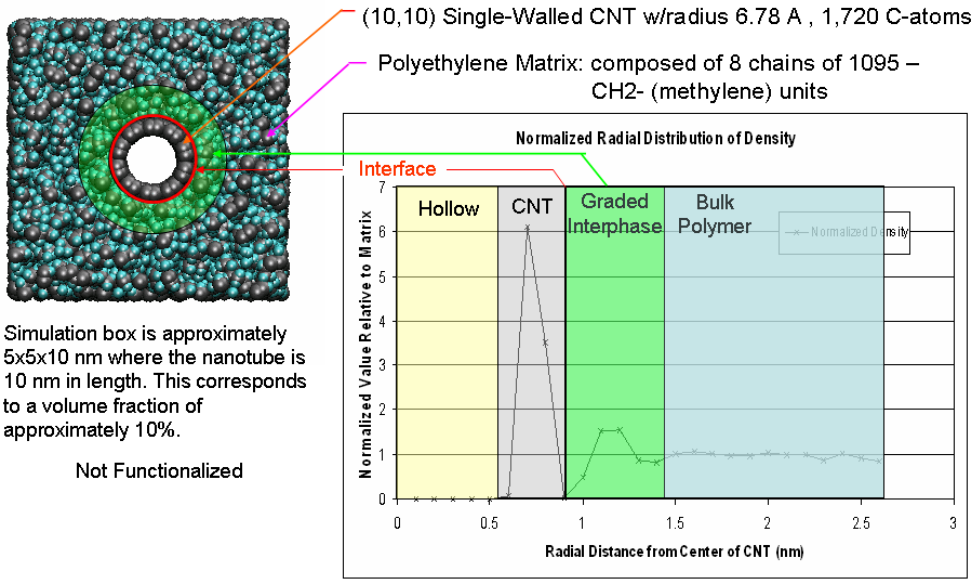

Fig. 61. Illustration of the use of molecular dynamics simulations in discerning the presence of graded interphase regions. The density distribution surrounding a CNT in a polyethylene matrix [99] is used to provide insight into the thickness and material properties of the polymer in the vicinity of the CNT.

CNTs in MD simulations like the one shown in Figure 61 have similarly been used to justify the presence of a matrix interphase region [99]. There it is observed that density drops sharply from the CNT carbon atoms to below the bulk polymer density to a value of nearly zero, seemingly indicating a small gap between the CNT surface and the polymer reflective of the van der Waals interactions. Over the course of approximately one CNT radius, the density distribution in the polymer sharply increases to a value greater than the bulk density, before subsequently decreasing and equilibrating to the bulk density of the polymer (in this example, polyethylene). Here it is believed that the initial gap between the CNT and the polymer lends some credence to the presence of the interfacial thermal resistance, while the subsequent large fluctuations in the polymer density give rise to corresponding large fluctuations

in the polymer conductivity.

The introduction of a matrix interphase layer in the generalized self-consistent composite cylinders micromechanics model consists of the inclusion of an additional layer in the composite cylinder assemblage, and therefore introduces two additional parameters, the matrix interphase conductivity (k^{int}) and thickness (t_{int}). The resulting total composite cylinder assemblage is therefore an $N = 4$ assemblage consisting of CNT (with $k_{22}^{(1)} = k_{33}^{(1)} = k^{\text{CNT}} = 2000$ W/mK and $k_{11}^{(1)} = \tilde{k}$ given by Eqn. 6.18), the Kapitza interphase layer (with $k_{11}^{(2)} = k_{22}^{(2)} = k_{33}^{(2)} = k^{\text{Kap}}$ given by Eqn. 6.11), the matrix interphase layer ($k_{11}^{(3)} = k_{22}^{(3)} = k_{33}^{(3)} = k^{\text{int}}$), and the matrix ($k_{11}^{(4)} = k_{22}^{(4)} = k_{33}^{(4)} = k^{M} = 0.16725$ W/mK). It is important to note that like the matrix, the matrix interphase layers are not included in the end effects associated with the interface thermal resistance as a result of the high aspect ratio of the composite cylinder assemblage.

The thickness of the matrix interphase layer can be estimated from TEM images or taken from the density distributions resulting from MD simulations. A parametric study on the effect of the matrix interphase region thickness for a given Kaptiza conductivity and matrix interphase conductivity is provided in Figure 62. For a Kapitza conductivity of $\beta = 0.02$ W/m^{2}K and matrix interphase to matrix conductivity ratio (k^{int}/k^{M}) of three, the thickness of the matrix interphase layer is varied from zero (i.e., from the $N = 3$ model), to the value of 1 nm observed in the MD density distribution, to the value of 1.75 nm observed in TEM images, and finally to a value twice that. It is noted that the resulting nanocomposite conductivity is quite sensitive to the matrix interphase thickness. It is also noted from the figure that the effective nanocomposite conductivity resulting from the thickness of 1.75 nm represents a broad range of the measured data from Winey et al. [74]. As such, this value of thickness is used in a second parametric study on influence of the matrix interphase layer conductivity.

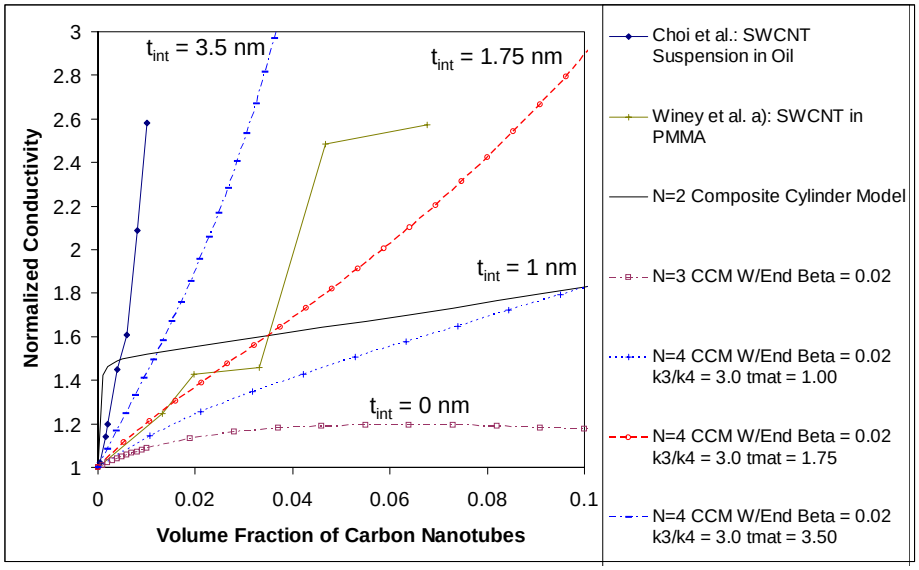

Fig. 62. Parametric study on matrix interphase thickness of $N = 4$ composite cylinder model for the lateral and end effects of the interface thermal resistance having a given matrix interphase conductivity of 3 times the matrix value ($k^{\text{int}}/k^M = 3$) and a Kapitza conductivity of $\beta = 0.02$ W/m^{2}K. Also included are the measured data from Choi et al. [235] and Winey et al. [74].

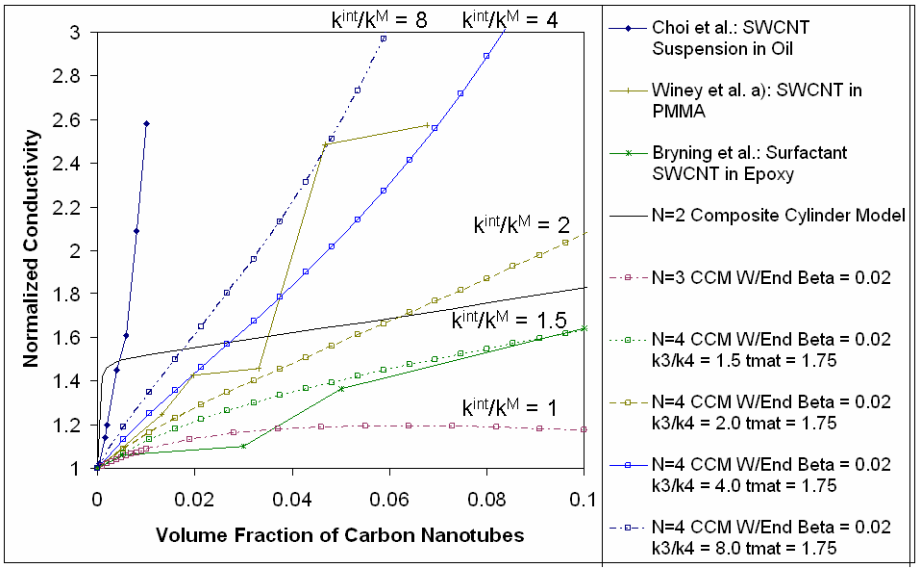

Fig. 63. Parametric study on matrix interphase conductivity of $N = 4$ composite cylinder model for the lateral and end effects of the interface thermal resistance having a given matrix interphase thickness of 1.75 nm and a Kapitza conductivity of $\beta = 0.02$ W/m^{2}K. Also included are the measured data from Choi et al. [235], Winey et al. [74], and Bryning et al. [73].

Retaining a Kapitza conductivity value of $\beta = 0.02$ W/m^{2}K and a matrix interphase thickness of 1.75 nm, Figure 63 provides a parametric study on the matrix interphase layer conductivity. The matrix interphase layer to matrix conductivity ratio (k^{int}/k^M) is varied from one (i.e., from the $N = 3$ model) to eight. From the figure, it is observed that the matrix interphase layer conductivity can also have significant influence on the predicted nanocomposite conductivity. In fact, it is noted that a ratio of $k^{\text{int}}/k^M = 4$ represents well the measured data of Winey et al. [74] while a ratio of $k^{\text{int}}/k^M = 1.5$ is noted to represent well the measured data from Bryning et al. [73]. Again, as these measured data are for different matrix materials (PMMA and epoxy, respectively) it is not unreasonable to have different values for the matrix interphase layer conductivity.

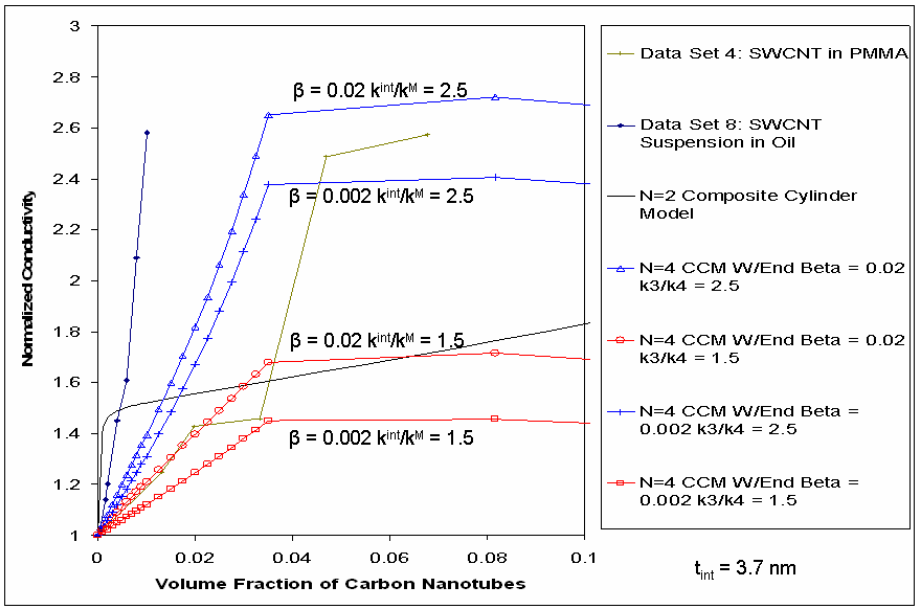

Fig. 64. Comparison of $N = 4$ (CNT-Kapitza layer-matrix interphase-matrix) generalized self-consistent composite cylinder model including interfacial thermal resistance end effects to measured data. Comparisons are made with data from Winey et al. [74] representing the average nanocomposite thermal conductivity and Choi et al. [235] representing the upper range of nanocomposite thermal conductivity. Generalized self-consistent composite cylinder model results are provided for different values of the interface thermal resistance (β) and of the matrix interphase conductivity ($k_{11}^{(3)} = k_{22}^{(3)} = k_{33}^{(3)}$).

However, this does not necessarily mean that these values for the Kapitza conductivity and matrix interphase thickness and conductivity correspond to the actual values of these quantities. As shown in Figure 64, for different values of the Kapitza conductivity, differences in matrix interphase conductivity (or in thickness) can also demonstrate relatively good agreement with the measured data. Figure 64 provides a parametric study of the combined effects of the Kapitza resistance and a matrix interphase layer on the effective composite thermal conductivity for β values of 0.02 W/m^{2}K and 0.002 W/m^{2}K and matrix interphase conductivities of 1.5 and

2.5 times the matrix conductivity (the thickness of the matrix interphase layer is set to correspond to the volume fraction at which the large increase in conductivity is observed between volume fractions of 0.033-0.046, or roughly 4 CNT radii). It is noted that as the volume fraction of the carbon nanotubes is increased to the critical volume fraction of 0.035, the $N = 4$ composite cylinder model transitions to an $N = 3$ composite cylinder model as the undisturbed matrix material is "consumed".

From Figure 64 it is again observed that the low volume fraction portion of the data can be well matched by a given combination of β and k^{int}, in this case, the best fit to the initial slope was obtained by $\beta = 0.02$ W/m^{2}K and $k^{\text{int}}/k^M = 1.5$. However this case did not capture the subsequent rapid increase in thermal conductivity observed in the measured data. Higher values of k^{int}/k^M were better able to capture the rapid increase conductivity, but were again overestimating the initial portion of the data. This indicates that there is not a unique combination of β, t_{int}, and k^{int}/k^M which captures well the observed behavior of the measured data. In fact, if one were to consider the matrix interphase region to be a graded material region, getting more conductive with increasing proximity to the nanotube, then one could represent such a graded behavior using a collection of matrix interphase layers, for example, with conductivities based on molecular dynamics simulations density distributions [79, 99] as illustrated in Figure 61.

For example, the data of Winey et al. [74] can also be well represented using an $N = 5$ (CNT-Kapitza layer-first matrix interphase-second matrix interphase-matrix) generalized self-consistent composite cylinder model with the end effects of the thermal resistance layer included, the results of which are provided in Figure 65. The best representation was obtained with a β value of 2 10^{-6} W/m^{2}K, a matrix interphase region with $k^{\text{int}_1}/k^M = 2.55$ and critical volume fraction of 0.05, and a second matrix interphase region with $k^{\text{int}_2}/k^M = 1.10$ and critical volume fraction of 0.025. It is

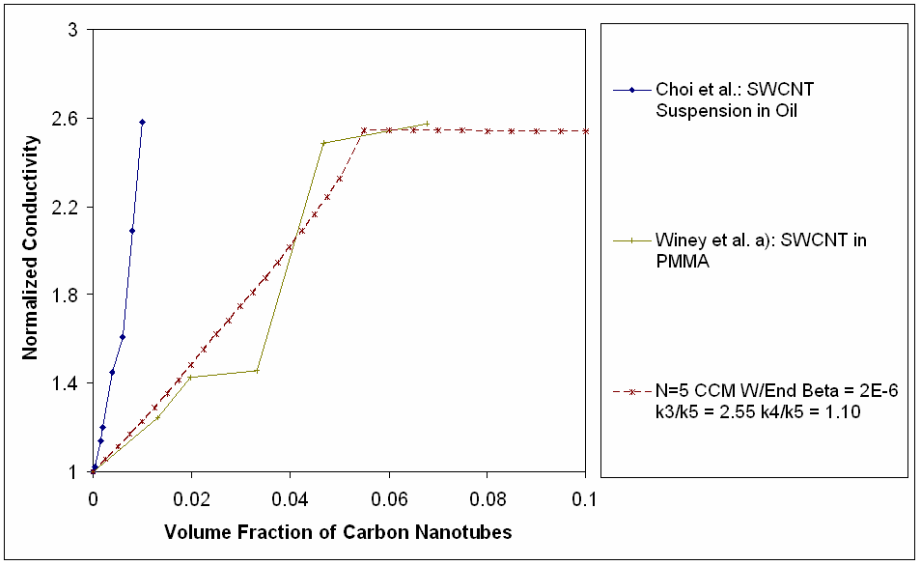

Fig. 65. Results for an $N = 5$ generalized self consistent composite cylinder model consisting of a CNT, a Kapitza resistance layer with end effects, and two matrix interphase layers with decreasing conductivity with increasing distance from the nanotube representing a graded interphase in comparison with data from the literature. The parameters for the composite cylinder model are selected to best represent the data of Winey et al. [74]. Also shown is the data from Choi et al. [235].

noted that further reductions in β would result in only minor changes in the predicted thermal conductivity as β is essentially saturated. This means that the CNTs are practically completely insulated, both along the lateral surfaces and at the ends, and that the matrix interphase regions thus play a critical role in obtaining good agreement with the measured data. In fact, from the results provided here, one could consider that, as a result of the governing nanoscale effect, the role of CNTs in terms of the effective thermal conductivity of nanocomposites not to be linked to the high conductivity of the CNTs, but rather to be a source of disturbance to the polymer structure, and therefore, to the polymer conductivity. This is in sharp contrast to the role of CNTs in terms of electrical conductivity where the governing nanoscale effects associated with the CNTs lead to orders of magnitude increases in conductivity.

While improving nanoscale simulations is beyond the scope of this work, it has been noted herein that MD simulations used to calculate values for the Kapitza resistance [78, 79] have obtained values well above the saturation limit for a perfectly conducting interface identified for the present micromechanics model. It is noted that these MD estimates rely on the calculation of a characteristic decay time in temperature transferred from the nanotube to the matrix, τ, which in these simulations is on the order of picoseconds and results in a Kapitza resistance on order of 10^{-8} $\mathrm{m^2K/W}$. Such values would correspond Kapitza conductivities on the order 10 $\mathrm{MW/m^2K}$ which are again noted to be well above the 20 $\mathrm{MW/m^2K}$ value which in the present model corresponds to an interface which is essentially perfectly conducting. In fact, it is further noted that for a value of the Kapitza conductivity of 0.02 $\mathrm{MW/m^2K}$, which in the present model was shown to have significant impact on the nanocomposite conductivity, would correspond to a decay time of 0.028 s. To even detect such a large decay time at present would require a substantial amount of computation time for MD simulations. Thus it is not clear if MD simulations

are presently able to give accurate estimates for the Kapitza resistance/conductivity. However, it is confirmed from the present work that without the inclusion of an interface thermal resistance, micromechanics predictions of the thermal conductivity of CNT-polymer nanocomposites will largely over predict the measured values for these nanocomposites.

Thus, while it is observed that the micromechanics model described herein can be used to help qualitatively understand the potential impact of nanoscale features such as interface thermal resistance layers and graded interphase regions, it is recognized that further nanoscale simulations are needed to make more quantitative assessments and to provide such micromechanics models with the necessary input for predicting nanocomposite properties by narrowing the range of interface thermal resistance values.

CHAPTER VII

CONCLUSIONS AND IDENTIFICATION OF FUTURE CHALLENGES

The present work has provided a micromechanics approach based on the generalized self-consistent composite cylinders method for assessing the impact of carbon nanotubes on the multi-functional nature of nanocomposites in which they are a constituent. Emphasis has been place on the effective elastic properties as well as electrical and thermal conductivities of nanocomposites consisting of randomly oriented single walled carbon nanotubes in epoxy. In order to place the generalized self-consistent composite cylinders method into perspective, a review of the classical micromechanics methods, including the Mori-Tanaka and self-consistent approaches, and of the generalized self-consistent composite cylinder method has been provided. Further, the generalized self-consistent composite cylinders method has been utilized in the determination of concentration tensors, thereby emphasizing the generalized self-consistent composite cylinders method as a non-Eshelby approach, and allowing the generalized self-consistent composite cylinders method to be applied to systems containing multiple inclusion types and orientations.

The generalized self-consistent composite cylinders method is subsequently employed in assessing the effective elastic properties of nanocomposites. The method is first applied in the determination of effective nanotube properties for use in classical micromechanics approaches. The effects of two nanotube parameters often discussed in the literature, the stiffness and the thickness, on the effective nanotube properties are placed into context with measured values in the literature. A nanotube stiffness of 1100 GPa and thickness of 0.34 nm, both representative with graphite, are observed to provide a reasonable result for use in nanocomposite modeling.

The effective elastic properties of aligned, fully encapsulated, as well as clustered

and well-dispersed nanotubes in epoxy are then discussed in the context of nanotube bundles in nanocomposites using both classical micromechanics and the generalized self-consistent composite cylinders method as well as using computational micromechanics techniques. Here it is observed that the Mori-Tanaka, self-consistent, generalized self-consistent composite cylinders and the computational micromechanics techniques yield nearly identical results for all elastic properties at currently achievable nanotube volume fractions. The Mori-Tanaka, generalized self-consistent composite cylinders method and the computational micromechanics techniques are observed to agree even at very large volume fractions. The Young's modulus along the nanotube axis is observed to obey a rule of mixtures approximation, while the remaining properties are observed to be dominated by the matrix material such that at 10% volume fraction, Young's modulus in the axial direction is 2300% larger than the matrix value while in the transverse direction, it is only 30% larger than the matrix.

The effects of both stiff and compliant interphase regions on the elastic properties of aligned nanotube bundles using both the generalized self-consistent composite cylinder method and computational micromechanics techniques are observed to strongly influence the properties transverse to the nanotube axis, 15% increase and 30% decrease for interphases that were ten times and one tenth, respectively, the matrix value, while the axial Young's modulus retains a rule of mixtures approximation. The effects of clustering of nanotubes within these bundles was also investigated using computational micromechanics. It was observed that the effects of clustering on the elastic properties of the bundles was to increase the transverse modulus on the order of 2%, slightly less than effects of curvature observed by Fisher et al. [37] to cause a reduction in modulus on the order 5% relative to straight fibers. Further, it was noted that the combined effects of clustering for nanotubes with compliant interphase regions yielded nearly identical results as the well-dispersed compliant in-

terphase cases. In contrast, the combined effects of clustering and stiff interphase regions yielded increases in the transverse properties of up to 25%, more than either effect independently. However, as load transfer in nanocomposites constitutes a significant issue, it is expected that interphase regions would most likely be compliant. Thus, the effects of interphase regions are deemed more significant than the effects of dispersion in terms of elastic properties.

As such, the effects of well-dispersed, randomly oriented nanotubes both with and without interphase regions are compared to measured data from the literature. Here it is found that the initial estimation of the nanocomposite Young's modulus obtained from the generalized self-consistent composite cylinder generally over estimates the measured values by nearly 30% at 1% wt. This seemingly confirms that there is less than perfect load transfer between the nanotubes and the epoxy which would be reflected in compliant interphase regions. However, it is also noted that there is a wide range of uncertainty in the input parameters, in particular, the interphase stiffness, the nanotube Young's modulus, and the nanotube thickness; the interphase thickness being more discernible from TEM imaging. Efforts at assessing the bounds of the effective nanocomposite properties based on this uncertainty in the input properties indicated that measured data for functionalized nanotubes fell very near the lower bound obtained from the uncertainty in the interphase stiffness. Further, it was observed that measured data for unfunctionalized nanotubes in epoxy were contained within the next lower bound associated with the uncertainty in the nanotube stiffness. Thus it is observed that the generalized self-consistent composite cylinder model can reflect well the measured data in the literature, however, there is identified a need for obtaining a better estimate of the nanotube and interphase stiffnesses either from lower length scale simulations or from improved nanoscale measurement techniques.

The generalized self-consistent composite cylinders model has also been applied

to model the electrical conductivity of carbon nanotube-epoxy nanocomposites. Here it was noted that for well-dispersed, randomly oriented nanotubes in epoxy, that the effective conductivity predicted by the generalized self-consistent composite cylinder model was strongly matrix dominated, not showing any signs of percolation. However, the measured data from the literature demonstrated percolation behavior at extremely low volume fractions which some attributed to the formation of nanotube networks. However, at such low volume fractions the formation of such networks would likely be an indication of poor dispersion. Others have instead argued that the conductivity of nanotube-epoxy nanocomposites is governed by nanoscale effects such as electron hopping. As such, an electron hopping mechanism was introduced into the generalized self-consistent composite cylinder model in the form of a graded interphase region. Using such a model, the method has been able to capture the double percolation limit phenomena observed prior to the onset of contact percolation believed to be due to the electron hopping mechanism. As this model assumes the nanotubes are well-dispersed and fully enveloped in the polymer, it can be considered an estimate for the conductivity of nanocomposites with an ideal dispersion of nanotubes, and thereby used to help identify good dispersions versus poorer ones. Further, it is noted that while clustering had little impact on the elastic properties, its effects on the effective electrical conductivity of nanocomposites may be significant as the interphase regions are largely more conductive than the matrix and therefore subject to interphase-clustering coupling, even prior to contact percolation, therefore indicating that functionalization for dispersion purposes may have competing roles in terms of mechanical and electrical properties. However, it is noted that before such an assessment could be put into practice, it is again necessary either from lower length scale simulations or from improved nanoscale measurement techniques to quantify better both the inherent conductivity of the nanotubes as well as the range and

conductivity associated with the hopping mechanism.

Despite the mathematical analogy between thermal and electrical conductivity, the nanoscale mechanisms governing the nanotube-epoxy nanocomposites are vastly different. In terms of thermal conductivity, the nanoscale effect takes the form of an interfacial thermal resistance. As such, a generalized self-consistent composite cylinder model for carbon nanotube-polymer nanocomposites was developed to include both the lateral and end effects of an interface thermal resistance layer on the effective thermal conductivity of nanocomposites. It was observed that the inclusion of just the lateral effects of the interface thermal resistance layer was insufficient for the micromechanics model to be able explain the measured values of nanocomposite thermal conductivity. Including the end effects of the interface thermal resistance layer allowed the micromechanics to better capture the low volume fraction effective thermal conductivities measured for nanocomposites, but not the subsequent increase in thermal conductivity with increasing nanotube volume fraction. Using observed variations in the density from molecular dynamics simulations as motivation, it was observed that a more accurate micromechanics model was obtained through the inclusion of a graded matrix interphase layer in conjunction with the interface thermal resistance lateral and end effects. The resulting model indicated that the interfacial thermal resistance essentially nullified the perceived benefits of the large thermal conductivity of carbon nanotubes. In fact, from the results provided here, one could consider that, as a result of the governing nanoscale effect, the role of CNTs in terms of the effective thermal conductivity of nanocomposites not to be linked to the high conductivity of the CNTs, but rather to be a source of disturbance to the polymer structure, and therefore, to the polymer conductivity. This is in sharp contrast to the role of CNTs in terms of electrical conductivity where the governing nanoscale effects associated with the CNTs lead to orders of magnitude increases in conductivity. How-

ever, while it is observed that the micromechanics model described herein can be used to help qualitatively understand the potential impact of nanoscale features such as interface thermal resistance layers and graded interphase regions, it is recognized that further nanoscale simulations are needed to make more quantitative assessments in providing the necessary input for predicting nanocomposite properties by narrowing the range of interface thermal resistance values and nanotube conductivity.

Thus, in conclusion, based on the analysis in the present work, the key influence on the effective elastic stiffness and electrical and thermal conductivities of carbon nanotube-polymer nanocomposites is the presence of interphase regions, be they the result of nanoscale effects at the nanotube-polymer interface, due to changes in polymer structure near nanotubes, or due to nanotube functionalization.

REFERENCES

[1] S. Iijima, Helical microtubules of graphitic carbon, Nature 354 (1991) 56.

[2] R. Saito, G. Dresselhaus, M. Dresselhaus, Physical Properties of Carbon Nanotubes, Imperial College Press, London, 1998.

[3] A. Oberlin, M. Endo, T. Koyama, Filamentous growth of carbon through benzene decomposition, Journal of Crystal Growth 32 (3) (1976) 335–349.

[4] M. Terrones, Science and technology of the twenty-first century: synthesis, properties, and applications of carbon nanotubes, Annual Review of Materials Research 33 (2003) 419–501.

[5] P. Harris, Carbon Nanotubes and Related Structures, Cambridge University Press, 1999.

[6] S. Roche, Carbon nanotubes: exceptional mechanical and electronic properties, Annales de Chemie Science des Materiaux 25 (2000) 529–532.

[7] B. Yakobson, R. Smalley, Fullerene nanotubes: C1,000,000 and beyond, American Scientist 85, review of Nanotubes.

[8] J.-P. Salvetat-Delmotte, A. Rubio, Mechanical properties of carbon nanotubes: a fiber digest for beginners, Carbon 40 (2002) 1729–1734.

[9] M.-F. Yu, B. S. Files, S. Arepalli, R. Ruoff, Tensile loading of ropes of single wall carbon nanotubes and their mechanical properties, Physical Review Letters 84 (24) (2000) 5552–5555.

[10] B. I. Yakobson, M. P. Campbell, C. J. Brabec, J. Bernholc, High strain rate fracture and c-chain unraveling in carbon nanotubes, Computational Materials Science 8 (1997) 341–348.

[11] Z. L. Wang, R. P. Gao, P. Poncharal, W. A. de Heer, Z. R. Dai, Z. W. Pan, Mechanical and electrostatic properties of carbon nanotubes and nanowires, Materials Science and Engineering C 16 (2001) 3–10.

[12] F. T. Fisher, Nanomechanics and the viscoelastic behavior of carbon nanotube-reinforced polymers, Mechanical Engineering, Northwestern University, Evanston, IL (2002).

[13] V. Popov, Carbon nanotubes: properties and applications, Materials Science and Engineering R 43 (2004) 61–102.

[14] S. Tans, A. Verschueren, C. Dekker, Room-temperature transistor based on a single carbon nanotube, Nature 393 (1998) 49–52.

[15] B. Wei, R. Vajtai, P. Ajayan, Reliability and current carrying capacity of carbon nanotubes, Applied Physics Letters 79 (8) (2001) 1172–1174.

[16] A. Thess, R. Lee, P. Nikolaev, H. Dai, P. Petit, J. Robert, C. Xu, Y. Lee, S. Kim, A. Rinzler, D. Colbert, G. Scuseria, D. Tomanek, J. Fischer, R. Smalley, Crystalline ropes of metallic carbon nanotubes, Science 273 (1996) 483–487.

[17] J. Hone, Phonons and thermal properties of carbon nanotubes, Topics in Applied Physics: Carbon Nanotubes 80 (2001) 273–286.

[18] P. Thakre, D. Lagoudas, J. Zhu, E. Barrera, T. Gates, Processing and characterization of epoxy/swcnt/woven fabric composites, in: 47th

AIAA/ASME/ASCE/AHS/ASC Structures, Stuctural Dynamics, and Materials Conference, AIAA/ASME/ASCE/AHS/ASC, Newport, Rhode Island, 2006, aIAA-2006-1857.

[19] J. Riddick, S. Frankland, T. Gates, Multiscale analysis of delamination of carbon fiber-epoxy laminates with carbon nanotubes, in: 47th AIAA/ASME/ASCE/AHS/ASC Structures, Stuctural Dynamics, and Materials Conference, AIAA/ASME/ASCE/AHS/ASC, Newport, Rhode Island, 2006, aIAA 2006-1676.

[20] G. Seidel, D. Lagoudas, S. Frankland, T. Gates, Micromechanics modeling of functionally graded interphase regions in carbon nanotube-polymer composites, in: 47th AIAA/ASME/ASCE/AHS/ASC Structures, Stuctural Dynamics, and Materials Conference, AIAA/ASME/ASCE/AHS/ASC, Newport, Rhode Island, 2006, aIAA 2006-1678.

[21] C. Martin, J. Sandler, M. Shaffer, M.-K. Schwarz, W. Bauhofer, K. Schulte, A. Windle, Formation of percolating networks in multi-wall carbon-nanotube-epoxy composites, Composites Science and Technology 64 (2004) 2309–2316.

[22] H. Kim, D. Kim, S. Lee, J. Joo, H. Yoon, S. Cho, S. Lyu, C. Lee, Charge transport properties of composites of multiwalled carbon nanotube with metal catalyst and polymer: application to electromagnetic interference shielding, Current Applied Physics 4 (2004) 577–580.

[23] S. Rawal, Multifunctional carbon nanocomposite coatings for space structures, in: 47th AIAA/ASME/ASCE/AHS/ASC Structures, Stuctural Dynamics, and Materials Conference, AIAA/ASME/ASCE/AHS/ASC, Newport, Rhode Island, 2006, aIAA-2006-1948.

[24] B. Yakobson, P. Avouris, Mechanical properties of carbon nanotubes, Topics in Applied Physics: Carbon Nanotubes 80 (2001) 287–327.

[25] B. Demczyk, Y. Wang, J. Cumings, M. Hetman, W. Han, A. Zettl, R. Ritchie, Direct mechanical measurement of the tensile strength and elastic modulus of multiwalled carbon nanotubes, Materials Science and Engineering A 334 (2002) 173–178.

[26] J. Hone, M. Whitney, C. Piskoti, A. Zettl, Thermal conductivity of single-walled carbon nanotubes, Physical Review B 59 (4) (1999) R2514–R2516.

[27] T. Ebbesen, H. Lezec, H. Hiura, J. Bennett, H. Ghaemi, T. Thio, Electrical conductivity of individual carbon nanotubes, Nature 382 (1996) 54–56.

[28] A. Peigney, C. Laurent, E. Flahaut, A. Rousset, Carbon nanotubes in novel ceramic matrix nanocomposites, Ceramics International 26 (2000) 677–683.

[29] M. Shaffer, A. H. Windle, Fabrication and characterization of carbon nanotube/poly(vinyl alcohol) composites, Advanced Materials 11 (11) (1999) 937–941.

[30] P. Potschke, A. Bhattacharyya, A. Janke, Carbon nanotube-filled polycarbonate composites produced by melt mixing and their use in blends with polyethylene, Carbon 42 (2004) 965–969.

[31] X. Gong, J. Liu, S. Baskaran, R. Voise, J. Young, Surfactant-assisted processing of carbon nanotube/polymer composites, Chemistry of Materials 12 (1049-1052).

[32] C. A. Cooper, D. Ravich, D. Lips, J. Mayer, H. Wagner, Distribution and

alignment of carbon nanotubes and nanofibrils in a polymer matrix, Composites Science and Technology 62 (2002) 1105–1112.

[33] J. Zhu, J. Kim, H. Peng, J. Margrave, V. Khabashesku, E. Barrera, Improving the dispersion and integration of single-walled carbon nanotubes in epoxy composites through functionalization, Nano Letters 3 (8) (2003) 1107–1113.

[34] A. Star, J. Stoddart, D. Steuerman, M. Diehl, A. Boukai, E. Wong, Preparation and properties of polymer-wrapped single-walled carbon nanotubes, Angewandte Chemie International Edition 40 (9) (2001) 1721–1725.

[35] L. Jin, C. Bower, O. Zhou, Alignment of carbon nanotubes in a polymer matrix by mechanical stretching, Applied Physics Letters 73 (9) (1998) 1197–1199.

[36] L. Schadler, S. C. Giannaris, P. M. Ajayan, Load transfer in carbon nanotube epoxy composites, Applied Physics Letters 73 (26) (1998) 3842–3844.

[37] F. T. Fisher, R. D. Bradshaw, L. C. Brinson, Effects of nanotube waviness on the modulus of nanotube-reinforced polymers, Applied Physics Letters 80 (24) (2002) 4647–4649.

[38] B. McCarthy, J. Coleman, R. Czerw, A. Dalton, M. in het Panhuis, A. Maiti, A. Drury, P. Bernier, J. Nagy, B. Lahr, H. Byrne, D. Carroll, W. Blau, A microscopic and spectroscopic study of interactions between carbon nanotubes and a conjugated polymer, Journal of Physical Chemistry B 106 (2002) 2210–2216.

[39] M. in het Panhuis, A. Maiti, A. Dalton, A. van den Noort, J. Coleman, B. McCarthy, W. Blau, Selective interaction in a polymer-single wall carbon nanotube composite, Journal of Physical Chemistry B 107 (2003) 478–482.

[40] H. Wagner, O. Lourie, Y. Feldman, R. Tenne, Stress-induced fragmentation of multiwall carbon nanotubes in a polymer matrix, Applied Physics Letters 72 (2) (1998) 188–190.

[41] O. Lourie, H. Wagner, Transmission electron microscopy observations of fracture of single-wall carbon nanotubes under axial tension, Applied Physics Letters 73 (24) (1998) 3527–3529.

[42] F. Du, R. Scogna, W. Zhou, S. Brand, J. Fischer, K. Winey, Nanotube networks in polymer nanocomposites: rheology and electrical conductivity, Macromolecules 37 (2004) 9048–9055.

[43] H. Koerner, W. Liu, M. Alexander, P. Mirau, H. Dowty, R. Vaia, Deformation-morphology correlations in electrically conductive carbon nanotube-thermoplastic polyurethane nanocomposites, Polymer 46 (2005) 4405–4420.

[44] T. McNally, P. Potschke, P. Halley, M. Murphy, D. Martin, S. Bell, G. Brennan, D. Bein, P. Lemoine, J. Quinn, Polyethylene multiwalled carbon nanotube composites, Polymer 46 (2005) 8222–8232.

[45] G. Hu, C. Zhao, S. Zhang, M. Yang, Z. Wang, Low percolation thresholds of electrical conductivity and rheology in poly(ethylene terephthalate) through the networks of multi-walled carbon nanotubes, Polymer 47 (2006) 480–488.

[46] S. Yang, J. Castilleja, E. Barrera, K. Lozano, Thermal analysis of an acrylonitrile-butadiene-styrene/swnt composite, Polymer Degradation and Stability 83 (2004) 383–388.

[47] P. Watts, D. Ponnampalam, W. Hsu, A. Barnes, B. Chambers, The complex

permittivity of mulit-walled carbon nanotube-polystyrene composite films in x-band, Chemical Physics Letters 378 (2003) 609–614.

[48] D. Qian, E. Dickey, R. Andrews, T. Rantell, Load transfer and deformation mechanisms in carbon nanotube-polystyrene composites, Applied Physics Letters 76 (20) (2000) 2868–2870.

[49] J. Zhu, H. Peng, F. Rodriguez-Macias, J. Margrave, V. Khabashesku, A. Imam, K. Lozano, E. Barrera, Reinforcing epoxy polymer composites through covalent integration of functionalized nanotubes, Advanced Functional Materials 14 (7) (2004) 643–648.

[50] R. Khare, S. Bose, Carbon nanotube based composites- a review, Journal of Minerals and Materials Characterization and Engineering 4 (1) (2005) 31–46.

[51] A. Allaoui, S. Bai, H. Cheng, J. Bai, Mechanical and electrical properties of a mwnt/epoxy composite, Composites Science and Technology 62 (2002) 1993–1998.

[52] O. Meincke, D. Kaempfer, H. Weickmann, C. Friedrich, M. Vathauer, H. Warth, Mechanical properties and electrical conductivity of carbon-nanotube filled polyamide-6 and its blends with acrylonitrile/butadiene/styrene, Polymer 45 (2004) 739–748.

[53] F. Gojny, M. Wichmann, B. Fiedler, I. Kinloch, W. Bauhofer, A. Windle, K. Schulte, Evaluation and identification of electrical and thermal conduction mechanisms in carbon nanotube/epoxy composites, Polymer 47 (2006) 2036–2045.

[54] J. Sandler, M. Shaffer, T. Prasse, W. Bauhofer, K. Schulte, A. Windle, Development of a dispersion process for carbon nanotubes in an epoxy matrix and the resulting electrical properties, Polymer 40 (1999) 5967–5971.

[55] J. Sandler, J. Kirk, I. Kinloch, M. Shaffer, A. Windle, Ultra-low electrical percolation threshold in carbon-nanotube-epoxy composites, Polymer 44 (2003) 5893–5899.

[56] W. Li, W. Wang, J. Dai, Anisotropic properties of aligned swnt modified poly (methyl methacrylate) nanocomposites, Bulletin of Materials Science 29 (3) (2006) 313–316.

[57] P. Potschke, S. Dudkin, I. Alig, Dielectric spectroscopy on melt processed polycarbonate-multiwalled carbon nanotube composites, Polymer 44 (2003) 5023–5030.

[58] P. Potschke, M. Abdel-Goad, I. Alig, S. Dudkin, D. Lellinger, Rheological and dielectrical characterization of melt mixed polycarbonate-multiwalled carbon nanotube composites, Polymer 45 (2004) 8863–8870.

[59] S. Curran, D. Zhang, W. Wondmagegn, A. Ellis, J. Cech, S. Roth, D. Carroll, Dynamic electrical properties of polymer-carbon nanotube composites: enhancement through covalent bonding, Journal of Materials Research 21 (4) (2006) 1071–1077.

[60] M. Rutkofsky, M. Banash, R. Rajagopal, J. Chen, Using a carbon nanotube additive to make electrically conductive commercial polymer composites, Tech. rep., Zyvex Corporation, 9709 (2006).

[61] S. Curran, P. Ajayan, W. Blau, D. Carroll, J. Coleman, A. Dalton, A. Davey,

A. Drury, B. McCarthy, S. Maier, A. Strevens, A composite from poly(m-phenylenevinyleneco-2,5-dioctoxy-p-phenylenevinylene) and carbon nanotubes: a novel material for molecular optoelectronics, Advanced Materials 10 (14) (1998) 1091–1093.

[62] J. Coleman, S. Curran, A. Dalton, A. Davey, B. McCarthy, W. Blau, R. Barklie, Percolation-dominated conductivity in a conjugated-polymer-carbon-nanotube composite, Physical Review B 58 (12) (1998) R7492–R7495.

[63] R. Andrews, D. Jacques, A. Rao, T. Rantell, F. Derbyshire, Y. Chen, J. Chen, R. Haddon, Nanotube composite carbon fibers, Applied Physics Letters 75 (9) (1999) 1329–1331.

[64] Z. Ounaies, C. Park, K. Wise, E. Siochi, J. Harrison, Electrical properties of single wall carbon nanotube reinforced polyimide composites, Composites Science and Technology 63 (2003) 1637–1646.

[65] R. Haggenmueller, F. Du, J. Fischer, K. Winey, Interfacial in situ polymerization of single wall carbon nanotube/nylon 6,6 nanocomposites, Polymer 47 (2006) 2381–2388.

[66] S.-L. Shi, J. Liang, Effect of multiwall carbon nanotubes on electrical and dielectric properties of yttria-stabilized zirconia ceramic, Communications of the American Ceramic Society 89 (11) (2006) 3533–3535.

[67] S. Torquato, Random Heterogeneous Materials: Microstructure and Macroscopic Properties, Springer-Verlag, New York, 2002.

[68] F. Du, J. Fischer, K. Winey, Effect of nanotube alignment on percolation con-

ductivity in carbon nanotube/polymer composites, Physical Review B 72 (2005) 121404–1–4.

[69] M. Foygel, R. Morris, D. Anez, S. French, V. Sobolev, Theoretical and computational studies of carbon nanotube composites and suspensions: electrical and thermal conductivity, Physical Review B.

[70] N. Lebovka, S. Tarafdar, N. Vygornitskii, Computer simulation of electrical conductivity of colloidal dispersions during aggregation, Physical Review E 73 (2006) 031402–1–6.

[71] R. Smith, J. Carey, R. Murphy, W. Blau, J. Coleman, S. Silva, Charge transport effects in field emission from carbon nanotube-polymer composites, Applied Physics Letters 87 (2005) 263105–1–3.

[72] Y. Song, J. Youn, Evaluation of effective thermal conductivity for carbon nanotube/polymer composites using control volume finite element method, Carbon 44 (2006) 710–717.

[73] M. Bryning, D. Milkie, M. Islam, J. Kikkawa, A. Yodh, Thermal conductivity and interfacial resistance in single-wall carbon nanotube epoxy composites, Applied Physics Letters 87 (2005) 161909–1–3.

[74] C. Guthy, F. Du, S. Brand, J. Fischer, K. Winey, Thermal conductivity of single-walled carbon nanotube/pmma nanocomposites, in: Materials Research Society Symposium Proceedings, Vol. 858E, 2005, hH3.31.1.

[75] F. Du, C. Guthy, T. Kashiwagi, J. Fischer, K. Winey, An infiltration method for preparing single-wall nanotube/epoxy composites with improved thermal conductivity, Journal of Polymer Science B 44 (2006) 1513–1519.

[76] Y. Xu, G. Ray, B. Abdel-Magid, Thermal behavior of single-walled carbon nanotube polymer-matrix composites, Composites Part A: Applied Science and Manufacturing 37 (2006) 114–121.

[77] C.-W. Nan, Z. Shi, Y. Lin, A simple model for thermal conductivity of carbon nanotube-based composites, Chemical Physics Letters 375 (2003) 666–669.

[78] S. Huxtable, D. Cahill, S. Shenogin, L. Xue, R. Ozisik, P. Barone, M. Usrey, M. Strano, G. Siddons, M. Shim, P. Keblinski, Interfacial heat flow in carbon nanotube suspensions, Nature Materials 2 (2003) 731–734.

[79] T. Clancy, T. Gates, Modeling of interfacial modification effects on thermal conductivity of carbon nanotube composites, Polymer 47 (2006) 5990–5996.

[80] H. Zhong, J. Lukes, Interfacial thermal resistance between carbon nanotubes: Molecular dynamics simulations andanalytical thermal modeling, Physical Review B 74 (2006) 125403–1–10.

[81] S. Shenogin, A. Bodapati, L. Xue, R. Ozisik, P. Keblinski, Effect of chemical functionalization on thermal transport of carbon nanotube composites, Applied Physics Letters 85 (12) (2004) 2229–2231.

[82] C.-W. Nan, G. Liu, Y. Lin, M. Li, Interface effect on thermal conductivity of carbon nanotube composites, Applied Physics Letters 85 (16) (2004) 3549–3551.

[83] R. Yang, G. Chen, M. Dresselhaus, Thermal conductivity of simple and tubular nanowire composites in the longitudinal direction, Physical Review B 72 (2005) 125418–1–125418–7.

[84] M.-T. Hung, O. Choi, Y. Ju, H. Hahn, Heat conduction in graphite-

nanoplatelet-reinforced polymer nanocomposites, Applied Physics Letters 89 (2006) 023117–1–3.

[85] C.-W. Nan, R. Birringer, D. Clarke, H. Gleiter, Effective thermal conductivity of particulate composites with interfacial thermal resistance, Journal of Applied Physics 81 (10) (1997) 6692–6699.

[86] K. Kudin, G. Scuseria, B. Yakobson, c_2f, bn, and c nanoshell elasticity from ab initio computations, Physical Review B 64 (2001) 235406–1–235406–10.

[87] B. Yakobson, C. Brabec, J. Bernholc, Nanomechanics of carbon nanotubes: instabilities beyond linear response, Physical Review Letters 76 (14) (1996) 2511–2514.

[88] S. Frankland, V. Harik, G. Odegard, D. Brenner, T. Gates, The stress-strain behavior of polymer-nanotube composites from molecular dynamics simulations, Tech. rep., NASA ICASE (2002).

[89] G. Odegard, T. Gates, K. Wise, C. Park, E. Siochi, Constitutive modeling of nanotube-reinforced polymer composites, Composites Science and Technology 63 (2003) 1671–1687.

[90] T. Chen, G. Weng, W.-C. Liu, Effect of kapitza contact and consideration of tube-end transport on the effective conductivity in nanotube-based composites, Journal of Applied Physics 97 (2005) 104312–1–4.

[91] F. Fisher, L. Brinson, Viscoelastic interphases in polymer-matrix composites: theoretical models and finite element analysis, Composites Science and Technology 61 (2001) 731–748.

[92] P. Zhang, Y. Huang, P. H. Geubelle, P. A. Klein, K. C. Hwang, The elastic modulus of single-wall carbon nanotubes: a continuum analysis incorporating interatomic potentials, International Journal of Solids and Structures 39 (2002) 3893–3906.

[93] M. Arroyo, T. Belytschko, An atomistic-based finite deformation membrane for single layer crystalline films, Journal of the Mechanics and Physics of Solids 50 (2002) 1941–1977.

[94] M. Huhtala, A. Kuronen, K. Kaski, Carbon nanotube structures: molecular dynamics simulation at realistic limit, Computer Physics Communications 146 (2002) 30–37.

[95] T. Belytschko, S. P. Xiao, G. C. Schatz, R. S. Ruoff, Atomistic simulation of nanotube fracture, Physical Review B 65 (2002) 235430–1–8.

[96] S. Namilae, N. Chandra, C. Shet, Mechanical behavior of functionalized nanotubes, Chemical Physics Letters 387 (2004) 247–252.

[97] D. Srivastava, C. Wei, K. Cho, Nanomechanics of carbon nanotubes and composites, Applied Mechanics Reviews 56 (2) (2003) 215–230.

[98] J. Gou, Z. Liang, C. Zhang, B. Wang, Computational analysis of effect of single-walled carbon nanotube rope on molecular interaction and load transfer of nanocomposites, Composites Part B: Engineering 36 (2005) 524–533.

[99] G. Seidel, D. Lagoudas, S. Frankland, T. Gates, Modeling functionally graded interphase regions in carbon nanotube reinforced composites, in: Proceedings of the 20th ASC Technical Conference, American Society for Composites, Drexel University, Philadelphia, PA, 2005.

[100] S. Frankland, V. Harik, G. Odegard, D. Brenner, T. Gates, The stress-strain behavior of polymer-nanotube composites from molecular dynamics simulation, Composites Science and Technology 63 (2003) 1655–1661.

[101] S. Frankland, A. Caglar, D. Brenner, M. Griebel, Molecular simulation of the influence of chemical cross-links on the shear strength of carbon nanotube-polymer interfaces, Journal of Physical Chemistry B 106 (2002) 3046–3048.

[102] T. C. Clancy, T. S. Gates, Mechanical properties of nanostructured materials determined through molecular modeling techniques, in: 46th AIAA/ASME/ASCE/AHS/ASC Structures, Structural Dynamics and Materials Conference, Austin, TX, United States, 2005.

[103] J. Oden, T. Belytschko, I. Babuska, T. Hughes, Research directions in computational mechanics, Computer Methods in Applied Mechanics and Engineering 192 (2003) 913–922.

[104] S. Zhang, S. Mielke, R. Khare, D. Troya, G. Ruoff, R.S.a nd Schatz, T. Belytschko, Mechanics of defects in carbon nanotubes: atomistic and multiscale simulations, Physical Review B 71 (2005) 115403–1–12.

[105] S. Xiao, T. Belytschko, A bridging domain method for coupling continua with molecular dynamics, Computer Methods in Applied Mechanics and Engineering 193 (2004) 1645–1669.

[106] C. Li, T.-W. Chou, Multiscale modeling of carbon nanotube reinforced polymer composites, Journal of Nanoscience and Nanotechnology 3 (6) (2003) 1–8.

[107] S. Frankland, G. Odegard, M. Herzog, T. Gates, C. Fay, Constitutive modeling of cross-linked nanotube materials with variable stiffness tethers, in:

ASC/ASTM-D30 Joint 19th Annual Technical Conference, ASC, Atlanta, GA, 2004.

[108] T. Gates, G. Odegard, M. Nemeth, S. Frankland, Predicting the influence of nano-scale material structure on the in-plane buckling of orthotropic plates, in: 45th AIAA/ASME/ASCE/AHS/ASC Structures, Structural Dynamics and Materials Conference, Palm Springs, CA, 2004.

[109] G. Odegard, S. Frankland, T. Gates, Effect of nanotube functionalization on the elastic properties of polyethylene nanotube composites, AIAA Journal 43 (8) (2005) 1828–1835, aIAA-9468-376.

[110] T. Gates, G. Odegard, S. Frankland, T. Clancy, Computational materials: multi-scale modeling and simulation of nanostructured materials, Composites Science and Technology 65 (2005) 2416–2434.

[111] X.-L. Gao, K. Li, A shear-lag model for carbon nanotube-reinforced polymer composites, International Journal of Solids and Structures 42 (2005) 1649–1667.

[112] Y. Liu, X. Chen, Evaluations of the effective material properties of carbon nanotube-based composites using nanoscale representative volume element, Mechanics of Materials 35 (2003) 69–81.

[113] G. Odegard, T. Gates, Constitutive modeling of nanotube/polymer composites with various nanotube orientatons, in: 2002 SEM Annual Conference on Experimental and Applied Mechanincs, June 10-12, 2002, Milwaukee, WI, SEM, Milwaukee, WI, 2002.

[114] G. Odegard, T. Gates, K. Wise, Constitutive modeling of nanotube-reinforced polymer composites, Tech. rep., AIAA (2002).

[115] G. Odegard, T. Gates, K. Wise, C. Park, E. Siochi, Constitutive modeling of nanotube-reinforced polymer composites, Tech. rep., NASA ICASE (2002).

[116] G. Odegard, V. Harik, K. Wise, T. Gates, Constitutive modeling of nanotube-reinforced polymer composite systems, Tech. rep., NASA (2001).

[117] F. Fisher, R. Bradshaw, L. Brinson, Fiber waviness in nanotube-reinforced polymer composites - i: modulus predictions using effective nanotube properties, Composites Science and Technology 63 (2003) 1689–1703.

[118] V. Hadjiev, D. Lagoudas, E.-S. Oh, P. Thakre, D. Davis, B. Files, L. Yowell, S. Arepalli, J. Bahr, J. Tour, Buckling instabilities of octadecylamine functionalized carbon nanotubes embedded in epoxy, Composites Science and Technology (2005) Accepted, In Press.

[119] H. Wagner, Nanotube-polymer adhesion: a mechanics approach, Chemical Physics Letters 361 (2002) 57–61.

[120] S. Frankland, A. Caglar, D. Brenner, M. Griebel, Reinforcement mechanisms in polymer nanotube composites: simulated non-bonded and cross-linked systems, in: Nanotubes and Related Materials Symposium, Vol. 633, Materials Research Society, Boston, Massachusetts, 2000, pp. A14.17.1–A14.17.5.

[121] M. Griebel, J. Hamaekers, Molecular dynamics simulations of the elastic moduli of polymer-carbon nanotube composites, Computer Methods in Applied Mechanics and Engineering 193 (2004) 1773–1788.

[122] Z. Gang, B. Li, Thermal conductivity of nanotubes: effects of chirality and isotope impurity, Journal of Physical Chemistry B 109 (2005) 23823–23826.

[123] Q. Xue, Model for the effective thermal conductivity of carbon nanotube composites, Nanotechnology 17 (2006) 1655–1660.

[124] P. Song, C. Liu, S. Fan, Improving the thermal conductivity of nanocomposites by increasing the length efficiency of loading carbon nanotubes, Applied Physics Letters 88 (2006) 153111–1–153111–3.

[125] D. McLachlan, C. Chiteme, C. Park, K. Wise, S. Lowther, P. Lillehei, E. Siochi, J. Harrison, Ac and dc percolative conductivity of single wall carbon nanotube polymer composites, Journal of Polymer Science B 43 (2005) 3273–3287.

[126] J. Kovacs, B. Velagala, K. Schulte, W. Bauhofer, Two percolation thresholds in carbon nanotube epoxy composites, Composites Science and Technology 67 (2007) 922–928.

[127] T. Mori, K. Tanaka, Average stress in matrix and average elastic energy of materials with misfitting inclusions, Acta Metallurgica 21 (1973) 571–574.

[128] Y. Benveniste, A new approach to the application of mori-tanaka's theory in composite materials, Mechanics of Materials 6 (1987) 147–157.

[129] D. Lagoudas, A. Gavazzi, H. Nigam, Elastoplastic behavior of metal matrix composites based on incremental plasticity and the mori-tanaka averaging scheme, Computational Mechanics 8 (1991) 193–203.

[130] R. Hill, A self-consistent mechanics of composite materials, Journal of Mechanics and Physics of Solids 13 (1965) 213–222.

[131] J. Eshelby, The determination of the elastic field of an ellipsoidal inclusion, and related problems, Proceedings of the Royal Society of London 241 (1226) (1957) 376–396.

[132] Y. Benveniste, G. Dvorak, T. Chen, Stress fields in composites with coated inclusions, Mechanics of Materials 7 (6) (1989) 305–317.

[133] A. Dasgupta, S. Bhandarkar, A generalized self-consistent mori-tanaka scheme for fiber-composites with multiple interphases, Mechanics of Materials 14 (1992) 67–82.

[134] R. Bradshaw, F. Fisher, L. Brinson, Fiber waviness in nanotube-reinforced polymer composites: Ii. modeling via numerical approximation of the dilute strain concentration tensor, Composites Science and Technology 63 (2003) 1705–1722.

[135] Y. Benveniste, G. Dvorak, T. Chen, On effective properties of composites with coated cylindrically orthotropic fibers, Mechanics of Materials 12 (1991) 289–297.

[136] H. Wagner, Thermal residual stress in composites with anisotropic interphases, Physical Review B 53 (9) (1996) 5055–5058.

[137] N. Anifantis, P. Kakavas, G. Papanicolaou, Thermal stress concentration due to imperfect adhesion in fiber-reinforced composites, Composites Science and Technology 57 (1997) 687–696.

[138] H. Wagner, J. Nairn, Residual thermal stresses in three concentric transversely isotropic cylinders: application to thermoplastic-matrix composites containing a transcrystalline interphase, Composites Science and Technology 57 (1997) 1289–1302.

[139] Y. Benveniste, T. Miloh, Imperfect soft and stiff interfaces in two-dimensional elasticity, Mechanics of Materials 33 (2001) 309–323.

[140] Z. Hashin, Thin interphase/imperfect interface in elasticity with application to coated fiber composites, Journal of the Mechanics and Physics of Solids 50 (2002) 2509–2537.

[141] J. Achenbach, H. Zhu, Effect of interphases on micro and macromechanical behavior of hexagonal-array fiber composites, ASME Journal of Applied Mechanics 57 (1990) 956–963.

[142] E. Sancaktar, P. Zhang, Nonlinear viscoelastic modeling of the fiber-matrix interphase in composite materials, ASME Journal of Mechancial Design 112 (1990) 605–619.

[143] S. Gardner, C. Pittman Jr., R. Hackett, Polymeric composite materials incorporating an elastomeric interphase: a mathematical assessment, Composites Science and Technology 46 (1993) 307–318.

[144] B. Low, S. Gardner, C. Pittman Jr., R. Hackett, A micromechanical characterization of graphite-fiber/epoxy composites containing a heterogeneous interphase region, Composites Science and Technology 52 (1994) 589–606.

[145] K. Jayaraman, K. Reifsnider, R. Swain, Elastic and thermal effects in the interphase: part ii. comments on modeling studies, Journal of Composites Technology and Research 15 (1993) 14–22.

[146] C. Kristi, N. Anifantis, Load carrying characteristics of short fiber composites containing a heterogenous interphase region, Computational Materials Science 20 (2001) 86–97.

[147] M. Rubin, Y. Benveniste, A cosserat shell model for interphases in elastic media, Journal of the Mechanics and Physics of Solids 52 (2004) 1023–1052.

[148] P. Wray, O. Richmond, H. Morrison, Use of the dirichlet tessellation for characterizing and modeling nonregular dispersions of second-phase particles, Metallography 16 (1983) 39–58.

[149] W. Spitzag, J. Kelly, O. Richmond, Quantative characterization of second phase populations, Metallography 18 (1985) 235–261.

[150] S. Ghosh, Z. Nowak, K. Lee, Quantitative characterization and modeling of composite microstructures by voronoi cells, Acta Materialia 45 (6) (1997) 2215–2234.

[151] J. Boselli, P. Pitcher, P. Gregson, I. Sinclair, Quantittative assessment of particle distribution effects on short crack growth in sicp reinforced al-alloys, Scripta Materialia 38 (1998) 839–844.

[152] J. Boselli, P. D. Pitcher, P. J. Gregson, I. Sinclair, Secondary phase distribution analysis via finite body tessllation, Journal of Microscopy 195 (2) (1999) 104–112.

[153] A. Bhattacharryya, D. C. Lagoudas, Effective elastic moduli of two-phase transversely isotropic composites with aligned clustered fibers, Acta Mechanica 145 (2000) 65–93.

[154] S. Ghosh, S. Moorthy, Elastic-plastic analysis of arbitrary heterogeneous materials with the voronoi cell finite element method, Computer Methods in Applied Mechanics and Engineering 121 (1995) 373–409.

[155] T. Tszeng, The effects of particle clustering on the mechanical behavior of particle reinforced composites, Composites Part B: Engineering 29B (1998) 299–308.

[156] J. Boyd, D. Lloyd, Clustering in particulate mmcs, Comprehensive Composite Materials 3 (2000) 139–148.

[157] Y. Kataoko, M. Taya, Analysis of mechanical behavior of a short fiber composite using micromechanics based model (effects of fiber clustering on composite stiffness), JSME International Journal 43 (1) (2000) 46–52.

[158] Z. Hashin, B. Rosen, The elastic moduli of fiber-reinforced materials, Journal of Applied Mechanics 31 (1964) 223–232.

[159] R. Christensen, K. Lo, Solutions for effective shear properties in three phase sphere and cylinder models, Journal of the Mechanics and Physics of Solids 27 (1979) 315–330.

[160] R. Christensen, A critical evaluation for a class of micromechanics models, Journal of the Mechanics and Physics of Solids 38 (3) (1990) 379–404.

[161] G. Seidel, D. Lagoudas, Micromechanical analysis of the effective elastic properties of carbon nanotube reinforced composites, Mechanics of Materials 38 (2006) 884–907.

[162] D. Hammerand, G. Seidel, D. Lagoudas, Computational micromechanics of clustering and interphase effects in carbon nanotube composites, Mechanics of Advanced Materials and Structures 14 (2007) 277–294.

[163] Z. Hashin, Thermoelastic properties and conductivity of carbon/carbon fiber composites, Mechanics of Materials 8 (1990) 293–308.

[164] G. Carman, R. Averill, K. Reifsnider, J. Reddy, Optimization of fiber coatings to minimize stress concentrations in composite materials, Journal of Composite Materials 27 (6) (1993) 589–612.

[165] E. Herve, A. Zaoui, Elastic behaviour of multiply coated fibre-reinforced composites, International Journal of Engineering Science 33 (10) (1995) 1419–1433.

[166] Z. Hashin, Thermoelastic properties of fiber composites with imperfect interface, Mechanics of Materials 8 (1990) 333–348.

[167] K. Jayaraman, K. Reifsnider, The residual stresses in a composite with continuously varying young modulus in the fiber matrix interphase, Journal of Composite Materials 26 (6) (1992) 770–791.

[168] I. Jasiuk, M. Kouider, The effect of an inhomogeneous interphase on the elastic constants of transversely isotropic composites, Mechanics of Materials 15 (1993) 53–63.

[169] M. Lutz, M. Ferrari, Effect of an inhomogeneous interphase region on the mechanical properties of a fiber composite, in: F. TECHNA (Ed.), Advanced structural fiber composites: proceedings of topical symposium III on advanced strurctural fiber composites of the 8th CIMTTEC-World Ceramics C, CIMTEC, 1995, pp. 559–566.

[170] W. Huang, S. Rokhlin, Generalized self-consistent model for composites with functionally graded and multilayered interphases: transfer matrix approach, Mechanics of Materials 22 (1996) 219–247.

[171] J. Nairn, Thermoelastic analysis of residual stresses in unidirectional, high-performance composites, Polymer Composites 6 (1985) 123–130.

[172] Y. Chu, S. Rokhlin, Determination of fiber-matrix interphase moduli from experimental moduli of composites with multi-layered fibers, Mechanics of Materials 21 (1995) 191–215.

[173] N. Pagano, G. Tandon, Elastic response of multi-directional coated-fiber composites, Composites Science and Technology 31 (1988) 273–293.

[174] R. Landauer, The electrical resistance of binary metallic mixtures, Journal of Applied Physics 23 (7) (1952) 779–784.

[175] E. Kerner, The electrical conductivity of composite media, Proceedings of the Physical Society B (1956) 802–807.

[176] J. Keller, Conductivity of a medium containing a dense array of perfectly conducting spheres or cylinders or nonconducting cylinders, Journal of Applied Physics 34 (4) (1963) 991–993.

[177] Z. Hashin, S. Shtrikman, A variational approach to the theory of the effective magnetic permeability of multiphase materials, Journal of Applied Physics 33 (10) (1962) 3125–3131.

[178] Z. Hashin, Assessment of the self consistent scheme approximation: conductivity of particulate composites, Journal of Composite Materials 2 (3) (1968) 284–300.

[179] Z. Hashin, Analysis of properties of fiber composites with anisotropic heterogeneous materials, Journal of Applied Mechanics 46 (1979) 543–550.

[180] D. Bergman, The dielectric constant of a composite material-a problem in classical physics, Physics Reports 43 (9) (1978) 377–407.

[181] G. Milton, The coherent potential approximation is a realizable effective medium scheme, Journal of Communications in Mathematical Physics 99 (4) (1985) 463–500.

[182] Y. Benveniste, On the effective thermal conductivity of multiphase composites, Zeitschrift fur Angewandte Mathematik und Physik 37 (5) (1986) 696–713, (ZAMP).

[183] Y. Benveniste, T. Miloh, On the effective thermal conductivity of coated short-fiber composites, Journal of Applied Physics 69 (3) (1991) 1337–1344.

[184] M. Ostoja-Starzewski, J. Schulte, Bounding of effective thermal conductivities of multiscale materials by essential and natural boundary conditions, Physical Review B 54 (1) (1996) 278–285.

[185] Y. Benveniste, Effective thermal conductivity of composites with a thermal contact resistance between the constituents: nondilute case, Journal of Applied Physics 61 (8) (1987) 2840–2843.

[186] T. Miloh, Y. Benveniste, A generalized self-consistent method for the effective conductivity of composites with ellipsoidal inclusions and cracked bodies, Journal of Applied Physics 63 (3) (1988) 789–796.

[187] L. Weber, J. Dorn, A. Mortensen, On the electrical conductivity of metal matrix composites containing high volume fractions of non-conducting inclusions, Acta Materialia 51 (2003) 3199–3211.

[188] L. Weber, C. Fischer, A. Mortensen, On the influence of the shape of randomly oriented, nonconducting inclusions in a conducting matrix on the effective electrical conductivity, Acta Materialia 51 (2003) 495–505.

[189] H. Hatta, M. Taya, Equivalent inclusion method for steady state heat conduction in composites, International Journal of Engineering Science 24 (7) (1986) 1159–1172.

[190] Y. Benveniste, T. Chen, G. Dvorak, The effective thermal conductivity of composites reinforced by coated cylindrically orthotropic fibers, Journal of Applied Physics 67 (6) (1990) 2878–2884.

[191] M. Taya, Micromechanics modeling of electronic composites, Journal of Engineering Materials and Technology 117 (4) (1995) 462–464.

[192] Y. Benveniste, G. Milton, New exact results for the effective electric, elastic, piezoelectric and other properties of composite ellipsoid assemblages, Journal of the Mechanics and Physics of Solids 51 (2003) 1773–1813.

[193] A. Decarlis, M. Jaeger, R. Martin, Determination of the effective thermal conductivity tensor of heterogeneous media using a self-consistent finite element method: application to the pseudo-percolation thresholds of mixtures containing nonspherical inclusions, Journal of Heat Transfer 122 (2000) 171–175.

[194] J. Spittle, K. Ravindran, S. Brown, Numerical prediction of the effective thermal conductivity of dendritic mushy zones, Modelling and Simulation in Materials Science and Engineering 7 (1999) 59–70.

[195] M. Ostoja-Starzewski, I. Jasiuk, W. Wang, K. Alzebdeh, Composites with functionally graded interphases: mesocontinuum concept and effective transverse conductivity, Acta Materialia 44 (5) (1996) 2057–2066.

[196] M. Lutz, R. Zimmerman, Effect of an inhomogeneous interphase zone on the bulk modulus and conductivity of a particlulate composites, International Journal of Solids and Structures 42 (2005) 429–437.

[197] T. Tanaka, Dielectric nanocomposites with insulating properties, IEEE Transactions on Dielectrics and Electrical Insulation 12 (5) (2005) 914–928.

[198] R. M. Christensen, Mechanics of Composite Materials, Krieger Publishing Company, Malabar, FL, 1979.

[199] J. Qu, M. Cherkaoui, Fundamentals of Micromechanics of Solids, John Wiley & Sons, Inc., Hoboken, New Jersey, 2006.

[200] W. Slaughter, The Linearized Theory of Elasticity, Birkhauser, Boston, 2002.

[201] W. Lai, D. Rubin, E. Krempl, Introduction to Continuum Mechanics, 3rd Edition, Butterworth-Heinemann Ltd, 1993.

[202] S. Jansson, Homogenized nonlinear constitutive properties and local stress concentrations for composites with periodic internal structure, International Journal of Solids and Structures 29 (17) (1992) 2181–2200.

[203] R. Hill, Elastic properties of reinforced solids: some theoretical principles, Journal of the Mechanics and Physics of Solids 11 (1963) 357–372.

[204] M. Fabrizio, A. Morro, Electromagnetism of Continuous Media: Mathematical Modelling and Applications, Oxford University Press, New York, 2003.

[205] J. Jackson, Classical Electrodynamics, 3rd Edition, John Wiley & Sons, Inc, New York, 1998.

[206] B. Budiansky, On the elastic moduli of some heterogeneous materials, Journal of Mechanics and Physics of Solids 13 (1965) 223–227.

[207] G. Weng, Some elastic properties of reinforced solids, with special reference to isotropic ones containing spherical inclusions, International Journal of Engineering Science 22 (1984) 845–856.

[208] N. Marzari, M. Ferrari, Textural and micromorphological effects on the overall elastic response of macroscopically anisotropic composites, Journal of Applied Mechanics 59 (1992) 269–275.

[209] P. Entchev, D. Lagoudas, Modeling porous shape memory alloys using micromechanical averaging techniques, Mechanics of Materials 34 (2002) 1–24.

[210] D. Lagoudas, A. Bhattacharyya, On the correspondence between micromechanical models for isothermal pseudoelastic response of shape memory alloys and the preisach model for hysteresis, Mathematics and Mechanics of Solids 2 (1997) 405–440.

[211] A. E. H. Love, A Treatise on the Mathematical Theory of Elasticity, Dover Publications, Inc, New York, 1944.

[212] T. Natsuki, K. Tantrakarn, M. Endo, Effects of carbon nanotube structures on mechanical properties, Applied Physics A 79 (2004) 117124.

[213] K. Tserpes, P. Papanikos, Finite element modeling of single-walled carbon nanotubes, Composites Part B: Engineering 36 (2005) 468–477.

[214] R. S. Ruoff, D. C. Lorents, Mechanical and thermal properties of carbon nanotubes, Carbon 33 (1995) 925–930.

[215] D. Qian, W. K. Liu, R. S. Ruoff, Load transfer mechanisms in carbon nanotube ropes, Composites Science and Technology 63 (2003) 1561–1569.

[216] M.-F. Yu, O. Lourie, M. J. Dyer, K. Maloni, T. F. Kelly, R. S. Ruoff, Strength and breaking mechanism of multi-walled carbon nanotubes under tensile load, Science 287 (28) (2000) 637–640.

[217] J. P. Lu, Elastic properties of single and multilayered nanotubes, Journal of Physics and Chemistry of Solids 58 (11) (1997) 1649–1652.

[218] Y.-H. Liao, Z. Liang, Y.-B. Park, B. Wang, C. Zhang, Fabrication and characterization of carbon nanotube/glass fiber-reinforced multiscale composites, in: 47th AIAA/ASME/ASCE/AHS/ASC Structures, Stuctural Dynamics, and Materials Conference, AIAA/ASME/ASCE/AHS/ASC, Newport, Rhode Island, 2006, aIAA-2006-1858.

[219] D. Penumadu, A. Dutta, G. Pharr, B. Files, Mechanical properties of blended single-wall carbon nanotube composites, Journal of Materials Research 18 (8) (2003) 1849–1853.

[220] X. Li, H. Gao, W. Scrivens, D. Fei, X. Xu, M. Sutton, A. Reynolds, M. Myrick, Nanomechanical characterization of single-walled carbon nanotube reinforced epoxy composites, Nanotechnology 15 (2004) 1416–1423.

[221] T. Mura, Micromechanics of Defects in Solids, 2nd Edition, Kluwer Academic Publishers, Dordrecht, 1987.

[222] G. Dvorak, J. Teply, Plasticity Today: Modeling, Methods and Applications, Elsevier, London, 1985.

[223] J. N. Coleman, K. P. Ryan, M. S. Lipson, A. Drury, M. Cadek, M. in het Panhuis, R. P. Wool, V. Barron, W. J. Blau, Effect of nanotube inclusions on polymer morphology in composite systems, Tech. rep., Material Ireland Polymer Research Centre, Department of Physics, Trinity College, Dublin, Ireland (Unknown).

[224] G. Odegard, T. Clancy, T. Gates, Modeling of the mechanical properties of nanoparticle/polymer composites, Polymer 46 (2005) 553–562.

[225] P. Thakre, D. Lagoudas, J. Zhu, E. Barrera, T. Gates, Effect of functionalization and weight fraction of single wall carbon nanotubes on mechanical properties of epoxy nanocomposites, in: International Conference on Computational and Experimental Engineering Sciences (ICCES), Chennai, India, 2005.

[226] D. Lagoudas, P. Thakre, A. Benzerga, Nanoindentation of cnt reinforced epoxy nanocomposites, in: European Conference on Fracture, Greece, 2006, eCF16.

[227] K. Whitten, K. Gailey, R. Davis, General Chemistry, 4th Edition, Saunders College Publishing, Fort Worth, 1992.

[228] S. Nakamura, T. Tomimura, K. Sanji, M. Hisida, Y. Hayakawa, Electrically conductive composites made with tpe and graphite, in: Proceedings of the 7th International Conference on Properties and Applications of Dielectric Materials, Nagoya, Japan, 2003.

[229] W. Pan, S. Yang, G. Li, J. Jiang, Electrical and structural analysis of conductive polyaniline/polyacrylonitrile composites, European Polymer Journal 41 (2005) 2127–2133.

[230] T. Ebbesen, Nanotubes, nanoparticles, and aspects of fullerene related carbons, Journal of Physics and Chemistry of Solids 58 (11) (1997) 1979–1982.

[231] B. Lesiak, A. Kosinski, A. Jablonski, L. Kover, J. Toth, D. Varga, I. Cserny, Determination of the inelastic mean free path of electrons in polyaniline samples by elastic peak electron spectroscopy, Surface and Interface Analysis 29 (9) (2000) 614–623.

[232] T. Odom, J.-L. Huang, P. Kim, C. Lieber, Atomic structure and electronic properties of single-walled carbon nanotubes, Nature 391 (1998) 62–64.

[233] E. Choi, J. Brooks, D. Eaton, M. Al-Haik, M. Hussaini, H. Garmestani, D. Li, K. Dahmen, Enhancement of thermal and electrical properties of carbon nanotube polymer composites by magnetic field processing, Journal of Applied Physics 94 (9) (2003) 6034–6039.

[234] J. Zhang, W. Cui, M. Juda, D. McCammon, R. L. Kelley, S. H. Moseley, C. K. Stahle, A. E. Szymkowiak, Non-ohmic effects in hopping conduction in doped silicon and germanium between 0.05 and 1 k, Physical Review B 57 (8) (1998) 4472–4481.

[235] S. Choi, Z. Zhang, W. Yu, F. Lockwood, E. Grulke, Anomalous thermal conductivity enhancement in nanotube suspensions, Applied Physics Letters 79 (14) (2001) 2252–2254.

[236] J. Hone, M. Llaguno, M. Biercuk, A. Johnson, B. Batlogg, J. Fischer, Thermal properties of carbon nanotubes and nanotube-based materials, Applied Physics A 74 (2002) 339–343.

[237] S. Berber, Y.-K. Kwon, D. Tomanek, Unusually high thermal conductivity of carbon nanotubes, Physical Review Letters 84 (20) (2000) 4613–4616.

[238] P. Kapitza, Heat transfer and superfluidity of helium ii, Physical Review 60 (1941) 354–355.

[239] R. Johnson, W. Little, Experiments on the kapitza resistance, Physical Review 130 (1963) 596–604.

[240] G. Pollack, Kapitza resistance, Reviews of Modern Physics 41 (1) (1969) 48–81.

[241] Y. Benveniste, T. Miloh, The effective conductivity of composites with imperfect thermal contact at constituent interfaces, International Journal of Engineering Science 24 (9) (1986) 1537–1552.

[242] H. Hatta, M. Taya, Effective thermal conductivity of a misoriented short fiber composite, Journal of Applied Physics 58 (7) (1985) 2478–2486.

[243] O. Levy, D. Stroud, Maxwell garnett theory for mixtures of anisotropic inclusions: application to conducting polymers, Physical Review B 56 (13) (1997) 8035–8046.

[244] D. Hansen, C. Ho, Thermal conductivity of high polymers, Journal of Polymer Science: Part A 3 (1965) 659–670.

[245] D. Blond, V. Barron, M. Ruether, K. Ryan, V. Nicolosi, W. Blau, J. Coleman, Enhancement of modulus, strength, and toughness in poly(methyl methacrylate)-based composites by the incorporation of poly(methyl methacrylate)-functionalized nanotubes, Advanced Functional Materials 16 (12) (2006) 1608–1614.

[246] M. Cadek, J. Coleman, V. Barron, K. Hedicke, W. Blau, Morphological and mechanical properties of carbon-nanotube-reinforced semicrystalline and amorphous polymer composites, Applied Physics Letters 81 (27) (2002) 5123–5125.

[247] B. Safadi, R. Andrews, E. Grulke, Multiwalled carbon nanotube polymer composites: synthesis and characterization of thin films, Journal of Applied Polymer Science 84 (2002) 2660–2669.

[248] J. Kearns, R. Shambaugh, Polypropylene fibers reinforced with carbon nanotubes, Journal of Applied Polymer Science 86 (2002) 2079–2084.

[249] X. Shi, J. Hudson, P. Spicer, J. Tour, R. Krishnamoorti, A. Mikos, Rheological behaviour and mechanical characterization of injectable poly(propylene fumarate)/single-walled carbon nanotube composites for bone tissure engineering, Nanotechnology 16 (2005) S531–S538.

[250] X. Zhang, T. Liu, T.a nd Sreekumar, S. Kumar, V. Moore, R. Hauge, R. Smalley, Poly(vinyl alcohol)/swnt composite film, Nano Letters 3 (9) (2003) 1285–1288.

[251] P. Gonnet, Thermal conductivity and coefficients of thermal expansion of swnts/epoxy nanocomposites, Industrial Engineering, The Florida State University, Tallahassee, FL (2004).

[252] C. Liu, H. Huang, Y. Wu, S. Fan, Thermal conductivity improvement of silicone elastomer with carbon nanotube loading, Applied Physics Letters 84 (21) (2004) 4248–4250.

[253] Y. Song, J. Youn, Influence of dispersion states of carbon nanotubes on physical properties of epoxy nanocomposites, Carbon 43 (2005) 1378–1385.

[254] H. Huang, C. Liu, Y. Wu, S. Fan, Aligned carbon nanotube composite films for thermal management, Advanced Materials 17 (2005) 1652–1656.

[255] J. Grunlan, Y.-S. Kim, S. Ziaee, X. Wei, B. Abdel-Magid, K. Tao, Thermal and mechanical behavior of carbon-nanotube-filled latex, Macromolecular Materials and Engineering 291 (2006) 1035–1043.

[256] H. Xie, H. Lee, W. Youn, M. Choi, Nanofluids containing multiwalled carbon nanotubes and their enhanced thermal conductivities, Journal of Applied Physics 94 (8) (2003) 4967–4971.

[257] M. Kouider, The effect of sliding interfaces and inhomogeneous interphases on thermal and elastic properties of composites, Ph.D. thesis, Michigan State University (1992).

[258] K. Pierson, J. Hales, K. Alvin, J. Mitchell, Adagio/Andante User's Guide Version 2.0, Sandia National Laboratories, Albuquerque, N.M., 87185 (2005).

[259] D. Flanagan, T. Belytschko, Uniform strain hexahedron and quadrilateral with orthogonal hourglass control, International Journal for Numerical Methods in Engineering 17 (5) (1981) 679–706.

[260] T. Belytschko, Correction of article by d.p. flanagan and t. belytschko, International Journal for Numerical Methods in Engineering 19 (3) (1983) 467–468, letters to the Editor.

APPENDIX A

SUMMARY OF AVAILABLE DATA ON CARBON NANOTUBES AND CNT NANOCOMPOSITES IN THE LITERATURE

A1. Carbon Nanotube Young's Modulus and Thickness

Tables summarizing the values from the literature for CNT Young's modulus and the corresponding thicknesses used in obtaining the value provided.

Reference [97]		
CNT Thickness (nm)	Young's Modulus (GPa)	
0.06	5500	SWCNT MD T-B
0.34	970	SWCNT Emp. Force Const
0.34	1200	SWCNT Tight Binding
0.34	800	SWCNT Ab Initio
0.95	950	MWCNT Ab Initio

Reference [97]		
CNT Thickness (nm)	Young's Modulus (GPa)	
0.34	1800	MWCNT Thermal Vib
0.34	1280	MWCNT Restoring Bending
0.34	1700	SWCNT Thermal Vib
0.34	1000	SWCNT Deflection Force

Reference [212]		
CNT Radius	Young's Modulus (Gpa)	Calculated Poisson's Ratio
0.85	625	0.275

Reference [213]		
CNT Thickness	Young's Modulus (Gpa)	From
0.066	5500	MD
0.074	5100	Tight Binding
0.075	4700	Local Density
0.089	3859	Ab Initio
0.075	4840	Continuum Shell
0.34	1010	Stiffness Mechanics
0.34	974	MD
0.34	1240	Tight Binding
0.34	1238	MD
0.066	5296	FE Truss (8,8)
0.074	4721	FE Truss (8,8)
0.075	4634	FE Truss (8,8)
0.089	3921	FE Truss (8,8)
0.075	4639	FE Truss (8,8)
0.34	1028	FE Truss (8,8)
0.34	1028	FE Truss (8,8)
0.34	1028	FE Truss (8,8)
0.34	1028	FE Truss (8,8)

Reference [92]		
CNT Thickness	Young's Modulus	From
0.335	475	Modified Cauch-Born
0.335	705	Modified Cauch-Born

Reference [25]		
CNT Thickness	MWNT Young's Modulus	Exp from
-	810	AFM-2 ends clamped
-	1280	AMF-1 end clamped
-	1260	TEM-Thermal Vib
-	910	TEM-Direct Tension

A2. Carbon Nanotube-Polymer Composite Young's Modulus

Tables summarizing the values from the literature for CNT-polymer composite Young's moduli and the corresponding weight percent or volume fraction in obtaining the value provided.

Reference [218]:	SWNT in EPON 862 cured W; Sonicated	
wt %	Storage Modulus (Gpa)	Normalized by Matrix
0	2.498	1
1	2.782	1.113691

Reference [36]:	MWNT in Shell EPON 828 triethylene tetraamine hardener;Ultrasonicated			
wt %	Tension Modulus (GPa)	Normalized	Compression Modulus (GPa)	Normalized
0	3.1	1	3.63	1
5	3.71	1.196774	4.5	1.239669

Reference [49]:	SWCNTs in Epoxy; Functionalized w/ dicarboxylic acid acyl peroxide treatment	
wt %	Young's Modulus (GPa)	Normalized
0	2.026	1
1	2.123	1.047878
1	2.65	1.307996
4	3.4	1.678184

Reference [219]:	Laser Ablation SWCNTs in EPON 862 w/ W; Sonicated from nanoindentation			
wt %	Young's Modulus (GPa)	Normalized	Young's Modulus (GPa)	Normalized
0	3.91	1	3.91	1
1	4.03	1.030691	3.99	1.02046
3	4.2	1.074169	4.2	1.074169
5	4.58	1.171355	4.51	1.153453

Reference [33]:	HiPCO SWCNTs in EPON 862 w/ W; Acid treated and Flourinated to Functionalize F-SWNT-COOH	
wt %	Tensile Testing E (GPa)	Normalized
0	2.026	1
1	2.123	1.047878
1	2.632	1.299112

Reference [220]:	Arc discharge SWCNTs in Epoxy Functionalized and termed f-SWNTs			
wt %	Nanoindentation Modulus (GPa)	Normalized	Storage Modulus (GPa)	Normalized
0	3.7	1	4	1
1	4.5	1.216216	5.5	1.375
3	5.9	1.594595	6	1.5
5	7	1.891892	7.1	1.775

Reference [245]:	(PMMA)-functionalized multiwalled carbon nanotubes	
vol. frac.	Tensile Modulus (GPa) from films	Normalized
0	0.71	1
0.0015	1.349	1.9
0.00019	0.925	1.302817
0.00038	1.02	1.43662
0.00075	1.27	1.788732
0.003	0.77	1.084507
0.006	1.05	1.478873

Reference [63]:	SWNTs in isotropic pitch fibers	
wt %	Fiber Tensile Modulus (GPa)	Normalized
0	34	1
1	41	1.205882
5	77	2.264706

Reference [246]:	MWNTs in PVA	
vol. frac.	Young's Modulus (GPa)	Normalized
0	7	1
0.00001	8.4	1.2
0.00002	9.1	1.3
0.00004	9.8	1.4
0.00006	12.6	1.8

Reference [246]:	MWNTs in PVK	
vol. frac.	Young's Modulus (GPa)	Normalized
0	2	1
0.000095	2.3	1.15
0.00015	3.1	1.55
0.00021	2.6	1.3
0.00028	3.7	1.85
0.00034	2.7	1.35
0.00048	5.5	2.75

Reference [51]:	MWNTs in Epoxy	
wt %	Tensile Test Young's Modulus (GPa)	Normalized
0	0.118	1
1	0.236	2
4	0.465	3.940678

Reference [247]:	MWNTs in Polystyrene Thin Films		
wt %	vol. frac.	Young's Modulus (GPa)	Normalized
0	0	1.53	1
1	0.487	2.1	1.372549
2	0.98	2.73	1.784314
5	2.49	3.4	2.222222

Reference [248]:	SWCNTs in Isotropic pitch fibers	
wt %	Fiber Young's Modulus (GPa)	Normalized
0	34	1
1	41	1.205882
5	78	2.294118

Reference [248]:	SWCNTs in PMMA fibers	
wt %	Young's Modulus (GPa)	Normalized
0	3.1	1
1	3.3	1.064516
5	5	1.612903
8	6	1.935484

Reference [248]:	SWCNTs in Polypropylene	
wt %	Young's Modulus (GPa)	Normalized
0	6.3	1
0.5	9.3	1.47619
1	9.8	1.555556

Reference [43]:	MWNTs in Polyurethane	
wt %	Young's Modulus (GPa)	Normalized
0	0.013	1
1	0.015	1.153846
5	0.04	3.076923
10	0.0625	4.807692
17	0.095	7.307692
20	0.164	12.61538

Reference [52]:	MWNTs in Polyamide-6	
wt %	Young's Modulus (GPa)	Normalized
0	2.59	1
1	2.98	1.150579
2	3.31	1.277992
4	3.49	1.34749
5	3.34	1.289575
6	3.76	1.451737
8	3.96	1.528958
10	4.13	1.594595
12	4.18	1.6139

Reference [249]:	SWNTs in Poly(propylene fumarate) (PPF); Functionalized with phenethylalcohol	
wt %	Compressive Modulus (GPa)	Normalized
0	0.318	1
0.05	0.468	1.471698
0.05	0.546	1.716981
0.05	0.554	1.742138

Reference [250]:	SWNTs in PVA/PVP/SDS		
wt %	Tensile Modulus (GPa)	Normalized by PVA	Normalized by PVA/PVP/SDS
0	1.9	1	-
0	2.5	x	1
5	4	2.105263	1.6

A3. Carbon Nanotube-Polymer Composite Electrical Conductivity

Tables summarizing the values from the literature for CNT-polymer composite electrical conductivity and the corresponding weight fraction or volume fraction in obtaining the value provided.

Reference [53] :	SWNT in epoxy
wt. frac.	Elec. Cond. S/cm
0	9.00E-11
0.0005	2.00E-05
0.001	2.00E-04
0.003	2.00E-03
0.005	0.01

Reference [61] :	nanotubes in PmPV
wt. frac.	Elec. Cond. S/cm
0	4.00E-12
0.05	3.00E-11
0.1	7.00E-08
0.15	1.00E-06
0.35	2.00E-05

Reference [63]:	SWNT in Pitch
wt. frac.	Elec. Cond. S/cm
0	117.6471
0.01	400
0.05	476.1905

Reference [56]:	SWNT in PMMA (film direction)
wt. frac.	Elec. Cond. S/cm
0	1.00E-12
0.005	1.50E-08
0.01	3.00E-06
0.015	2.00E-05
0.02	1.00E-04
0.025	6.00E-04
0.03	7.00E-04
0.035	8.00E-04
0.04	9.00E-04
0.045	1.00E-03
0.05	1.00E-03
0.055	1.00E-03
0.06	1.00E-03
0.065	1.00E-03
0.07	1.00E-03
0.08	1.00E-03
0.09	1.00E-03
0.1	1.00E-03

Reference [56]:	SWNT in PMMA (perpendicular to film)
wt. frac.	Elec. Cond. S/cm
0	1.00E-12
0.005	1.00E-11
0.01	1.00E-10
0.015	1.00E-09
0.02	3.00E-09
0.025	7.00E-09
0.03	2.00E-08
0.035	3.00E-08
0.04	5.00E-08
0.045	8.00E-08
0.05	9.00E-08
0.055	1.00E-07
0.06	1.50E-07
0.065	2.00E-07
0.07	3.00E-07
0.08	6.00E-07
0.09	9.00E-07
0.1	1.00E-06

Reference [30]:	MWNT in Polycarbonate (150 rpm 5 min)
wt. frac.	Elec. Cond. S/cm
0	2E-15
0.005	5E-13
0.01	5.56E-13
0.015	0.000345
0.02	0.000588
0.03	0.02
0.04	0.090909
0.05	0.105263
0.15	0.111111

Reference [30]:	MWNT in Polycarbonate (Haake)
wt. frac.	Elec. Cond. S/cm
0	2.5E-14
0.005	5E-14
0.01	1.02E-13
0.02	0.000588
0.05	0.02
0.15	0.166667

Reference [30]:	MWNT in Polycarbonate (50 rpm 15 min)
wt. frac.	Elec. Cond. S/cm
0.01	1.25E-10
0.015	0.005
0.02	0.007692
0.03	0.018868
0.05	0.102041

Reference [30]:	MWNT in Polycarbonate (150 rpm 15 min)
wt. frac.	Elec. Cond. S/cm
0.01	1.67E-06
0.015	5.26E-07
0.02	0.007143

Reference [30]:	MWNT in Polycarbonate (50 rpm 5 min)
wt. frac.	Elec. Cond. S/cm
0.02	0.000118

Reference [51]:	MWNT in epoxy
wt. frac.	Elec. Cond. S/cm
0	3.00E-10
0.005	3.80E-10
0.01	2.00E-04
0.04	3.80E-03

Reference [64]:	SWNT in Polyimide
vol. frac.	Elec. Cond. S/cm
0	6.00E-18
0.00025	3.00E-17
0.001	1.50E-08
0.002	5.00E-08
0.005	1.30E-07
0.01	1.60E-07

Reference [22]:	MWNT in PMMA w/FE
wt. frac.	Elec. Cond. S/cm
1.00E-03	1.10E-09
2.00E-03	1.00E-06
4.00E-03	1.50E-03
6.00E-03	9.00E-03
3.00E-02	2.50E-01
5.00E-02	8.00E-01
8.00E-02	2.00E+00
1.00E-01	4.00E+00
1.25E-01	6.00E+00
2.00E-01	1.00E+01
3.00E-01	2.00E+01
4.00E-01	2.50E+01

Reference [22]:	MWNT in PMMA w/Co
wt. frac.	Elec. Cond. S/cm
5.00E-03	6.00E-04
1.00E-02	1.40E-03
2.00E-02	7.00E-02
1.00E-01	1.40E+00
2.00E-01	2.00E+00

Reference [42]:	SWNT in PMMA
wt. frac.	Elec. Cond. S/cm
0.0039	2.00E-11
0.005	7.00E-09
0.01	1.00E-06
0.02	1.00E-05

Reference [62]:	Nanotube powder in PMPV
wt. frac.	Elec. Cond. S/cm
0	4.00E-12
0.005	6.00E-12
0.027	6.90E-12
0.063	1.00E-11
0.077	3.00E-08
0.088	5.00E-06
0.109	1.00E-01
0.15	2.00E-01
0.16	8.00E-01
0.358	4.00E+00

Reference [54]:	MWNT in epoxy
vol. frac.	Elec. Cond. S/cm
0.00015	5.00E-11
0.00022	7.80E-05
0.00034	7.00E-05
0.00059	2.00E-04
0.00071	2.40E-04
0.00089	4.90E-03
Reference [57]:	MWNT in PC
wt. frac.	Elec. Cond. S/cm
0	1.80E-16
0.005	2.00E-16
0.01	4.00E-16
0.015	6.00E-06
0.02	3.00E-04
0.03	6.00E-03
0.04	9.00E-03
0.05	1.50E-02

Reference [58]:	MWNT in PC
wt. frac.	Elec. Cond. S/cm
0.01	7.00E-11
0.01125	1.50E-06
0.0125	3.00E-05
0.0135	6.00E-05
0.0175	1.00E-03
0.02	3.00E-03
0.0225	7.00E-03
0.025	1.30E-02
0.03	5.00E-02

Reference [52]:	MWNT in PA
wt. frac.	Elec. Cond. S/cm
0	1E-15
0.02	1E-13
0.03	2E-12
0.04	5E-11
0.05	1.56E-09
0.06	7.14E-08
0.08	4.17E-05
0.1	0.000588
0.12	0.035714

Reference [43]:	MWNT in PU
vol. frac.	Elec. Cond. S/cm
0.01	2.80E-05
0.01125	6.00E-05
0.0125	3.90E-03
0.025	1.00E-01
0.04	5.20E-01
0.068	1.10E+00
0.085	4.00E+00
0.108	5.00E+00
0.125	8.50E+00
0.142	1.80E+01
0.16	2.00E+01
Reference [45]:	MWNT in PET
vol. frac.	Elec. Cond. S/cm
0	7.00E-17
0.005	9.00E-16
0.01	1.00E-08
0.02	1.00E-05
0.048	8.00E-05
0.09	3.00E-04

Reference [59]:	MWNT in PS
wt. frac.	Elec. Cond. S/cm
0	1.00E-16
0.0005	6.00E-08
0.00185	1.00E-06
0.0025	1.00E-06
0.005	1.00E-06
0.006	1.00E-06
0.007	4.00E+01
0.008	4.00E+01
0.009	4.00E+01
Reference [21]:	MWNT in epoxy
wt. frac.	Elec. Cond. S/cm
0	1.00E-11
0.00001	1.10E-11
0.000025	3.00E-10
0.00005	1.60E-05
0.0001	3.00E-05

Reference [55]	Aligned MWNTs in Epoxy
wt. frac.	Elec. Cond. S/cm
0.00001	1.00E-11
0.000024	3E-10
0.00005	0.000016
0.0001	0.00003
0.0005	0.0005
0.001	0.0004
0.01	0.02

Reference [55]:	Entangled MWNTs in Epoxy
wt. frac.	Elec. Cond. S/cm
0.0001	2.5E-11
0.0004	0.000088
0.00059	0.000089
0.0008	0.000089
0.001	0.00021
0.0012	0.0003
0.0016	0.005

Reference [60]:	SWNT in PS
wt. %	Elec. Cond. S/cm
0	9.50E-17
0.125	1.00E-06
0.25	6.50E-05
0.5	8.00E-04
1	1.40E-03
3	5.00E-03
5	1.00E-02
7	3.00E-02
10	1.20E-01

Reference [65]	Purified unfunctionalized and functionalized SWNT/nylon 6,6	
wt %	conductivity	
0	9E-12	
2	0.00002	Purified SWNT Nylon 6,6
5.1	0.003	Purified SWNT Nylon 6,6
2	0.000007	SWNT-NaDDBS Nylon 6,6
2	0.000001	SWNT-COOH Nylon 6,6
2	4E-09	SWNT-f12 Nylon 6,6
1.55	5E-12	SWNT -f18 Nylon 6,6
4.75	1.6E-10	SWNT -f18 Nylon 6,6

A4. Carbon Nanotube-Polymer Composite Thermal Conductivity

Tables summarizing the values from the literature for CNT-polymer composite thermal conductivity and the corresponding weight fraction or volume fraction in obtain-

ing the value provided.

Reference [72]:	SWNT in epoxy axial direction homog model CNT 100	
vol. frac.	Conductivity W/mK	Normalized
0.0005	0.15	1.229508
0.0028	0.38	3.114754
0.0058	0.6	4.918033

Reference [72]:	SWNT in epoxy parallel direction homog model CNT 100	
vol. frac.	Conductivity W/mK	Normalized
0.0005	0.1211	0.992623
0.0028	0.1216	0.996721
0.0058	0.1224	1.003279

Reference [72]:	SWNT in epoxy exp data	
vol. frac.	Conductivity W/mK	Normalized
0.0028	0.205	1.22571
0.0058	0.24	1.434978

Reference [76]:	SWNT in PVDF	
vol. frac.	Conductivity W/mK	Normalized
0	0.223	1
0.05	0.278	1.246637
0.1	0.314	1.408072
0.19	0.366	1.641256
0.29	0.453	2.03139
0.39	0.479	2.147982
0.49	0.537	2.408072

Reference [53]:	DWCNT in Epoxy	
vol. frac.	Conductivity W/mK	Normalized
0	0.2421	1
0.0012	0.2445	1.009913
0.0036	0.2501	1.033044
0.00601	0.2521	1.041305

Reference [251]:	SWNT in Epoxy (assumed 0.2421 for epoxy)	
wt. frac.	Conductivity W/mK	Normalized
0	0.2421	1
0.002	0.406728	1.68
0.005	0.384939	1.59
0.01	0.544725	2.25

Reference [73]:	DMF Hipco SWNT in Epoxy	
vol. frac.	Conductivity W/mK	Normalized
0	0.198	1
0.000059	0.199	1.005051
0.00029	0.205	1.035354
0.0007	0.21	1.060606
0.0016	0.215	1.085859
0.0021	0.218	1.10101
0.0051	0.251	1.267677

Reference [73]:	Surfactant Hipco SWNT in Epoxy	
vol. frac.	Conductivity W/mK	Normalized
0	0.198	1
0.0051	0.21	1.060606
0.03	0.218	1.10101
0.05	0.27	1.363636
0.1	0.325	1.641414

Reference [233]:	at 300K for random SWNT in Epoxy	
wt. frac.	Conductivity W/mK	Normalized
0	2.25	1
0.03	5.9	2.622222

Reference [233]:	at 300K for aligned SWNT in Epoxy	
wt. frac.	Conductivity W/mK	Normalized
0	2.25	1
0.03	6.45	2.866667

Reference [75]:	SWNT in PMMA			
wt. frac.	Lower Range Conductivity W/mK	Upper Range Conductivity W/mK	Lower Normalized	Upper Normalized
0	0.18	0.19	1	1
0.02	0.185	0.25	1.027778	1.315789
0.03	0.21	0.275	1.166667	1.447368
0.05	0.245	0.27	1.361111	1.421053
0.07	0.395	0.46	2.194444	2.421053

Reference [74]:	SWNT in PMMA avg val	
wt. frac.	Conductivity W/mK	Normalized
0	0.175	1
0.02	0.218	1.245714
0.03	0.25	1.428571
0.05	0.255	1.457143
0.07	0.435	2.485714
0.1	0.45	2.571429

Reference [235]:	SWNT in olefin oil suspension	
vol. frac.	Conductivity W/mK	Normalized
0	0.1448	1
0.0004	0.147696	1.02
0.0015	0.165072	1.14
0.002	0.17376	1.2
0.004	0.20996	1.45
0.006	0.233128	1.61
0.008	0.302632	2.09
0.01	0.373584	2.58
Reference [252]:	SWNT in silicone elastomer	
wt. frac.	Conductivity W/mK	Normalized
0	1.1	1
0.0075	1.25	1.136364
0.0225	1.41	1.281818
0.038	1.8	1.636364
Reference [253]:	MWNT in epoxy well dispersed	
wt. frac.	Conductivity W/mK	Normalized
0	0.121	1
0.005	0.209	1.727273
0.01	0.234	1.933884
0.015	0.256	2.115702

Reference [253]:	MWNT in epoxy poorly dispersed	
wt. frac.	Conductivity W/mK	Normalized
0	0.121	1
0.005	0.131	1.082645
0.01	0.161	1.330579
0.015	0.19	1.570248
Reference [254]:	MWNT in S160 aligned in film	
wt. frac.	Conductivity W/mK	Normalized
0	0.56	1
0.00125	0.86	1.535714
0.003	1.21	2.160714
Reference [254]:	MWNT in S160 dispersed in film	
wt. frac.	Conductivity W/mK	Normalized
0	0.56	1
0.003	0.59	1.053571
0.01	0.635	1.133929
0.03	0.71	1.267857
Reference [255]:	SWNT in PVAc Latex film	
wt. frac.	Conductivity W/mK	Normalized
0	0.21118	1
0.009	0.20822	0.985984
0.015	0.2204	1.043659
0.02	0.22937	1.086135
0.025	0.23293	1.102993
0.03	0.22685	1.074202

Reference [256]:	Surfactant Treated CNTs in decene (DE) suspension	
vol. frac.	Conductivity W/mK	Normalized
0	0.14	1
0.0025	0.7	5
0.005	1.33	9.5
0.0075	2.1	15
0.01	2.87	20.5
0.0125	3.64	26
0.015	4.69	33.5

APPENDIX B

ILLUSTRATIVE EXAMPLE FOR ORIENTATIONAL AVERAGING

As an illustrative example of orientational averaging, consider taking a composite of identical inhomogeneities (assume ellipsoidal shapes for the time being to facilitate discussion) as shown in Figure 66. Defining the effective elastic properties via volume averages as indicated in Eqn. 2.56a. Using phase constitutive relations one may write (assuming homogeneous phases as in Eqn. 2.63a)

$$\langle \sigma_{ij} \rangle = c_1 L^1_{ijkl} \langle \varepsilon^1_{kl} \rangle + c_2 L^2_{ijkl} \langle \varepsilon^2_{kl} \rangle \tag{B.1}$$

which by definition of the strain concentration tensor, can be written as in Eqn. 2.67a so that effective stiffness is given by

$$L^{\text{eff}}_{ijmn} = c_1 L^1_{ijkl} A^1_{klmn} + c_2 L^2_{ijkl} A^2_{klmn} \tag{B.2}$$

or by applying the concentration tensor consistency condition, i.e. Eqn. 2.69a, we can write

$$\langle \sigma_{ij} \rangle = \{ L^2_{ijmn} + c_1 (L^1_{ijkl} - L^2_{ijkl}) A^1_{klmn} \} \langle \varepsilon_{mn} \rangle \tag{B.3}$$

so that the effective stiffness can be written as

$$L^{\text{eff}}_{ijmn} = L^2_{ijmn} + c_1 (L^1_{ijkl} - L^2_{ijkl}) A^1_{klmn} \tag{B.4}$$

Now suppose that half of the aligned inhomogeneities instead have one orientation defined by the angles φ_1, ψ_1 and the other half have another orientation defined by the angles φ_2, ψ_2 as shown in Figure 67 These local inhomogeneity orientations are related to the microscale RVE coordinate system by a change of basis which is determined from a series of rotations as $Q_{ij} = Q^2_{ik} Q^1_{kj}$ where Q^1_{ij} and Q^2_{ij} are related to single axis

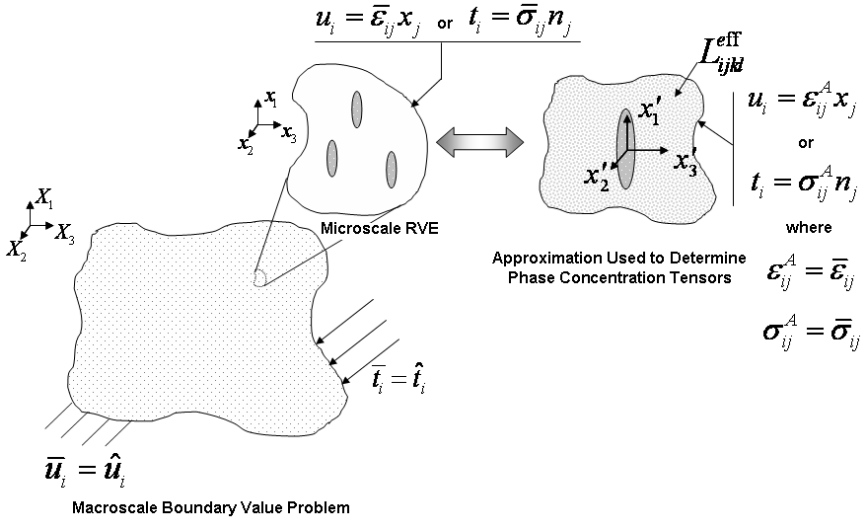

Fig. 66. Identical inhomogeneities aligned in the matrix and a self-consistent approximation.

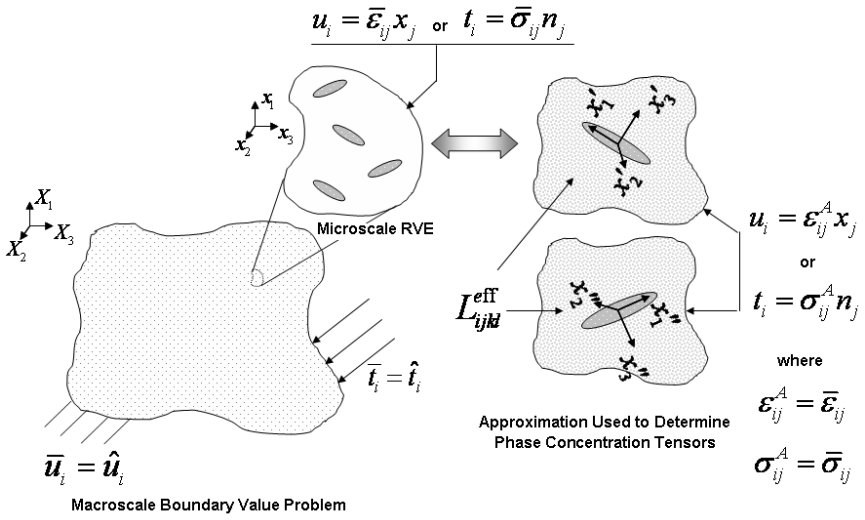

Fig. 67. Identical inhomogeneities at two different orientations in the matrix in the RVE coordinate system and self-consistent approximations of each orientation in the local inhomogeneity coordinate system.

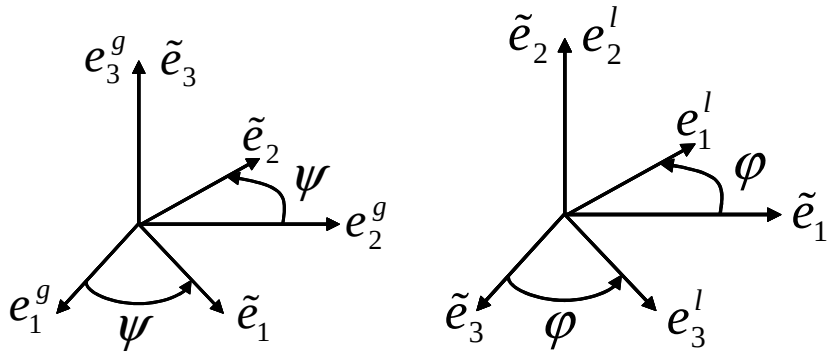

(a) Change of Basis Q^1 (b) Change of Basis Q^2

Fig. 68. Single axis rotations defining changes of basis Q^1 and Q^2.

rotations as shown in Figure 68. Thus Q_{ij} is expressed in engineering notation by[1]

$$\left[Q^2\right]\left[Q^1\right] = \begin{bmatrix} \sin(\varphi) & 0 & \cos(\varphi) \\ 0 & 1 & 0 \\ -\cos(\varphi) & 0 & \sin(\varphi) \end{bmatrix} \begin{bmatrix} \cos(\psi) & \sin(\psi) & 0 \\ -\sin(\psi) & \cos(\psi) & 0 \\ 0 & 0 & 1 \end{bmatrix} \tag{B.5}$$

so that

$$[Q] = \begin{bmatrix} \cos(\psi)\sin(\varphi) & \sin(\psi)\sin(\varphi) & \cos(\varphi) \\ -\sin(\psi) & \cos(\psi) & 0 \\ -\cos(\psi)\cos(\varphi) & -\sin(\psi)\cos(\varphi) & \sin(\varphi) \end{bmatrix} \tag{B.6}$$

Because the inhomogeneity phase is now treated as two separate phases, Eqn. B.1 can be written as

$$\langle\hat{\sigma}_{ij}\rangle = \sum_{J=1}^{3} c_J \hat{L}^J_{ijkl} \langle\hat{\varepsilon}^J_{kl}\rangle \tag{B.7}$$

where the matrix volume fraction is $c_3 = 1-\bar{c}$, the volume fraction of inhomogeneities with orientation (φ_1, ψ_1) is $c_1 = \frac{1}{2}\bar{c}$, and the volume fraction of inhomogeneities with orientation (φ_2, ψ_2) is $c_2 = \frac{1}{2}\bar{c}$, with $\bar{c}$ denoting the total inhomogeneity volume frac-

[1]It is noted that only two angles are needed here because we have assumed that the axis of material symmetry is aligned with the major axis of the ellipsoid. If it were not, then we would need the third angle as well, as rotating about the major axis would cause differences.

tion irrespective of orientation. The $\hat{\cdot}$ denotes quantities expressed in the microscale RVE coordinate system, i.e. (assuming the matrix phase is isotropic)

$$\hat{L}^1_{ijkl} = {}^1Q_{im}\,{}^1Q_{jn}L^1_{mnpq}\,{}^1Q_{kp}\,{}^1Q_{lq} \tag{B.8a}$$

$$\hat{L}^2_{ijkl} = {}^2Q_{im}\,{}^2Q_{jn}L^2_{mnpq}\,{}^2Q_{kp}\,{}^2Q_{lq} \tag{B.8b}$$

$$\hat{L}^3_{ijkl} = L^3_{ijkl} \tag{B.8c}$$

where ${}^1Q_{ij} = Q_{ij}(\varphi_1, \psi_1)$ and ${}^2Q_{ij} = Q_{ij}(\varphi_2, \psi_2)$.

Defining the strain concentration tensor in the microscale RVE system as $\langle\hat{\varepsilon}^J_{ij}\rangle = \hat{A}^J_{ijkl}\langle\hat{\varepsilon}_{ij}\rangle$, then Eqn. B.7 can be written as

$$\langle\hat{\sigma}_{ij}\rangle = \sum_{J=1}^{3} c_J \hat{L}^J_{ijkl}\hat{A}^J_{klmn}\langle\hat{\varepsilon}_{mn}\rangle \tag{B.9}$$

so that the effective stiffness in the microscale RVE coordinate system is given by

$$\hat{L}^{\text{eff}}_{ijmn} = \sum_{J=1}^{3} c_J \hat{L}^J_{ijkl}\hat{A}^J_{klmn} \tag{B.10}$$

Applying the consistency condition in the global system, i.e. $c_3\hat{A}^3_{ijkl} = I_{ijkl} - \sum_{J=1}^{2} c_J\hat{A}^J_{ijkl}$, one can write

$$\langle\hat{\sigma}_{ij}\rangle = \left\{\hat{L}^3_{ijmn} + \sum_{J=1}^{2} c_J(\hat{L}^J_{ijkl} - \hat{L}^3_{ijkl})\hat{A}^J_{klmn}\right\}\langle\hat{\varepsilon}_{mn}\rangle \tag{B.11}$$

so that the effective stiffness in the microscale RVE coordinate system is given by

$$\hat{L}^{\text{eff}}_{ijmn} = \hat{L}^3_{ijmn} + \sum_{J=1}^{2} c_J(\hat{L}^J_{ijkl} - \hat{L}^3_{ijkl})\hat{A}^J_{klmn} \tag{B.12}$$

So therefore, in the global coordinate system, Eqns. B.7 and B.11 are analogous to Eqns. B.1 and B.3.

However, when approximating the concentration tensor, it is easier to work in the local coordinate system, especially if all inhomogeneities are the same, except for

their different orientations, as you can then solve one concentration tensor and rotate as necessary. So if A^J_{ijkl} is the approximated strain concentration tensor in the local coordinate system (.i.e. for single inhomogeneity problem) obtained from

$$\langle \varepsilon^J_{ij} \rangle = A^J_{ijkl} \langle \varepsilon_{kl} \rangle \tag{B.13}$$

then the fourth order coordinate transformation of the concentration tensor in the local inhomogeneity coordinate system to that of the microscale RVE is given as

$$\hat{A}^J_{ijkl} = {}^J Q_{im}\, {}^J Q_{jn} A^1_{mnpq}\, {}^J Q_{kp}\, {}^J Q_{lq} \tag{B.14}$$

where it is emphasized that A^1_{mnpq} is used as both inhomogeneities in the present example have the same concentration tensor in their local inhomogeneity coordinate systems, though those local systems have different orientations relative to the microscale RVE coordinate system so that the transformation is ${}^J Q_{ij}$. Thus the effective stiffness can be obtained from Eqn. B.12 as:

$$\begin{aligned} &\hat{L}^{\text{eff}}_{ijkl} = \hat{L}^3_{ijkl} + \\ &\sum_{J=1}^{2} c_J (\, {}^J Q_{ip}\, {}^J Q_{jq} L^1_{pqrs}\, {}^J Q_{mr}\, {}^J Q_{ns} - \hat{L}^0_{ijmn})\, {}^J Q_{mt}\, {}^J Q_{nv} A^1_{tvab}\, {}^J Q_{ka}\, {}^J Q_{lb} \end{aligned} \tag{B.15}$$

where $c_1 = \dfrac{\bar{c}}{2}$ and $c_2 = \dfrac{\bar{c}}{2}$.[2] From similar approaches the effective compliance, conductivity and resistivity can also be obtained.

[2]Here it was assumed that half of the inhomogeneities were at φ_1, ψ_1 and half at φ_2, ψ_2, but one could have assumed a different distribution, for example $c_1 = \frac{\bar{c}}{4}$ and $c_2 = \frac{3\bar{c}}{4}$. However, this would not change Eqn. B.15 as it is simply a different distribution of $\bar{c}$.

Assuming now that there are M orientations (i.e. so that the number of phases is $N = M + 1$), then Eqn. B.15 can be written as

$$\hat{L}^{\text{eff}}_{ijkl} = \hat{L}^{N}_{ijkl} + \sum_{J=1}^{M} c_J(\varphi,\psi)(\tilde{L}^{J}_{ijmn}(\varphi,\psi) - \hat{L}^{N}_{ijmn})\tilde{A}^{J}_{mnkl}(\varphi,\psi) \tag{B.16}$$

where

$$\tilde{L}^{J}_{ijmn}(\varphi,\psi) = {}^{J}Q_{ip}\,{}^{J}Q_{jq}L^{1}_{pqrs}\,{}^{J}Q_{mr}\,{}^{J}Q_{ns} \tag{B.17a}$$

$$\tilde{A}^{J}_{ijmn}(\varphi,\psi) = {}^{J}Q_{ip}\,{}^{J}Q_{jq}A^{1}_{pqrs}\,{}^{J}Q_{mr}\,{}^{J}Q_{ns} \tag{B.17b}$$

$$c_J(\varphi,\psi) = w_J\bar{c} \tag{B.17c}$$

and where w_J is the weight factor for the fraction of inhomogeneities with a given (φ,ψ).

Assuming further that as $M \to \infty$, that a continuous distribution of orientations over a unit sphere, $\rho(\varphi,\psi)$, is obtained, such that one may write

$$\hat{L}^{\text{eff}}_{ijkl} = \hat{L}^{N}_{ijkl} + \frac{\int_0^{2\pi}\int_0^{\pi}\rho(\varphi,\psi)\bar{c}[\tilde{L}_{ijmn}(\varphi,\psi) - \hat{L}^{N}_{ijmn}]\tilde{A}_{mnkl}(\varphi,\psi)\sin(\varphi)\,d\varphi\,d\psi}{\int_0^{2\pi}\int_0^{\pi}\rho(\varphi,\psi)\sin(\varphi)\,d\varphi\,d\psi} \tag{B.18}$$

Therefore, for a random orientation, each (φ,ψ) is equally likely therefore $\rho(\varphi,\psi) = \rho_0$ and

$$\hat{L}^{\text{eff}}_{ijkl} = \hat{L}^{N}_{ijkl} + \frac{\bar{c}}{4\pi}\int_0^{2\pi}\int_0^{\pi}[\tilde{L}_{ijmn}(\varphi,\psi) - \hat{L}^{N}_{ijmn}]\tilde{A}_{mnkl}(\varphi,\psi)\sin(\varphi)\,d\varphi\,d\psi \tag{B.19a}$$

$$\hat{M}^{\text{eff}}_{ijkl} = \hat{M}^{N}_{ijkl} + \frac{\bar{c}}{4\pi}\int_0^{2\pi}\int_0^{\pi}[\tilde{M}_{ijmn}(\varphi,\psi) - \hat{M}^{N}_{ijmn}]\tilde{B}_{mnkl}(\varphi,\psi)\sin(\varphi)\,d\varphi\,d\psi \tag{B.19b}$$

$$\hat{k}^{\text{eff}}_{ij} = \hat{k}^{N}_{ij} + \frac{\bar{c}}{4\pi}\int_0^{2\pi}\int_0^{\pi}[\tilde{k}_{im}(\varphi,\psi) - \hat{k}^{N}_{im}]\tilde{A}_{mj}(\varphi,\psi)\sin(\varphi)\,d\varphi\,d\psi \tag{B.19c}$$

$$\hat{\xi}^{\text{eff}}_{ij} = \hat{\xi}^{N}_{ij} + \frac{\bar{c}}{4\pi}\int_0^{2\pi}\int_0^{\pi}[\tilde{\xi}_{im}(\varphi,\psi) - \hat{\xi}^{N}_{im}]\tilde{B}_{mj}(\varphi,\psi)\sin(\varphi)\,d\varphi\,d\psi \tag{B.19d}$$

resulting in effective properties for the composite which are isotropic [153, 209, 210].

It should be noted that the use of Eqn. B.14 can be directly applied when using the self-consistent and generalized self-consistent concentration tensor approximations. However, when using the Mori-Tanaka approximation, one must use caution as the Mori-Tanaka consistency condition must be applied in the global coordinate system. Therefore one actually obtains global concentration tensor in the Mori-Tanaka approach and can use the inverse of Eqn. B.14 to find the local concentration tensor consistent with the use of Eqn. B.14 and the subsequent derivation. See Appendix C for more details.

APPENDIX C

CONSISTENCY CONDITIONS FOR ORIENTATIONAL AVERAGING

C1. Self-Consistent Consistency Condition and Random Orientation

Considering the self-consistent approximation for the concentration tensor as shown in Figure 69. Therefore in the local system, the Eshelby equivalence principle yields the heat flux in the inhomogeneity as

$$\acute{q}_i^J = \acute{k}_{ij}^J(\acute{H}_j^C + \acute{H}_j^A) = \acute{k}_{ij}^{\text{eff}}(\acute{H}_j^C + \acute{H}_j^A - \acute{H}_j^T) \tag{C.1}$$

where if k_{ij}^{eff} is anisotropic, it is noted that $\acute{k}_{ij}^{\text{eff}} \neq k_{ij}^{\text{eff}}$.

Therefore one can write

$$\acute{H}_i^T = \acute{\xi}_{ij}^{\text{eff}}(\acute{k}_{jk}^{\text{eff}} - \acute{k}_{jk}^J)\acute{H}_k^J \tag{C.2}$$

but

$$\acute{H}_i^J = \acute{H}_i^C + \acute{\tilde{H}}_i = \acute{S}_{ij}\acute{H}_j^T + \acute{\tilde{H}}_i \tag{C.3}$$

therefore

$$\acute{H}_j^J = [I_{ij} + \acute{S}_{ik}\acute{\xi}_{kl}^{\text{eff}}(\acute{k}_{lj}^J - \acute{k}_{lj}^{\text{eff}})]^{-1}\acute{\tilde{H}}_i \tag{C.4}$$

so that

$${}^{SC}\acute{T}_{ji}^{\ J} = [I_{ij} + \acute{S}_{ik}\acute{\xi}_{kl}^{\text{eff}}(\acute{k}_{lj}^J - \acute{k}_{lj}^{\text{eff}})]^{-1} \tag{C.5}$$

Expressing Eqn. C.5 in the global system to identify the concentration tensor

$$H_i^J = {}^J Q_{ij}\acute{H}_j^J = {}^J Q_{ij}\ {}^{SC}\acute{T}_{jk}^J\acute{\tilde{H}}_k \tag{C.6}$$

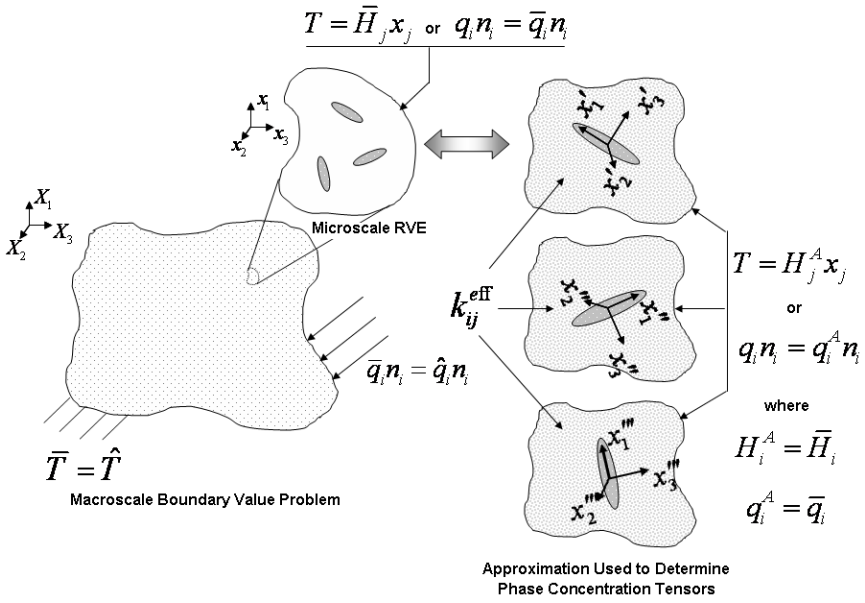

Fig. 69. Schematic of local orientations of the self-consistent approximation for concentration tensor to check consistency condition. Where the microscale RVE and local inhomogeneity coordinate systems are related by $v_i = {}^{J}Q_{ij}\acute{v}_j$ so that for the equivalent inclusion problem, $\acute{H}_i^A = \acute{\bar{H}}_i$ where $\acute{\bar{H}}_i = {}^{J}Q_{ij}^T\bar{H}_j$ and $\bar{H}_i = \langle H_i \rangle$.

therefore since $\acute{\bar{H}}_i = {}^{J}Q^{T}_{ij}\bar{H}_j$

$$H^J_i = {}^{J}Q_{ij}\acute{H}^J_j = {}^{J}Q_{ij}\ {}^{SC}\acute{T}^J_{jk}\ {}^{J}Q^T_{kl}\bar{H}_l \tag{C.7}$$

and noting that intensity in the inhomogeneity is uniform, the concentration tensor is identified as

$${}^{SC}A^J_{ij} = {}^{J}Q_{ik}\ {}^{SC}\acute{T}^J_{kl}\ {}^{J}Q^T_{lj} \tag{C.8}$$

and therefore satisfies the consistency condition as expressed in Eqn. 2.161b. This will also hold for the generalized self consistent approximation.

C2. Mori-Tanaka Consistency Condition and Random Orientation

Considering the Mori-Tanaka approximation for the concentration tensor as shown in Figure 70 Therefore in the local system, the Eshelby equivalence principle yields the heat flux in the inhomogeneity as

$$\acute{q}^J_i = \acute{k}^J_{ij}(\acute{H}^C_j + \acute{H}^A_j) = \acute{k}^N_{ij}(\acute{H}^C_j + \acute{H}^A_i - \acute{H}^T_i) \tag{C.9}$$

where if k^N_{ij} is isotropic it is noted that $\acute{k}^N_{ij} = k^N_{ij}$.

Therefore one can write

$$\acute{H}^T_i = \acute{\xi}^N_{ij}(\acute{k}^N_{jk} - \acute{k}^J_{jk})\acute{H}^J_k \tag{C.10}$$

but

$$\acute{H}^J_i = \acute{H}^C_i + \acute{\bar{H}}_i + \acute{\tilde{H}}_i = \acute{S}_{ij}\acute{H}^T_j + \acute{\bar{H}}_i + \acute{\tilde{H}}_i \tag{C.11}$$

therefore

$$\acute{H}^J_j = [I_{ij} + \acute{S}_{ik}\acute{\xi}^N_{kl}(\acute{k}^J_{kj} - \acute{k}^N_{kj})]^{-1}(\acute{\bar{H}}_i + \acute{\tilde{H}}_i) \tag{C.12}$$

so that

$${}^{MT}\acute{T}^J_{ji} = [I_{ij} + \acute{S}_{ik}\acute{\xi}^N_{kl}(\acute{k}^J_{kj} - \acute{k}^N_{kj})]^{-1} \tag{C.13}$$

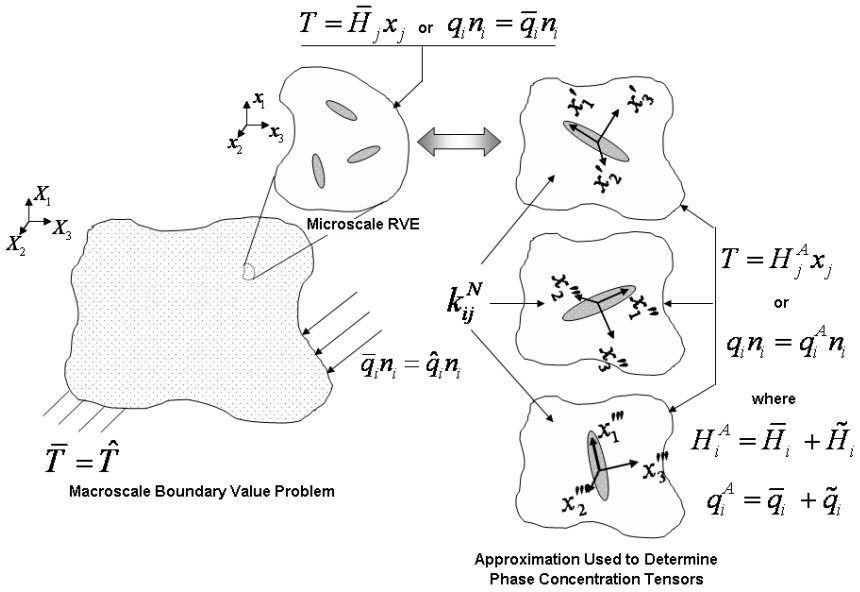

Fig. 70. Schematic of local orientations of the Mori-Tanaka approximation for concentration tensor to check consistency condition. Where the microscale RVE and local inhomogeneity coordinate systems are related by $v_i = {}^J Q_{ij} \acute{v}_j$ so that for the equivalent inclusion problem, $\acute{H}_i^A = \acute{\bar{H}}_i + \acute{\tilde{H}}_i$ where $\acute{\bar{H}}_i = {}^J Q_{ij}^T \bar{H}_j$ and $\bar{H}_i = \langle H_i \rangle$ and where $\acute{\tilde{H}}_i = {}^J Q_{ij}^T \tilde{H}_j$ and $\tilde{H}_i = \frac{1}{V_N} \int_{V_N} H_i^{\mathrm{Tot}} - \bar{H}_i \, dV$.

The consistency condition is applied over all inhomogeneities and therefore should be applied in the global coordinate system, i.e.

$$\langle H_i \rangle = c_N \langle H_i^N \rangle + \sum_{J=1}^{N-1} c_J \langle H_i^J \rangle \tag{C.14}$$

but the average intensity in the matrix is noted to be

$$\langle H_i^N \rangle = \bar{H}_i + \tilde{H}_i \tag{C.15}$$

In the inhomogeneity one may write

$$H_i^J = {}^J Q_{ij} \acute{H}_j^J = {}^J Q_{ij} \, {}^{MT}\acute{T}_{jk}^J (\acute{\bar{H}}_k + \acute{\tilde{H}}_k) \tag{C.16}$$

so therefore

$$H_i^J = {}^J Q_{ij} \acute{H}_j^J = {}^J Q_{ij} \, {}^{MT}\acute{T}_{jk}^J \, {}^J Q_{kl}^T (\bar{H}_l + \tilde{H}_l) \tag{C.17}$$

Noting that the intensity in the inhomogeneity is uniform, one can therefore write

$$\langle H_i \rangle = \bar{H}_i = \left[c_N I_{ij} + \sum_{J=1}^{N-1} c_J \, {}^J Q_{ik} \, {}^{MT}\acute{T}_{kl}^J \, {}^J Q_{lj}^T \right] (\bar{H}_j + \tilde{H}_j) \tag{C.18}$$

and finally the perturbation in the matrix is given by

$$\tilde{H}_j = \left\{ \left[c_N I_{ij} + \sum_{J=1}^{N-1} c_J \, {}^J Q_{ik} \, {}^{MT}\acute{T}_{kl}^J \, {}^J Q_{lj}^T \right]^{-1} - I_{ji} \right\} \bar{H}_i \tag{C.19}$$

so that in the inhomogeneity one observes

$$\begin{aligned} H_i^J = {}& {}^J Q_{ij} \, {}^{MT}\acute{T}_{jk}^J \, {}^J Q_{kl}^T \bar{H}_l + \\ & {}^J Q_{ij} \, {}^{MT}\acute{T}_{jk}^J \, {}^J Q_{kl}^T \left\{ \left[c_N I_{ml} + \sum_{K=1}^{N-1} c_K \, {}^K Q_{mn} \, {}^{MT}\acute{T}_{np}^K \, {}^K Q_{pl}^T \right]^{-1} - I_{im} \right\} \bar{H}_m \end{aligned} \tag{C.20}$$

and again noting that the intensity in the inhomogeneity is uniform

$$H_i^J = {}^J Q_{ij}\ {}^{MT}\acute{T}_{jk}^J\ {}^J Q_{kl}^T \left[c_N I_{ml} + \sum_{K=1}^{N} c_K\ {}^K Q_{mn}\ {}^{MT}\acute{T}_{np}^K\ {}^K Q_{pl}^T \right]^{-1} H_m \tag{C.21}$$

so that the concentration tensor is identified as

$${}^{MT}A_{im}^J = {}^J Q_{ij}\ {}^{MT}\acute{T}_{jk}^J\ {}^J Q_{kl}^T \left[c_N I_{ml} + \sum_{K=1}^{N} c_K\ {}^K Q_{mn}\ {}^{MT}\acute{T}_{np}^K\ {}^K Q_{pl}^T \right]^{-1} \tag{C.22}$$

Therefore in order to satisfy the consistency condition, one can not directly rotate the concentration tensor from local to global coordinates as expressed in Eqn. 2.161b the Mori-Tanaka approximation.

APPENDIX D

DERIVATION OF DISPLACEMENT FIELDS FOR COMPOSITE CYLINDERS METHOD

D1. Multi-Layer Composite Cylinder: In Plane Bulk Modulus Isotropic Phase Displacement

Assume the following displacement field in each phase:

$$u_r = U_r(r) \tag{D.1}$$

$$u_\theta = u_z = 0 \tag{D.2}$$

Sub into the strain-displacement relations:

$$\varepsilon_{rr} = \frac{\partial u_r}{\partial r} = \frac{dU_r}{dr} \tag{D.3}$$

$$\varepsilon_{\theta\theta} = \frac{1}{r}\frac{\partial u_\theta}{\partial \theta} + \frac{u_r}{r} = \frac{U_r}{r} \tag{D.4}$$

$$\varepsilon_{zz} = \frac{\partial u_z}{\partial z} = 0 \tag{D.5}$$

$$\varepsilon_{r\theta} = \frac{1}{2}\left(\frac{1}{r}\frac{\partial u_r}{\partial \theta} + \frac{\partial u_\theta}{\partial r} - \frac{u_\theta}{r}\right) = 0 \tag{D.6}$$

$$\varepsilon_{rz} = \frac{1}{2}\left(\frac{\partial u_r}{\partial z} + \frac{\partial u_z}{\partial r}\right) = 0 \tag{D.7}$$

$$\varepsilon_{\theta z} = \frac{1}{2}\left(\frac{1}{r}\frac{\partial u_z}{\partial \theta} + \frac{\partial u_\theta}{\partial z}\right) = 0 \tag{D.8}$$

Sub into the constitutive relations:

$$\sigma_{rr} = (2\mu + \lambda)\,\varepsilon_{rr} + \lambda\,(\varepsilon_{\theta\theta} + \varepsilon_{zz}) = (2\mu + \lambda)\,\frac{dU_r}{dr} + \lambda\frac{U_r}{r} \tag{D.9}$$

$$\sigma_{\theta\theta} = (2\mu + \lambda)\,\varepsilon_{\theta\theta} + \lambda\,(\varepsilon_{rr} + \varepsilon_{zz}) = (2\mu + \lambda)\,\frac{U_r}{r} + \lambda\frac{dU_r}{dr} \tag{D.10}$$

$$\sigma_{zz} = (2\mu + \lambda)\,\varepsilon_{zz} + \lambda\,(\varepsilon_{rr} + \varepsilon_{\theta\theta}) = \lambda\frac{dU_r}{dr} + \lambda\frac{U_r}{r} \tag{D.11}$$

$$\sigma_{r\theta} = 2\mu\varepsilon_{r\theta} = 0 \tag{D.12}$$

$$\sigma_{rz} = 2\mu\varepsilon_{rz} = 0 \tag{D.13}$$

$$\sigma_{\theta z} = 2\mu\varepsilon_{\theta z} = 0 \tag{D.14}$$

Sub into the equilibrium equations: r-direction

$$\frac{\partial\sigma_{rr}}{\partial r} + \frac{1}{r}\frac{\partial\sigma_{r\theta}}{\partial\theta} + \frac{\partial\sigma_{rz}}{\partial z} + \frac{1}{r}\,(\sigma_{rr} - \sigma_{\theta\theta}) = 0 \tag{D.15}$$

$$\frac{d^2U_r}{dr^2} + \frac{1}{r}\frac{dU_r}{dr} - \frac{1}{r^2}U_r = 0 \tag{D.16}$$

which has solution

$$U_r = Ar + \frac{B}{r} \tag{D.17}$$

In the theta-direction:

$$\frac{\partial\sigma_{r\theta}}{\partial r} + \frac{1}{r}\frac{\partial\sigma_{\theta\theta}}{\partial\theta} + \frac{\partial\sigma_{\theta z}}{\partial z} + \frac{2}{r}\sigma_{r\theta} = 0 \tag{D.18}$$

therefore

$$0 = 0 \tag{D.19}$$

In the z-direction:

$$\frac{\partial\sigma_{rz}}{\partial r} + \frac{1}{r}\frac{\partial\sigma_{\theta z}}{\partial\theta} + \frac{\partial\sigma_{zz}}{\partial z} + \frac{1}{r}\sigma_{rz} = 0 \tag{D.20}$$

therefore

$$0 = 0 \tag{D.21}$$

D2. Multi-Layer Composite Cylinder: In Plane Bulk Modulus Effective Cylinder Displacement

Assume the following displacement field in each phase:

$$u_r = U_r(r) \tag{D.22}$$

$$u_\theta = u_z = 0 \tag{D.23}$$

Sub into the strain-displacement relations:

$$\varepsilon_{rr} = \frac{\partial u_r}{\partial r} = \frac{dU_r}{dr} \tag{D.24}$$

$$\varepsilon_{\theta\theta} = \frac{1}{r}\frac{\partial u_\theta}{\partial \theta} + \frac{u_r}{r} = \frac{U_r}{r} \tag{D.25}$$

$$\varepsilon_{zz} = \frac{\partial u_z}{\partial z} = 0 \tag{D.26}$$

$$\varepsilon_{r\theta} = \frac{1}{2}\left(\frac{1}{r}\frac{\partial u_r}{\partial \theta} + \frac{\partial u_\theta}{\partial r} - \frac{u_\theta}{r}\right) = 0 \tag{D.27}$$

$$\varepsilon_{rz} = \frac{1}{2}\left(\frac{\partial u_r}{\partial z} + \frac{\partial u_z}{\partial r}\right) = 0 \tag{D.28}$$

$$\varepsilon_{\theta z} = \frac{1}{2}\left(\frac{1}{r}\frac{\partial u_z}{\partial \theta} + \frac{\partial u_\theta}{\partial z}\right) = 0 \tag{D.29}$$

Sub into the constitutive relations:

$$\sigma_{rr} = C_{rrrr}\varepsilon_{rr} + C_{rr\theta\theta}\varepsilon_{\theta\theta} + C_{rrzz}\varepsilon_{zz} = C_{rrrr}\frac{dU_r}{dr} + C_{rr\theta\theta}\frac{U_r}{r} \tag{D.30}$$

$$\sigma_{\theta\theta} = C_{rr\theta\theta}\varepsilon_{rr} + C_{\theta\theta\theta\theta}\varepsilon_{\theta\theta} + C_{\theta\theta zz}\varepsilon_{zz} = C_{rr\theta\theta}\frac{dU_r}{dr} + C_{\theta\theta\theta\theta}\frac{U_r}{r} \tag{D.31}$$

$$\sigma_{zz} = C_{rrzz}\varepsilon_{rr} + C_{\theta\theta zz}\varepsilon_{\theta\theta} + C_{zzzz}\varepsilon_{zz} = C_{rrzz}\frac{dU_r}{dr} + C_{\theta\theta zz}\frac{U_r}{r} \tag{D.32}$$

$$\sigma_{r\theta} = C_{r\theta r\theta}\varepsilon_{r\theta} = 0 \tag{D.33}$$

$$\sigma_{rz} = C_{rzrz}\varepsilon_{rz} = 0 \tag{D.34}$$

$$\sigma_{\theta z} = C_{\theta z\theta z}\varepsilon_{\theta z} = 0 \tag{D.35}$$

Sub into the equilibrium equations: r-direction

$$\frac{\partial \sigma_{rr}}{\partial r} + \frac{1}{r}\frac{\partial \sigma_{r\theta}}{\partial \theta} + \frac{\partial \sigma_{rz}}{\partial z} + \frac{1}{r}\left(\sigma_{rr} - \sigma_{\theta\theta}\right) = 0 \tag{D.36}$$

$$C_{rrrr}\frac{d^2U_r}{dr^2} + \frac{1}{r}\left(C_{rr\theta\theta} + C_{rrrr} - C_{rr\theta\theta}\right)\frac{dU_r}{dr} - \frac{1}{r^2}\left(C_{rr\theta\theta} - C_{rr\theta\theta} + C_{\theta\theta\theta\theta}\right)U_r = 0 \tag{D.37}$$

$$C_{rrrr}\frac{d^2U_r}{dr^2} + C_{rrrr}\frac{1}{r}\frac{dU_r}{dr} - C_{\theta\theta\theta\theta}\frac{1}{r^2}U_r = 0 \tag{D.38}$$

$$\frac{d^2U_r}{dr^2} + \frac{1}{r}\frac{dU_r}{dr} - \frac{1}{r^2}U_r = 0 \tag{D.39}$$

Therefore,

$$U_r = Ar + \frac{B}{r} \tag{D.40}$$

D3. Multi-Layer GSC-CC: Transverse Shear Modulus Isotropic Phase Displacement

Assume[3] the following displacement field in each phase from 1 to N:

$$u_r^i = B_1^i U_r^1 + B_2^i U_r^2 + B_3^i U_r^3 + B_4^i U_r^4 \tag{D.41}$$

$$u_\theta^i = B_1^i U_\theta^1 + B_2^i U_\theta^2 + B_3^i U_\theta^3 + B_4^i U_\theta^4 \tag{D.42}$$

$$u_z^i = 0 \tag{D.43}$$

where

$$U_r^1 = \frac{\partial \phi_1}{\partial r} \tag{D.44}$$

$$U_r^2 = r^2\frac{\partial \phi_1}{\partial r} + \alpha_1^i \phi_1 r \tag{D.45}$$

$$U_r^3 = \frac{\partial \phi_2}{\partial r} \tag{D.46}$$

$$U_r^4 = r^2\frac{\partial \phi_2}{\partial r} + \alpha_2^i \phi_2 r \tag{D.47}$$

[3]This can be derived in a similar manner to the previous displacement fields in assuming a functional from for the displacement and identifying general solutions to the equilibrium equations. This representation is derived from the method of plane harmonics which Hashin [158] simplified from Love's [211] representation.

and

$$U_\theta^1 = \frac{1}{r}\frac{\partial \phi_1}{\partial \theta} \tag{D.48}$$

$$U_\theta^2 = r^2\frac{1}{r}\frac{\partial \phi_1}{\partial \theta} \tag{D.49}$$

$$U_\theta^3 = \frac{1}{r}\frac{\partial \phi_2}{\partial \theta} \tag{D.50}$$

$$U_\theta^4 = r^2\frac{1}{r}\frac{\partial \phi_2}{\partial \theta} \tag{D.51}$$

and where

$$\phi_1 = x_2 x_3 = r^2 \cos(\theta)\sin(\theta) \tag{D.52}$$

$$\phi_2 = \frac{x_2 x_3}{r^4} = r^{-2}\cos(\theta)\sin(\theta) \tag{D.53}$$

$$\alpha_1^i = \frac{-2(3-4\nu_i)}{(3-2\nu_i)} \tag{D.54}$$

$$\alpha_2^i = \frac{2(3-4\nu_i)}{(3-2\nu_i)} \tag{D.55}$$

which after substitution gives

$$u_r^i = \left(B_1^i r + \left(\frac{\lambda_i}{3\mu_i + 2\lambda_i}\right)B_2^i r^3 - B_3^i r^{-3} + \left(\frac{2\mu_i + \lambda_i}{\mu_i}\right)B_4^i r^{-1}\right)\sin(2\theta) \tag{D.56}$$

$$u_\theta^i = \left(B_1^i r + B_2^i r^3 + B_3^i r^{-3} + B_4^i r^{-1}\right)\cos(2\theta) \tag{D.57}$$

$$u_z^i = 0 \tag{D.58}$$

The displacement field for the effective homogeneous solid material, is given by:

$$\begin{aligned} u_r^{(*)} &= \left(\frac{r_3}{4G_{23}}\right)\left(\frac{2}{r_3}r\right)\sin(2\theta) \\ u_\theta^{(*)} &= \left(\frac{-r_3}{4G_{23}}\right)\left(-\frac{2}{r_3}r\right)\cos(2\theta) \qquad \text{for } 0 \le r \le r_3 \\ u_z^{(*)} &= 0 \end{aligned} \tag{D.59}$$

where the boundary conditions have been applied, and the condition that the dis-

placement remained bounded has been enforced.

APPENDIX E

SOLUTIONS FOR DISPLACEMENT FIELD CONSTANTS FOR $N = 2$ AND $N = 3$ NON-GRADED LAYERS AND GRADED LAYERS

The following displacement constants correspond to hollow composite cylinder assemblages.

E1. Solutions for $N = 2$ Isotropic Homogeneous Layers

Solutions for the displacement field constants for a composite cylinder assemblage (Figure 16) of $N = 2$ isotropic, non-graded layers are provided for the displacement fields associated with the determination of the in-plane bulk modulus, the axial Young's modulus, the axial stiffness component, and the axial shear modulus. These solutions are developed by starting with the application of the innermost boundary and matching conditions and proceeding outward to the N^{th} layer boundary condition. As such, the constants are provided from the i^{th} to the first layer as each $(i+1)^{\text{th}}$ layer set of constants is expressed in terms of the N^{th} constants.

1. In-plane Bulk Modulus $N = 2$ Constants

The solution of Eqns 3.6 and 3.7 for $N = 2$ isotropic layers results in the displacement field constants of Eqn. 3.2 being given by:

$$D_2^2 = \frac{\varepsilon_0}{\left[\dfrac{1}{r_2^2} - \dfrac{1}{r_1^2}\left(\dfrac{\alpha_1\alpha_2 + \mu_2}{\alpha_1\alpha_2 - (\mu_2 + \lambda_2)}\right)\right]} \tag{E.1a}$$

$$D_1^2 = \left(\frac{-(\alpha_1\alpha_2 + \mu_2)}{r_1^2[\alpha_1\alpha_2 - (\mu_2 + \lambda_2)]}\right) D_2^2 \tag{E.1b}$$

$$D_2^1 = \frac{\alpha_1}{\mu_1}\left(D_1^2 + \frac{1}{r_1^2}D_2^2\right) \tag{E.1c}$$

$$D_1^1 = \left(\frac{\mu_1}{r_0^2(\mu_1+\lambda_1)}\right)D_2^1 \tag{E.1d}$$

where μ_i and λ_i are the i^{th} layer Lamé constants and where α_1 and α_2 are given by:

$$\alpha_1 = \frac{\mu_1}{\left[\left(\frac{\mu_1}{\mu_1+\lambda_1}\right)\frac{1}{r_0^2} + \frac{1}{r_1^2}\right]} \tag{E.2a}$$

$$\alpha_2 = \left(\frac{1}{r_0^2} - \frac{1}{r_1^2}\right) \tag{E.2b}$$

2. Axial Young's Modulus $N = 2$ Constants

The solution of Eqns 3.23 and 3.7 for $N = 2$ isotropic layers results in the displacement field constants of Eqn. 3.20 being given by:

$$D_2^2 = \frac{\beta_3}{\alpha_6}\varepsilon_0 \tag{E.3a}$$

$$D_1^2 = \frac{\beta_2}{\alpha_4}\varepsilon_0 + \frac{\alpha_5}{\alpha_4}\frac{1}{r_1^2}D_2^2 \tag{E.3b}$$

$$D_2^1 = \alpha_2\left(\beta_1\varepsilon_0 + D_1^2 + \frac{1}{r_1^2}D_2^2\right) \tag{E.3c}$$

$$D_1^1 = \alpha_1\frac{1}{r_0^2}D_2^1 - \beta_1\varepsilon_0 \tag{E.3d}$$

where the α_i are given by:

$$\alpha_1 = \frac{\mu_1}{\mu_1+\lambda_1} \tag{E.4a}$$

$$\alpha_2 = \frac{1}{\left(\alpha_1\frac{1}{r_0^2} + \frac{1}{r_1^2}\right)} \tag{E.4b}$$

$$\alpha_3 = 2\left(\mu_1+\lambda_1\right)\alpha_1\frac{1}{r_0^2} - 2\mu_1\frac{1}{r_1^2} \tag{E.4c}$$

$$\alpha_4 = \alpha_2\alpha_3 - 2(\mu_2+\lambda_2) \tag{E.4d}$$

$$\alpha_5 = -\alpha_2\alpha_3 - 2\mu_2 \tag{E.4e}$$

$$\alpha_6 = 2(\mu_2 + \lambda_2)\frac{\alpha_5}{\alpha_4}\frac{1}{r_1^2} - 2\mu_2\frac{1}{r_2^2} \tag{E.4f}$$

and where the β_i are given by:

$$\beta_1 = \frac{\lambda_1}{2(\mu_1 + \lambda_1)} \tag{E.5a}$$

$$\beta_2 = \lambda_2 - \lambda_1 + \beta_1[2(\mu_2 + \lambda_2) - \alpha_2] \tag{E.5b}$$

$$\beta_3 = -\lambda_2 - 2(\mu_2 + \lambda_2)\frac{\beta_2}{\alpha_4} \tag{E.5c}$$

3. Axial Stiffness Component $N = 2$ Constants

The solution of Eqns 3.24 and 3.7 for $N = 2$ isotropic layers results in the displacement field constants of Eqn. 3.20 being given by:

$$D_2^2 = \frac{-\beta_2}{\alpha_4\left(\frac{\alpha_5}{\alpha_4}\frac{1}{r_1^2} + \frac{1}{r_2^2}\right)}\varepsilon_0 \tag{E.6a}$$

$$D_1^2 = \frac{\beta_2}{\alpha_4}\varepsilon_0 + \frac{\alpha_5}{\alpha_4}\frac{1}{r_1^2}D_2^2 \tag{E.6b}$$

$$D_2^1 = \alpha_2\left(\beta_1\varepsilon_0 + D_1^2 + \frac{1}{r_1^2}D_2^2\right) \tag{E.6c}$$

$$D_1^1 = \alpha_1\frac{1}{r_0^2}D_2^1 - \beta_1\varepsilon_0 \tag{E.6d}$$

where the α_i are given by:

$$\alpha_1 = \frac{\mu_1}{\mu_1 + \lambda_1} \tag{E.7a}$$

$$\alpha_2 = \frac{1}{\left(\alpha_1\frac{1}{r_0^2} + \frac{1}{r_1^2}\right)} \tag{E.7b}$$

$$\alpha_3 = 2\left(\mu_1 + \lambda_1\right)\alpha_1\frac{1}{r_0^2} - 2\mu_1\frac{1}{r_1^2} \tag{E.7c}$$

$$\alpha_4 = \alpha_2\alpha_3 - 2(\mu_2 + \lambda_2) \tag{E.7d}$$

$$\alpha_5 = -\alpha_2\alpha_3 - 2\mu_2 \tag{E.7e}$$

and where the β_i are given by:

$$\beta_1 = \frac{\lambda_1}{2(\mu_1 + \lambda_1)} \tag{E.8a}$$

$$\beta_2 = \lambda_2 - \lambda_1 + \beta_1[2(\mu_2 + \lambda_2) - \alpha_2] \tag{E.8b}$$

where it is noted that, due to the similarities between the axial Young's modulus and stiffness components, the only difference in the displacement constants visible in Eqn. E.6 as compared to Eqn. E.3 is the expression for D_2^2 (i.e., only Eqn. E.6a differs from Eqn. E.3a) . However, the remaining D_j^i in Eqn. E.6 depend on D_2^2 and thus, the D_j^i of the axial stiffness component test are in fact quite different from those obtained for the axial Young's modulus test.

4. Axial Shear Modulus $N = 2$ Constants

The solution of Eqns 3.34 and 3.35 for $N = 2$ isotropic layers results in the displacement field constants of Eqn. 3.31 being given by:

$$D_2^2 = \frac{2\varepsilon_0}{\left(\frac{\alpha_4}{\alpha_3}\frac{1}{r_1^2} + \frac{1}{r_2^2}\right)} \tag{E.9a}$$

$$D_1^2 = \frac{\alpha_4}{\alpha_3}\frac{1}{r_1^2}D_2^2 \tag{E.9b}$$

$$D_2^1 = \frac{1}{\alpha_1}\left(D_1^2 + \frac{1}{r_1^2}D_2^2\right) \tag{E.9c}$$

$$D_1^1 = \frac{1}{r_0^2}D_2^1 \tag{E.9d}$$

where the α_i are given by:

$$\alpha_1 = \left(\frac{1}{r_0^2} + \frac{1}{r_1^2}\right) \tag{E.10a}$$

$$\alpha_2 = \left(\frac{1}{r_0^2} - \frac{1}{r_1^2}\right) \tag{E.10b}$$

$$\alpha_3 = \left(\frac{\alpha_2}{\alpha_1} - \frac{\mu_2}{\mu_1}\right) \tag{E.10c}$$

$$\alpha_4 = \left(-\frac{\alpha_2}{\alpha_1} - \frac{\mu_2}{\mu_1}\right) \tag{E.10d}$$

5. In-plane Shear Modulus $N = 2$ Constants

For determining the effective in-plane shear modulus, only one displacement field constant solution was needed (i.e., D_4^{N+1} or D_4^3 for $N = 2$). However, in order to determine the components of the concentration tensor associated with the in-plane shear modulus, all of the displacement constants are needed. As such, the solution of Eqns 3.45 and 3.46 for $N = 2$ isotropic layers results in the displacement field constants of Eqns. 3.42 and 3.59. However, the expressions are too lengthy to present in detail here.

6. Transverse Extension $N = 2$ Constants

Here, as with the in-plane shear modulus, the expressions for the displacement field constants are too lengthy to present in detail, but are obtained from Eqns. 3.57 and 3.58.

E2. Solutions for $N = 3$ Isotropic Homogeneous Layers

As a result of the solution of the boundary and matching conditions proceeding from the innermost surface of the composite to the outermost, the equations used to determine the first three displacement field constants for $N = 2$ (i.e., D_1^1, D_2^1, and D_1^2) remain the same for $N = 3$ and as such, so do the functional forms of the these displacement field constants. However, because these displacement constants ultimately

are dependent on the remaining constants (i.e., D_2^2, D_1^3, and D_2^3), the final values determined for the displacement constants for the $N = 3$ composite cylinder assemblage are quite different from those determined for $N = 2$. The $N = 3$ displacement constants for each test are summarized below.

1. In-plane Bulk Modulus $N = 3$ Constants

The solution of Eqns 3.6 and 3.7 for $N = 3$ isotropic layers results in the displacement field constants of Eqn. 3.2 being given by:

$$D_2^3 = \frac{\varepsilon_0}{\left(\alpha_6 \frac{1}{r_2^2} + \frac{1}{r_3^2}\right)} \tag{E.11a}$$

$$D_1^3 = \alpha_6 \frac{1}{r_2^2} D_2^3 \tag{E.11b}$$

$$D_2^2 = \frac{D_1^3 + \frac{1}{r_2^2} D_2^3}{\left(\alpha_3 \frac{1}{r_1^2} + \frac{1}{r_2^2}\right)} \tag{E.11c}$$

where D_2^1, D_1^2, and D_1^1 are given by Eqns. E.1b, E.1c, and E.1d, respectively, and where the α_i are given by:

$$\alpha_3 = -\frac{\alpha_1 \alpha_2 + \mu_2}{\alpha_1 \alpha_2 - (\mu_2 + \lambda_2)} \tag{E.12a}$$

$$\alpha_4 = \left(\alpha_3 (\mu_2 + \lambda_2) \frac{1}{r_1^2} - \mu_2 \frac{1}{r_2^2}\right) \tag{E.12b}$$

$$\alpha_5 = \left(\alpha_3 \frac{1}{r_1^2} + \frac{1}{r_2^2}\right) \tag{E.12c}$$

$$\alpha_6 = -\frac{\left(\frac{\alpha_4}{\alpha_5} + \mu_3\right)}{\left[\frac{\alpha_4}{\alpha_5} - (\mu_3 + \lambda_3)\right]} \tag{E.12d}$$

where α_1 and α_2 are given by Eqns. E.2a and E.2b, respectively.

2. Axial Young's Modulus $N = 3$ Constants

The solution of Eqns 3.23 and 3.7 for $N = 3$ isotropic layers results in the displacement field constants of Eqn. 3.20 being given by:

$$D_2^3 = \frac{\beta_4}{\alpha_{10}}\varepsilon_0 \tag{E.13a}$$

$$D_1^3 = \frac{\alpha_9}{\alpha_8}\frac{1}{r_2^2}D_2^3 + \beta_3\varepsilon_0 \tag{E.13b}$$

$$D_2^2 = \alpha_6\left(D_1^3 + D_2^3\frac{1}{r_2^2} - \frac{\beta_2}{\alpha_4}\varepsilon_0\right) \tag{E.13c}$$

where D_2^1, D_1^2, and D_1^1 are given by Eqns. E.3b, E.3c, and E.3d, respectively, and where the α_i are given by:

$$\alpha_6 = \frac{1}{\left(\frac{\alpha_5}{\alpha_4}\frac{1}{r_1^2} + \frac{1}{r_2^2}\right)} \tag{E.14a}$$

$$\alpha_7 = 2(\mu_2 + \lambda_2)\frac{\alpha_5}{\alpha_4}\frac{1}{r_1^2} - 2\mu_2\frac{1}{r_2^2} \tag{E.14b}$$

$$\alpha_8 = \alpha_6\alpha_7 - 2(\mu_3 + \lambda_3) \tag{E.14c}$$

$$\alpha_9 = -\alpha_6\alpha_7 - 2\mu_3 \tag{E.14d}$$

$$\alpha_{10} = 2(\mu_3 + \lambda_3)\frac{\alpha_9}{\alpha_8}\frac{1}{r_2^2} - 2\mu_3\frac{1}{r_3^2} \tag{E.14e}$$

with α_1 through α_5 of the same form as provided in Eqn. E.4 and where it should be noted that α_6 in Eqn. E.14a is different from α_6 in Eqn. E.4f. The β_i are given by:

$$\beta_3 = \lambda_3 - \lambda_2 + \frac{\beta_2}{\alpha_4}(\alpha_6\alpha_7 - 2(\mu_2 + \lambda_2)) \tag{E.15a}$$

$$\beta_4 = -\lambda_3 - 2(\mu_3 + \lambda_3)\beta_3 \tag{E.15b}$$

with β_1 and β_2 of the same form as provided in Eqn. E.5 and where it should be noted that β_3 in Eqn. E.15a is different from β_3 in Eqn. E.5c.

3. Axial Stiffness Component $N = 3$ Constants

The solution of Eqns 3.24 and 3.7 for $N = 3$ isotropic layers results in the displacement field constants of Eqn. 3.20 being again identical in functional form to those obtained for the axial Young's modulus for $N = 3$ provided in Eqns. E.3 and E.13 for D_1^1, D_2^1, and D_1^2 and for D_2^2 and D_1^3, respectively. The only term with a difference in functional form between the axial Young's modulus and axial stiffness component is D_2^3 which for the axial stiffness component is instead given by:

$$D_2^3 = -\frac{\beta_3}{\left(\frac{\alpha_9}{\alpha_8}\frac{1}{r_2^2} + \frac{1}{r_3^2}\right)}\varepsilon_0 \tag{E.16}$$

The α_i and β_i used for the axial stiffness component are therefore of identical functional form as those provided for the axial Young's modulus in Eqns E.4 and E.14 for α's one through five and six through nine, respectively, and in Eqns. E.5 and E.15 for β's one and two and three, respectively. Note that for the axial stiffness component, it was not necessary to define an α_{10} or β_4.

4. Axial Shear Modulus $N = 3$ Constants

The solution of Eqns 3.34 and 3.35 for $N = 3$ isotropic layers results in the displacement field constants of Eqn. 3.31 being given by:

$$D_2^3 = \frac{2\varepsilon_0}{\left(\frac{\alpha_8}{\alpha_7}\frac{1}{r_2^2} + \frac{1}{r_3^2}\right)} \tag{E.17a}$$

$$D_1^3 = \frac{\alpha_8}{\alpha_7}\frac{1}{r_2^2}D_2^3 \tag{E.17b}$$

$$D_2^2 = \frac{1}{\alpha_5}\left(D_1^3 + \frac{1}{r_2^2}D_2^3\right) \tag{E.17c}$$

where D_2^1, D_1^2, and D_1^1 are given by Eqns. E.9b, E.9c, and E.9d, respectively, and where the α_i are given by:

$$\alpha_5 = \left(\frac{\alpha_4}{\alpha_3} \frac{1}{r_1^2} + \frac{1}{r_2^2} \right) \tag{E.18a}$$

$$\alpha_6 = \left(\frac{\alpha_4}{\alpha_3} \frac{1}{r_1^2} - \frac{1}{r_2^2} \right) \tag{E.18b}$$

$$\alpha_7 = \left(\frac{\alpha_6}{\alpha_5} - \frac{\mu_3}{\mu_2} \right) \tag{E.18c}$$

$$\alpha_8 = \left(-\frac{\alpha_6}{\alpha_5} - \frac{\mu_3}{\mu_2} \right) \tag{E.18d}$$

with α_1 through α_4 of the same form as provided in Eqn. E.10

E3. Solutions for $N = 3$ Layers: Homogeneous-Graded-Homogeneous

1. In-plane Bulk Modulus $N = 3$ Constants

Solutions for the displacement field constants for a composite cylinder assemblage (Figure 19) with $N = 3$ where the interphase region has a gradation in material properties as given by $E_2(r) = \xi_n \, r^n$ are provided for the displacement fields associated with the determination of the in-plane bulk modulus. These solutions are developed by starting with the application of the innermost boundary and matching conditions and proceeding outward to the N^{th} layer boundary condition. As such, the constants are provided from the i^{th} to the first layer as each $(i+1)^{\text{th}}$ layer set of constants is expressed in terms of the N^{th} constants. The solution of Eqns 3.6 and 3.7 for $N = 3$ with a graded interphase layer results in the displacement field constants of Eqns. 3.2 and 3.75 (with $\gamma = \gamma_2$ and $\nu = \nu_2$) being given by:

$$D_2^3 = \frac{\varepsilon_0 \, {r_3}^2 \, \alpha_8}{\alpha_7 \, {r_3}^2 + \alpha_8} \tag{E.19a}$$

$$D_1^3 = \frac{\alpha_7 \, D_2^3}{\alpha_8} \tag{E.19b}$$

$$c_2 = \frac{\alpha_5 \left(D_1^3 \, {r_2}^2 + D_2^3\right)}{\alpha_6} \tag{E.19c}$$

$$c_1 = \frac{\alpha_4 \, c_2}{\alpha_5} \tag{E.19d}$$

$$D_2^1 = \frac{\alpha_1 \, c_1}{\alpha_3} + \frac{\alpha_2 \, c_2}{\alpha_3} \tag{E.19e}$$

$$D_1^1 = \frac{\mu_1 \, D_2^1}{{r_0}^2 \left(\mu_1 + \lambda_1\right)} \tag{E.19f}$$

where the α_i are given by:

$$\alpha_1 = {r_0}^2 \, r_1 \left({r_1}^{\varrho_1} \, \mu_1 + {r_1}^{\varrho_1} \, \lambda_1\right) \tag{E.20a}$$

$$\alpha_2 = {r_0}^2 \, r_1 \left({r_1}^{\varrho_2} \, \mu_1 + {r_1}^{\varrho_2} \, \lambda_1\right) \tag{E.20b}$$

$$\alpha_3 = \mu_1 \, {r_1}^2 + {r_0}^2 \, \mu_1 + {r_0}^2 \, \lambda_1 \tag{E.20c}$$

$$\begin{aligned} \alpha_4 = {} & 4 \, \alpha_2 \, \mu_1 \, {r_1}^2 \, {\nu_2}^2 + \xi_n \, {r_1}^n \, \nu_2 \, {r_0}^2 \, \alpha_3 \, r_1 \, {r_1}^{\varrho_2} + \xi_n \, {r_1}^n \, {r_0}^2 \, \alpha_3 \, r_1 \, {r_1}^{\varrho_2} \, \varrho_2 \\ & - \xi_n \, {r_1}^n \, {r_0}^2 \, \alpha_3 \, r_1 \, {r_1}^{\varrho_2} \, \varrho_2 \, \nu_2 + 2 \, {r_0}^2 \, \alpha_2 \, \mu_1 - 2 \, {r_0}^2 \, \alpha_2 \, \mu_1 \, \nu_2 - 4 \, {r_0}^2 \, \alpha_2 \, \mu_1 \, {\nu_2}^2 \\ & - 2 \, \alpha_2 \, \mu_1 \, {r_1}^2 + 2 \, \alpha_2 \, \mu_1 \, {r_1}^2 \, \nu_2 \end{aligned} \tag{E.20d}$$

$$\begin{aligned} \alpha_5 = {} & 2 \, \alpha_1 \, \mu_1 \, {r_1}^2 - \xi_n \, {r_1}^n \, \nu_2 \, {r_0}^2 \, \alpha_3 \, r_1 \, {r_1}^{\varrho_1} - \xi_n \, {r_1}^n \, {r_0}^2 \, \alpha_3 \, r_1 \, {r_1}^{\varrho_1} \, \varrho_1 \\ & + \xi_n \, {r_1}^n \, {r_0}^2 \, \alpha_3 \, r_1 \, {r_1}^{\varrho_1} \, \varrho_1 \, \nu_2 - 2 \, {r_0}^2 \, \alpha_1 \, \mu_1 + 2 \, {r_0}^2 \, \alpha_1 \, \mu_1 \, \nu_2 + 4 \, {r_0}^2 \, \alpha_1 \, \mu_1 \, {\nu_2}^2 \\ & - 2 \, \alpha_1 \, \mu_1 \, {r_1}^2 \, \nu_2 - 4 \, \alpha_1 \, \mu_1 \, {r_1}^2 \, {\nu_2}^2 \end{aligned} \tag{E.20e}$$

$$\alpha_6 = r_2 \left(\alpha_4 \, {r_2}^{\varrho_1} + {r_2}^{\varrho_2} \, \alpha_5\right) \tag{E.20f}$$

$$\begin{aligned} \alpha_7 = {} & -2 \, \mu_3 \, \alpha_6 \, \nu_2 + 2 \, \mu_3 \, \alpha_6 - \xi_n \, {r_2}^n \, r_2 \, \alpha_5 \, {r_2}^{\varrho_2} \, \varrho_2 \, \nu_2 + \xi_n \, {r_2}^n \, r_2 \, \alpha_4 \, {r_2}^{\varrho_1} \, \varrho_1 \\ & - 4 \, \mu_3 \, \alpha_6 \, {\nu_2}^2 + \xi_n \, {r_2}^n \, \nu_2 \, r_2 \, \alpha_4 \, {r_2}^{\varrho_1} - \xi_n \, {r_2}^n \, r_2 \, \alpha_4 \, {r_2}^{\varrho_1} \, \varrho_1 \, \nu_2 \\ & + \xi_n \, {r_2}^n \, r_2 \, \alpha_5 \, {r_2}^{\varrho_2} \, \varrho_2 + \xi_n \, {r_2}^n \, \nu_2 \, r_2 \, \alpha_5 \, {r_2}^{\varrho_2} \end{aligned} \tag{E.20g}$$

$$
\begin{aligned}
\alpha_8 = {r_2}^2 (&\xi_n {r_2}^n r_2 \alpha_5 {r_2}^{\varrho_2} \varrho_2 \nu_2 - \xi_n {r_2}^n r_2 \alpha_4 {r_2}^{\varrho_1} \varrho_1 + 2 \lambda_3 \alpha_6 \\
&- \xi_n {r_2}^n \nu_2 r_2 \alpha_5 {r_2}^{\varrho_2} - \xi_n {r_2}^n \nu_2 r_2 \alpha_4 {r_2}^{\varrho_1} + 2 \mu_3 \alpha_6 \\
&+ \xi_n {r_2}^n r_2 \alpha_4 {r_2}^{\varrho_1} \varrho_1 \nu_2 - \xi_n {r_2}^n r_2 \alpha_5 {r_2}^{\varrho_2} \varrho_2 - 4 \lambda_3 \alpha_6 {\nu_2}^2 - 2 \lambda_3 \alpha_6 \nu_2 \\
&- 2 \mu_3 \alpha_6 \nu_2 - 4 \mu_3 \alpha_6 {\nu_2}^2)
\end{aligned}
\tag{E.20h}
$$

APPENDIX F

MULTI-LAYER COMPOSITE CYLINDER: VOLUME/SURFACE EQUIVALENCIES

F1. In-plane Bulk Modulus

- Prove:

$$\kappa_{23}^{\text{eff}} = \frac{\langle \sigma_{rr} \rangle}{2 \langle \varepsilon_{rr} \rangle} = \frac{\sigma_{rr}^{N}\big|_{r=r_N}}{2\left(u_r^N|_{r=r_N} \Big/ r_N\right)} \tag{F.1}$$

- Proof:

The average stress is identified as:

$$\langle \sigma_{ij} \rangle = \frac{1}{V} \int_V \sigma_{ij} dV = \frac{1}{V} \int_V \sigma_{ik} x_{j,k} dV \tag{F.2}$$

$$\langle \sigma_{ij} \rangle = \frac{1}{V} \int_V \left(-\sigma_{ik,k} x_j + (\sigma_{ik} x_j)_{,k} \right) dV = \frac{1}{V} \int_V (\sigma_{ik} x_j)_{,k} \, dV \tag{F.3}$$

$$\langle \sigma_{ij} \rangle = \frac{1}{V} \int_S \sigma_{ik} x_j n_k dS = \frac{1}{V} \int_S t_i x_j dS \tag{F.4}$$

Therefore in cylindrical coordinates,

$$\langle \sigma_{rr} \rangle = \frac{1}{V} \int_S t_r r dS = \frac{1}{V} \int_S \sigma_{rr} r^2 d\theta dz \tag{F.5}$$

$$\langle \sigma_{rr} \rangle = \frac{1}{V} \int_S \sigma_{rr}|_{r=r_N} r_N^2 d\theta dz = \frac{1}{V} \sigma_{rr}\Big|_{r=r_N} r_N^2 \int_S d\theta dz \tag{F.6}$$

$$\langle \sigma_{rr} \rangle = \frac{2\pi L}{V} \, \sigma_{rr}|_{r=r_N} \, r_N^2 \tag{F.7}$$

The average strain is identified as:

$$\langle \varepsilon_{ij} \rangle = \frac{1}{V} \int_V \varepsilon_{ij} dV = \frac{1}{V} \int_V \frac{1}{2} \left(u_{i,j} + u_{j,i} \right) dV = \frac{1}{V} \frac{1}{2} \left[\int_V u_{i,j} dV + \int_V u_{j,i} dV \right] \tag{F.8}$$

$$\langle \varepsilon_{ij} \rangle = \frac{1}{V} \frac{1}{2} \left[\int_S u_i n_j dS + \int_S u_j n_i dS \right] \tag{F.9}$$

Therefore in cylindrical coordinates,

$$\langle \varepsilon_{rr} \rangle = \frac{1}{V} \frac{1}{2} \left[\int_S u_r n_r dS + \int_S u_r n_r dS \right] = \frac{1}{V} \int_S u_r n_r dS = \frac{1}{V} \int_S u_r r d\theta dz \tag{F.10}$$

$$\langle \varepsilon_{rr} \rangle = \frac{1}{V} \int_S u_r^N \big|_{r=r_N} r_N d\theta dz = \frac{1}{V} u_r^N \big|_{r=r_N} r_N \int_S d\theta dz = \frac{2\pi L}{V} u_r^N \big|_{r=r_N} r_N \tag{F.11}$$

Therefore

$$\kappa_{23}^{\text{eff}} = \frac{\langle \sigma_{rr} \rangle}{2 \langle \varepsilon_{rr} \rangle} = \frac{\frac{2\pi L}{V} \sigma_{rr}^N \big|_{r=r_N} r_N^2}{2 \left(\frac{2\pi L}{V} u_r^N \big|_{r=r_N} r_N \right)} = \frac{\sigma_{rr}^N \big|_{r=r_N}}{2 \left(u_r^N \big|_{r=r_N} \Big/ r_N \right)} \tag{F.12}$$

Since the original volume integrals are equivalent to the energy, so too then are these surface respresentations.

F2. Axial Young's Modulus

- Prove:

$$E_{11}^{\text{eff}} = \frac{\langle \sigma_{11} \rangle}{\langle \varepsilon_{11} \rangle} = \frac{\langle \sigma_{zz} \rangle}{\varepsilon_0} \tag{F.13}$$

- Proof:

The average strain is identified as:

$$\langle \varepsilon_{zz} \rangle = \frac{1}{V} \int_V \varepsilon_{zz} dV = \frac{1}{V} \left(\varepsilon_0 \pi r_0^2 L + \sum_{i=1}^{N} \int_{V_i} \varepsilon_{zz}^i dV \right) \tag{F.14}$$

$$\begin{aligned}\langle \varepsilon_{zz} \rangle &= \frac{1}{V}\left(\varepsilon_0 \pi r_0^2 L + \varepsilon_0 2\pi L \sum_{i=1}^{N} \int_{r_{i-1}}^{r_i} r dr\right) \\ &= \frac{2\pi L}{\pi r_N^2 L}\left(\frac{\varepsilon_0 r_0^2}{2} + \varepsilon_0 \sum_{i=1}^{N} \frac{r_i^2 - r_{i-1}^2}{2}\right)\end{aligned} \tag{F.15}$$

Therefore

$$\langle \varepsilon_{zz} \rangle = \frac{2}{r_N^2}\left(\frac{\varepsilon_0 r_0^2}{2} + \frac{\varepsilon_0 \left(r_N^2 - r_0^2\right)}{2}\right) = \varepsilon_0 \tag{F.16}$$

The average stress in the axial direction is:

$$\langle \sigma_{zz} \rangle = \frac{1}{V}\int_V \sigma_{zz} dV = \frac{1}{V}\sum_{i=1}^{N} \int_{V_i} \sigma_{zz}^i dV \tag{F.17}$$

$$\begin{aligned}\langle \sigma_{zz} \rangle &= \frac{1}{V}\left(2\pi L \sum_{i=1}^{N} \int_{r_{i-1}}^{r_i} \sigma_{zz}^i r dr\right) = \frac{2\pi L}{\pi r_N^2 L} \sum_{i=1}^{N} \int_{r_{i-1}}^{r_i} \sigma_{zz}^i r dr \\ &= \frac{2}{r_N^2} \sum_{i=1}^{N} \int_{r_{i-1}}^{r_i} \sigma_{zz}^i r dr\end{aligned} \tag{F.18}$$

Therefore,

$$E_{11}^{\text{eff}} = \frac{\langle \sigma_{11} \rangle}{\langle \varepsilon_{11} \rangle} = \frac{\langle \sigma_{zz} \rangle}{\langle \varepsilon_{zz} \rangle} = \frac{2}{\varepsilon_0 r_N^2} \sum_{i=1}^{N} \int_{r_{i-1}}^{r_i} \sigma_{zz}^i r dr \tag{F.19}$$

where it is noted that, as a result of the traction-free internal surface boundary condition, the stress in the void is zero and therefore does not enter the sum above.

F3. Axial Shear Modulus

- Prove:

$$\left\langle \sigma_{ij} \right\rangle \left\langle \varepsilon_{ij} \right\rangle = \left\langle \sigma_{ij}^{\text{eff}} \right\rangle \left\langle \varepsilon_{ij}^{\text{eff}} \right\rangle \tag{F.20}$$

can be expressed as

$$\mu_N \left.\frac{\partial u_z^N}{\partial r}\right|_{r=r_N} = \mu_{12}^{\text{eff}} \left.\frac{\partial u_z^{\text{eff}}}{\partial r}\right|_{r=r_N} \tag{F.21}$$

- Proof:

From the Hill-Mandel theorem.

$$\left\langle \sigma_{ij}\varepsilon_{ij} \right\rangle = \left\langle \sigma_{ij}^{\text{eff}}\varepsilon_{ij}^{\text{eff}} \right\rangle \tag{F.22}$$

$$\frac{1}{V}\int_V \sigma_{ij}\varepsilon_{ij}dV = \frac{1}{V}\int_V \sigma_{ij}^{\text{eff}}\varepsilon_{ij}^{\text{eff}}dV \tag{F.23}$$

$$\frac{1}{V}\int_S t_i u_i dS = \frac{1}{V}\int_S t_i^{\text{eff}}u_i^{\text{eff}}dS \tag{F.24}$$

So for the assumed axial displacement we have:

$$\frac{1}{V}\int_S \sigma_{rz}^N u_z^N r d\theta dz = \frac{1}{V}\int_S \sigma_{rz}^{\text{eff}}u_z^{\text{eff}} r d\theta dz \tag{F.25}$$

$$\frac{1}{V}\int_S \mu_N \frac{\partial u_z^N}{\partial r}u_z^N r d\theta dz = \frac{1}{V}\int_S \mu_{rz}^{\text{eff}}\frac{\partial u_z^{\text{eff}}}{\partial r}u_z^{\text{eff}} r d\theta dz \tag{F.26}$$

$$\begin{aligned}&\frac{1}{V}\int_S \mu_N \left(B_1^N - \frac{B_2^N}{r^2}\right)\cos(\theta)\left(B_1^N + \frac{B_2^N}{r}\right)\cos(\theta) r d\theta dz \\ &= \frac{1}{V}\int_S \mu_{rz}^{\text{eff}}\left(B_1^{\text{eff}} - \frac{B_2^{\text{eff}}}{r^2}\right)\cos(\theta)\left(B_1^{\text{eff}} + \frac{B_2^{\text{eff}}}{r}\right)\cos(\theta) r d\theta dz\end{aligned} \tag{F.27}$$

$$\begin{aligned}&\frac{1}{V}\mu_N \left(B_1^N - \frac{B_2^N}{r_N^2}\right)\left(B_1^N + \frac{B_2^N}{r_N}\right) r_N \int_S \cos^2(\theta)\, d\theta dz \\ &= \frac{1}{V}\mu_{rz}^{\text{eff}}\left(B_1^{\text{eff}} - \frac{B_2^{\text{eff}}}{r_N^2}\right)\left(B_1^{\text{eff}} + \frac{B_2^{\text{eff}}}{r_N}\right) r_N \int_S \cos^2(\theta)\, d\theta dz\end{aligned} \tag{F.28}$$

where

$$\int_S \cos^2(\theta)\, d\theta dz = \left(\frac{1}{2}\cos(\theta)\sin(\theta) + \frac{1}{2}\theta\right)_0^{2\pi} L \tag{F.29}$$

so that

$$\mu_N \left(B_1^N - \frac{B_2^N}{r_N^2}\right)\left(B_1^N + \frac{B_2^N}{r_N}\right) = \mu_{rz}^{\text{eff}}\left(B_1^{\text{eff}} - \frac{B_2^{\text{eff}}}{r_N^2}\right)\left(B_1^{\text{eff}} + \frac{B_2^{\text{eff}}}{r_N}\right) \tag{F.30}$$

$$\begin{aligned}&\mu_N\left(B_1^N-\frac{B_2^N}{r_N^2}\right)\cos(\theta)\left(B_1^N+\frac{B_2^N}{r_N}\right)\cos(\theta)\\&=\mu_{rz}^{\text{eff}}\left(B_1^{\text{eff}}-\frac{B_2^{\text{eff}}}{r_N^2}\right)\cos(\theta)\left(B_1^{\text{eff}}+\frac{B_2^{\text{eff}}}{r_N}\right)\cos(\theta)\end{aligned}\tag{F.31}$$

$$\mu_N\left.\frac{\partial u_z^N}{\partial r}\right|_{r=r_N}\left.u_z^N\right|_{r=r_N}=\mu_{rz}^{\text{eff}}\left.\frac{\partial u_z^{\text{eff}}}{\partial r}\right|_{r=r_N}\left.u_z^{\text{eff}}\right|_{r=r_N}\tag{F.32}$$

therefore,

$$\mu_N\left.\frac{\partial u_z^N}{\partial r}\right|_{r=r_N}=\mu_{12}^{\text{eff}}\left.\frac{\partial u_z^{\text{eff}}}{\partial r}\right|_{r=r_N}\tag{F.33}$$

F4. Axial Poisson's Ratio

- Prove:

$$\nu_{12}^{\text{eff}}=-\frac{\langle\varepsilon_{22}\rangle}{\langle\varepsilon_{11}\rangle}=-\frac{\langle\varepsilon_{rr}\rangle}{\langle\varepsilon_{zz}\rangle}=-\frac{\left.u_r^N\right|_{r=r_N}/r_N}{\varepsilon_0}\tag{F.34}$$

- Proof:

The average strain is identified as:

$$\langle\varepsilon_{ij}\rangle=\frac{1}{V}\int_V\varepsilon_{ij}dV=\frac{1}{V}\int_V\frac{1}{2}\left(u_{i,j}+u_{j,i}\right)dV=\frac{1}{V}\frac{1}{2}\left[\int_V u_{i,j}dV+\int_V u_{j,i}dV\right]\tag{F.35}$$

$$\langle\varepsilon_{ij}\rangle=\frac{1}{V}\frac{1}{2}\left[\int_S u_in_jdS+\int_S u_jn_idS\right]\tag{F.36}$$

The average strain in the radial direction is:

$$\langle\varepsilon_{rr}\rangle=\frac{1}{V}\frac{1}{2}\left[\int_S u_rn_rdS+\int_S u_rn_rdS\right]=\frac{1}{V}\int_S u_rn_rdS=\frac{1}{V}\int_S u_rrd\theta dz\tag{F.37}$$

$$\langle\varepsilon_{rr}\rangle=\frac{1}{V}\int_S\left.u_r^N\right|_{r=r_N}r_Nd\theta dz=\frac{1}{V}\left.u_r^N\right|_{r=r_N}r_N\int_S d\theta dz=\frac{2\pi L}{V}\left.u_r^N\right|_{r=r_N}r_N\tag{F.38}$$

The average strain in the axial direction is:

$$\langle \varepsilon_{zz} \rangle = \frac{1}{V} \int_V \varepsilon_{zz} dV = \frac{1}{V} \int_V \varepsilon_0 dV = \frac{V}{V} \varepsilon_0 = \varepsilon_0 \tag{F.39}$$

Therefore,

$$\nu_{12}^{\text{eff}} = -\frac{\langle \varepsilon_{22} \rangle}{\langle \varepsilon_{11} \rangle} = -\frac{\langle \varepsilon_{rr} \rangle}{\langle \varepsilon_{zz} \rangle} \tag{F.40}$$

$$\nu_{12}^{\text{eff}} = -\frac{\frac{2\pi L}{V} \left. u_r^N \right|_{r=r_N} r_N}{\varepsilon_0} = -\frac{\frac{2\pi L}{\pi r_N^2 L} \left. u_r^N \right|_{r=r_N} r_N}{\varepsilon_0} = -\frac{\left. u_r^N \right|_{r=r_N} \Big/ r_N}{\varepsilon_0} \tag{F.41}$$

APPENDIX G

ADDITIONAL DISPLACEMENT FIELDS FOR CONTINUOUS GRADED INTERPHASE REGIONS

The displacement fields satisfying the equilibrium equations for continuous graded interphase regions having a power-law gradation in Young's modulus and constant Poisson's ratio are provided herein for the axial Young's modulus, axial shear modulus, and axial Poisson's ratio, with displacement field for the in-plane bulk modulus previously given in Eqn. 3.75. The derivations of these displacement fields follow the same procedure as for the in-plane bulk modulus where the functional dependence of the displacement field and the desired material property gradation are substituted into the equilibrium equations, and the form of the displacement field obtained. The derivations can be found in work by Jaisuk and Kouider [168, 257].

The displacement field satisfying equilibrium for the axial Young's modulus boundary conditions is in fact similar to that provided in Eqn. 3.75 and is given by

$$\begin{aligned} u_r^i &= c_1\, r^{(n-n\nu+\varrho)} + c_2\, r^{(n-n\nu-\varrho)} - \nu\varepsilon_0 r \\ u_\theta^i &= 0 \\ u_z^i &= 0 \end{aligned} \tag{G.1}$$

where

$$\varrho = \frac{\sqrt{(\nu-1)[\nu(n+2)^2-(n^2+4)]}}{2(\nu-1)} \tag{G.2}$$

The displacement field satisfying equilibrium for the simple axial shear boundary conditions is given by

$$\begin{aligned} u_r^i &= 0 \\ u_\theta^i &= 0 \\ u_z^i &= \left(c_1\, r^{(-n+\sqrt{n^2+4})/2} + c_2\, r^{(-n-\sqrt{n^2+4})/2} \right) \cos(\theta) \end{aligned} \tag{G.3}$$

The displacement field employed for determining the transverse shear modulus is assumed to be of the form

$$\begin{aligned} u_r^i &= (c_1 r^{y_1} + c_2 r^{y_2} + c_3 r^{y_3} + c_4 r^{y_4}) \sin(2\theta) \\ u_\theta^i &= (\rho_1 c_1 r^{y_1} + \rho_2 c_2 r^{y_2} + \rho_3 c_3 r^{y_3} + \rho_4 c_4 r^{y_4}) \cos(2\theta) \\ u_z^i &= 0 \end{aligned} \tag{G.4}$$

where the y_j and ρ_j are yet be determined exponents and factors, respectively. The displacement field in Eqn. G.4 is substituted into the equilibrium equations. Both the r- and θ-direction equilibrium equation are non-trivial. As the c_j are constants determined from the boundary and matching conditions, the resulting equilibrium equations are satisfied by the cofactors of the c_j being zero. This results in two equations for each c_j which are then solved for the ρ_j and y_j. If the resulting ρ_j and y_j are real, they are substituted into the displacement field provided in Eqn. G.4, and the effective transverse shear modulus determined through the generalized self-consistent composite cylinder method.

If, however, the resulting ρ_j and y_j are imaginary, the displacement field in the graded interphase region for determining the effective transverse shear modulus is

taken from [257] and is given by

$$\begin{aligned}
u_r^i &= (c_1\cos(\beta_1\ \ln(r))r^{\alpha_1} - c_2\sin(\beta_2\ \ln(r))r^{\alpha_2} \\
&\quad + c_3\cos(\beta_3\ \ln(r))r^{\alpha_3} - c_4\sin(\beta_4\ \ln(r))r^{\alpha_4})\sin(2\theta) \\
u_\theta^i &= \{c_1[\phi_1\cos(\beta_1\ln(r)) - \psi_1\sin(\beta_1\ln(r))]r^{\alpha_1} \\
&\quad - c_2[\phi_2\sin(\beta_2\ln(r)) + \psi_2\cos(\beta_2\ln(r))]r^{\alpha_2} \\
&\quad + c_3[\phi_3\cos(\beta_3\ln(r)) - \psi_3\sin(\beta_3\ln(r))]r^{\alpha_3} \\
&\quad - c_4[\phi_4\sin(\beta_4\ln(r)) + \psi_4\cos(\beta_4\ln(r))]r^{\alpha_4}\}\cos(2\theta) \\
u_z^i &= 0
\end{aligned} \tag{G.5}$$

where the α_j and β_j are the real and imaginary parts, respectively, of the exponent y_j, i.e.

$$y_j = \alpha_j + \beta_j I \tag{G.6}$$

and where

$$\begin{aligned}
\phi_j &= (a1_j a2_j + b1_j b2_j)/(a2_j^2 + b2_j^2) \\
\psi_j &= (b1_j a2_j - a1_j b2_j)/(a2_j^2 + b2_j^2)
\end{aligned} \tag{G.7}$$

with

$$\begin{aligned}
a1_j &= -C - \alpha_j(B + A(\alpha_j - 1)) + A\beta_j^2 \\
a2_j &= E + \alpha_j D \\
b1_j &= -(\beta_j(B + A(\alpha_j - 1)) + \alpha_j\beta_j A) \\
b2_j &= \beta_j * D
\end{aligned} \tag{G.8}$$

and with

$$
\begin{aligned}
A &= 1-\nu \\
B &= (n+1)(1-\nu) \\
C &= ((n+5)\nu-3) \\
D &= -1 \\
E &= -2(n+2)\nu+3;
\end{aligned}
\tag{G.9}
$$

APPENDIX H

COMPUTATIONAL MICROMECHANICS FORMULATION

The finite element cases are run with ADAGIO [258], Sandia National Laboratories' finite element software for linear and nonlinear quasi-static analysis of structures. A summary of the equations solved in ADAGIO is provided in reference [162]. Here, examples of the meshes and boundary conditions employed in the computational micromechanics approach implemented in ADAGIO are provided.

Sample meshes of the well-dispersed RVE for both the hollow and effective fiber CNT representations are shown in Figure 71. These meshes are three-dimensional with a single element used in the Z-direction, which is sufficient as no gradients in the Z-direction result when the periodic boundary conditions are applied. ADAGIO offers a range of elements, but here the computations are performed using the under-integrated, mean quadrature 8-node brick element. The hourglass modes are controlled via a fictitious hourglass force scheme similar to that described in [259] and [260]. It is noted that, new meshes are generated for each fiber volume fraction for which the effective elastic properties are determined. As the fiber dimensions are considered to be fixed, changes in fiber volume fraction result in changes in the size of the RVE.

In order to facilitate the discussion of the applied periodic boundary conditions, the six faces will be referred to as $+X/-X$, $+Y/-Y$, and $+Z/-Z$ which are perpendicular to the X-, Y-, and Z-axes, respectively. Also, a numbering scheme will be used for the principal material directions such that 1 refers to the fiber axis direction (Z-axis) and 2 and 3 correspond to the X- and Y-axes, respectively, or the transverse axes. A total of six numerical simulations are used to determine the effective

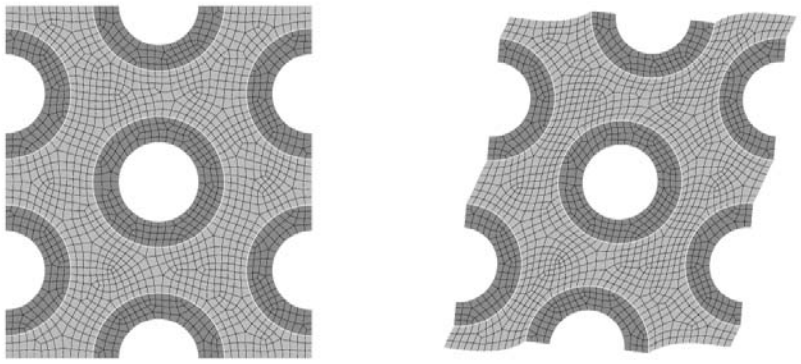

(a) Hollow Fiber Representation

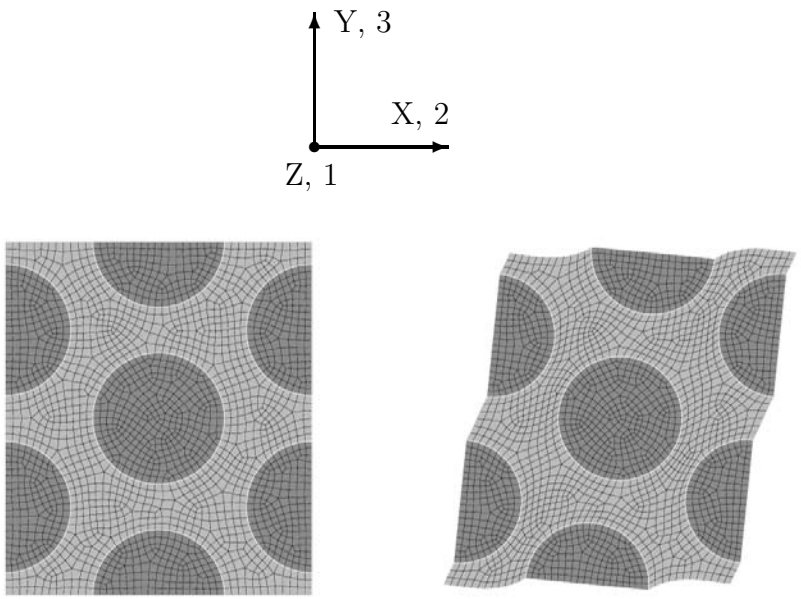

(b) Effective Fiber Representation

Fig. 71. Original and deformed FEA meshes. Meshes are for aligned, well-dispersed hollow fiber (3554 nodes/1648 elements) and effective fiber (4496 nodes/2154 elements) representations at 50% volume fraction. The deformed meshes are for the case of applied shear, $\overline{\gamma}_{23}$, of 1%, with 20X displacement magnification demonstrating that straight edges are not required to remain straight for the applied periodic boundary conditions.

composite properties at a given fiber volume fraction for both the well-dispersed and clustered fiber arrangements. Each simulation corresponds to the application of an average strain state with a single non-zero component. These six simulations are necessary to determine the complete set of engineering elastic constants of an orthotropic material, i.e., the three Young's moduli (E_{11}, E_{22}, and E_{33}), the three Poisson's ratios (ν_{12}, ν_{23}, and ν_{31}) and the three shear moduli (G_{12}, G_{23}, and G_{31}), from which all other effective moduli can be calculated. The resulting sets of volume averaged stress components for a an applied average strain are then determined from the FEA solution, allowing the components of the corresponding column of the effective stiffness matrix to be obtained by dividing the average stress components by the applied average strain. Once the effective stiffness is computed, it is inverted to obtain the effective compliance from which the corresponding engineering effective elastic constants are determined. It should be noted that in the well-dispersed case, where the effective elastic properties are transversely isotropic, only three simulations are needed to obtain the five independent engineering properties. The additional three tests become consistency checks for the well-dispersed cases.

The periodic boundary conditions can be expressed in terms of the displacement components on face pairs. For example, taking the origin of the mesh coordinate system to be at the RVE centroid, the periodic conditions for the $+X/-X$ face pair can be expressed as:

$$\begin{aligned} u(L_X^o/2, Y, Z) &= u(-L_X^o/2, Y, Z) \\ v(L_X^o/2, Y, Z) &= v(-L_X^o/2, Y, Z) \\ w(L_X^o/2, Y, Z) &= w(-L_X^o/2, Y, Z) \end{aligned} \tag{H.1}$$

where u, v, and w are the components of the displacement in the X, Y, and Z directions, respectively, and where the undeformed mesh has an original length along the X-axis of L_X^o. Similarly, on the $+Y/-Y$ and $+Z/-Z$ face pairs, the periodic conditions are expressed as:

$$\begin{aligned} u(X, L_Y^o/2, Z) &= u(X, -L_Y^o/2, Z) \\ v(X, L_Y^o/2, Z) &= v(X, -L_Y^o/2, Z) \\ w(X, L_Y^o/2, Z) &= w(X, -L_Y^o/2, Z) \end{aligned} \tag{H.2}$$

and

$$\begin{aligned} u(X, Y, L_Z^o/2) &= u(X, Y, -L_Z^o/2) \\ v(X, Y, L_Z^o/2) &= v(X, Y, -L_Z^o/2) \\ w(X, Y, L_Z^o/2) &= w(X, Y, -L_Z^o/2) \end{aligned} \tag{H.3}$$

respectively, and where the undeformed mesh has original lengths of L_Y^o, and L_Z^o along the Y and Z coordinate axes. In order to perform one of the required six numerical simulations, the desired non-zero average strain component is introduced into the periodic conditions in the form of a relative displacement. For example, in order to determine the first column of the stiffness tensor, the only non-zero average strain, $\bar{\varepsilon}_{11}$, is applied by the addition of a relative displacement between $+Z$ and $-Z$ in the w component of Eqn. H.3, i.e.,

$$w(X, Y, L_Z^o/2) = w(X, Y, -L_Z^o/2) + \varepsilon^o L_Z^o \tag{H.4}$$

where the relative displacement is given by $w_{rel} = \varepsilon^o L_Z^o$, where ε^o is the applied strain. For this case, the remaining displacement components in Eqn. H.3 are unaltered, and the same is true of all of the displacement components in Eqns. H.1 and H.2. The

other columns of the stiffness tensor are determined in much the same way, with the only difference being to which face and to which displacement component a relative displacement is applied. The specifics of the periodic boundary conditions (PBCs) used in each simulation to apply the desired component of average strain ($\bar{\varepsilon}_{ij}$) are listed in Table XI, where the corresponding relative displacements are denoted by u_{rel}, v_{rel}, and w_{rel}. Note that most nodes belong to a single PBC pair ($+Z/-Z$), while some belong to two PBC pairs ($+Z/-Z$ with either $+X/-X$ or $+Y/-Y$) and the eight corner nodes belong to all three PBC pairs. Also note that the inner surface of the fiber in the hollow fiber FEA representation of the CNTs is taken to be stress free. Finally, note that initially straight edges need not remain straight under the applied periodic boundary conditions as is also shown in Figure 71.

Table XI. Details of applied periodic boundary conditions in FEA analysis. The non-zero relative displacements necessary to achieve the desired average strain over the RVE are given. All unlisted relative displacements are specified to be zero. In all numerical simulations for a given RVE, a single applied strain level of ε^o is used and L_X^o, L_Y^o, and L_Z^o refer to undeformed RVE lengths in the X-, Y-, and Z-directions, respectively, and u_{rel}, v_{rel}, and w_{rel} are the corresponding relative displacements.

Simulation	Average Applied Strain	$+X/-X$ PBC	$+Y/-Y$ PBC	$+Z/-Z$ PBC
1. Z-Direction Extension	$\bar{\varepsilon}_{11} = \bar{\varepsilon}_{zz} = \varepsilon^o$	–	–	$w_{rel} = \varepsilon^o L_Z^o$
2. X-Direction Extension	$\bar{\varepsilon}_{22} = \bar{\varepsilon}_{xx} = \varepsilon^o$	$u_{rel} = \varepsilon^o L_X^o$	–	–
3. Y-Direction Extension	$\bar{\varepsilon}_{33} = \bar{\varepsilon}_{yy} = \varepsilon^o$	–	$v_{rel} = \varepsilon^o L_Y^o$	–
4. ZX Shear	$2\bar{\varepsilon}_{12} = 2\bar{\varepsilon}_{zx} = \varepsilon^o$	$w_{rel} = \varepsilon^o L_X^o$	–	–
5. XY Shear	$2\bar{\varepsilon}_{23} = 2\bar{\varepsilon}_{xy} = \varepsilon^o$	–	$u_{rel} = \varepsilon^o L_Y^o$	–
6. YZ Shear	$2\bar{\varepsilon}_{31} = 2\bar{\varepsilon}_{yz} = \varepsilon^o$	–	$w_{rel} = \varepsilon^o L_Y^o$	–

VITA

Gary Don Seidel is a native of Houston, Texas. He enrolled at Texas A&M University in College Station, Texas in the fall of 1994 and earned a Bachelor of Science degree in Aerospace Engineering in the spring of 1999, graduating Magna Cum Laude. After completing his B.S. degree, he entered graduate school at Texas A&M University earning a Master of Science degree in Aerospace Engineering in August of 2002 under the guidance of Dr. David H. Allen for his thesis titled, *A Model for Predicting the Evolution of Damage in the Plastic Bonded Explosive LX17*. During this time, he participated in two Sandia National Laboratories summer internship programs, in the summer of 1999 as part of the Science and Technology Outreach Program at the Albuquerque, New Mexico facility and in the summer of 2000 as part of the Engineering Sciences Summer Institute at the Livermore, California facility. Both internships were focused on application of cohesive zone modeling of damage in materials, the former in rock salt and the latter in rubber o-rings.

In August of 2002, Gary was awarded the inaugural Sandia National Laboratories/Texas A&M University Doctoral Fellowship in Engineering and began his doctoral studies in the Aerospace Engineering department at Texas A&M under the guidance of Dr. Dimitris Lagoudas. His research interests include mechanics of materials and continuum mechanics, micromechanics analysis of composites, fracture mechanics using cohesive zone models, bridging atomistic and continuum length and time scales in nanocomposites, and multiscale modeling of multifunctional composites. A current curriculum vitae containing detailed lists of his publications and conference presentations is available by contacting Gary Don Seidel via email at Gary.Seidel@gmail.com. He may also be reached at the Aerospace Engineering Department, Texas A&M University 3141 TAMU College Station, TX 77843-3141.